ARMMIC25

Applied Research in Mining and Metallurgy International Congress

Chief Editor:
Julio Valenzuela

Editors:
Mohammad Maleki · Manuel Cánovas · Daniel Calisaya

ARMMIC25

Applied Research in Mining and Metallurgy International Congress

Chief Editor:
Julio Valenzuela

Editors:
Mohammad Maleki · Manuel Cánovas · Daniel Calisaya

Applied Research in Mining and Metallurgy International Congress
November 04-07, 2025
Antofagasta, Chile

Chief Editor:
Julio Valenzuela

Editors:
Mohammad Maleki · Manuel Cánovas · Daniel Calisaya

ISBN: 978-956-287-509-7

Download the digital version here

Universidad Católica del Norte
https://ror.org/02akpm128

Index


DOCTORADO EN
minería
UCN

UNIVERSIDAD CATÓLICA DEL NORTE
CHILE

CNA
UNIVERSIDAD ACREDITADA
NIVEL DE EXCELENCIA
GESTIÓN INSTITUCIONAL
DOCENCIA DE PREGRADO
DOCENCIA DE POSTGRADO
INVESTIGACIÓN
VINCULACIÓN CON EL MEDIO

UCN

UCN

About the Organizers

The Applied Research in Mining and Metallurgy International Congress, ARMMIC25, has been organized by the PhD Program in Mining of the Department of Metallurgical and Mining Engineering at Universidad Católica del Norte (UCN).

Established in 2022, the PhD Program in Mining at UCN was created to train researchers capable of producing high-quality scientific knowledge in the mining field. The program aims to prepare professionals from diverse disciplines to address the complex challenges faced by the mining industry, promoting inter- and multidisciplinary collaboration as a core value.

The program is supported by an experienced academic team from the Department of Metallurgical and Mining Engineering (DIMM), renowned for its expertise and commitment to applied research. It also benefits from state-of-the-art infrastructure, advanced laboratory equipment, and a faculty composed predominantly of PhD-level academics. The program's development is further strengthened by funding from Programa de Fortalecimiento ANID 86220023, which supports its scientific and technological consolidation.

The PhD Program in Mining focuses on training researchers to tackle strategic challenges in the mining sector, such as declining ore grades, limited energy resources, and the integration of new technologies. Its comprehensive and multidisciplinary approach covers the entire mining cycle—from extraction to tailings management—encouraging sustainable and innovative solutions in collaboration with industry.

In September 2025, the program was accredited by the Comisión Nacional de Acreditación (CNA-Chile) for a period of three years, recognizing its academic excellence and its contribution to the scientific and technological advancement of mining in Chile.

The organization of ARMMIC25 reflects the vision and commitment of the PhD Program in Mining at Universidad Católica del Norte to promote applied research, strengthen collaboration with the mining industry, and contribute to sustainable development at both national and regional levels.

Organizing Committee

Julio Valenzuela, PhD in Mining Director
Ítalo Montofré, Mining Business School Program Director
Manuel Cánovas, Academic Mining (DIMM)
Daniel Calisaya, Academic Metallurgy (DIMM)
Gabriela Reyes, Coordinator PhD in Mining
Gissella Cárdenas, Administrative Support
María Angélica Carvajal, Finance
Carlos Leiva, Head of the Mining Civil Engineering Program
Cecilia Cerda, Head of the Metallurgical Civil Engineering Program
Mohammad Maleki, Research Department Director (DIMM)

Scientific Committee

René Rojas, Professor, Faculty of Chemistry and Pharmacy. Pontificia Universidad Católica de Chile.
Enrique Jélvez, Professor, Department of Mining Engineering. Pontificia Universidad Católica de Chile.
Xavier Emery, Professor, Department of Mining Engineering – AMTC. Universidad de Chile.
Óscar Restrepo, Professor, Department of Materials and Minerals. Universidad Nacional de Colombia.
Emmanouil Varouckakis, Professor, School of Mineral Resources Engineering. Technical University of Crete.
Francisco Tapia, Professor, Doctorate in Industrial Engineering. Universidad Católica del Norte.
Nadia Mery, Professor, Department of Mining Engineering. Universidad de Chile.
Aldo Quelopana, Professor, Department of Systems and Computing Engineering. Universidad Católica del Norte
Evelyn Melo, Professor, Department of Engineering and Metallurgy. Universidad Católica del Norte.
Jonathan Cisterna, Professor, Department of Chemistry. Universidad Católica del Norte.
Nasser Madani, Professor, School of Mining & Geosciences. Nazarbayev University.
Vanesa Bazan, Professor, PhD Mineral Processing. Universidad Nacional de San Juan, Argentina
Luis Silva, Professor, Department of Mechanical Engineering. Universidad de La Serena.
Sandra Fuentes, Professor, Department of Pharmaceutical Sciences. Universidad Católica del Norte
Gerardo Zamora, Emeritus Professor, Department of Metallurgy and Mines. Universidad Técnica de Oruro, Bolivia.
Aldo Quiero, Professor, Civil Mining Engineering. Universidad Arturo Prat.
Sara Kasmageyazdi, Professor, Mining Engineering Geostatistics DICAM. University of Bologna.
Francisco Remonsellez, Professor, Doctorate in Sustainable Engineering. Universidad Católica del Norte.
Claudio Acuña Pérez, Professor, Department of Chemical and Environmental Engineering. Universidad Técnica Federico Santa Maria
Eduardo Campos Correa, Professor, Department of Geological Science. Universidad Católica del Norte.

Foreword

The first edition of the International Congress on Applied Research in Mining and Metallurgy (ARMMIC) represents a significant milestone in the ongoing effort to strengthen scientific and technological research aimed at addressing both current and future challenges in the mining sector. This event was conceived as an initiative of the Doctorate in Mining Program at Universidad Católica del Norte (UCN), with the purpose of creating a platform for academic exchange and innovation among universities, research centers, industry, and the public sector — all committed to fostering a more sustainable, efficient, and environmentally responsible mining industry.

This compendium brings together the works presented during this inaugural edition, encompassing a wide range of topics: from material characterization and advanced metallurgical processes to the recovery of critical elements, waste valorization, the development of clean technologies, and the integration of circular economy principles into production processes. Each contribution reflects the scientific rigor of its authors and their collective determination to generate applicable knowledge that drives progress within the mining and metallurgical sectors.

ARMMIC aspires to become a permanent meeting point for the scientific and technological community engaged in mining-related research. Its mission extends beyond the mere presentation of research outcomes: it seeks to inspire new ideas, foster international collaboration networks, and contribute to the education of highly qualified professionals capable of leading the transition toward twenty-first-century mining.

We trust that this first edition marks the beginning of a lasting tradition that will continue to evolve in response to the changing needs of both the territory and the industry. We extend our sincere gratitude to all the researchers, students, companies, and institutions that have believed in this project and who, through their enthusiasm and commitment, have made this publication possible.

This document stands as the beginning of a shared journey in which science, technology, and collaboration converge in the service of society — with the ultimate goal of building a sustainable future for mining.

Dr. Julio Valenzuela Elgueta

Director of ARMMIC 25

Preface

The Applied Research in Mining and Metallurgy International Congress, ARMMIC25, which has taken place from November 4 to 7 in the city of Antofagasta, brought together academics, researchers, students, and industry leaders from the mining and metallurgical sectors of Chile and the world. As one of the most significant scientific events in the Northern Macrozone, it aims to disseminate advancements in applied research, address global challenges in the sector, and strengthen strategic collaborations with key stakeholders to foster innovation and sustainable development.

Organized by the PhD Program in Mining of the Department of Metallurgical and Mining Engineering at Universidad Católica del Norte, ARMMIC25 has established itself as the premier scientific event in the Northern Macrozone, uniting academics, researchers, students, and representatives from the national and international mining industry to share advancements, build strategic alliances, and promote innovation and sustainability in the sector.

Discussions and contributions have been framed around critical themes for the future of the industry: Mining Engineering, Metallurgical Engineering, Green Mining, Mining 4.0, Materials Science, and Applied Nanotechnology. These areas have allowed an interdisciplinary approach to the technical, environmental, and social challenges faced by contemporary mining.

The importance of this congress lies in its ability to promote innovative solutions to the increasing challenges faced by the mining and metallurgical industries. ARMMIC25 has positioned itself as a reference event, enabling the creation of academic and industrial alliances and driving the generation of scientific and technological knowledge for the benefit of the productive sector and society.

This book of abstracts embodies the outcome of that collective effort and stands as a testimony to the commitment of the scientific and professional community to the mining industry of today and tomorrow.

Acknowledgments

The Organizing Committee of the Applied Research in Mining and Metallurgy International Congress (ARMMIC25) extends its deepest gratitude to all authors whose contributions made this Book of Abstracts possible. Their dedication and scholarly work have shaped a diverse set of topics that reflect the current advancements and challenges in mining and metallurgy, giving life to the first international congress of its kind organized by the Ph.D. Program in Mining of the Department of Metallurgical and Mining Engineering at Universidad Católica del Norte.

We extend our appreciation to every researcher for their commitment and active participation in the various thematic areas that enriched this event. The quality and depth of the papers presented stand as testimony to the scientific excellence and collaborative spirit that define our academic community.

Our sincere thanks go to the Scientific Committee, whose careful review and correction of the papers ensured the academic quality of this publication, and to all individuals involved in the organization of this congress for their invaluable dedication and teamwork.

We also wish to give special recognition to the Plenary and Keynote Speakers who have joined us from different regions of Chile and around the world to share their insights and experiences:

Plenary Speakers: Julián M. Ortiz-Cabrera, Yousef Ghorbani and Eduardo Bitran Colodro.

Keynote Speakers: Aldonza Jaques, Nadia Mery Guerrero, René Rojas Guerrero and Iván Cornejo García.

Their participation has greatly enriched the discussions at ARMMIC25 and provided inspiring perspectives on the future of the mining and metallurgical sectors.

We gratefully acknowledge the generous support of our Sponsors, whose contribution has been essential to the success of ARMMIC25:

Copper Category: SQM Litio, Lithium I+D+i UCN

Lithium Category: Glencore Lomas Bayas, Glencore Alto Norte, Sierra Gorda SCM

Molybdenum Category: Geoblast, Heuma

We also recognize the valuable collaboration of our Institutional Supporters:

Ministry of Mining; Ministry of Science, Technology, Knowledge and Innovation; Sernatur; Corfo; Sonami; Antofagasta Industrial Association (AIA); Fundación Jóvenes Mineros; WIM (Women in Mining); PCT (Fundación Parque Científico-Tecnológico); ENM (Escuela de Negocios Mineros); UCN Communications; UCN Postgraduate Office; and UCN Community Engagement Department.

We extend our thanks to our media partners, El Mercurio de Antofagasta and Norte Minero Minería & Energía, for their support in promoting this important event.

Finally, we are proud to highlight our partnership with the Journal of Sustainable Mining, with whom we share the mission of fostering applied research, innovation, and sustainability in the mining and metallurgical industries.

The Organizing Committee expresses its heartfelt gratitude to all those who have been part of this first edition of ARMMIC, a milestone that marks the beginning of a new stage of scientific collaboration and development in the Northern Macrozone and the global mining community.

Chapter 01

Mining Engineering

Accuracy of Gaussian Transformations in Modeling Spatial and Statistical Structures in Multivariate Simulation

Jordan Plaza-Carvajal[1*], Mohammad Maleki[1], and Xavier Emery[2,3]

1. Department de Metallurgical and Mining Engineering, Universidad Católica del Norte, Antofagasta, Chile.
2. Department of Mining Engineering, Universidad de Chile, Santiago, Chile.
3. Advanced Mining Technology Center, Universidad de Chile, Santiago, Chile.

**Corresponding author at: Department of Metallurgical and Mining Engineering, Universidad Católica del Norte, Angamos 0610, Antofagasta, Chile. E-mail address: jordan.plaza@ce.ucn.cl.*

ABSTRACT

Accurate modeling of geological and geometallurgical variables is fundamental for reliable mineral resource evaluation, mining project development, and operational decision-making. To achieve this, Gaussian transformations, such as the univariate Normal Score Transformation (NST) and the Projection Pursuit Multivariate Transformation (PPMT), are often employed to condition data prior to geostatistical simulation. Despite their effectiveness, each method entails inherent trade-offs. The NST, though simple and widely used, tends to overlook the interdependencies among variables. Conversely, the PPMT offers a more sophisticated treatment of multivariate relationships but may distort the spatial continuity of geological features. This study undertakes a comparative assessment of NST and PPMT using a real-world case study of a lateritic nickel deposit. Results indicate that, while PPMT more faithfully reproduces collocated statistical relationships, it simultaneously alters the spatial structure of the modeled variables. To address this challenge, we examine the incorporation of geological domaining as a practical enhancement to NST, enabling the separate modeling of distinct data populations in accordance with geological boundaries. Our findings highlight that no single Gaussian transformation method universally outperforms others. Instead, problem-specific and context-sensitive approaches are required to achieve balanced models that preserve both statistical coherence and spatial realism.

Keywords: Multivariate geostatistics; Normal Score Transformation; Projection Pursuit Multivariate Transformation; Gaussian transformations; Complex dependency structures.

Introduction

The development of spatial prediction models for geological and geometallurgical variables, together with the quantification of their uncertainty, is a decisive factor in the success of mining projects and operations (Boisvert et al., 2013; Talebi et al., 2016; Mery et al., 2017; Preece et al., 2023). Geostatistical simulation has been used to address this objective, producing multiple equiprobable scenarios (realizations) for the spatial behavior of the variables (Journel, 1974). To model quantitative variables, such as ore grades, the multi-Gaussian model (Chilès & Delfiner, 2012) has become the standard, due to its conceptual simplicity, straightforward implementation, and ability to reproduce spatial correlation patterns. For univariate cases, the model assumes a monotonical transformation

from the original space to a Gaussian random field. This transformation, known as normal score transformation (NST), orders the data, calculates percentiles, and maps values to equivalent quantiles in a standard normal distribution. Although effective for single-variable modeling, this approach often fails in multivariate cases, as the joint multivariate normality assumption may be violated when variables exhibit complex dependencies and significant correlations. For this reason, selecting a transformation method that goes beyond independently applying NST to each variable is essential in multivariate simulation. Some strategies involve transforming NST outputs into orthogonal factors applying MAF (Minimum/maximum Autocorrelation Factors) (Desbarats & Dimitrakopoulos, 2000) or U-WEDGE (Mueller & Ferreira, 2012), which can then be modeled as independent Gaussian variables. More recently, several joint transformation techniques have been developed to preserve complex relationships, including Stepwise Conditional Transformation (SCT) (Leuangthong & Deutsch, 2003), Projection Pursuit Multivariate Transformation (PPMT) (Barnett et al., 2014), Flow Anamorphosis (FA) (van den Boogaart et al., 2017), Rotation-Based Iterative Gaussianization (RBIG) (Cook et al., 2021), and Spatial Multivariate Morphing Transformation (SMMT) (Avalos & Ortiz, 2023). These methodologies have been successfully applied in mineral resource modeling, where they have demonstrated their capacity to improve the characterization of spatial variability, enhance the accuracy of resource estimation, and provide more robust frameworks for decision-making in both exploration and production stages (Sepulveda et al., 2017; Hosseini and Asghari, 2019; Talebi et al., 2019; Abulkhair et al., 2023).

The present study evaluates the performance of PPMT in comparison with two approaches based on the NST algorithm. The first approach applies the standard procedure, while the second introduces a modification in which NST is implemented through the partitioning of the original dataset into simulation domains. From a methodological perspective, such partitioning not only enhances the adaptability of the algorithm to heterogeneous geological contexts but also mitigates potential biases associated with assuming uniform statistical behavior across the entire dataset. Although NST was not designed to maintain inter-variable dependencies, its ease of use explains its continued adoption in the mining industry. Assessing procedural adaptations that enhance their capacity to reproduce complex multivariate structures remains a relevant and promising research direction.

Methodology

Successive Univariate Normal Score Transformations

The first approach consists of independent univariate transformations of the original variables

$$Y_i = G^{-1}[F_i(Z_i)], \quad i = 1, \dots, N,$$

into Gaussian variables applying the following monotonic transformation (Chilès & Delfiner, 2012): where $Z_i,\dots,Z_N$ denote the original variables, G is the standard Gaussian cumulative distribution function, F_i is the cumulative distribution function of Z_i, and Y_i is the corresponding transformed variable. Original data is sorted in ascending order, and the cumulative probability is calculated. For each value, this probability is matched with their Gaussian equivalent. To return from Gaussian to original space, an inverse transformation is applied.

Multivariate Gaussian transformations

The second approach is based on an iterative Gaussianization known as PPMT (Barnett et al., 2014). This method is divided into two stages. In the first stage, or preprocessing, the variables are normal-score transformed and orthogonalized to generated uncorrelated factors. Then, in the second stage, or projection pursuit, the PPMT searches for the least Gaussian projection in each factor and iteratively applies a normal score transformation to standardize every projection. This stage stops when a projection index, that measures Gaussianity, reaches convergences or when the user-defined quantity of iterations has been reached Additionally, a decorrelation process is performed at a second lag distance using the Minimum/Maximum Autocorrelation Factors (MAF) method (Desbarats & Dimitrakopoulos, 2000). In general, the Gaussian factors are obtained through:

$$\begin{pmatrix} Y_i \\ \vdots \\ Y_N \end{pmatrix} = \Psi \begin{pmatrix} Z_i \\ \vdots \\ Z_N \end{pmatrix},$$

where Ψ is a mapping of each variable from the original space to a Gaussian one. The back-transformation of the factors is achieved by inverse mapping.

General workflow overview

To generate the simulations for the proposed case study, a sequence of stages was defined, beginning with data preparation and exploratory analysis. This initial step provides the statistical reference framework required for subsequent comparisons with the results. Once the data are prepared, the next stage involves applying transformations to the original dataset using the selected algorithms (NST and PPMT-MAF) in order to derive the corresponding Gaussian variables/factors.

Non-conditional simulations are then executed within the Gaussian value space, after which the simulated data are transformed back to the original variable space. The outcomes are systematically analyzed to evaluate their consistency and reliability. Based on these results, a case-specific strategy is proposed to enhance the performance of the NST algorithm, aiming to refine both efficiency and predictive capacity. This strategy is subsequently applied, and its outcomes are thoroughly assessed and discussed.

This sequential approach ensures not only the reproducibility of the methodology but also enables the identification of strengths and limitations within each stage. By integrating iterative refinement and critical evaluation, the process contributes to a more robust understanding of the algorithms' behavior under practical conditions.

Results and Discussions

Case study: Nickel-laterite deposit

A nickel-laterite deposit has been characterized through 700 blast hole samples with information on alumina (Al_2O_3), iron (Fe), and silica (SiO_2). Declustering was performed initially and the declustered statistical parameters of the variables are extracted for further analysis. Figure 1 presents the spatial location of samples and the relationships between the studied variables, where the complex behavior that governs these relationships, and the high levels of correlation among the variables, are clearly observable.

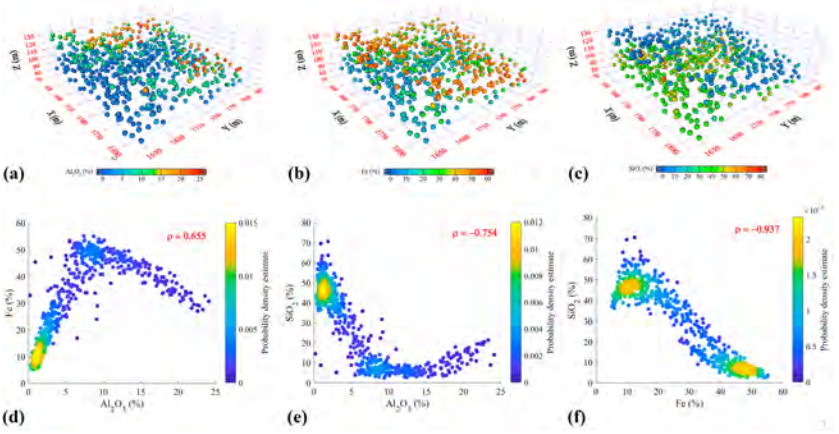

Figure 1. Spatial distribution of **(a)** Al_2O_3, **(b)** Fe, and **(c)** SiO_2. Underneath **(d, e, f)** the bivariate relationships and correlation coefficients are presented. Different bivariate complexities, such as non-linearity and heteroscedasticity, can be noted.

In the first stage, the original data are transformed into Gaussian variables by applying the successive univariate normal score transformations based on the NST algorithm. Figures 2d, 2e, and 2f present scatter plots of the transformed variables. To better illustrate the effects of this transformation, the figures are color-coded using one of the variables in each plot as a reference. This visualization highlights the modifications produced by the transformation in both the spatial arrangement and the inter-variable relationships.

From this analysis, it can be inferred that the transformation does not significantly alter the spatial continuity among the variables; however, the newly obtained variables do not exhibit the expected multi-Gaussian behavior. Furthermore, the correlations among variables remain at levels comparable to those observed in the original dataset. Following this transformation, a linear model of coregionalization (LMC) is fitted to capture and model the spatial cross-correlations between the Gaussian variables. This step is essential, as the LMC provides the mathematical framework for jointly modeling multiple variables while ensuring the coherence of their spatial relationships.

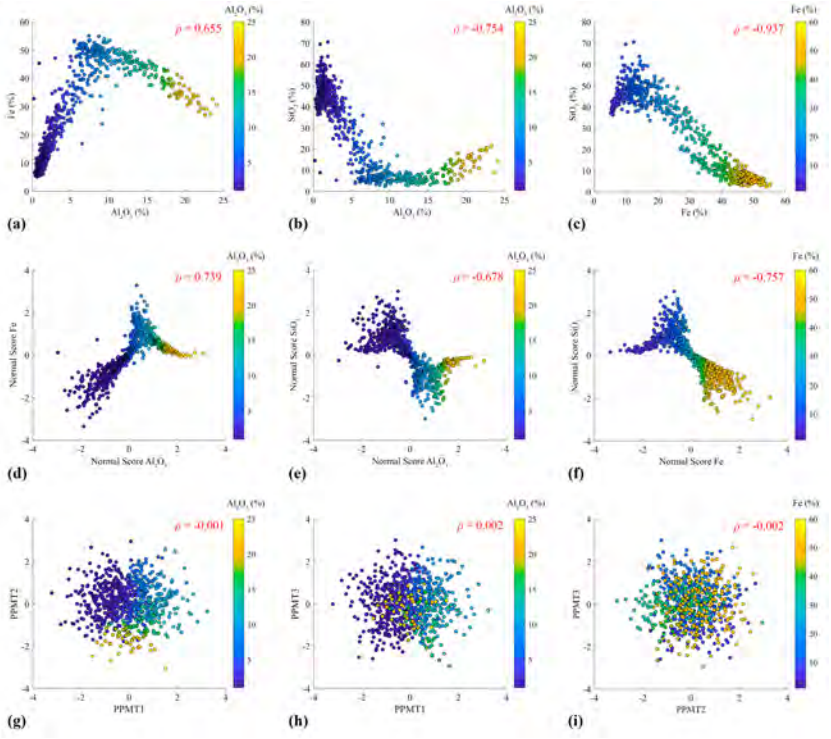

Figure 2. Scatter plots and correlation coefficients are presented for the original variables **(a, b, c)**, the variables transformed using the NST **(d, e, f)**, and the factors derived through PPMT-MAF **(g, h, i)**. In each case, a color scale is applied, using one of the variables in the plot as a reference, to trace and highlight the modifications introduced after the application of the transformation methods.

Alternatively, the original variables were subjected to the PPMT-MAF transformation process. The results of this transformation are shown in Figures 2g, 2h, and 2i. In this case, the plots more closely resemble the expected multi-Gaussian distribution. However, the spatial configuration of the data has been noticeably altered, which may imply that spatial continuity is compromised during the transformation process. The correlations among the obtained factors were almost entirely removed; consequently, fitting a LMC is unnecessary, and a separate variogram model can be directly fitted to each factor.

Once the original variables were transformed into Gaussian variables using both transformation approaches (NST and PPMT-MAF), simulations were performed through the turning bands method (Emery et al., 2016) at the sample locations, yielding 100 non-conditional realizations for each case. Subsequently, the simulated data were back-transformed to return to the original value space. Figure 3 displays the scatter plots between the simulated variables, while Figure 4 presents the corresponding variograms. The scatter plots reveal that the complexities present in the original data are poorly reproduced in the simulated outcomes when the NST method is applied. By contrast, the PPMT-MAF approach demonstrates a slight improvement, although the reproduction of dependence structures remains limited. Variogram analysis of the simulated data derived from

PPMT-MAF factors (Figure 4) highlights a pronounced nugget effect, which can be explained by the distortion of data locations after transformation (Figure 2). In this process, high-grade samples are often repositioned in close proximity to low-grade samples. This rearrangement can generate inconsistencies in the back-transformation stage, as samples that are spatially close may correspond to markedly different values, thus amplifying short-range variability.

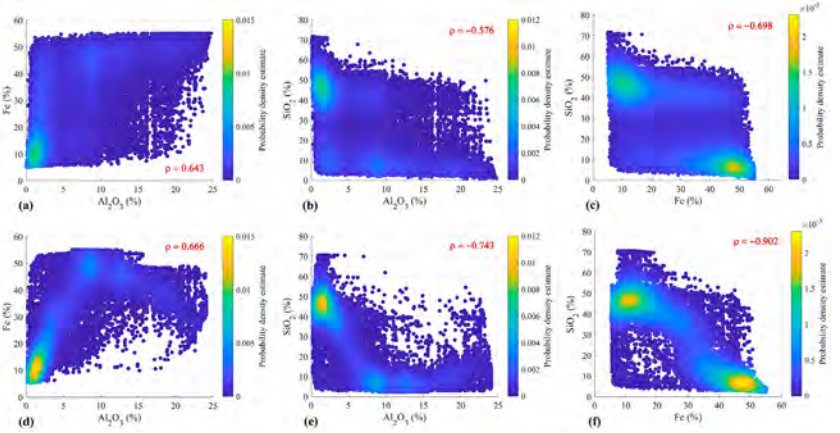

Figure 3. Scatter plots and correlation coefficients between the simulated data using NST **(a, b, c)** and PPMT-MAF **(d, e, f)** for 100 non-conditional realizations.

In simple terms, the PPMT-MAF approach demonstrates a higher capacity than the NST-based method to reproduce the statistical relationships among variables. However, it remains only partially effective in capturing and replicating the spatial dependencies within the simulated data

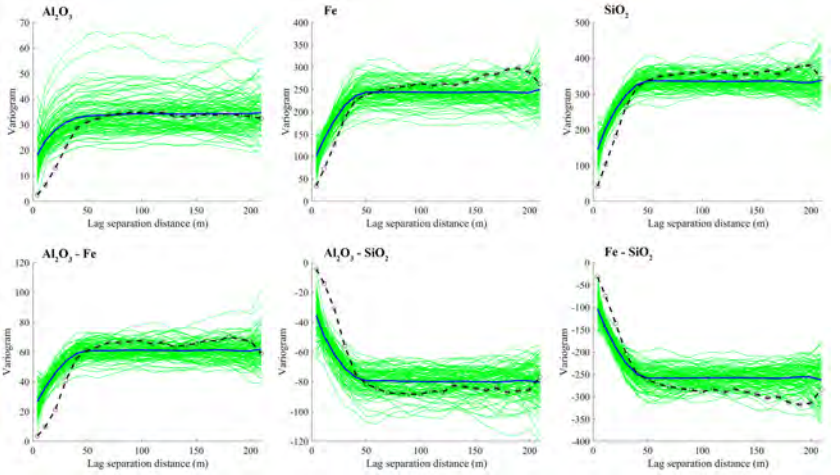

Figure 4. Variograms of the data simulated with PPMT-MAF for 100 non-conditional realizations (green lines), the average of these 100 realizations (blue line), and the variogram of the original data (black dashed line).

Improving NST-based simulation

Considering the capacities and advantages of the NST method, an approach to simulation based on the transformation of data through this method, but with procedural modifications designed to overcome its limitations, is proposed. The rationale for introducing such modifications arises from two key aspects. The first concerns the bimodality of the data, which becomes evident in scatter plots where distinct segments of data appear mixed. This phenomenon is directly related to the geological behavior of the type of deposit under study. A practical way to address this issue is to partition the dataset into different domains. However, due to the lack of lithological information, the assignment of domains relies on the Al_2O_3 variable (Figures 5 and 6). This strategy enables a clearer differentiation of the possible underlying geological structures, ensuring that statistical coherence is maintained while minimizing the effect produced by data heterogeneity.

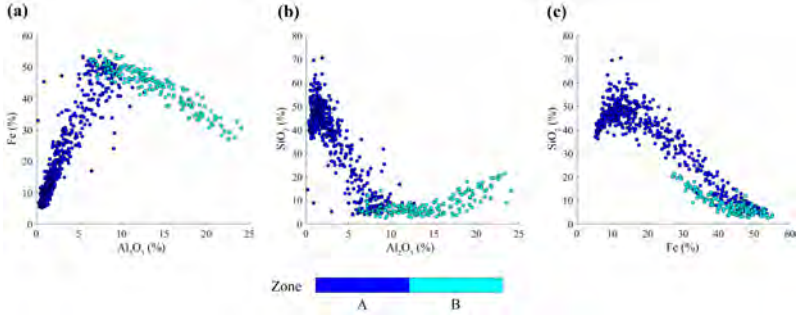

Figure 5. Scatter plots of the original data subdivided into domains A and B, based on the distributional behavior of the Al_2O_3 variable.

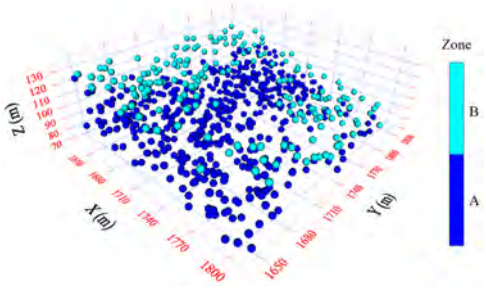

Figure 6. Spatial distribution of the original data partitioned into domains A and B, according to the statistical behavior of the Al_2O_3 variable.

After applying the segmentation to the original dataset, the NST method is independently applied to each domain in order to generate Gaussian variables. The corresponding LMC is then fitted, followed by simulation, yielding 100 non-conditional realizations. Subsequently, the data are back-transformed to their original scale, recovering the values of the original variables. Finally, the simulated datasets corresponding to both domains are merged to obtain a unified dataset.

Figures 7 and 8 illustrate the scatter plots and variograms of the simulated data, respectively. An analysis of the scatter plots reveals a marked improvement in the reproduction of the original complexities (Figure 1) compared with the results obtained prior to segmentation (Figure 3). Similarly, the spatial structure of the simulated data behaves consistently with that of the original dataset, producing superior outcomes relative to the process based on PPMT-MAF (Figure 4).

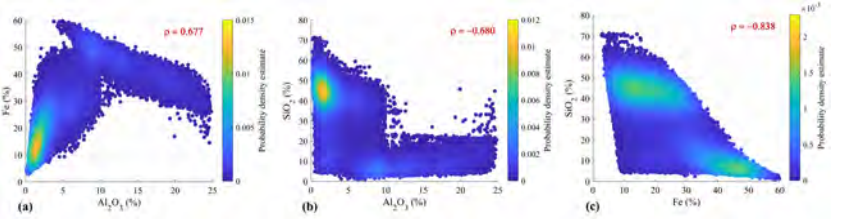

Figure 7. Scatter plots and correlation coefficients of the data obtained using the segmentation and simulation approach with NST for the non-conditional realizations.

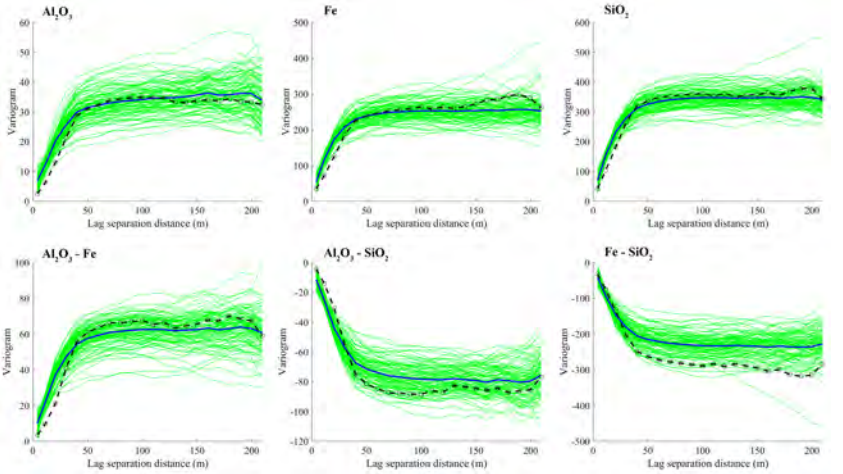

Figure 8. Variograms of the data generated using the segmentation and simulation approach with NST for 100 non-conditional realizations (green lines), the average of these 100 realizations (blue line), and the variogram of the original data (black dashed line).

The strategy based on partitioning the original data according to quasi-geological criteria results in notable improvements in simulation outcomes. However, several considerations arise from the adoption of this specific strategy. First, clear criteria must be established regarding the number of partitions generated, as an increase in the number of partitions can considerably complicate the modeling process. Additionally, the type of contact—whether hard or soft—between the generated domains must be carefully considered, since the modeling outcome depends on the nature of the transitions between domains. Furthermore, each variable involved may correspond to a specific domain type, adding another layer of complexity. The intricacy of these factors may be oversimplified by the aforementioned Gaussian data transformation methods; therefore, it is essential to assess the challenges of each particular case and to develop a tailored, ad hoc solution.

Conclusions

The Gaussian transformation of the original data constitutes a fundamental step in geostatistical simulation processes. For this reason, several techniques and transformation methods have been developed to ensure the generation of Gaussian variables. Among these, NST is one of the most widely used due to its simplicity and practical applicability. However, in multivariate contexts, NST may prove insufficient, particularly when it comes to reproducing the complex relationships among the studied variables. To address these limitations, it becomes necessary to explore

alternative NST-based approaches that can be adapted to the specific requirements of each case. For instance, the segmentation and definition of domains provide a strategy that accounts for the inherent behavior of the original data, ultimately enhancing the quality of the simulated outcomes. Incorporating such strategies allows for a more nuanced reproduction of spatial structures and improves consistency with geological reality.

The findings underscore a critical trade-off between achieving Gaussianity and preserving spatial relationships. While PPMT-MAF offers a marginal advantage over NST in reproducing multivariate structures, its tendency to disrupt spatial coherence raises concerns for subsequent simulation results. Considering methodological alternatives and integrating strategies to address the challenges of geostatistical simulation remains a central concern in mineral resource modeling. In particular, the capacity to balance methodological simplicity with the need for accuracy in multivariate scenarios continues to define the geostatistical practices. Future research should therefore focus on developing flexible approaches that adapt to diverse geological settings while ensuring both statistical rigor and geological plausibility.

References

Abulkhair, S., Dowd, P.A., Xu, C., 2023. Geostatistics in the presence of multivariate complexities: Comparison of multi-gaussian transforms. Mathematical Geosciences, 55 (6), 713–734.

Avalos, S. and Ortiz, J.M., 2023. Spatial multivariate morphing transformation. Mathematical Geosciences, 55, 735–771.

Barnett, R.M., Manchuk, J.G., Deutsch, C.V., 2014. Projection pursuit multivariate transform. Mathematical Geosciences, 46, 337–359.

Boisvert, J., Rossi, M., Ehrig, K., Deutsch, C., 2013. Geometallurgical modeling at Olympic Dam mine, South Australia. Mathematical Geosciences, 45, 901–925.

Chilès, J.-P. and Delfiner, P., 2012. Geostatistics: Modeling spatial uncertainty. John Wiley & Sons.

Cook, A., Rondon, O., Graindorge, J., Booth, G., 2021. Iterative Gaussianisation for multivariate transformation. Geostatistics Toronto 2021 (pp. 21–35). Cham: Springer.

Desbarats, A. and Dimitrakopoulos, R., 2000. Geostatistical simulation of regionalized pore-size distributions using min/max autocorrelation factors. Mathematical Geology, 32, 919–942.

Emery, X., Arroyo, D., Porcu, E., 2016. An improved spectral turning-bands algorithm for simulating stationary vector Gaussian random fields. Stochastic Environmental Research and Risk Assessment, 30 (7), 1863–1873.

Hosseini, S.A. and Asghari, O., 2019. Multivariate geostatistical simulation on block-support in the presence of complex multivariate relationships: Iron ore deposit case study. Natural Resources Research, 28, 125–144.

Journel, A., 1974. Geostatistics for conditional simulation of ore bodies. Economic Geology, 69 (5), 673–687.

Leuangthong, O. and Deutsch, C.V., 2003. Stepwise conditional transformation for simulation of multiple variables. Mathematical Geology, 35, 155–173.

Mery, N., Emery, X., Cáceres, A., Ribeiro, D., Cunha, E., 2017. Geostatistical modeling of the geological uncertainty in an iron ore deposit. Ore Geology Reviews, 88, 336–351.

Mueller, U.A. and Ferreira, J., 2012. The U-WEDGE transformation method for multivariate geostatistical simulation. Mathematical Geosciences, 44, 427–448.

Preece, R., Robles, C., Salazar, A., 2023. Geometallurgical modeling of the Escondida deposit. Mining, Metallurgy & Exploration, 40, 1585–1619.

Sepulveda, E., Dowd, P., Xu, C., Addo, E., 2017. Multivariate modelling of geometallurgical variables by projection pursuit. Mathematical Geosciences, 49, 121–143.

Talebi, H., Mueller, U., Tolosana-Delgado, R., van den Boogaart, K., 2019. Geostatistical simulation of geochemical compositions in the presence of multiple geological units: Application to mineral resource evaluation. Mathematical Geosciences, 51, 129–153.

Talebi, H., Sabeti, E., Azadi, M., Emery, X., 2016. Risk quantification with combined use of lithological and grade simulations: Application to a porphyry copper deposit. Ore Geology Reviews, 75, 42–51.

Van den Boogaart, K.G., Mueller, U., Tolosana-Delgado, R., 2017. An affine equivariant multivariate normal score transform for compositional data. Mathematical Geosciences, 49, 231–251.

Application of Principal Component Analysis (Pca) for Haul Road Surface Evaluation in Mining

Maior, G. R. S. [1], 2*; Peroni, R. L. [1]; Mariz, J. L. V. [1]; Kuckartz, B. [1], Rodrigues, A. L. [1]

1. Federal University of Rio Grande do Sul (UFRGS), Department of Mining Engineering, Brazil
2. Federal Institute of Espírito Santo (IFES), Coordination of Mining Engineering, Brazil

**Corresponding author at: Federal University of Rio Grande do Sul (UFRGS), Department of Mining Engineering, PhD Student, Av. Bento Gonçalves, 9500 - Setor IV, Prédio 43426, Sala 211, Agronomia, Porto Alegre, Rio Grande do Sul, Brasil. Phone:+5528999514935. Email: gleiconmaior@gmail.com / gleicon.maior@ifes.edu.br*

ABSTRACT

The surface condition of unpaved mining haul roads is a critical factor influencing truck productivity, fuel consumption, and maintenance costs due to its direct impact of rolling resistance (RR). Traditional assessment methods based on visual inspection or 2D profiles are limited in capturing the three-dimensional variability of road surfaces. This study introduces the Quantitative Quality Index (QQI), a roughness metric derived from Principal Component Analysis (PCA) applied to UAV-based dense point clouds, coupled with a K-Nearest Neighbors (KNN) algorithm. The methodology was tested on haul roads from two mines in Rio Grande do Sul, Brazil, using UAV surveys at 60, 90, and 120 meters. Results demonstrate that QQI correlates consistently with field-estimated RR, with smoother sites (RR ≈ 2%) yielding low QQI and rougher sites (RR = 3–4%) showing higher values. QQI also exhibits a near-linear dependence on Ground Sampling Distance (GSD), confirming that coarser resolution inflates roughness estimates. Flights at 90 m proved to be the most effective operational compromise, balancing coverage and accuracy. The proposed PCA+KNN framework establishes a standardized, resolution-aware indicator for haul road management, enabling cross-site comparability, prioritization of maintenance interventions, and integration into haulage cost optimization models.

Keywords: Mining haul roads; Rolling resistance; UAV photogrammetry; Principal Component Analysis (PCA); Quantitative Quality Index (QQI).

Introduction:

The surface roughness of unpaved mining haul roads is a primary driver of truck performance and operating cost because it amplifies rolling resistance (RR), fuel consumption, and mechanical wear (PERONI et al., 2025). In operational terms, RR can be interpreted as an additional effective grade—or an energy loss — caused by tire deformation and soil–tire interaction over irregular surfaces. As RR increases, more tractive effort is required for a given payload and speed, directly reducing fleet productivity and elevating maintenance and fuel costs (TANNANT & REGENSBURG, 2001; THOMPSON et al., 2019; SOOFASTEI & FOULADGAR, 2022).

Consequently, characterizing and monitoring roughness with objective, repeatable metrics is paramount to inform maintenance planning and to minimize the cost of haulage. Fig. 1 shows a road with high roughness, which is an indication of high rolling resistance for haul trucks.

Figure 1. Example of an unpaved mining haul road exhibiting transverse irregularities and surface corrugation, which cause increased rolling resistance, fuel consumption, and maintenance requirements for haul trucks.

Conventional practices still rely on visual inspection or on 2D surface profiles extracted from longitudinal sections. While useful for quick appraisals, these approaches struggle to capture the inherently three-dimensional nature of haul road surface, where small-scale undulations and transverse features interact with tire dynamics and loading conditions. The availability of modern surveying technologies—particularly unmanned aerial vehicle (UAV) photogrammetry and LiDAR—has transformed this scenario by providing dense 3D point clouds and, therefore, truly surface-based roughness analysis. However, these datasets are not uniform: their spatial resolution depends on acquisition parameters expressed by the Ground Sampling Distance (GSD), which varies with flight altitude, image pixel size, and camera focal length (CORREIA NETO et al., 2020). Because roughness descriptors are sensitive to sampling density, comparisons across surveys with different GSDs can be biased if this effect is not accounted for. Moreover, additional care is required in the production and handling of point clouds to avoid artifacts from dust, vegetation, or acquisition/processing errors that can masquerade as texture (TONIETTO et al., 2022).

Within this context, Principal Component Analysis (PCA) offers a principle-based statistical framework to derive robust geometric information from point clouds. PCA reduces dimensionality while retaining the dominant variance structure (JOLLIFFE, 1986; HAIR et al., 2009) and has been widely adopted in data-rich domains, including computer-vision-assisted inspection and machine-learning pipelines (DU et al., 2016). For local surface analysis, PCA computed on neighborhoods around each point yields three eigenvectors: the first two span the directions of greatest spread, and the third approximates the local surface normal to a best-fit plane (GOMES et al., 2016). Deviations of points from that plane (e.g., orthogonal distances or statistics derived therefrom) provide natural, noise-aware measures of roughness. Prior works have exploited PCA to detect irregularity patterns, optimize surface response representation, or predict roughness from imagery, underscoring its versatility for quantitative surface assessment (SILVA, 2012; COSTA & SILVA, 2009; LOPES et al., 2013; JOSHI & PATIL, 2020).

Despite these advances, a gap remains for the mining context: a standardized, 3D, point-cloud-based indicator that (i) is sensitive to operationally relevant surface irregularities linked to RR and (ii) is comparable across surveys conducted with different flight altitudes and sensors. Addressing this gap is critical because maintenance teams and mining engineers must integrate measurements gathered under heterogeneous conditions into a single decision framework.

This study tackles that problem by employing PCA on UAV-derived point clouds of unpaved haul roads to formulate the Quantitative Quality Index (QQI), a new metric of surface irregularity grounded in local plane fitting and variance structure. We then explicitly model the QQI's sensitivity to spatial resolution by relating it to GSD and introduce a correction factor that normalizes the metric across different acquisition settings. In practical terms, this allows to compare roughness states measured on different days, with different aircraft or cameras, and at different flight altitudes, without confounding resolution effects. Finally, we assess the engineering relevance of the corrected QQI by examining its relationship with field-estimated RR following the procedure of Thompson et al. (2019), thereby linking the geometric descriptor directly to a driver of energy use and cost.

The specific contributions are threefold: (i) a roughness indicator (QQI) derived from local PCA of dense point clouds, tailored to the characteristics of unpaved haul roads; (ii) an explicit GSD-based calibration and correction that standardizes QQI across surveys, enabling temporal and cross-site comparability; and (iii) an empirical evaluation of the QQI–RR relationship, demonstrating how the metric informs maintenance prioritization and fleet optimization.

Taken together, these elements yield a scalable and objective framework for condition monitoring of unpaved mining roads. By unifying modern 3D surveying with statistically grounded surface descriptors and resolution normalization, the proposed approach supports data-driven maintenance planning, more consistent budgeting for road works, and improved forecasting of haulage performance under real, variable field conditions.

Methodology

High-resolution aerial imagery was collected using two UAV platforms: the MATRICE 210 (equipped with sensor Zenmuse X5S) and the MAVIC 2 Pro, flying at altitudes of 60 m, 90 m, and 120 m. The images were processed in Agisoft Metashape 2.0 to produce dense 3D point clouds. Ground Control Points (GCPs) were used to ensure geospatial accuracy. To extract surface roughness features, PCA was applied to local subsets of the point clouds. This approach captures the spatial variation of the third component (height) relative to the local plane defined by the first two principal components, allowing a quantitative assessment of geometric irregularities.

The PCA index (Eq. 1), where θ is the angle between the local surface and the horizontal plane, serves as the foundational roughness metric in this study. To unify the analysis and account for spatial variability, a novel Quantitative Quality Index (QQI) was developed (Eq. 2). This index integrates the PCA index and incorporates the number of points within each analysis window, determined via a K-Nearest Neighbors (KNN) approach with a fixed search radius of 0.5 meters. This strategy ensures that PCA is applied only to localized subsets of the point cloud, avoiding global computations over extended road segments. As a result, it enhances either the sensitivity to microvariations and the computational efficiency of the roughness analysis, providing a more precise and scalable measure of local road surface quality.

$$PCA\ index = \frac{(PC_3)}{(PC_1 * PC_2)} * \cos^{-1}\theta \quad (1)$$

$$QQI = \left(PCA\ index / KNN\right) * 1000 \quad (2)$$

PC1, PC2 and PC3 are the eigenvalues obtained from the Principal Component Analysis, ordered such that PC1 and PC2 represent the directions of maximum variance and PC3 corresponds to the variance orthogonal to the best-fit plane. θ represents the angle between the eigenvector orthogonal to the local surface (PC3) and the vertical direction (normal to the horizontal plane), which is equivalent to the angle between the local surface and the horizontal plane. KNN is the

number of neighbors considered in the local surface analysis, providing a normalization factor that accounts for point density variability.

The lower the PCA index value, the better the road, due to reduced deviations of surface points from the best-fit plane, indicating smoother topography and less irregularity. Furthermore, the lower the QQI values, the better the road condition, due to the normalization of roughness by point density, which reduces the influence of acquisition resolution and provides a standardized indicator of surface quality.

It is important to note that the Ground Sampling Distance (GSD), included in the framework, represents the effective spatial resolution of the survey. GSD is not a free parameter but rather a consequence of the sensor characteristics (pixel size, focal length) and the flight altitude adopted during data acquisition. As such, incorporating GSD ensures that the QQI accounts for differences in image resolution, enabling fair comparisons across surveys conducted with different UAV platforms and flight settings.

A schematic representation of the full methodology is provided in Fig. 2, illustrating the workflow from data acquisition to index generation.

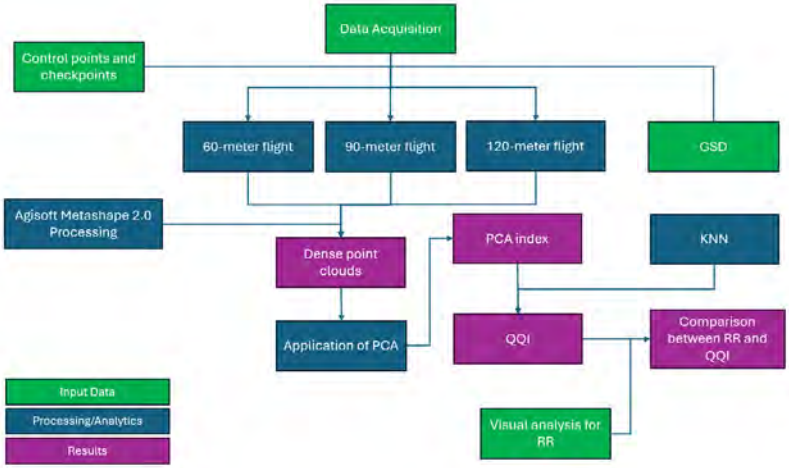

Figure 2. Flowchart of the methodology applied in this study.

Results and Discussions

To apply the proposed methodology, flights were conducted over unpaved mining roads. Roads from two different mines were mapped, with sections presenting distinct quality conditions and, consequently, different levels of rolling resistance. These areas are shown in Fig. 3. Area 1 corresponds to a coal mine, while Area 2 refers to an aggregate mine; both located in the state of Rio Grande do Sul, Brazil.

Each section studied underwent visual inspection following the methodology of Thompson et al. (2019) where the defects were accounted for and scored between 1 and 5 for the degree of the defect and 1 to 5 for the extent of the defect. Thus, it was possible to apply the QQI x GSD methodology and compare it with the visual inspection method.

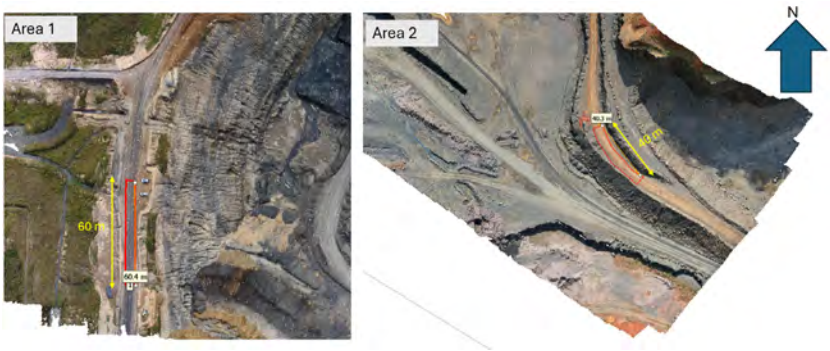

Figure 3. Dense point clouds generated in the studied areas of the projects generated from the processing of the photos of the aerial surveys made at a flight height of 60 meters.

Across all surveys, the Quantitative Quality Index (QQI) increased with Ground Sampling Distance (GSD), indicating that coarser spatial resolution inflates roughness estimates if left uncorrected. This pattern is evident when flights were made at the same site under multiple altitudes. In Area 2 (RR = 2%), QQI rises monotonically for both platforms, using MAVIC 2 Pro or MATRICE 210. Using the first, QQI values were 0.82 (60 m), 2.57 (90 m), and 6.54 (120 m). On the other hand, using the latter, QQI values were 0.89 (60 m), 2.78 (90 m), and 9.43 (120 m), highlighting the direct role of GSD on the metric. Conversely, lower altitudes (e.g., 60 m) yield finer GSD and lower QQI but at the expense of coverage and with an increased risk of collision with higher obstacles, which can be limiting for network-scale road assessments. In practice, flights at 90 m delivered a consistent compromise between spatial resolution and areal coverage, preserving a strong QQI–RR alignment while avoiding the dispersion and inflation observed at 120 m.

At matched conditions, platform effects were also observed. In Area 2 (RR = 2%), the MATRICE 210 systematically reported higher QQI than the MAVIC 2 Pro at all altitudes—+8.5% at 60 m (0.89 vs. 0.82), +8.2% at 90 m (2.78 vs. 2.57), and +44.2% at 120 m (9.43 vs. 6.54)—suggesting greater sensitivity to small-scale variations in surface texture for the MATRICE 210 imaging chain. While this difference is clear under matched-site controls, broader platform comparisons are confounded by site roughness (e.g., many high-RR scenes were acquired with the MAVIC 2 Pro), so interpretations should remain site- and GSD-aware.

Table 1 summarizes the per-area, per-platform, and per-altitude results, including RR (field estimation following Thompson et al., 2019), GSD, PCA roughness index, neighborhood size (KNN), and the derived QQI used in the analyzes above.

Taken together, the table shows that smoother sites (RR ≈ 2%) consistently return low QQI across platforms and altitudes, while rougher sites (RR = 3–4%) exhibit elevated QQI, often with marked inflation at 120 m. This alignment between geometric roughness (QQI) and field-estimated rolling losses (RR) supports the use of QQI as an operational indicator. The few apparent departures from monotonic altitude trends (e.g., Area 3 with QQI = 50.00 at 60 m under RR = 3%) likely reflect localized texture features or sub-scene heterogeneity captured at fine scale; they reinforce the importance of pairing QQI with consistent neighborhood definitions (KNN) and of reporting GSD alongside roughness statistics.

Table 1 Comparison between RR and PCA roughness.

SECTION	RR (%)	DRONE	HEIGHT (m)	GSD (cm/pixel)	PCA Index	KNN	QQI
Section 1	2	MATRICE 210	120	2.62	1.65	214	7.71
	2	MATRICE 210	90	1.97	1.02	337	3.03
Section 2	3	MAVIC 2 PRO	60	1.41	1.39	268	5.18
	3	MAVIC 2 PRO	90	2.11	2.11	107	19.78
	2	MATRICE 210	120	2.62	2.03	216	9.43
	2	MATRICE 210	60	1.31	0.65	735	0.89
	2	MATRICE 210	90	1.97	1.00	359	2.78
	2	MAVIC 2 PRO	120	2.82	1.30	199	6.54
	2	MAVIC 2 PRO	60	1.41	0.56	687	0.82
	2	MAVIC 2 PRO	90	2.11	0.89	345	2.57
Section 3	3	MAVIC 2 PRO	60	1.41	1.29	263	4.90
	3	MAVIC 2 PRO	90	2.11	2.07	105	19.70
	3	MAVIC 2 PRO	60	1.41	2.65	53	50.00
Section 4	2	MAVIC 2 PRO	120	2.82	2.79	232	12.03
	2	MAVIC 2 PRO	120	2.82	1.42	194	7.30
	2	MAVIC 2 PRO	60	1.41	1.59	817	1.94
	2	MAVIC 2 PRO	60	1.41	0.60	670	0.90
	2	MAVIC 2 PRO	90	2.11	2.18	402	5.43
	2	MAVIC 2 PRO	90	2.11	1.01	339	2.99
Section 5	2	MAVIC 2 PRO	120	2.82	2.45	247	9.89
	2	MAVIC 2 PRO	60	1.41	1.60	819	1.95
	2	MAVIC 2 PRO	90	2.11	2.18	402	5.43
Section 6	4	MAVIC 2 PRO	120	2.82	3.69	42	86.88
	4	MAVIC 2 PRO	60	1.41	1.26	130	9.73
	4	MAVIC 2 PRO	90	2.11	2.42	68	35.48
Section 7	3	MAVIC 2 PRO	120	2.82	4.77	44	107.79
	3	MAVIC 2 PRO	60	1.41	2.11	133	15.81
	3	MAVIC 2 PRO	90	2.11	3.65	71	51.44
Section 8	4	MAVIC 2 PRO	120	2.82	3.70	42	87.14
	4	MAVIC 2 PRO	60	1.41	1.31	130	10.06
	4	MAVIC 2 PRO	90	2.11	2.01	68	29.69

Finally, Fig. 4 consolidates the dependence of QQI on GSD within fixed RR bands (2%, 3%, and 4%), showing a clear, near-linear increase in QQI as GSD grows and steeper responses in the rougher classes, as can be seen in the separation of the curves across the different RR levels. In practical terms, the results justify 90 m as the preferred operational altitude for routine monitoring: it retains strong QQI–RR coupling and adequate spatial detail, while providing substantially better coverage than 60 m and avoiding the inflation and dispersion observed at 120 m. Moreover, this altitude represents a safer operational condition, reducing the risk of collision with higher obstacles compared to 60 m flights, while still enabling network-scale assessments with efficiency and reliability.

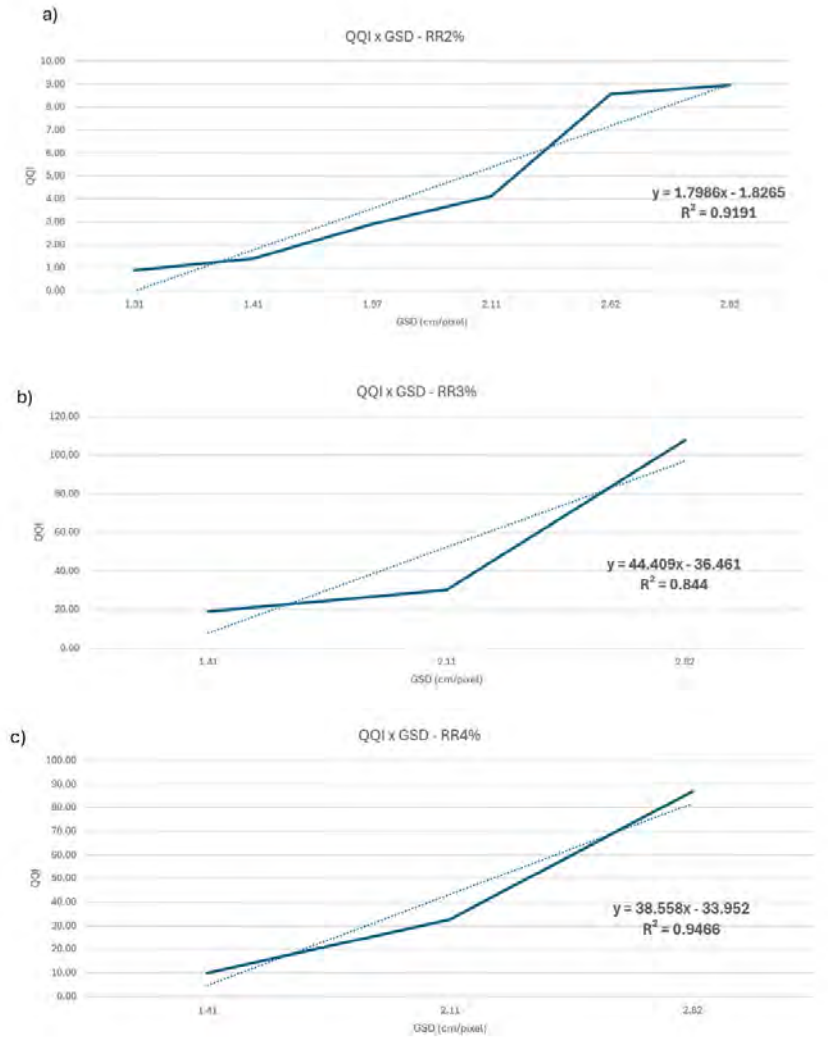

Figure 4. Relationship between the QQI and the GSD for different ranges of RR. Subfigures illustrate the QQI variation with GSD under constant RR conditions: (a) RR = 2%; (b) RR = 3%; and (c) RR = 4%.

Conclusions

This study shows that a PCA-based descriptor of surface geometry, operationalized as the Quantitative Quality Index (QQI), provides a robust and scalable way to assess the condition of unpaved haul roads from UAV point clouds. By coupling local PCA with a neighborhood term (KNN), QQI captures departures from locally fitted planes while stabilizing estimates across variable point densities, enabling objective roughness quantification beyond traditional visual or profile-based methods.

Empirically, QQI aligns with field-estimated rolling resistance (RR): smoother sites (RR ≈ 2%) consistently exhibit low QQI, whereas rougher sites (RR = 3–4%) show elevated values. Within fixed RR bands, QQI increases near-linearly with Ground Sampling Distance (GSD), confirming that coarser resolution inflates roughness estimates if left uncorrected. The slopes and fits observed in our data (e.g., $R^2 \approx 0.86$ at RR = 2% and $R^2 \approx 0.78$–0.95 across RR = 3%) reinforce the need for resolution-aware normalization when comparing surveys acquired at different altitudes and with different sensors.

From an operational standpoint, flights at ≈90 m offered a pragmatic balance between spatial detail and areal coverage: they preserved a strong QQI–RR relationship while avoiding the dispersion and inflation more evident at 120 m and the limited coverage inherent to 60 m. Under matched conditions, platform effects were detectable (e.g., higher QQI with the MATRICE 210 versus the MAVIC 2 Pro in the same area and RR class), suggesting sensor-chain differences in sensitivity to micro-texture; such effects should be accounted for when benchmarking across platforms.

Together, these findings support QQI as a management metric for haul roads. Practical uses include: (i) ranking segments for maintenance, (ii) tracking before/after interventions, (iii) benchmarking contractors or operating areas surveyed under varying flight settings, and (iv) informing haulage models by linking geometric condition to RR and, consequently, to fuel and productivity. A standardized, GSD-corrected QQI facilitates time-series comparisons and cross-site audits without constraining field crews to a single acquisition recipe.

Regarding the limitations of this scope, RR values were obtained by field estimation, which introduces observer and context variability (traffic load, tire inflation/compound, speed regime, and moisture). Photogrammetric point clouds remain sensitive to environmental artifacts (dust, vegetation, shadows), and QQI depends on neighborhood selection (KNN) and outlier handling. These factors warrant explicit reporting and, where possible, calibration.

As future works, we will seek the normalization of the resolution to formalize and validate a GSD correction curve for QQI, allowing direct comparability between altitudes/sensors in routine monitoring. Thus, associate the QQI values with the GSDs to estimate the independent RR of the drones used.

In summary, the proposed PCA+KNN framework yields an interpretable, resolution-aware indicator that links 3D surface geometry to a key operational KPI (RR). With modest standardization of acquisition and a GSD-aware calibration, QQI can underpin data-driven maintenance planning and more reliable forecasting of haulage performance in mining operations.

Acknowledgments

We would like to thank the Federal University of Rio Grande do Sul (UFRGS), the Brazilian CAPES-PROEX program for the funding provided to the post-graduate program PPGE3M, the National Council for Scientific and Technological Development (CNPq) and the Federal Institute of Espírito Santo (IFES) for their support and partial financing of this study.

References

Correia Neto, J. M. L. et al. Elaboration of planimetric model of open pit with multiple benches through the conventional methodology and the use of unmanned aerial vehicles (UAV). Tecnologia em Metalurgia, Materiais e Mineração, 2020.

Costa, G. C.; Silva, D. C. Classification of aerial photogrammetric mapping with images from non-metric digital cameras for the purpose of road projects. Brazilian Journal of Cartography, 2009.

Du, M.; Ding, S.; Jia, H. Study on density peaks clustering based on k-nearest neighbors and principal component analysis. Knowledge-Based Systems, v. 135, p. 135-145, mai. 2016.

Gomes, R. K.; Oliveira, L. P. L.; Gonzaga Jr, L.; Tognoli, F. M. W.; Veronez, M. R.; Souza, M. K. An algorithm for automatic detection and orientation estimation of planar structures in LiDAR-scanned outcrops. Computers & Geosciences, v. 170, mai. 2016.

Hair, J. F.; Black, W. C.; Babin, B. J.; Anderson, R. E. Multivariate Data Analysis. 6th ed. Porto Alegre: Bookman, 2009. 688 p.

Jollife, I. T. Principal Component Analysis. 1. ed. New York: Springer Science+Business Media, LLC, 1986.

Joshi, K.; Patil, B. Prediction of Surface Roughness by Machine Vision using Principal Components based Regression Analysis. Procedia Computer Science, 2020. 382-391.

Lopes, L.g.d., Gomes, J.h.f., Paiva, A.p., Barca, L.f., Ferreira, J.r., & Balestrassi, P.p. A multivariate surface roughness modeling and optimization under conditions of uncertainty. Measurement, 46(7), 2555–2568. Elsevier, 2013.

Peroni, R. L.; Mariz, J. L. V.; Neto, E. G. O.; Souza, D. J.; Afrapoli, A. M. Analysing the haul road design from simulation perspective – theoretical and real improvements. In: Proceedings of International Symposium on Application of Computers and Operations Research in the Mineral Industry (APCOM 2025). Perth, Australia: The Australasian Institute of Mining and Metallurgy, 2025 p. 847–858.

Silva, D. C. Evolution of photogrammetry in Brazil. Brazilian Journal of Cartography, 2012.

Soofastei, A.; Fouladgar, M. Advanced Analytics for Haul Trucks Energy-Efficiency Improvement in Surface Mines. In: SOOFASTEI, Ali Advanced Analytics in Mining Engineering. Brisbane: Springer, 2022. Cap. 17, p. 539 - 556.

Tannant, D. D.; Regensburg, B. Guidelines for Mine Haul Road Design. Alberta: [s.n.], 2001.

Thompson, R. J.; Peroni, R. L.; Visser, A. T. Mining Haul Roads: Theory and Practice. London: CRC Press, 2019.

Tonietto, L.; Arnold, D. C. M.; Oliveira, V. C.; Menegotto, A. E. B. G.; Costa, C. A.; Veronez, M. R.; Kazmierczak, C. S.; Gonzaga Jr., L. Method for evaluating roughness and valley areas coefficients of surfaces acquired by laser scanner. Scientific Reports, v. 12, 2022.

Characterization of the Dilatancy Angle Based on Laboratory Strength Test Results

Javier Arzúa[1,2,*], Edison Martínez-Bautista[1], Daniel Ibarra-González[1], Leandro Alejano[2]

1. Departamento de Ingeniería Metalúrgica y Minas, Universidad Católica del Norte, Antofagasta, Chile.
2. CINTECX, Grupo GESSMIN, Departamento de Ingeniería de los Recursos Naturales y Mediao Ambiente, Universidad de Vigo, España.

** Corresponding author at: Departamento de Ingeniería Metalúrgica y Minas, Universidad Católica del Norte, Associate Professor, Avda. Angamos 0610, Antofagasta, Chile. Phone: +569552351020, e-mail: javier.arzua@ucn.cl.*

ABSTRACT

Dilatancy is the change in volume that a material undergoes when plastic deformation occurs because of shear distortion of the material. The dilatancy angle is the most appropriate parameter to characterize this behavior, as it can be related to incremental plastic strains and is useful for obtaining the slope of the tangent to the locus of irrecoverable volumetric strains. Because this parameter considers the variations in plastic strains, it becomes relevant when these plastic strains are predominant, that is, starting from the stress known as Crack Damage and extending its relevance through the entire post-peak behavior phase. This paper explains the traditional methodology for obtaining this parameter and identifies the challenges that need to be addressed to achieve a better characterization of this behavior. Despite the identified opportunities for improvement, it can be concluded from this study that obtaining the dilatancy angle at the laboratory scale is possible, and it is a relevant source of information for optimizing the design of excavations in which plastic strains occur.

Methodology

From the experimental axial and radial stress-strain curves of a uniaxial compression strength test (Figure 1.a), the plastic components of these strains can be determined simply by drawing lines parallel to the elastic parts of the curves (Figure 1.b) until they intersect the abscissa axis. In triaxial compression strength tests, radial strain measurements cannot be performed with LVDTs (and strain gauges are not capable of capturing strain beyond the peak strength); therefore, it is common to rely on measuring the volume of hydraulic fluid displaced from or into the triaxial cell to obtain the volumetric strain and derive the radial strain from it. However, it is not possible to experimentally determine the plastic component of the volumetric strain, because it is not possible to identify an elastic section of the curve. Therefore, it is necessary to use loading and unloading cycles to determine what is known as the irrecoverable volumetric strain locus, which will allow to obtain the values of the plastic volumetric strain (Figure 1.c).

After obtaining these plastic strain values throughout the test, the Vermeer and De Borst (1984) equation can be used to determine the evolution of the dilatancy angle at different moments of the test (Figure 1.d).

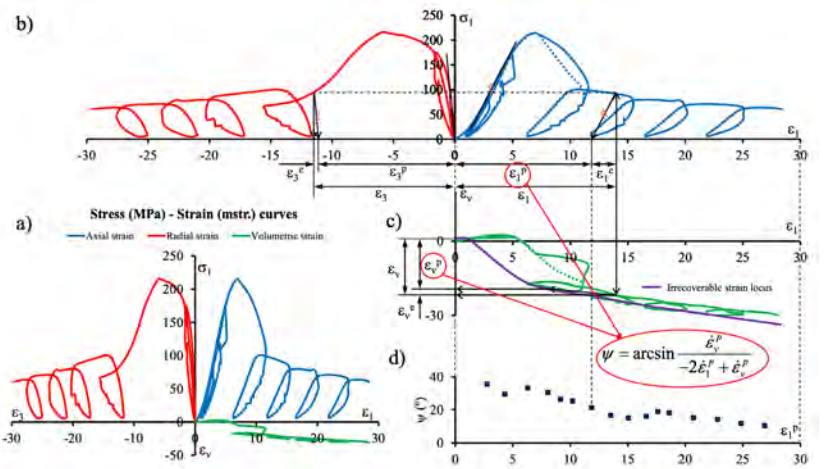

Figure 1: a) Complete stress-strain curves of a triaxial strength test; b) methodology to determine axial and radial plastic strains; c) methodology to determine volumetric plastic strains; and d) equation of Vermeer and De Borst (1983) and evolution of the dilatancy angle against the plastic axial strain.

Results and Conclusions:

The described methodology allows the evolution of the dilatancy angle to be determined based on uniaxial or triaxial compression test results of rocks at the laboratory scale. The main initial hypothesis is that the elastic properties of the rock remain constant throughout the entire test, which, although it is known to be not entirely true, is nevertheless a reasonable first approach to the actual rock behavior. The next step would be to consider the evolution of the elastic "constants" throughout the test to determine the evolution of the dilatancy angle more precisely.

The characterization of the post-peak behavior of rocks and rock masses becomes relevant when considering that underground mining operations are reaching greater depths, meaning that the stresses to which they are subjected are also increasing. This, in turn, leads to a higher probability of failure, and therefore, greater fortification requirements to ensure stability. If the post-peak behavior is considered, one can take advantage of these strength properties when optimizing fortification.

Development of a Computational Tool for the Comparison of Pillar Design Models in Underground Mining

Daniel Ibarra-González1*, Manuel Cánovas[1], Edison Martínez-Bautista[1] and Javier Arzúa[1,2]

1. Departamento de Ingeniería Metalurgia y Minas, Universidad Católica del Norte, Antofagasta, Chile
2. Departamento de Ingeniería de los Recursos Naturales y Medio Ambiente, Universidad de Vigo, España.

**Corresponding author at: Departamento de Ingeniería Metalúrgica y Minas, Universidad Católica del Norte, Antofagasta, e-mail adress: daniel.ibarra@ce.ucn.cl*

ABSTRACT

The room-and-pillar method is one of the most widely used underground mining methods, owing to its simplicity, safety, and low cost. Pillar design is fundamental to ensure the stability of the operation and to increase ore recovery. In recent decades, various empirical formulas have been developed to estimate pillar strength under different geometric and geomechanical conditions, each of which considers specific conditions of application and presents a series of limitations. The aim of this study is to develop pillar design software that allows for a quick and systematic comparison between different empirical models, always under the same geomechanical conditions, in order to make valid comparisons. The application was developed using Python code, incorporating widely used models in room-and-pillar mining, such as Lunder-Pakalnis, Bieniawski, Hedley-Grant, and Salamon-Munro, among others. Additionally, the tool allows users to enter new models that follow the structure of the shape and size effect equations, thereby expanding its applicability. To validate its effectiveness, a case study was evaluated to demonstrate the differences in excavation stability predictions according to the various models. It can be concluded that the tool developed, simple, and easy to use, is useful for preliminary pillar stability analysis as a support in the initial stages of mine design, and it may also be useful for educational purposes in the field of mine design. Finally, the main advantages, limitations, and opportunities for improvement were discussed.

Keywords: Underground Mining; Room-and-Pillar; Pillar Design; Python

Introduction

Underground mining has gained significant relevance in recent years and is mainly driven by the progressive depletion of easily accessible and shallow deposits (Fitsak et al., 2017; Ghorbani et al., 2023). This scenario has led to the adoption of various underground methods in which pillar design is a fundamental component for ensuring the stability and safety of excavations. This consideration is particularly critical in the room-and-pillar method, where pillars are the main source of support throughout the entire life of the operation (Jessu et al., 2022).

The room-and-pillar method is generally applied to flat, stratified mineralized bodies of limited thickness, such as copper slate deposits, coal seams, salt and potash deposits, limestone, dolomite, among others (Hart,an & Mutmansky, 2007). Its advantages include continuous production, rapid development rate, simple ventilation design, moderate operational costs, and high selectivity (Nieto, 2010).

The development of computational tools has gained great relevance in recent years, both in industrial and research applications, where Python has established itself as an accessible language that allows for the automation of calculations, the generation of interactive visualizations, and a reduction in reliance on extensive spreadsheets, thereby reducing the probability of human error. The creation of tools in Python improves both the efficiency of data processing and technical decision making through simple interfaces.

In this context, the main objective of this study is to develop a computational tool in Python that allows for a quick and systematic comparison of different empirical models under the same geomechanical conditions. Additionally, the tool is intended to be applicable both in the preliminary phases of mine design and in educational and research contexts, facilitating an understanding of the factors that influence pillar design.

Desginf of pillars

A pillar refers to the mass of in situ rock left between two or more excavations (Coates, 1981; Martin & Maybee, 2000). There are different ways to classify pillars depending on their functionality, shape, geometry, or location within the extraction method. Some of the most common classifications are as follows:

- **According to functionality:** they differentiate between those that serve a support role, either globally or locally, or provide protection for structures of interest (Jessu et al., 2022).
- **According to geometry:** square, rectangular, barrier, or irregular pillars are distinguished depending on the geometry of their basal section (Hoek & Brown, 1980).
- **According to shape:** they are categorized according to their shape and width/height ratio into slender pillars, intermediate pillars, and squat pillars, which directly influence the failure mode and strength of the pillar (Mark, 1999).
- **According to their location and orientation within the mining design:** they are categorized as rib pillars, sill pillars, and crown pillars (Betourany, 1989).

A good design can determine the feasibility of a project, as it involves both safety and economic aspects. On the one hand, undersized pillars can cause local or even global collapses due to the "domino" effect (Jesse et al., 2022) or even generate air blasts that affect nearby infrastructure (MSHA, 2021). On the other hand, oversized pillars can have a significant impact on the profitability of mining operations (Jesse et al., 2022).

Interest in pillar design increased significantly after the Coolbrook coal mine disaster in South Africa in 1960, when the collapse resulted in the death of 437 workers. This event marked a turning point in the development of research focused on pillar stability (Jesse et al., 2022). As a result, it is now possible to find different design approaches by applying both empirical methods and more complex methods.

According to Mark (2000), the classical empirical methodology for pillar design involves three steps:

i) estimating the load on the pillar using the tributary area theory (TAT),
ii) estimating the pillar strength using one of the existing formulas, and
iii) calculating the design safety factor. In addition, the above should be complemented by determining mineral recovery without losing sight of the profitability of mining operations.

Load on the pillar

The determination of the load or the forces acting on a pillar is carried out using tributary area theory or computational techniques, or even with more rigorous methods that involve measuring the forces in situ (Castro-Caicedo et al., 2019).

The tributary area theory (TAT) has been universally and successfully used as the main methodology for assessing the loads acting on pillars (Vlachogiannis & Benardos, 2024). This theory implies that the load acting on each pillar is a function of the column of rock directly above the pillar as well as the rock situated between an individual pillar and any of its adjacent pillars (Maybee, 2000). For a rectangular pillar layout with width W, length L, and room width and length left in each direction BL and Bw, respectively, the following scheme reflects the theory (Figure 1).

Figure 1. Diagram of rectangular pillar design.

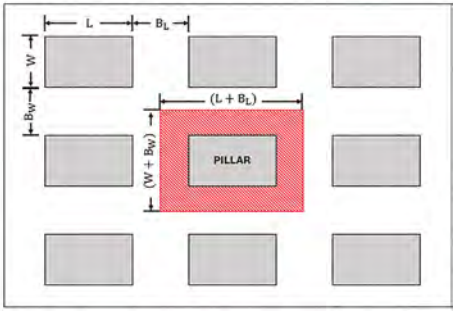

The tributary area theory (TAT) uses the following equation to estimate the load acting on the column (S_p):

$$S_p = \rho g H \frac{(W + B_w)(L + B_L)}{(W \cdot L)} \quad (1)$$

where ρ is the density of the rock (kg/m3), g is the gravitational constant (9.81 m/s2) and H is the depth at which the pillar is located (m). For square pillars, it is assumed that the width and length are equal, thereby simplifying the equation.

Although the tributary area theory is widely used, mainly because of its simplicity, it presents a series of assumptions and limitations that must be considered in pillar design. For example, this theory assumes that the vertical pre-mining stress is uniformly supported by all pillars in the same manner (Figure 2a). However, this condition is only satisfied when the overburden is weak, shallow (less than or equal to the design span), and the pillars are arranged in homogeneous environments (Figure 2b). When the design is implemented at greater depths, in narrow bodies, or under strong overburden, this distribution changes, with the central pillars tending to bear most of the stress, whereas the pillars near the edge are protected by a pressure arch (Figure 2c) (MSHA, 2021). This difference between the ideal and actual distributions of the vertical stress can induce errors or overestimation of the safety factor.

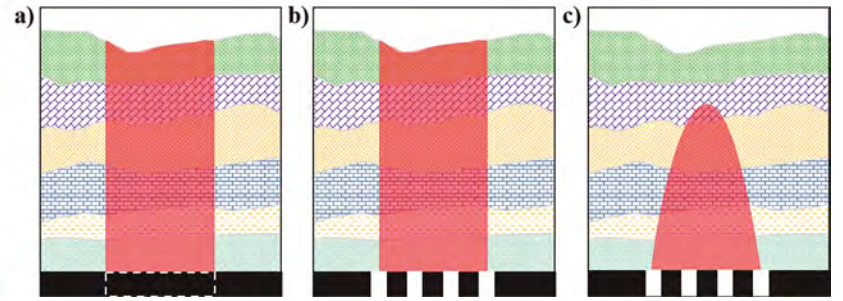

Figure 2. a) Load on the area of interest before excavation; b) stress distribution on the pillar according to TAT, and c) actual distribution (after de Mark & Agioutantis (2019)

Pillar strength

The strength of a pillar depends on its dimensions and shape (width/height ratio), as well as the dimensions of the room (Brady & Brown, 1999). Experimental, numerical, and empirical techniques were used to estimate the strength of the pillars (Castro-Caicedo et al., 2019). Throughout the literature, various empirical formulas can be found, most of which are obtained through a back-calculation approach, that is, a retrospective analysis of historical data from stable and failed pillars (Martin & Maybee, 2000). These equations aim to relate the pillar strength to geomechanical and geometric parameters for specific terrains.

Lunder & Pakalnis (1997) pointed out that the empirical equations developed generally take two forms: i) shape effect and ii) size effect. Shape effect formulas consider that a pillar with a certain width/height ratio has the same strength, regardless of its volume. On the other hand, the size effect formulas assume that a pillar of a given shape (width/height ratio) reduces its strength as its size increases.

Equations governed by the shape effect take a linear form, whereas those following the size effect take a power-law form. Both relationships can be represented by the following unified general equation:

$$\sigma_p = K\left(A + B\frac{W^{\alpha}}{H^{\beta}}\right) \quad (2)$$

where K, A, B, α and β are adjustment factors dependent on the terrain associated with the excavation. It can be assumed that, when α = β=1, it reduces to the representative equation for the shape effect, and when A=B=1 the formulas that follow the size effect methodology are obtained.

Although most of the empirical methods available in the literature allow for the calculation of strength for square pillars, equations for rectangular pillars have also been developed, for example, Mark-Bieniawski (Mark & Chase, 1997). Another approach, widely used to address the design of rectangular pillars, corresponds to the use of the equivalent width (Weff) proposed by Wagner (1980), which relates the area (A) and the perimeter of the pillar (O) (Equation 3).

$$W_{eff} = \frac{4A_p}{O} = \frac{2WL}{(W+L)} \quad (3)$$

The most common empirical equations for pillar design follow the general unified form, which includes models such as Obert-Duvall, Hedley-Grant, among others (Table 1).

Table 1. Simple models based on the general form.

Models	K	A	B	α	β	Rock type
Obert & Duvall (1967)	σ_c	0.778	0.222	-	-	Coal
Krauland & Soder (1987)	$0.354\sigma_c$	0.778	0.222	-	-	Limestone
Sjoberg (1992)	$0.308\sigma_c$	0.778	0.222			Limestone
Salamon & Munro (1967)	9.115	-	-	0.46	0.66	Coal
Sheorey *et al.* (1987)	0.27	-	-	0.50	0.86	Coal
Hedley & Grant (1972)	$0.578\sigma_c$			0.50	0.75	Hard rock

While classical empirical equations are mainly based on simple geometric relationships between dimensions, there are more complex models that incorporate parameters and use other foundations, increasing the accuracy and realism, but at the same time increasing the complexity of the analysis (Table 2).

Table 2. Compilation of pillar design models

Models	Equations	Parameters
Bieniawski (1984)	$\sigma_p = \sigma_1\left(0.64 + 0.36\frac{W}{h}\right)$ $\sigma_1 = \sigma_c(D/36)^{0.5}$	σ_1: Unconfined compressive strength of a large cube of rock (MPa) D: specimen diameter (in)
Laubscher (1990)	$\sigma_p = DRMS\frac{W^{0.5}}{h^{0.7}}$	DRMS: design rock mass strength (MPa)
Stacey & Page (1986)	$Si, \frac{W}{h} < 4.5 \rightarrow$ Laubscher (1990) $Si, \frac{W}{h} > 4.5 \rightarrow \sigma_p = DRMS\frac{2.5}{V^{0.07}}[0.13\left(\left(\frac{4{,}5w_{ef}}{h}\right)^{4.5} - 1\right) + 1]$	DRMS: design rock mass strength (MPa) V: pillar volume (m^3)
Lunder & Pakalnis (1997)	$\sigma_p = 0.44\sigma_c(0.68 + 0.52\kappa)$ $\kappa = \tan[\text{acos}\left(\frac{1-C_{pav}}{1+C_{pav}}\right)]$ $C_{pav} = 0.46[log\left(\frac{W}{h} + 0.75\right)]^{1.4/(W/h)}$	κ : internal friction of the pillar C_{pav}: average pillar confinement.
González-Nicieza *et al.* (2006)	$\sigma_p = \left(\sigma_c e^{\frac{RMR_{89}-100}{20}}\right)\frac{W^{0.5}}{h^{0.75}}$	RMR_{89}: rock mass rating 1989
NIOSH (Esterhuizen *et al.*, 2011)-	$\sigma_p = (0{,}65\sigma_c(1 - DDF \cdot FF))\frac{W^{0.5}}{h^{0.75}}$	DDF: discontinuity dip factor FF: frequency factor
Hoek & Brown (1980)	$\sigma_1 = \sigma_3 + \sigma_c\left(m_i e^{\left(\frac{GSI-100}{28-14D}\right)}\frac{\sigma_3}{\sigma_c} + e^{\left(\frac{GSI-100}{9-3D}\right)}\right)^{\frac{1}{2}+\frac{1}{6}\left(e^{\left(\frac{-GSI}{15}\right)} - e^{\left(\frac{-20}{3}\right)}\right)}$	GSI: Geological Strength Index m_i and s: rock parameters D: disturbance factor σ_3: confinement, obtained from the width/height ratio

It is important to note that each of these methods for estimating pillar strength can be adapted to rectangular pillars by using Equation 3.

Safety factor and recovery

The stability of the pillar was evaluated using the safety factor (FS), which corresponds to the ratio between the strength of the pillar (σ_p) and the stress to which it is subjected

$$FS = \frac{\sigma_p}{S_p} \tag{4}$$

A safety factor of one indicates a limit equilibrium condition, where the strength is equal to the applied load. In practice, an FS greater than 1 is required to ensure stability.

Several authors have proposed acceptable minimum FS values, depending on the type of rock, geomechanical conditions, and criticality of the design. For example, Lunder and Pakalnis (1997) suggested an FS of 1.4 as a general criterion for hard rock, Lunder (1994) recommended values greater than 1.6, and NIOSH considered an FS of 1.8 for mining operations in the US.

In addition to stability, the profitability of the design must be ensured. For this purpose, the extraction ratio (e) was used, which represents the amount of material extracted relative to the amount of available ore; this should be maximized without compromising the stability of the excavation.

$$e = \frac{excavated\ area}{total\ area} = 1 - \frac{WL}{(W + B_w)(L + B_L)} \tag{5}$$

Use of python

In recent years, the potential of Python has been recognized in the development of computational tools applied to various areas of mining, such as geomechanics (Martínez-Bautista et al., 2024), drilling and blasting (Vivero et al., 2024), and loading and hauling (Manríquez et al., 2020), among others.

Regarding pillar design, there are prominent programs such as the S-Pillar software, developed by NIOSH (National Institute for Occupational Safety and Health), the CPillar software by Roscience for crown pillar design, and the ACPS (Analysis of Coal Pillar Stability) software proposed by Mark & Agioutantis (2019) for longwall mining design.

Metodology

An interactive application was developed for the preliminary design of pillars in underground mining using Python. The tkinter library was used to create an interactive graphical interface, allowing the user to enter data, select models, and view results, as well as the math library for basic mathematical operations. The program enables users to input relevant geomechanical and geometric parameters for the design in addition to selecting the empirical models they wish to evaluate, thus obtaining the safety factors (FS) under the same input conditions. The calculation logic integrates functions that include both classic empirical and complex models based on advanced parameters.

Subsequently, the tool was packaged as a standalone executable (. exe) using pyinstaller, allowing it to be used and distributed without requiring additional Python installations from the user.

The main implemented algorithm allows for:

- Capturing user input data corresponding to geomechanical properties (density and σ_c), depth, and the geometry of the pillar and room
- Validate that all entries are consistent (positive and complete)
- Calculate the vertical stress applied to the pillar as a function of the TAT
- Estimate the effective width of the pillar (Weff) depending on whether its shape is square or rectangular
- Calculate the load acting on the pillar and the extraction ratio
- Visualization of the generated pattern and tributary area of the evaluated pillar
- Enter complex parameters using models or a new model that follows a general unified form (optional)
- Calculate the safety factor for each model evaluated.

A flowchart of this process is shown in Figure 3.

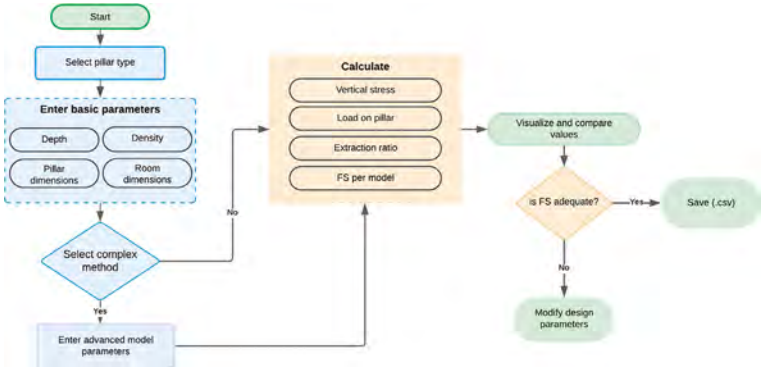

Figure 3. Flowchart of the tool operation for pillar design.

Case study

To compare the effectiveness of the tool and the behavior of the models, a case study was proposed, defined by the following parameters, which correspond to typical values commonly found in the literature (e.g., Lunder & Pakalnis, 1997; Martin & Maybee, 2000):

Table 3. Parameters of case study

Parameters	Value
Depth (m)	75
Pillar dimensions (m)	3x4
Pillar height (m)	5
Room dimensions (m)	6x7
Overburden material density (t/m^3)	2.5
UCS (MPa)	80
Specimen diameter (mm)	64

Results and discussion

To evaluate the performance of the tool, it was first validated against theoretical and real-case data reported in the literature for different models to assess the consistency of the models' behavioral trends. For example, empirical models that account for the shape effect show an improvement in FS as the width-to-height ratio increases, as indicated by various studies. Likewise, when the depth increases or the pillar dimensions decrease, reductions in FS are observed, which is expected considering the parameters that affect the calculation of load and strength.

The tool was then applied to a case study to systematically compare the different empirical models under the same geomechanical and geometric conditions (Table 3).

From the tool, it is possible to initially view the proposed design scheme and its corresponding tributary area (Figure 4a) and subsequently compare the safety factors reported by different authors (Figure 4b).

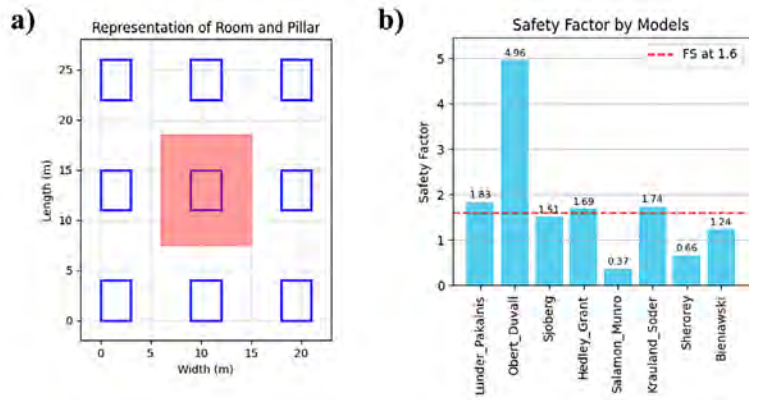

Figure 4. Software output parameters: a) representation of the entered design and b) safety factors by the model.

As can be seen, the tool allows for the evaluation of only those models for which all required parameters are available. Initially, the application provided the vertical stress, load on the pillar, extraction ratio, and width/height ratio (Table 4).

Table 4. Stress and load results of case study

Parameters	Value
Vertical stress (σ_v) (MPa)	1.84
Load on the pillar (S_p) (MPa)	15.17
Extraction ratio	88%
Width/height ratio (W_{eff}/h)	0.69

From the FS results, it can be observed that models applied to coal, such as the Obert-Duvall model, tend to overestimate the safety factor value. This result is consistent with what has been reported by other authors, who proposed a conservative approach that considers a minimum safety factor of four for underground design.

On the other hand, it can be seen that the models of Lunder & Pakalnis, Hedely & Grant, and Krauland & Soder yield safety factors higher than the minimum of 1.6 recommended by Lunder (1994). Meanwhile, the Bieniawski and Sjoberg models obtain values of 1.42 and 1.51, respectively, which can be attributed to a more conservative approach, further reducing the in situ pillar strength.

Finally, it should be noted that the models by Salamon & Munro and Sheorey deviate significantly from the minimum design value, delivering considerably lower results—0.37 and 0.66, respectively, explained by the modified power form used in these equations, which take size effects into account. Consequently, despite the extraction ratio being approximately 90%, it is recommended to consider the type of pillar rock, as it conditions the applicability of the model. Thus, it is possible to achieve a more representative design and obtain more reliable safety factors that guarantee excavation stability.

From the analysis, it can be seen that the tool is of practical use in both educational and industrial contexts, as it allows for the immediate visualization of the effect of parameter variation and enables a quick and simple preliminary analysis, ideal for the pre-feasibility or conceptual engineering phases. In addition, the tool allows for the entry of new formulas that follow the form of a unified general equation.

It is important to note that the tool is not intended to replace advanced numerical techniques or other specialized software. Moreover, some of the included empirical models require specific geomechanical information that may not be known during the early stages of a mining project.

Conclusions

The room-and-pillar method is one of the simplest, safest, and most economical mining methods available. A proper pillar design is fundamental to ensuring the success of operations using this method; otherwise, both safety and feasibility are compromised.

This study presents a computational tool for the comparative analysis of empirical pillar design models using identical geometric and geomechanical conditions. The application, developed in Python, allows for the estimation of the safety factor (FS) by considering various classic approaches, such as Lunder & Pakalnis, Salamon & Munro, Bieniawski, Hedley & Grant, among others. In addition, it offers the possibility of including additional models that follow the extended pillar formula, allowing for adaptation to different scenarios.

The tool was validated by evaluating the performance of different models against behavioral trends reported in the literature. Then, a case study was conducted, where variations in the safety factor according to the different models were observed, with the highest value provided by Obert & Duvall and the lowest by Salamon & Munro. Despite the nearly 90% recovery provided by the design, it is recommended that a more detailed study be conducted considering the type of rock and geomechanical conditions of the area under study.

As a future line of research, it is proposed to implement a greater number of empirical formulations, include an automatic sensitivity analysis module, and develop functions that assist users in design decision-making.

References

Betourany, M.C., 1989. What do we really know about surface crown pillars? In Proc. Int. Conf. On Surface Crown Pillar Evaluation for Active and Abandoned Metal Mines.

Bieniawski, Z.T., 1984. Rock mechanics design in mining and tunnelling. A.A. Balkema, Rotterdam, 200.

Brady, B.H.G. and Brown, E.T., 1999. Rock Mechanics for Underground Mining. In: Rock Mechanics. Springer, Dordrecht

Castro-Caicedo, A.J., Alejano, L.R., Monsalve, J.E. and Bernal, A., 2019. Geotechnical design of pillars in underground mines of gold veins in cases of Colombia. DYNA (Colombia), 86(209), 337–346.

Coates, D.F., 1981. Rock mechanics principles. CANMET, Canada.

Esterhuizen, G.S., Dolinar, D.R., D.R., Ellenberg, J.L., 2011. Pillar strength in underground stone mines in the United States

Fitsak, V.V., Lomakina, E.S., Strakhova, A.A. and V.I. Chernobai V.I., 2017. Determination of Room-and-Pillar system parameters for Transition to Greater Depths. Int. J. Appl. Eng. Res., 12(22), 12322-12331

Ghorbani, Y., Nwaila, G.T., Zhang, S.E., Bourdeau, J.E., Cánovas, M., Arzúa, J. and Nikadat, N., 2023. Moving towards deep underground mineral resources: Drivers, challenges and potential solutions. Resources Policy, 80, 103222.

González-Nicieza, C., Álvarez-Fernández, M.I., Menéndez-Díaz, A. and Álvarez-Vigil, A.E., 2006. A comparative analysis of pillar design methods and its application to marble mines. Rock Mech. Rock. Eng., 39(5), 421-444.

Hartman, H.L. and Mutmansky, J.M., 2007. Introductory mining engineering (2nd ed.). Wiley India.

Hedley, D.G.F. and Grant, F., 1972. Stope-and-pillar design for the Elliot Lake Uranium Mines. Bull. Canadian Institute of Mining, Metallurgy and Petroleum, 57, 37-44.

Hoek, E. & Brown, 1980. Underground Excavations in Rock. Institution of Mining and Metallurgy.

Jessu, K.V., Spearing, A.J.S and Sharifzadeh, M., 2022. An improved pillar design methodology. J. South Afr. Inst. Min. Metall., 122 (10), 587-596.

Krauland, N. and Soder, P., 1987. Determining pillar strength from pillar failure observations. Eng. Min. J., 8, 34-40

Laubscher, D.H., 1990. A geomechanics classification system for the rating of rock mass in mine design. J.S. Afr. Inst. Min. Metall., 90(10), 257-273

Lunder, P. J., and Pakalnis, R. C., 1997. A determination of the strength of hard-rock mine pillars. CIM Bulletin, 90(1013), 51–55.

Lunder, P.J.,1994. Hard rock pillar strength estimation an applied empirical approach (Master's Thesis). The University of British Columbia.

Manríquez, F., Pérez, J. and Morales, N., 2020. A simulation optimization framework for short-term underground mine production scheduling. Optimization and Engineering.

Mark, C. ,1999. Empirical Methods for Coal Pillar Design. Proceedings of the Second International Workshop on Coal Pillar Mechanics and Design. U.S. Department of Health and Human Services, National Institute for Occupational Safety and Health (NIOSH); IC 9448, pp. 145-154.

Mark, C., 2000. State-of-the-art in coal pillar design. Proc. Soc. Min. Metall. Explor., 308, 1-8.

Mark, C. and Agioutantis, Z., 2019. Analysis of coal pillar stability (ACPS): A new generation of pillar design software. International Journal of Mining Science and Technology, 29, 87–91.

Mark, C. and Chase, F.E.,1997. Analysis of retreat mining pillar stability. Proc. New technology for ground control in retreat mining, 1-34

Martin, C.D. and Maybee, W.G., 2000. The strength of hard-rock pillars. Int. J. Rock Mech. Min. Sci., 37, 1239-1246.

Martínez-Bautista, E., Bravo-Tobar, J., Arzúa, J., Ibarra-González, D, Cánovas, M., 2024. Sistematización en la estimación de propiedades pre-peak de ensayos de compresión triaxial mediante Python. In: Proceedings UMining III Congreso Iberoamericano en Minería Subterránea y a Cielo Abierto 2024, 128-140.

MSHA 2021. Assessing pillar collapse and airblast hazards in underground stone mines.

Nieto, A., 2010. Key deposits indicators (KDI) and key mining method indicators (KMI) in underground mining method selection. Transactions of the Institution of Mining and Metallurgy.

Obert, L. and Duvall, W., 1967. Rock mechanics and the design of structures in rock. Willey.

Salamon, M.D.G and Munro, A.H., 1967. A study of the strength of coal pillars. J. South Afr. Inst. Min. Metall., 55-67.

Sheorey, P.R., Das, M.N., Barat, D., Prasad, R.K. and Singh, B., 1987. Coal pillar strength estimation from failed and stable cases. Int. J. Rock. Mech. Min. Sci. & Geomech., 24, 347-355.

Sjoberg, J., 1992. Failure modes and pillar behavior in the Zinkgruvan mine. In proceedings of 33rd US rock mechanics symposium. pp 491-500

Stacey, T.R. and Page, C.H., 1986. Practical Handbook for Underground Rock Mechanics. Series on Rock and Soil Mechanics, 12, 53-64.

Vivero, G., Hekmat, A., Fustos, F. Díaz, R., Villaseca, F., 2024. Software basado en inteligencia artificial para la optimización de tronadura en minería subterránea. In: Proceedings UMining III Congreso Iberoamericano en Minería Subterránea y a Cielo Abierto 2024, 502-515.

Vlachogiannis, I. and Benardos, A., 2024. Proposed formulas for pillar stress estimation in a regular room-and-pillar pattern. Int. J. Rock Mech. Min. Sci., 180, 105826.

Wagner, H., 1980. Pillar design in coal mines. J. South Afr. Inst. Min. Metall., 80, 37-45

Electromobility in Underground Mining: Simulation and Multicriteria Decision Analysis of Scenarios to Reduce Emissions

Belén Herrera[1,2], Camilo Espinosa[2], Bruno Martínez[2], Diego Mancilla[2], Gonzalo Monsalve[3], Gonzalo Ramírez[3], Marcos E. Orchard[4,5], Javier Ruiz-del-Solar[2,4], Ángela Flores-Quiroz[4,6] and Luis Felipe Orellana[1,2]

1. Department of Mining Engineering, University of Chile, Chile
2. Advanced Mining Technology Centre (AMTC), University of Chile, Santiago, Chile
3. Corporate Innovation and Technology Management, CODELCO, Santiago, Chile
4. Department of Electrical Engineering, University of Chile, Chile
5. Sustainable Electromobility Acceleration Center (CASE), University of Chile, Chile
6. Institute for Complex Systems Engineering (ISCI), University of Chile, Chile

**Corresponding author at: belen.herrera.rivas@ug.uchile.cl*

ABSTRACT

The energy transition is critical for achieving the mining sector's climate commitments. The electrification of mobile equipment represents the industry's main strategy to reduce emissions. However, the adoption of new technologies requires understanding their real impact on productivity, while ensuring that emission reduction targets are achieved under different operational contexts. This work aims to provide an analytical basis through simulations for the quantification of emissions. The study is framed within a block caving mining operation, where the material handling system at the production level is modeled. The simulation considers LHD (load–haul–dump) equipment under different technological configurations: diesel, battery-electric with onboard charging, and battery-electric with swap systems, analyzing their performance under varying operating conditions. Scenarios were defined by varying technological configuration, mixed fleet operations, production demand, number of charging stations available, and battery management strategies. In each scenario, productivity and emissions corresponding to scope 1 (diesel combustion) and scope 2 (electricity consumption) were quantified. Based on the simulated data, environmental and technical criteria were integrated using a multicriteria analysis (AHP), which allows weighting and ranking of technological alternatives. The results indicate that, under optimal operating conditions, LHDs with swap batteries achieve operational continuity similar to diesel fleets, maintaining comparable production cycles. Battery swapping is preferable to onboard charging, given its robustness against logistical constraints. In terms of emissions, reductions were observed from approximately $1.5\ tCO_2/day$ *per unit with battery-electric technologies. These findings demonstrate the feasibility of battery-electric equipment not only in terms of emissions but also regarding productivity and continuous operation, supporting an effective transition toward more sustainable underground mining.*

Introduction

The transition toward more sustainable mining operations has driven interest in zero-emission technologies, particularly in underground mining, where the use of diesel equipment generates significant greenhouse gas (GHG) emissions and adverse operational conditions. In this context, Load–Haul–Dump (LHD) equipment plays a critical role, as it is essential for the production cycle and accounts for a significant share of energy consumption at the production level.

This study aims to evaluate the productive and environmental impact of adopting electric technologies in LHD equipment, comparing them with traditional diesel operations. For this purpose, simulations were developed using the ELMOMine-UG software, representing realistic operating conditions under different technological scenarios: onboard battery charging, battery swapping, and diesel as the baseline.

From these simulations, key indicators such as cycle times, estimated productivity, and Scope 1 and Scope 2 GHG emissions were quantified, applying IPCC (2006) factors and information from the Chilean National Electricity System (CNE, 2023).

As part of the results analysis, technical and environmental criteria were integrated through an Analytic Hierarchy Process (AHP) model, which makes it possible to weight and prioritize technological alternatives based on their performance. This approach supports strategic decision-making for the energy transition in mining, incorporating expert judgment from the sector to assign relative weights to different criteria.

This work contributes to filling a gap in the literature regarding systematic comparisons between electric and diesel LHD technologies, from both technical and environmental perspectives, under a replicable methodology of simulation and multicriteria evaluation. The paper is organized as follows: first, the methodological framework and simulation structure are presented, followed by productivity and emissions results, and finally, the prioritization of alternatives and strategic conclusions.

Methodology

The methodology is based on operational simulation using ELMOMine-UG (Figure 1), focused on the production level in underground block/panel caving operations. Three technological scenarios were modeled based on Load–Haul–Dump (LHD) equipment: diesel, onboard battery charging, and battery swapping. For diesel, Sandvik LH517i units were used, while electric configurations operated with Sandvik LH518B units. The simulations allow calculating operational indicators such as effective time, utilization, availability, and tonnes per shift, under a common structure of operating parameters.

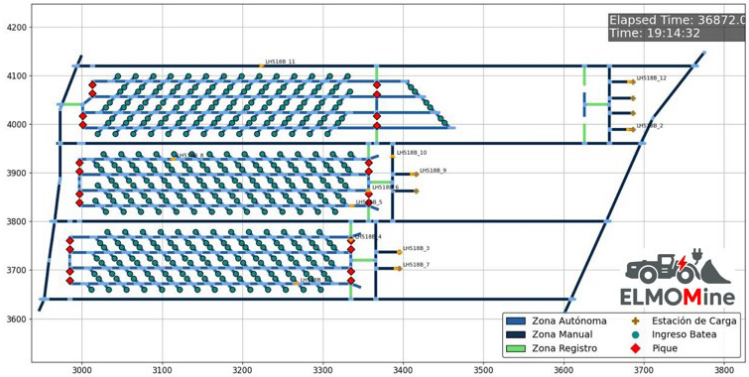

Figure 1. Production level layout of the simulated mine

Based on the simulated operational results, GHG emissions for Scope 1 and Scope 2 were quantified using specific emission factors. For diesel, IPCC 2006 values were applied ($2.74\ \mathrm{kg\ CO_2e/Lt}$):

$$Emissions(CO2e) = Consumption_{diesel} \cdot EF_{diesel}$$

For electricity, the factor from the Chilean National Electricity System was used ($238.4\ \mathrm{kg\ CO_2e/}$ MWh for the baseline year):

$$Emissions(CO2e) = Consumption_{electric} \cdot EF_{electricity}$$

Once the results of the different simulated scenarios were obtained, they were evaluated using the Analytic Hierarchy Process (AHP) methodology. This method allows prioritizing decision alternatives based on multiple qualitative and quantitative criteria, organized in a hierarchical structure that represents the main objective, evaluation criteria, and available alternatives.

Based on the objectives of the ore transport system, six main criteria were defined:

- Daily production (DP)
- GHG emissions (Scopes 1 and 2) (EG)
- Operational availability (OA)
- Charging and refueling time (CT)
- Energy OPEX: fuel cost (OE)
- CAPEX: initial investment (CI)

The assignment of weights to each criterion was carried out through expert judgment, via a structured survey sent to a panel of professionals with experience in electromobility and underground mining. Each criterion was weighted using a pairwise comparison matrix, following Saaty's fundamental scale (Figure 2). The pairwise comparison matrices obtained were aggregated using the geometric mean, as recommended by Saaty (2007), to generate the global priority matrix.

The Fundamental Scale for Pairwise Comparisons		
Intensity of Importance	**Definition**	**Explanation**
1	Equal importance	Two elements contribute equally to the objective
3	Moderate importance	Experience and judgment slightly favor one element over another
5	Strong importance	Experience and judgment strongly favor one element over another
7	Very strong importance	One element is favored very strongly over another; its dominance is demonstrated in practice
9	Extreme importance	The evidence favoring one element over another is of the highest possible order of affirmation
Intensities of 2, 4, 6, and 8 can be used to express intermediate values. Intensities 1.1, 1.2, 1.3, etc. can be used for elements that are very close in importance.		

Figure 2. Saaty's Fundamental Scale for Pairwise Comparisons

The consistency of judgments was verified using the Consistency Index (CI) and Consistency Ratio (CR):

$$CI = \frac{\lambda_{max} - n}{n - 1}, \quad CR = \frac{CI}{RI}$$

Where:

- λmax: maximum eigenvalue of the matrix.
- n: number of criteria (in this case, 6)
- RI: random index, which for n=6 is 1.24

A CR ≤ 0.1 was considered acceptable. Each alternative was evaluated with respect to each criterion using the results simulated with ELMOMine-UG, such as energy consumption, estimated productivity, and GHG emissions. The values were normalized and multiplied by the weights defined in the previous step. Finally, a global score was calculated for each alternative, enabling prioritization. This result identifies which option presents a better balance between productive and environmental performance under representative underground operating conditions.

Results and Discussions

This section presents the simulation results associated with the production level. LHD fleets in three contrasting operational configurations were analysed: onboard charging, battery swapping, and diesel.

Figure 3 shows the evolution of the state of charge (SoC) and the operational cycle of the LH518B model in the onboard-battery configuration over a 3-day (72-hour) horizon. An effective autonomy of approximately 3.5 hours per charge cycle is observed, with a minimum SoC of 20% and an average recharge duration of 42 minutes. Under these conditions, production per shift reaches about 3 kt, with an operational availability of 15.2 h/d.

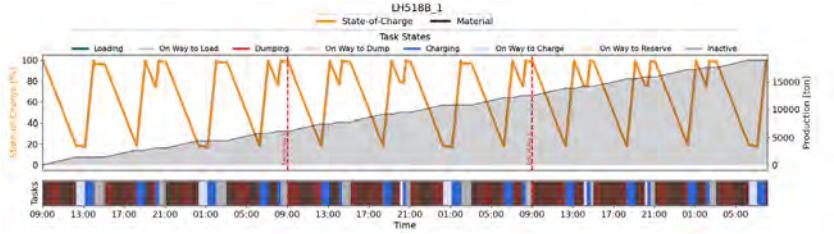

Figure 3. Operational cycle and state of charge of Electric LHD LH518B_1 (onboard battery) over 72 hours

Figure 4 presents the same analysis for the battery-swapping fleet. Although effective autonomy remains around 3.5 hours, the average recharge time is reduced to approximately 9 minutes, allowing up to four recharge events per shift. This results in a significant increase in productivity, reaching about 4 kt per shift and an operational availability of 18.7 h/d.

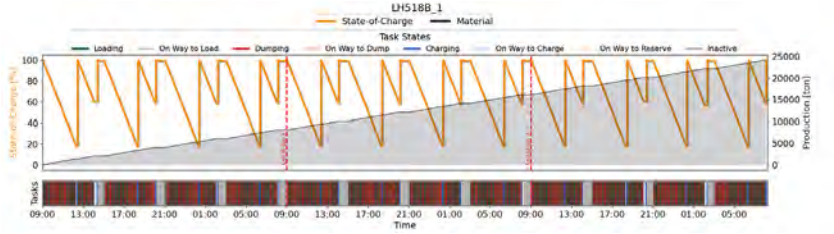

Figure 4. Operational cycle and state of charge of Electric LHD LH518B_1 (swap battery) over 72 hours

Finally, Figure 5 corresponds to the diesel case (LH517i model), in which cycles remain practically continuous, with interruptions limited to breaks and shift changes. Production reaches about 3.4 kt per shift and an operational availability of 19.4 h/d, confirming the advantage in operational continuity of this configuration compared to the electric alternatives.

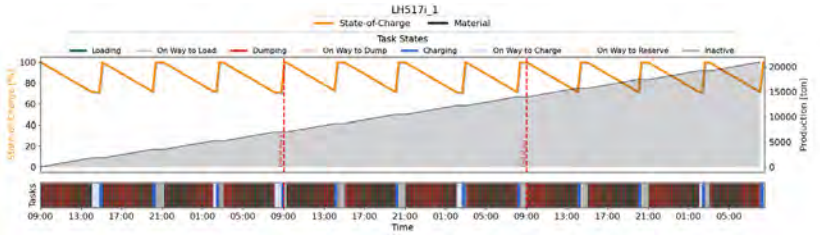

Figure 5. Operational cycle and state of charge of Diesel LHD LH517i over 72 hours

From daily energy and diesel consumption, emissions by technology were obtained:

Table 1. Daily emissions per unit

Technology	Energy Consumption (kWh/day)	Diesel Consumption (L/day)	Emissions (tCO_2/day)
Onboard battery	1332	-	0.32
Diesel	-	662	1.81
Swap battery	1731	-	0.42

For the multicriteria model, AHP was constructed with expert weighting matrices. The geometric mean of the experts' matrices is presented below:

Table 2. Pairwise comparison matrix for criteria evaluation

Criteria	DP	EG	OA	CT	OE	CI
DP	1	4	2	5	2	3
EG	0.25	1	0.26	2	0.47	2
OA	0.58	4	1	1.5	0.81	2
CT	0.21	0.43	0.67	1	0.56	2
OE	0.41	2	1	2	1	1
CI	0.37	0.61	0.64	0.64	0.88	1

Table 3 confirms that the results are consistent, and the judgments are acceptably consistent:

Table 3. Consistency verification

λ_max	6.42
CI	0.08
RI (n=6)	1.24
CR	7%

Regarding the ranking of the alternatives, Table 4 presents the normalized results of each alternative for each criterion.

Table 4. Evaluation of alternatives with respect to criteria (normalized)

Criteria	Tipo (Max/Min)	A1: BEV batería fija	A2: BEV batería swap	A3: Diésel
DP	Max	0.00	1.00	0.40
EG	Min	1.00	0.93	0.00
OA	Max	0.00	0.83	1.00
CT	Min	0.00	1.00	0.82
OE	Min	1.00	0.85	0.00
CI	Min	0.00	0.00	1.00

Then, after applying the sum-product with the criterion weights, the alternative analysis shows that the best-evaluated option corresponds to A2: BEV with a battery swap system, which achieved the highest global score of 0.837, ranking first. In second place is A3: Diesel, with an intermediate score of 0.502. Finally, in third position is A1: BEV with onboard battery, which obtained the lowest score of 0.273.

Conclusions

The results show that although diesel technology maintains advantages in autonomy and ease of implementation, electric alternatives—particularly battery swapping—offer a superior balance between productivity and emission reduction. This demonstrates that underground electromobility is not only feasible, but also a concrete solution to advance the sector's decarbonization, while maintaining competitive levels of operational performance.

References

Comisión Nacional de Energía (CNE), 2023. Factores de emisión del Sistema Eléctrico Nacional. Santiago, Chile.

Electric Mine Consortium, 2022. Electric Mine Simulation Framework.

IPCC. (2006). 2006 IPCC Guidelines for National Greenhouse Gas Inventories.

International Energy Agency (IEA). (2022). Global EV Outlook 2022: Securing supplies for an electric future.

Saaty, T., 2007. Decision making with the analytic hierarchy process. International Journal of Services Sciences, 1(1), 83-98.

Evolution and Projection of the Surface Impact of Open-Pit Mining Through Multitemporal Analysis of Satellite Images

Fernanda Espínola[1,2*], Emilio Castillo[1,3] and Luis Felipe Orellana[1,2]

1. Department of Mining Engineering, FCFM, University of Chile, Santiago, Chile
2. Advanced Mining Technology Center, FCFM, University of Chile, Santiago, Chile
3. Solar Research Center, FCFM, University of Chile, Santiago, Chile

**Corresponding author at: Department of Mining Engineering, FCFM, University of Chile, Santiago, Chile.*
E-mail address: fernanda.espinola@uchile.cl

ABSTRACT

Mining activity is essential for the supply of mineral resources that sustain global development based on clean energy. While its material contribution is undeniable, mining generates significant impacts on environmental conservation, particularly on soil, water, air, and biodiversity. In this context, understanding the magnitude and evolution of the surface impact associated with open-pit mining is fundamental to guide more responsible territorial planning strategies and to develop comprehensive assessments of its effects.

This study analyzes the surface expansion of large-scale copper mining in chile through a multitemporal analysis of sentinel and landsat satellite images, covering the period 1984–2024. The methodology enabled the quantification of mine and tailings area growth, as well as the projection of future scenarios of territorial occupation.

The results show that the surface footprint of open-pit mining maintains a growth trend, although with different rates across operations. In some cases, a clear stabilization is observed, while in others the expansion remains significant, especially due to the contribution of external tailings. Overall, the analysis confirms that territorial expansion is conditioned by technical and environmental factors that define its future limits.

Introduction

Mineral resources are fundamental to modern society, providing more than 95% of global energy and over 80% of industrial raw materials. However, accelerated economic growth and the increasing demand for energy have intensified mining expansion worldwide (Qian et al. 2018). Among extractive methods, open-pit mining represents one of the most significant anthropogenic pressures on terrestrial ecosystems, generating extensive surface disturbances, vegetation loss, topographic alterations, and cumulative transformations of the natural landscape (Huang et al. 2015). These modifications compromise ecological functionality, reduce the provision of ecosystem services, and may indirectly affect local communities that depend on these resources (Castello & Macedo 2016).

In addition to landscape transformation, open-pit operations cause a series of environmental impacts, including soil erosion, biodiversity decline, contamination of surface and groundwater, and emissions of dust and noise that intensify ecological degradation (Chukwuma 2011).

Understanding and monitoring the magnitude of these surface disturbances is therefore essential to promote more sustainable mining practices and to support ecological restoration strategies. Remote sensing provides an effective approach for assessing land surface changes related to mining. In particular, multitemporal satellite imagery, such as Landsat and Sentinel, has been widely applied to study land use dynamics, ecological degradation, and industrial impacts (Bian & Lu 2013). Nevertheless, studies specifically focused on long-term monitoring of mining footprints remain limited, especially in arid regions with intense extractive activity such as northern Chile (Boulila et al. 2011).

This study applies a systematic multitemporal analysis of freely available satellite imagery to quantify the territorial expansion of large-scale copper mining in Chile between 1984 and 2024. The aim is to evaluate the evolution of surface disturbance caused by open-pit mining, explore potential future scenarios of expansion, and generate robust spatial evidence to inform sustainable mining planning. The paper is structured as follows: Section 2 describes the methodology used for multitemporal and spatial analysis of satellite imagery and surface change detection; Section 3 presents the results, focusing on the evolution of mine areas, open pits, and tailings; Section 4 discusses the strengths of the applied approach and its usefulness for projecting future transformations of mining territories; and Section 5 summarizes the main conclusions, highlighting implications for mining management and planning while outlining opportunities for improvement and future applications.

Methodology

Study Area

The study area extends from the Arica y Parinacota Region in the far north to the Metropolitan Region of Santiago in central Chile, encompassing a broad portion of the national territory. This zone concentrates most of the country's copper production, making it one of the most important mining regions worldwide. Within this area, climatic conditions show strong contrasts: while the northern sector is characterized by extremely arid deserts, the central sector transitions into semi-arid and sub-humid regimes with seasonal rainfall. These geographical and climatic differences shape both the natural environment and the development of mining activities across territory.

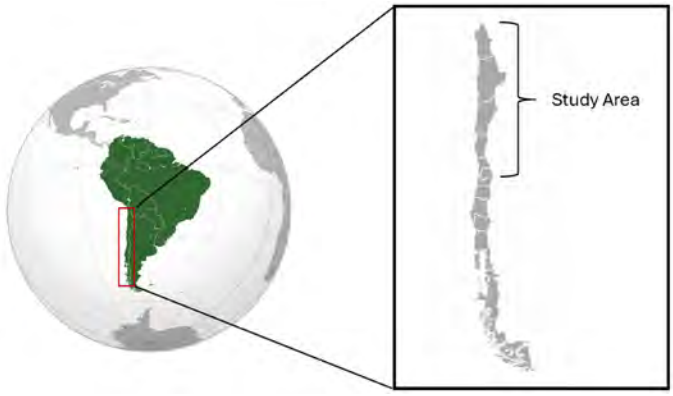

Figure 1. Selected study area in northern and central Chile, extending from the Arica y Parinacota Region (XV) to the Metropolitan Region (RM).

Data Sources and Acquisition

More than 1,200 Sentinel and Landsat satellite images corresponding to the 1984–2024 period were compiled, selecting those with low cloud cover and consistent dates to ensure temporal comparability. These images were processed in a standard format and reprojected into a common coordinate system to maintain spatial consistency throughout the entire historical series. Only the original bands were used, avoiding additional transformations or indices, in order to reduce potential distortions in arid environments where low spectral contrast and highly reflective surfaces can lead to interpretation errors.

Data Processing and Analysis

Satellite images were processed in QGIS, where manual digitization was performed to delineate polygons representing the mining complex and, when applicable, the combined area of mine plus external tailings. From these polygons, surface areas were calculated in km^2, generating a multitemporal dataset covering the period 1984–2024.

The extracted values were organized into spreadsheets and later plotted to analyze the evolution of the occupied surface. Based on this information, different growth functions were tested to fit the observed trajectories and project the potential expansion of each operation through 2050. Among the approaches considered, linear, quadratic, exponential, and logistic models were applied, along with other complementary adjustments, in order to identify which functions best represented the territorial dynamics of each mining site.

The analysis focused on comparing the area of the mining complex with the combined mine plus external tailings, using 2024 as a reference year to estimate future growth trends and characterize the spatial evolution of large-scale copper operations.

Error Assessment

The multitemporal analysis of satellite imagery, as with any methodology based on remote sensing, inevitably involves a certain margin of uncertainty that must be considered when interpreting the results. In this case, the accuracy of surface estimations may be influenced by several factors. On the one hand, there are the inherent limitations of the spatial resolution of the sensors used, which determine the level of detail with which both large areas and smaller components of mining complexes can be represented. On the other hand, variability is also introduced during the manual digitization process, where the visual interpretation of the analyst may lead to slight differences in the delineation of polygons.

Although these factors introduce a degree of error into the quantification, it was verified that the deviations remain within reasonable ranges for studies of this nature. In other words, while minor discrepancies are expected due to sensor resolution or human interpretation, their effect does not significantly alter the general trends observed in the expansion of mining and tailings areas.
For this reason, a representative global error value was adopted to synthesize the overall uncertainty of the analysis. This value does not aim to eliminate the existence of variations, but rather to establish a range of confidence that allows the results to be interpreted consistently throughout the analyzed period. Consequently, it can be stated that, despite the methodological limitations inherent to this type of approach, the estimations obtained are sufficiently robust to support the conclusions presented in this study.

Results and Discussions

The multitemporal analysis of more than 1,200 satellite images between 1984 and 2024 made it possible to quantify the evolution of mining surfaces in Chile and to generate projections through 2050. To this end, different growth functions—linear, quadratic, exponential, and logistic—were tested in order to identify those that best represented the observed trends in each operation.

The model that provided the most consistent results was the logistic function, which is widely recognized as suitable for describing growth processes that begin with rapid expansion and gradually tend to stabilize over time. In this study, the logistic approach proved to be well aligned with the dynamics observed in the mining areas, as it captured both the initial stages of accelerated growth and the tendency toward slower expansion as operations mature and encounter environmental or territorial constraints.

An important strength of this model is that it not only offered a good fit to the historical data but also allowed the incorporation of an uncertainty assessment in the projections. This assessment highlights that while short-term estimations remain relatively reliable, variability increases as the time horizon extends, particularly when approaching 2050. Such widening uncertainty is expected in long-term modeling and reflects the probabilistic nature of projecting complex territorial processes.

When compared with other functional forms tested—such as linear, exponential, or quadratic models—the logistic curve provided more balanced and realistic results. Linear and exponential functions tended to exaggerate future growth, especially in mature operations that are already reaching their maximum extent, while the quadratic function, although useful in some cases, lacked consistency across the different sites. For these reasons, the logistic model, complemented by the uncertainty analysis, was selected as the methodological basis for the projections developed in this work.

Analysis of mining complexes

The evaluation of mining complexes shows that, although an overall increase in occupied surface is projected toward 2050, this growth is far from uniform across operations. Some mines appear to be in more mature stages, with surface areas that remain almost stable and only minor increases expected. Others, however, display more substantial expansion trends, in some cases exceeding half of their current footprint.

Most operations fall within intermediate growth ranges, reflecting a mix of factors such as ore body maturity, geographic conditions that either enable or restrict further development, and environmental or regulatory constraints that are becoming increasingly influential. This differentiated behavior highlights that the territorial evolution of mining does not follow a single trajectory but instead responds to the interplay between technical, geological, and contextual conditions unique to each site.

Figure 2 illustrates representative cases that highlight contrasting patterns:

- Mine A (Figure 2a): The model indicates that Mine A maintains a clear expansion trend, projected to continue growing steadily until around 2040. After that point, the rate of increase slows down, suggesting that the operation is gradually approaching a stage of stabilization. This pattern reflects a relatively younger mine compared to others, where there is still territorial space available and ore reserves that support sustained development. Nevertheless, the projection also shows that even in these conditions, growth is not indefinite, and the mine will eventually encounter natural and operational limits.
- Mine B (Figure 2b): In contrast, Mine B presents a trajectory of continuous growth projected up to 2050, showing a more prolonged expansion compared to other sites. This behavior is associated with its intermediate stage of development, where the enlargement of pits and the incorporation of satellite deposits have played a central role in extending its territorial footprint. The model suggests that this expansion remains feasible in the medium and long term, although, as with all operations, it will eventually face constraints imposed by geography, resources, or external regulations.

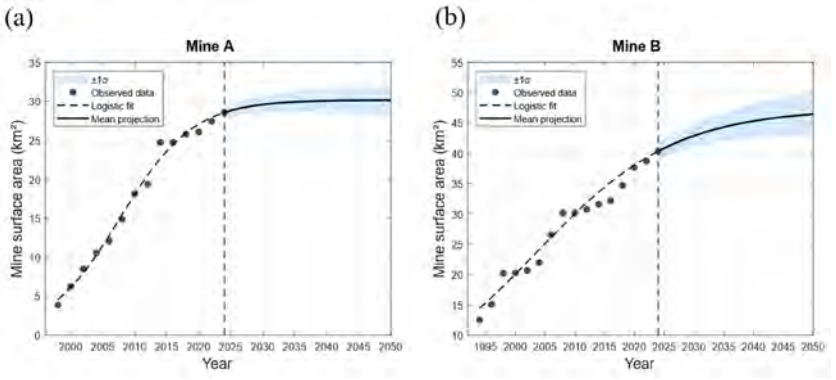

Figure 2. Logistic projection of mine surface area for four representative operations: (a) Mine A, (b) Mine B.

Analysis of mining complexes + external tailings

When the analysis is expanded from the mining complex alone to also include external tailings facilities, the perspective on territorial footprint changes significantly. It is not only the area directly associated with the mine itself, but also the additional space required for waste disposal, which in many cases becomes a decisive factor in shaping future expansion.

The results reveal that this effect is far from uniform. In some operations, external tailings have only a marginal influence, and the overall footprint remains relatively stable, reflecting sites that are more consolidated or with limited room for growth. In others, however, tailings emerge as the main driver of projected expansion, accounting for a substantial portion of the increase in occupied land. This diversity highlights that the evolution of mining surfaces does not follow a single trajectory but is instead conditioned by a combination of technical, environmental, and territorial factors. While certain operations show signs of stabilization, others continue to project more noticeable increases, where the management of tailings becomes central to understanding the scale and direction of expansion.

The results reveal that external tailings can significantly affect the projected footprint in certain operations, as illustrated in Figure 3.

- **Mine A (Figure 3a):** When external tailings are considered, the projected footprint of Mine A expands noticeably compared to the mining complex alone. This reflects the significant role of waste disposal facilities in shaping the mine's long-term territorial presence. While the curve shows that growth will eventually slow down after 2040, the inclusion of tailings clearly pushes the overall surface upward, emphasizing that the mine still has room for expansion in both extraction and waste management. The projection suggests that Mine A, being a relatively younger operation, remains in a growth stage, although gradually approaching the natural and territorial limits that will ultimately constrain its expansion.

- **Mine B (Figure 3b):** In the case of Mine B, tailings facilities emerge as a decisive factor in the projected footprint, accounting for a very substantial share of future growth. The model indicates that nearly one-third of the expansion toward 2050 is explained by the presence and enlargement of external tailings, highlighting that the mine's territorial dynamics are not only driven by the mining complex itself but also by the infrastructure required to manage increasing volumes of waste. This behavior reflects the mine's intermediate stage of development, where both pit expansion and waste facilities combine to extend its surface, making tailings a central element for understanding the trajectory of its long-term growth.

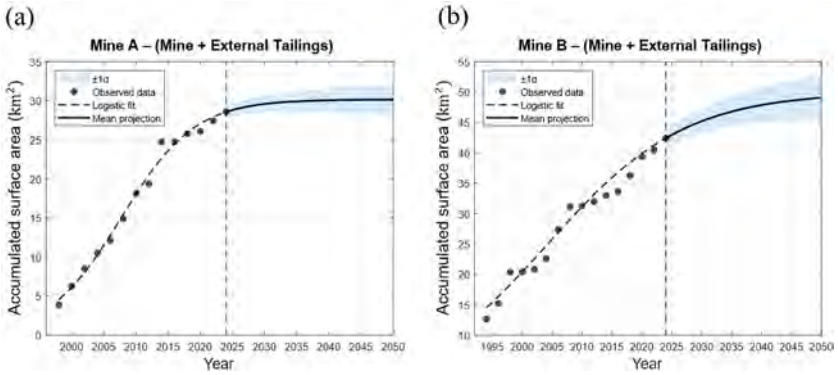

Figure 3. Logistic projection of mine + external tailings surface area for four representative operations: (a) Mine A, (b) Mine B.

Critical synthesis

The analysis makes clear that the evolution of mining surfaces is not a uniform process but one that varies considerably from site to site. Some operations are already showing signs of stabilization, while others remain on a path of continuous expansion. This uneven behavior reflects the complexity of mining development, where technical factors such as ore body maturity and extraction methods, territorial aspects linked to geographic space, topography, and land availability, and environmental conditions related to water scarcity, biodiversity conservation, and regulatory restrictions interact in different ways.

A particularly relevant observation is the influence of external tailings, which in many cases emerge as a decisive factor in shaping the projected footprint. Their presence demonstrates that the long-term impact of mining extends well beyond the pit itself, with waste management becoming an increasingly important element of territorial transformation.

Overall, the results suggest that expansion has limits, and that future growth will be progressively constrained by natural, environmental, and regulatory boundaries. More than providing exact figures, these findings emphasize the magnitude of the footprint and the importance of anticipating its consequences. In this sense, the study offers a broader perspective on how mining reshapes the territory and highlights the need to integrate such impacts into future planning and sustainability strategies.

Conclusions and future work

This study applied multitemporal satellite imagery to analyze the territorial expansion of large-scale copper mining in Chile and to project its potential future trajectories. The results demonstrate that mining complexes maintain a clear trend of surface growth, with external tailings facilities emerging as a decisive driver of territorial occupation. This finding underlines that the long-term impact of mining cannot be understood solely from the perspective of the open pit, but must also incorporate the increasing relevance of waste disposal infrastructure.

At the same time, the projections indicate that this expansion is not unlimited. As operations evolve, they inevitably face technical, environmental, and regulatory constraints that shape their maximum extent. These limits reflect the combined influence of ore body maturity, geographic restrictions, and sustainability requirements, all of which must be considered in the planning of

future mining activities. Recognizing these boundaries is key to anticipating the spatial pressures that mining generates and to embedding sustainability principles into land-use management and decision-making processes.

Future research should not only continue to refine projection models but also integrate surface expansion dynamics with production, ecological, and socio-economic indicators. Such a comprehensive approach will provide a more accurate understanding of the long-term sustainability of mining development and contribute to strategies that balance resource extraction with environmental conservation and responsible territorial planning.

References

Bian, Zhengfu, and Qingqing Lu. 2013. «Ecological Effects Analysis of Land Use Change in Coal Mining Area Based on Ecosystem Service Valuing: A Case Study in Jiawang». Environmental Earth Sciences 68(6):1619-30. doi:10.1007/s12665-012-1855-0.

Boulila, W., I. R. Farah, K. Saheb Ettabaa, B. Solaiman and H. Ben Ghézala. 2011. «A Data Mining Based Approach to Predict Spatiotemporal Changes in Satellite Images». International Journal of Applied Earth Observation and Geoinformation 13(3):386-95. doi:10.1016/j.jag.2011.01.008.

Castello and Marcia. 2016. «Large-scale Degradation of Amazonian Freshwater Ecosystems». Global Change Biology 22(3):990-1007. doi:10.1111/gcb.13173.

Chukwuma and Chrysanthus. 2011. «Environmental Impact Assessment, Land Degradation and Remediation in Nigeria: Current Problems and Implications for Future Global Change in Agricultural and Mining Areas». International Journal of Sustainable Development & World Ecology 18(1):36-41. doi:10.1080/13504509.2011.543837.

Huang, Yi, Feng Tian, Yunjia Wang, Meng Wang and Zhaoling Hu. 2015. «Effect of Coal Mining on Vegetation Disturbance and Associated Carbon Loss». Environmental Earth Sciences 73(5):2329-42. doi:10.1007/s12665-014-3584-z.

Qian, Dawen, Changzhen Yan, Lina Xiu and Kun Feng. 2018. «The Impact of Mining Changes on Surrounding Lands and Ecosystem Service Value in the Southern Slope of Qilian Mountains». Ecological Complexity 36:138-48. doi:10.1016/j.ecocom.2018.08.002.

Numerical and Experimental Analysis of the Dilation Angle in Intact Rock Under Different Confining Conditions

Edison Martínez-Bautista[1*], Daniel Ibarra-González[1], Javier Arzúa[1,2], Manuel González-Fernández[2], Leandro Alejano[2]

1. Department of Metallurgical and Mining Engineering, Universidad Católica del Norte, Chile
2. CINTECX. GESSMin Group. Department of Natural Resources and Environmental Engineering, Universidade de Vigo, Spain

**Corresponding author at: Department of Metallurgical and Mining Engineering, Angamos 0610, Antofagasta, edison.martinez@ce.ucn.cl.*

ABSTRACT

Recent researchers on the dilatancy angle have focused on developing mathematical expressions that improve the understanding of this parameter and the post-peak behavior of rocks and rock masses, with the goal of enhancing the accuracy of numerical simulations. In this sense, several approaches have been proposed to estimate the dilatancy angle, ranging from its simplification as a fixed proportion of the internal friction angle to more sophisticated models that explicitly relate it to confining pressure and plastic shear strain. In the present study, a methodology is proposed that relies solely on the dependence of the dilatancy angle on confining pressure and internal friction angle, using numerical simulations carried out in FLAC2D. The numerical tests were designed to replicate triaxial compression experiments performed on intact Blanco Mera granite specimens, with a diameter of 54 mm, under confining pressures ranging from 0.2 to 15 MPa. From these simulations, stress–strain curves were obtained and subsequently compared with experimental results. This comparison enabled the estimation of the proportion of the friction angle that best represents the dilatancy angle at each confining level. The results confirmed that this proportion decreases as the confining pressure increases, highlighting the progressive suppression of volumetric expansion with higher confinement. Moreover, the observed trend was more accurately captured by rational and exponential mathematical models, achieving coefficients of determination of 0.91 and 0.93, respectively. These findings provide a simplification for the quantitative assessment of dilatancy, thereby contributing to more reliable constitutive descriptions in rock mechanics.

Keywords: rock mechanics, dilation, numerical analysis, laboratory.

Introduction

In modern mining, operations are carried out at increasingly greater depths, which poses more demanding technical, economic, and safety challenges. In this context, a rigorous characterization of the rock mass is essential to understand its stress–strain response under a given stress field. Traditionally, analyses of this behavior have focused on the pre-failure stage, particularly the peak strength, with the aim of preventing collapse. However, for the initial design of pillars and tunnels, peak strength alone is insufficient; it is also necessary to evaluate the post-peak behavior (Alejano and Alonso, 2005; Gao and Kang, 2016; Yi et al., 2020). Within this framework, numerical modeling becomes a key tool for replicating case studies and testing hypotheses, as it enables the reproduction of physical phenomena from input data. In rock mechanics, numerical models are

widely used to analyze the deformational behavior of intact materials and rock masses, as well as their interaction with other elements, both at laboratory and field scale. Advances in computational methods have made it possible to reproduce physical processes with greater realism, thus facilitating a deeper understanding of material responses to external interactions, such as stress field perturbations.

Traditionally, rock mechanics studies have examined stress–strain processes to assess slope stability (Lin et al., 2020) or the stability of underground excavations (Yi et al., 2020). Nevertheless, numerical simulations can also be applied at laboratory scale to validate physical and mathematical assumptions (Tan et al., 2015), using digital rock models governed by constitutive equations under hypothetical conditions defined by the user. Alejano et al. (2005) investigated the post-failure behavior of rocks and rock masses, highlighting that the strain-softening model adequately represents the progressive degradation observed beyond peak strength. Unlike perfectly plastic models, this approach allows for a gradual transition from peak to residual values of cohesion, friction angle, and dilatancy angle, controlled by plastic shear strain and grounded in the incremental theory of plasticity (Hill, 1950). This provides a realistic description of shear-band formation and other deformation phenomena observed in triaxial tests, which are crucial for capturing the post-peak response of rock.

The FLAC2D code (ITASCA, 2024), based on the finite difference method (FDM), implements a strain-softening (and hardening) model by introducing two hardening parameters (k^s and k^t), defined as the sum of increments of plastic shear and tensile strains in each zone (Eqs. 1–3).

$$\Delta k^s = \frac{1}{\sqrt{2}}\sqrt{\left(\Delta\varepsilon_1^{ps} - \Delta\varepsilon_m^{ps}\right)^2 + \left(\Delta\varepsilon_m^{ps}\right)^2 + \left(\Delta\varepsilon_3^{ps} - \Delta\varepsilon_m^{ps}\right)^2} \quad (1)$$

$$\Delta\varepsilon_m^{ps} = \frac{1}{3}\left(\Delta\varepsilon_1^{ps} + \Delta\varepsilon_3^{ps}\right) \quad (2)$$

$$\Delta k^t = \left|\Delta\varepsilon_3^{pt}\right| \quad (3)$$

where $\Delta\varepsilon_1^{ps}$, $\Delta\varepsilon_3^{ps}$ y $\Delta\varepsilon_m^{ps}$ represent the increments of axial, radial, and mean plastic shear strains, respectively; and $\Delta\varepsilon_3^{pt}$ denotes the increment of plastic tensile strain.

The plastic strain increments can be obtained from the following equations:

$$\Delta\varepsilon_1^{ps} = \lambda^s \quad (4)$$

$$\Delta\varepsilon_3^{ps} = -\lambda^s N_\psi \quad (5)$$

$$\Delta\varepsilon_3^{pt} = \lambda^t \quad (6)$$

$$N_\psi = \frac{1 + \sin\psi}{1 - \sin\psi} \quad (7)$$

where λ^s y λ^t are the plastic multipliers for shear and tensile components, respectively; and ψ is the dilatancy angle.

On the other hand, dilatancy refers to the volumetric change experienced by a material when plastic deformations occur because of shear distortion within the material (Castro-Filgueira et al., 2020). This phenomenon is influenced by multiple factors, including stress conditions such as confining and normal stresses, unloading and reloading cycles, porosity, grain shape, temperature, and scale effects (Zhao & Li, 2024). The parameter that most effectively represents this behavior is the dilatancy angle, which serves as the most appropriate descriptor of dilatancy. Based on plasticity theory, Vermeer and de Borst (1984) proposed an equation to characterize the dilatancy

angle at a fixed confining pressure by relating it to increments of plastic strains (Eq. 8).

$$\psi = \arcsin\frac{\dot{\varepsilon}_v^P}{-2\dot{\varepsilon}_1^P + \dot{\varepsilon}_v^P} \tag{8}$$

where $\dot{\varepsilon}_v^P$ and $\dot{\varepsilon}_1^P$ are the increments of volumetric and axial plastic strains, respectively

The dilatancy angle is related to incremental plastic strains, and experimental studies have consistently demonstrated that dilatancy is highly dependent on confining pressure, decreasing in magnitude as confinement increases, since volumetric expansion is progressively suppressed under compression (Ren et al., 2021).

Currently, three main approaches are commonly used to account for the dilatancy angle (Yang et al., 2016). The first approach consists of directly applying the associated flow rule, that is, assuming the dilatancy angle to be equal to the internal friction angle (ϕ), which is considered a purely shear case (Alejano & Alonso, 2005). The second approach involves adopting a non-associated flow rule, where the dilatancy angle is taken as a constant value, most often assumed to be zero, implying that the rock does not undergo volumetric change during deformation. Within this approach, several approximations have been proposed, such as those of Vermeer and de Borst (1984), who indicated that the dilatancy angle is at least 20° lower than the internal friction angle. It is also worth noting that Hoek and Brown (1997) suggested dilatancy angles depending on rock mass quality, recommending a value of $\phi/4$ for very good quality masses, $\phi/8$ for average quality masses, and 0° for very poor quality masses. Furthermore, Alejano et al. (2010) proposed an equation to calculate the dilatancy angle as a function of the Geological Strength Index (GSI) and the internal friction angle, as shown in the following equation:

$$\psi = \frac{5 \cdot GSI - 125}{1000}\phi \tag{9}$$

Although dilatancy was originally considered a constant parameter, it has been demonstrated that it varies significantly with confining pressure and with damage, usually quantified through plastic shear strain (Walton et al., 2017). Consequently, the third approach focuses on establishing a quantitative relationship between dilatancy angle, plastic strain, and confining pressure. Several empirical attempts have been proposed to describe dilatancy, with models that capture its evolution as a function of confinement and stress–strain history (Alejano & Alonso, 2005; Zhao & Cai, 2010; Rahjoo & Eberhardt, 2016). Stress–strain curve analyses show that, from crack initiation (CI), minor plastic radial strains develop, while after crack damage (CD), both radial and axial plastic strains become significant. Based on this behavior, different models have been formulated taking CD as the reference point (Ren et al., 2021; Walton & Diederichs, 2015; Zhao & Cai, 2010). CI is commonly disregarded as the onset of plastic deformation because it leads to negative dilatancy angles between CI and CD, and the plastic strains in this stage are negligible compared to those occurring beyond CD (Zhao & Cai, 2010). From these considerations, the following expression can be derived:

$$\gamma^p_{shifted} = \gamma^p - \gamma^p_{CD} = |\varepsilon^p_1 - \varepsilon^p_3| - \gamma^p_{CD} \tag{10}$$

where γ^p is the plastic shear strain and $\gamma^p{}_{shifted}$ is the plastic shear strain, shifted relative to CD.

However, this approach is limited to empirical formulations with a strong mathematical focus, often resulting in rather complex expressions. A representative example is the model proposed by Zhao and Cai (2010), which requires nine fitting parameters (Eqs. 11-14).

$$a = a_1 + a_2 e^{\frac{-\sigma_3}{a_3}} \tag{11}$$

$$b = b_1 + b_2 e^{\frac{-\sigma_3}{b_3}} \tag{12}$$

$$c = c_1 + c_2 \sigma_3^{c_3} \tag{13}$$

$$\psi = \frac{ab\,(e^{-b\gamma^p} - e^{-c\gamma^p})}{c - b} \tag{14}$$

where σ_3 is confining stress.

Methodology

The database used in this study includes 70 triaxial compression tests conducted under confining pressures ranging from 0.2 to 15 MPa at the John P. Harrison Rock Mechanics Laboratory, School of Mining and Energy Engineering, Universidade de Vigo (Fig. 1a). The intact granite Blanco Mera specimens, with a diameter of 54 mm (Fig. 1b), were collected from the province of Lugo, located in the province of Lugo, Galicia, in northwestern Spain.

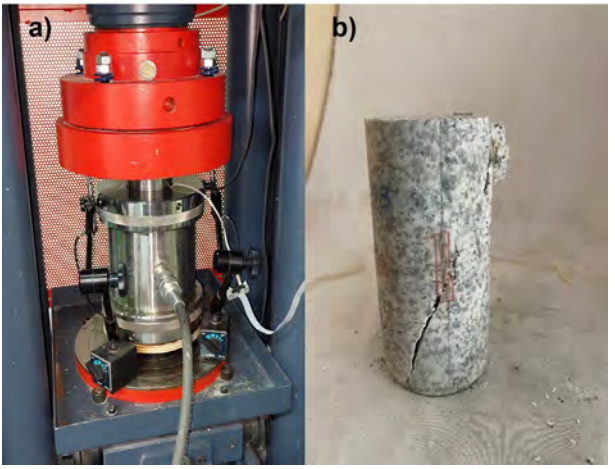

Figure 1. (a) Hydraulic press, (b) Blanco Mera granite specimen.

The methodology included a preliminary experimental analysis, in which the stress–strain curves were processed to obtain the average initial parameters for each confining level required in the constitutive equations, such as Young's modulus (E), Poisson's ratio (υ), and CD. In addition, the average density of the tested specimens was determined, and the tensile strength value reported by Pérez-Rey et al. (2023) was incorporated. To compute the plastic strains, the following equations were considered:

$$\varepsilon_1^p = \varepsilon_1 - \frac{\sigma_1}{E} \tag{15}$$

$$\varepsilon_3^p = \varepsilon_3 - \varepsilon_1 v \tag{16}$$

$$\varepsilon_v^p = \varepsilon_1^p + 2\varepsilon_3^p \tag{17}$$

This allowed the determination of the evolution of the friction angle and cohesion as a function of plastic shear strain, using the Mohr–Coulomb criterion (Fig. 2).

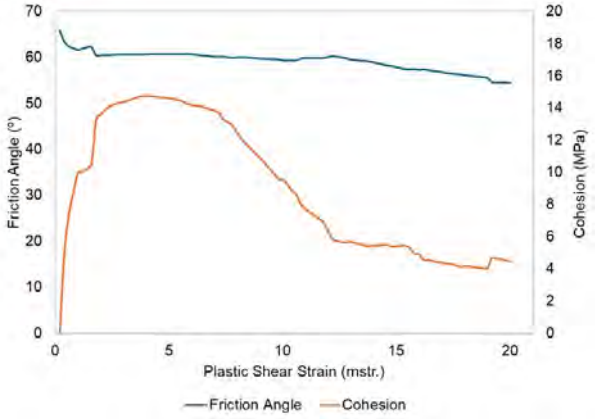

Figure 2. Friction angle and cohesion as a function of plastic shear strain.

Once these parameters were obtained, a numerical model was developed in FLAC2D using the strain-softening constitutive model, with the aim of analyzing the behavior of the dilatancy angle and coherently reproducing the response observed in the experimental results. The cylindrical specimens were represented through an axisymmetric model, by projecting an equivalent rectangle, thereby simplifying the analysis to two dimensions. A mesh with a 20 × 40 cell configuration was employed (Fig. 3), as recommended by Arzúa and Alejano (2013), and the initial and boundary conditions were defined according to the confinement levels and specimen dimensions.

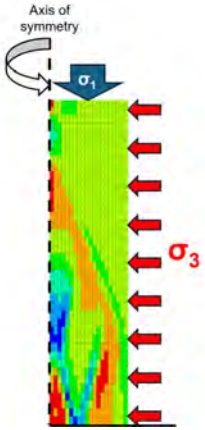

Figure 3. Mesh of the numerical model with boundary conditions and axis of symmetry.

According to Hoek and Brown (1997), the dilatancy angle can be considered as a fraction of the friction angle, while other authors, such as Zhao and Cai (2010), have noted that it depends on confinement and plastic shear strain. In this study, the fraction of the friction angle (α) was evaluated in percentage terms (Eq. 18) with respect to each confining pressure, to identify the dilatancy angle that best represents the experimental dataset. As shown in Fig. 4, for a confining pressure of 6 MPa, the most representative value corresponds to 60% of the friction angle. The same procedure was applied for all confinement levels. It should be noted that, for the unconfined condition, the proportion was assumed to be 100%, corresponding to the maximum possible value.

$$\psi=\alpha\phi \qquad (18)$$

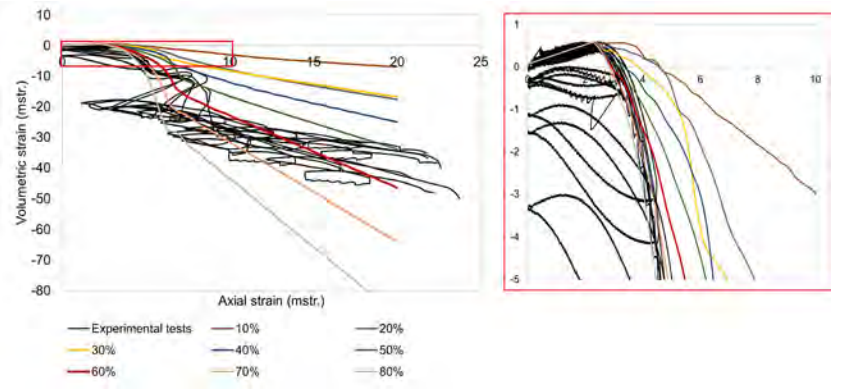

Figure 4. Comparison of simulated and experimental strain curves.

Results and Discussions

The variation of the percentages with respect to confinement was fitted using Eqs. 19 and 20, which exhibit a decreasing trend and are simpler compared to the model proposed by Zhao and Cai (2010).

$$\psi = \phi e^{-a{\sigma_3}^b} \qquad (19)$$

$$\psi = \frac{\phi}{1 + a{\sigma_3}^b} \qquad (20)$$

The results show that the proportion of the friction angle associated with the dilatancy angle decreases progressively with increasing confining pressure, displaying a pronounced drop at low pressures and a tendency to stabilize at higher confinement levels. This behavior reflects the restraining effect of confinement on the volumetric expansion of the rock. To represent this evolution, two empirical expressions were employed. The exponential fitting (Eq. 19) achieved a coefficient of determination of 0.92, accurately reproducing both the initial drop and the subsequent stabilization. The rational fitting (Eq. 20) also provided a satisfactory fit, with a coefficient of determination of 0.91, adequately capturing the overall curvature. Although the exponential model showed slightly better performance, both formulations offer simple and effective alternatives to more complex models such as that of Zhao and Cai (2010), facilitating their application in numerical simulations and improving the understanding of post-peak behavior (Fig. 5).

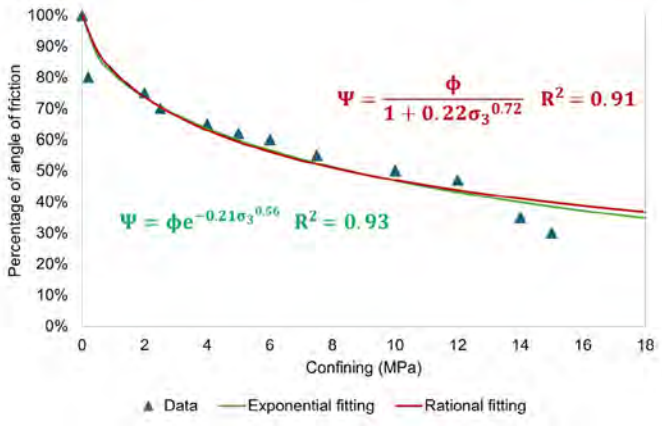

Figure 5. Curve fitting of friction angle percentages.

Conclusions

The study confirmed that, for Blanco Mera granite specimens, the dilatancy angle decreases progressively with increasing confining pressure, exhibiting a pronounced drop at low confining levels and stabilization at higher confinement levels. This behavior was adequately described by simple empirical expressions. The exponential fitting (Eq. 19) achieved the best fit, with a coefficient of determination of 0.93, while the rational fitting (Eq. 20) also provided a satisfactory fit, with a coefficient of determination of 0.91. Compared to more complex models, such as that of Zhao and Cai (2010), the proposed formulations are simpler and more practical, offering a solid basis for improving the understanding of post-failure behavior in rock mechanics.

References

Alejano, L. R. and Alonso, E., 2005. Considerations of the dilatancy angle in rocks and rock masses. Int. J. Rock Mech. Min. Sci., 42(4), 481–507. https://doi.org/10.1016/j.ijrmms.2005.01.003

Alejano, L. R., Alonso, E., Rodríguez-Dono, A. and Fernández-Manín, G., 2010. Application of the convergence-confinement method to tunnels in rock masses exhibiting Hoek-Brown strain-softening behaviour. Int. J. Rock Mech. Min. Sci., 47(1), 150–160. https://doi.org/10.1016/j.ijrmms.2009.07.008

Arzúa, J., Barbiero, J. and Alejano, L. R., 2013. Strain-softening characterization of granitic rocks and numerical simulation of servo-controlled strength tests. ISRM International Symposium - EUROCK 2013, 379–384. https://doi.org/10.1201/b15683-64

Castro-Filgueira, U., Alejano, L. R. and Ivars, D. M., 2020. Particle flow code simulation of intact and fissured granitic rock samples. J. Rock Mech. Geotech. Eng., 12(5), 960–974. https://doi.org/10.1016/j.jrmge.2020.01.005

Gao, F. Q. and Kang, H. P., 2016. Effects of pre-existing discontinuities on the residual strength of rock mass - Insight from a discrete element method simulation. J. Struct. Geol., 85, 40–50. https://doi.org/10.1016/j.jsg.2016.02.010

Hill, R., 1950. The mathematical theory of plasticity. Oxford: Oxford University Press.

Hoek, E. and Brown, E. T., 1997. Practical Estimates of Rock Mass Strength. Int. J. Rock Mech. Min. Sci., 34(8), 1165–1186.

ITASCA 2024. Itasca Software 9.0 Documentation: New User Guide. Minnesota: Itasca Consulting Group, Inc.

Lin, H. da, Wang, W. C. and Li, A. J., 2020. Investigation of dilatancy angle effects on slope stability using the 3D finite element method strength reduction technique. Computers and Geotechnics, 118. https://doi.org/10.1016/j.compgeo.2019.103295

Pérez-Rey, I., Muñoz-Ibáñez, A., González-Fernández, M. A., Muñiz-Menéndez, M., Herbón Penabad, M., Estévez-Ventosa, X., Delgado, J. and Alejano, L. R., 2023. Sisé effects on the tensile strength and fracture toughness of granitic rock in different tests. Journal of Rock Mechanics and Geotechnical Engineering, 15(9), 2179–2192. https://doi.org/10.1016/j.jrmge.2022.11.005

Rahjoo, M. and Eberhardt, E., 2021. Development of a 3-D confinement-dependent dilation model for brittle rocks; part 2, formulation and parameterization based on the Cartesian plastic strain increments ratios approach. Int. J. Rock Mech. Min. Sci., 148(November), 104773. https://doi.org/10.1016/j.ijrmms.2021.104773

Ren, C., Yu, J., Cai, Y., Yao, W., Lai, Y. and Li, B., 2021. A novel constitutive model with plastic internal and damage variables for brittle rocks. Eng. Fract. Mech., 248(April), 107731. https://doi.org/10.1016/j.engfracmech.2021.107731

Tan, X., Konietzky, H. and Frühwirt, T., 2015. Numerical simulation of triaxial compression test for brittle rock sample using a modified constitutive law considering degradation and dilation behavior. Journal of Central South University, 22(8), 3097–3107. https://doi.org/10.1007/s11771-015-2846-6

Vermeer, P. A. and de Borst, R., 1984. Non-associated plasticity for soils, concrete and rock. Heron, 29, 1–64.

Walton, G. and Diederichs, M. S., 2015. A New Model for the Dilation of Brittle Rocks Based on Laboratory Compression Test Data with Separate Treatment of Dilatancy Mobilization and Decay. Geotech. Geol. Eng., 33(3), 661–679. https://doi.org/10.1007/s10706-015-9849-9

Walton, G., Hedayat, A., Kim, E. and Labrie, D., 2017. Post-yield Strength and Dilatancy Evolution Across the Brittle–Ductile Transition in Indiana Limestone. Rock Mech. Rock Eng., 50(7), 1691–1710. https://doi.org/10.1007/s00603-017-1195-1

Yang, F., Zhou, H., Zhang, C., Hu, D., Lu, J. and Meng, F., 2016. An elastoplastic coupling mechanical model for hard and brittle marble with consideration of the first stress invariant effect. European Journal of Environmental and Civil Engineering, 22(4), 405–428. https://doi.org/10.1080/19648189.2016.1197160

Yi, K., Kang, H., Ju, W., Liu, Y. and Lu, Z., 2020. Synergistic effect of strain softening and dilatancy in deep tunnel analysis. Tunn. Undergr. Space Technol., 97(January), 103280. https://doi.org/10.1016/j.tust.2020.103280

Zhao, R. and Li, C., 2022. A New Dilation Angle Model for Rocks. Rock Mech. Rock Eng., 55(9), 5345–5354. https://doi.org/10.1007/s00603-022-02835-6

Zhao, X. G. and Cai, M., 2010. A mobilized dilation angle model for rocks. Int. J. Rock Mech. Min. Sci., 47(3), 368–384. https://doi.org/10.1016/j.ijrmms.2009.12.007

Sampling Variability and Optimal Frequency in Multisource Feed to Chuquicamata Concentrator

Rocío Paineo Antio[1] and Paula Peñaloza Navarro [1]

1. Mine Resource Management and Development Department / Quality Superintendence, CODELCO, Chile

**Corresponding author at: Mine Resource Management and Development Department / Quality Superintendence,CODELCO – Chuquicamata Division, Av. Central Sur s/n, Calama, Antofagasta Region, Chile, rpain001@codelco.cl and ppena018@codelco.cl.*

ABSTRACT

Chuquicamata Division is a large-scale copper and molybdenum mining operation, comprising both open-pit and underground deposits, located at 2,900 meters above sea level and 15 km north of Calama, in Chile's Antofagasta Region, El Loa Province. In continuous operation since 1915, the division produced 289 thousand metric tons of fine copper in 2024. Its commercial products include electrorefined and electrowon cathodes with 99.99% purity, copper concentrate, and, as by-products, molybdenum concentrate and anode slimes.

The division integrates hydrometallurgical and pyrometallurgical processes. Within the latter, the Chuquicamata Concentrator plays a pivotal role in ensuring divisional operability and optimizing production outcomes. The plant currently processes approximately 8,000 tons of ore per hour, sourced from three principal mines: Chuquicamata open pit, Chuquicamata underground, and Radomiro Tomic.

The multiplicity of these sources creates a complex operational environment. Blending ores of varying proportions introduces mineralogical variability that directly affects metallurgical performance. In recent years, Chuquicamata has undergone significant transformation—driven by the pursuit of operational continuity, process safety, improved performance, and CODELCO's long-term business plan. These changes have altered the relative contribution of each source, posing constant challenges for the plant in terms of operational standards, reagent dosage, flotation cell kinetics, and maintenance schedules, all while sustaining rougher recoveries above 82%.

Within this framework, the Mine Resource Management and Development Department (GRMD) is tasked with managing and controlling the equipment used to measure grades of elements of interest in the Concentrator feed, specifically at the SAG mill line and the A2 flotation line, through automatic samplers. Characterizing ore variability is essential to determining the optimal sampling frequency, given the heterogeneous nature of the feed.

At present, sampling cuts are performed every 15 minutes. This study evaluates variability tests under three representative scenarios of ore source contribution, with the objective of analyzing copper grade behavior and defining an optimal sampling frequency that aligns with quality standards and the operational requirements of Chuquicamata Division.

Methodology

To evaluate the variability of the automatic sampling system and determine the optimal sampling frequency, a controlled sampling campaign was conducted at the feed to Chuquicamata's A2 plant. Sixty consecutive samples were collected under three different scenarios, specifically designed to represent distinct ore feed sources to the concentrator.

Each campaign consisted of 60 samples taken at 2-minute intervals directly from the automatic sampling system. The samples were subsequently prepared in the division's internal laboratory and chemically analyzed at CODELCO's Central Chemical Laboratory (LQC). The analytical results were recorded through the Laboratory Information Management System (LIMS) and processed using the EMPV software (Evaluador Metalúrgico de Producción Variabilidad), which evaluates sampling variability. All results were analyzed in terms of copper content, since copper represents the corporation's principal commercial product.

The three sampling campaigns are summarized in the following table:

Table 1. Estabished sampling campaigns

Campaign	Feed Source
#1	40% Chuquicamata Underground – 60% Chuquicamata Open Pit
#2	100% Radomiro Tomic
#3	100% Chuquicamata Underground

For each case, the variability of copper grade across the 60 time-based samples was analyzed. The statistical error was calculated at each time interval, and error curves were plotted as Sampling Error (%) versus Time (min). From these curves, the optimal sampling time for each campaign was determined, defined as the point at which the total error remained below the 1% threshold. This follows CODELCO's internal criteria in line with Pitard (1993), who established that for base metals the standard deviation of the total sampling error should not exceed approximately 1% relative, or even less.

The analysis focused exclusively on copper content, given that copper is the primary commercial product and the core of CODELCO's business. The described methodology thus enabled the assessment of the impact of feed source variability on the sampling frequency required to maintain the defined quality control standards.

Results and Discussions

The study demonstrates that the variability of the A2 plant automatic sampling system is strongly influenced by the feed source delivered to the concentrator. Figure 1 confirms that in all analyzed scenarios there is an inverse relationship between sampling interval and representativeness; that is, the longer the interval between cuts, the greater the error in grade estimation.

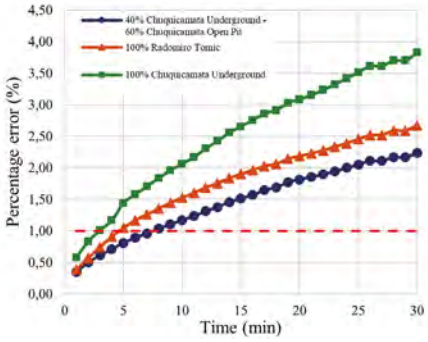

Figure 1. Error curve vs. time interval.

It is important to emphasize that the results presented correspond exclusively to copper, since the analyzed stream represents the concentrator feed. Copper was selected as the focus of analysis due to its criticality for operational control and its central role as the cornerstone of CODELCO's business.

Mineralogy of Ore Sources

The different case studies reflect distinct behaviors in the plant as a function of the mineralogical and metallurgical characteristics of each ore source.

Chuquicamata Open Pit: The mineralogy is characterized mainly by iron sulfides, with pyrite as the predominant mineral across all extraction stages. Primary copper sulfides such as chalcopyrite and bornite dominate, while secondary sulfides such as chalcocite and covellite occur in lower proportions. Copper grades from this source average around 0.5% CuT.

Chuquicamata Underground: This ore presents greater mineralogical heterogeneity. As in the open pit, pyrite is the most abundant mineral. However, significant proportions of secondary sulfides—including covellite, chalcocite, digenite, and enargite—are present, along with primary sulfides such as chalcopyrite and bornite, though in smaller amounts. Molybdenum sulfides, primarily molybdenite, are also identified. Copper grades from this source reach values close to 0.95% CuT. Radomiro Tomic (RT): This open-pit mine differs from Chuquicamata, exhibiting lower pyrite content and a higher proportion of primary sulfides (chalcopyrite and bornite), together with secondary sulfides such as chalcocite and covellite. In this case, copper grades range around 0.6% CuT.

The mineralogical characteristics considered in the three variability test campaigns are summarized in Figure 2.

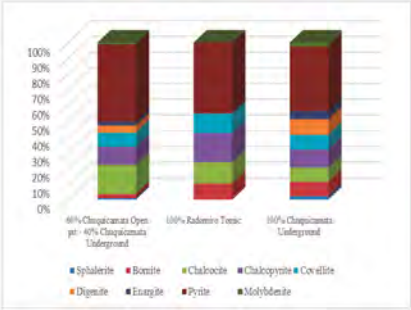

Figure 2. Sulfide-based mineralogy by campaign.

Results by Campaign

Campaign #1 (40% Chuquicamata Underground – 60% Chuquicamata Open Pit): This scenario showed the most stable behavior. The 1% error threshold was maintained up to 7.55 minutes, while under the current 15-minute interval, the error reached 1.51%, representing the closest value to the acceptable limit.

Campaign #2 (100% Radomiro Tomic): The 1% threshold was reached at 4.66 minutes. At 15 minutes, the error increased to 1.90%, indicating that the current practice does not meet the established condition.

Campaign #3 (100% Chuquicamata Underground): The most restrictive scenario. The 1% threshold was reached at 3.97 minutes, and at 15 minutes the error was 2.65%, reflecting the strong heterogeneity of the underground ore.

Table 2. Summary of results by feed source (A2 Plant).

Feed Source	Maximum Time at 1% Error (min)	Error at 15 min (%)	Recommended Frequency (min)
40% Chuquicamata Underground – 60% Open Pit	7,55	1,54	≤7
100% Radomiro Tomic	4,66	1,90	≤5
100% Chuquicamata Underground	3,97	2,5	≤4

Theoretical Ideal vs. Current Practice

Figure 3 shows the comparison between the theoretical sampling intervals required to maintain the 1% error threshold and the current operational practice of 15-minute cuts at the A2 plant. In the critical scenarios (Campaigns #2 and #3), optimal values are between 3 and 5 minutes, highlighting the gap between theoretical requirements and operational practice.

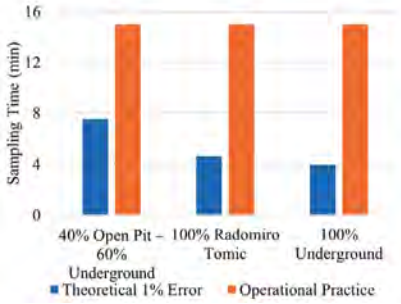

Figure 3. Comparison between theoretical optimal interval and current operational interval.

Sample Projection

At present, samples are taken every 15 minutes, and the composite sample is retrieved every 2 hours. This corresponds to 8 increments per composite and approximately 96 daily samples per feed line.

Adopting the theoretical intervals derived from the variability tests would substantially increase the number of samples per day, as shown in **Table 3** and **Figure 4.**

Table 3. Projection of samples according to cut interval by scenario.

Scenario	Sampling Interval (min)	Samples per 2-h Composite	Daily Samples
Current Operational Practice	15	8	96
40% Chuquicamata Underground – 60% Open Pit	7,55	16	191
100% Radomiro Tomic	4,66	26	309
100% Chuquicamata Underground	3,97	30	363

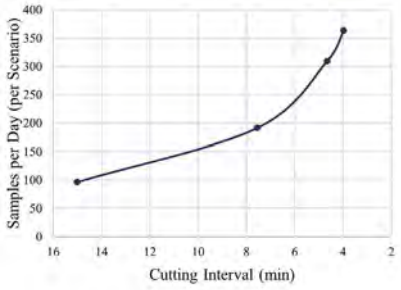

Figure 4. Impact of sampling frequency on the number of daily samples.

This analysis shows that adopting theoretical sampling intervals of 4–5 minutes would at least triple, and in some cases quadruple, the number of daily samples, exceeding the installed capacity for cutting, preparation, and laboratory analysis.

Operational and Economic Feasibility

The current 15-minute sampling frequency reflects the operational and economic feasibility of the process. Implementing 4–5 minute intervals would not only overload laboratory capacity—rising from 96 to over 300 daily samples—but also delay turnaround times.

Since the assay results are used directly in plant operations to adjust parameters and validate feed conditions, delayed availability of results reduces the effectiveness of process control. In practice, more samples do not necessarily translate into better operational control if results cannot be processed and delivered within the required timeframes. The actual operational workflow is illustrated in Figure 5.

Figure 5. Information flow from sampling to operational decision-making.

Increasing the sampling frequency to 4–5 minutes would therefore extend the time required for results to be delivered. Given the central role of this information in guiding plant adjustments, the bottleneck generated by such theoretical intervals is not viable for continuous operation. Thus, although the current 15-minute interval does not comply with the theoretical 1% threshold, it represents a balance between statistical representativeness and the turnaround times required for effective operational decision-making.

Strategic Considerations

These results should not be interpreted as a criticism of the current operational system, but rather as evidence of the inherent statistical risk in automatic sampling. While current errors exceed the 1% threshold, the 15-minute interval aligns more closely with the operational realities of the plant, balancing reliability, cost, and response time.

Looking ahead, however, it is important to anticipate the division's future challenges. With the imminent closure of the open-pit mine, Chuquicamata's concentrator will rely primarily on ore from the underground mine. This represents the most restrictive scenario identified in this study (≤4 minutes to maintain a 1% error), which will become the permanent operating condition.

This reinforces the need to explore technological, managerial, and adaptive sampling alternatives to sustain data reliability without unmanageable increases in sample load. The transition toward an exclusively underground ore feed represents a strategic challenge for process control, in which both sampling frequency and laboratory response times will play a critical role.

Conclusions

- The analysis of copper grades demonstrated that sampling frequency is directly conditioned by the feed source. This relationship is explained by the sulfide-based mineralogy characteristic of each origin, whose elemental heterogeneity determines copper variability in the concentrator feed. The results indicate optimal cutting frequencies of ≤7 minutes for blended feed in a 40/60 proportion, ≤5 minutes for ore from Radomiro Tomic, and ≤4 minutes for material from Chuquicamata Underground.

- The current 15-minute frequency does not comply with the theoretical error limit established by Francis Pitard, reaching 2.65% in the case of underground ore feed.

- Adopting the theoretical intervals would lead to an exponential increase in the number of samples to be prepared and analyzed, rising from 96 to more than 360 daily, thereby exceeding the current laboratory capacity and further extending the turnaround times required for plant operation.

- The current 15-minute interval represents a balance between representativeness and feasibility, enabling timely operational decision-making despite errors exceeding the 1% threshold.

- Given the projected closure of Chuquicamata Open Pit in the coming years, the concentrator will be fed exclusively by the underground mine. This implies that the most critical scenario observed in this study (2.65% error under current practice) will become the standard operating condition. This reinforces the need to implement mitigating and adaptive measures to ensure the reliability of the data required both for plant operation and for metallurgical balances.

References

Pitard, F. F., 1993. Pierre Gy's Sampling Theory and Sampling Practice: Heterogeneity, Sampling Correctness, and Statistical Process Control. CRC Press, Boca Raton, FL.

Pitard, F. F., 2019. Theory of sampling and sampling practice. Chapman and Hall/CRC.

CODELCO., 2021. Normative CNAM-007, Rev-3: Conditions of Sampling Stations for Flows and Product Transfer. Internal document.

Codelco., 2009, 25 de marzo. Informe principales decisiones [Archivo PDF]. Retrieved from https://www.codelco.com/prontus_codelco/site/artic/20110706/asocfile/20110706150616/informe_principales_decisiones_rev_p_25_03_2009.pdf

Seismicity-Based Methodology for Evaluating Fault Reactivation in Underground Mining

Lucy Bravo[1,2*], Luis Felipe Orellana[1,2],Tomás Roquer[3,4], Roberto Gonzalez[5], Italo Leon[5] and Diego Diaz[5]

1. Departamento de Ingeniería de Minas, FCFM – Universidad de Chile, Chile
2. Advanced Mining Technology Center, FCFM – Universidad de Chile, Chile
3. Department of Mining Engineering, Metallurgy and Materials – Universidad Técnica Federico Santa María, Chile
4. Research and Innovation in Mining Group – Universidad Técnica Federico Santa María, Chile
5. Superintendencia de Geología GRMD División El Teniente CODELCO, Chile.

**Corresponding author at: lucy.bravo@uchile.cl*

ABSTRACT

Underground mining is advancing to greater depths due to depletion of near-surface resources and the need to minimize environmental impacts such as subsidence or damage to glaciers. In this context, understanding fault behaviour at depth is critical, particularly in young deposits where the uncertainty makes it difficult to anticipate instability. This study aims to improve the understanding of the conditions that promote mining-induced fault reactivation in an underground deposit. For this purpose, the orientation of principal stress axes (s1 ≥ s2 ≥ s3) and their relative magnitude (f = (s2-s3)/ (s1-s3)) were obtained from seismicity using the iterative stress inversion method. In addition, differential stress values and friction coefficients were combined in Monte Carlo simulations to evaluate the fault reactivation criterion (η) *and estimate the probability of obtaining specific* η *values. The results demonstrate that under a conservative scenario, there exists a high reactivation potential that increases as production fronts advance toward major fault systems. The p50 case shows smaller but persistent critical areas, while the P90 case depicts predominantly stable conditions. The comparison of percentiles underscores the value of a probabilistic framework and contribute to a better understanding of the relationship between fault reactivation, which is essential for improving damage mitigation strategies and risk management in underground mining.*

Introduction

Due to the depletion of superficial resources and an increase in global mineral demand, as well as to minimize the environmental impact, such as subsidence and damage to glaciers, underground mining moves forward to deeper levels, which generates stability challenges that are posed by a surrounding zone of fractures (Ranjith et al., 2017). Added to this is the presence of geological faults play a central role, because they disrupt the continuity of the rock mass and are related to different hazards such as subsidence, collapses, or rockbursts that can affect the underground activities (Du et al., 2024; Witkowski et al., 2024; Xia et al., 2022). For this, knowing the fault behaviour in a deep environment is important and essential, especially in young deposits where the uncertainty makes it difficult to anticipate the possible reactivation of these geological structures.

Faults represent natural systems of crustal deformation, typically comprising a fault core where most of the displacement is accommodated and a surrounding damage zone formed by dense fracture networks and subsidiary faults (Faulkner et al., 2010). These systems act as pre-existing planes of weakness that can modify stress paths during mining and generate a redistribution of stresses, creating zones for failure and acting as triggers for seismic events (Mitchell & Faulkner, 2009; Sainoki et al., 2021).

The challenge of managing faults in deep underground mining is important, particularly in geologically young deposits where uncertainty in structural characterization complicates the ability to know their mechanical response. The combination of high stress magnitudes at depth and the heterogeneity of lithological units and variability of fault zone properties makes these environments highly susceptible to hazardous geomechanical behaviour.

Therefore, this study aims to advance the knowledge of conditions that promote fault reactivation in high-stress underground mining at a world-class deposit. Through integrated analysis of geomechanical parameters, induced seismicity, and fault geometry, the main controlling factors of this phenomenon are identified.

Methodology

In this work, a seismicity catalog was available with heterogeneous data of focal mechanisms, which provide strike, dip, and rake angles of the nodal planes, and it is the essential input for stress inversion. These data were used to reconstruct the spatial and temporal variability of stress conditions within the deposit. To carry out the analysis, different sectors were selected within the deposit, based on the geological boundaries, mining geometry, and seismic density. A uniform grid was generated to create a consistent analytical framework and spatial resolution across all analysis sectors. For each cell, the orientation of the principal stress axes $(\sigma 1 \geq \sigma 2 \geq \sigma 3)$ and the relative magnitude $(\phi = (\sigma 2 - \sigma 3)/(\sigma 1 - \sigma 3))$ were obtained from the seismicity using the iterative inversion method of Levandowski et al. (2018), which is suitable for heterogeneous seismic catalogs. This approach is based on the fundamental principle that seismic focal mechanisms reflect the orientation and relative magnitude of the local stress tensor at the time of rupture, and offers advantages such as robustness to outliers, uncertainty quantification providing confidence intervals for stress parameters, and handling variable focal mechanism quality and nodal plane ambiguity.

To account for uncertainties in geomechanical parameters, Monte Carlo simulations were performed to evaluate a fault reactivation criterion denominated as η. For this, two variables were sampled from uniform distributions: the friction coefficient (μ), ranging between 0.3 and 0.7, and the differential stress $(\Delta\sigma)$, ranging between 1 and 15 MPa. These ranges represent realistic bounds based on laboratory testing and field observations for fault zone materials and in situ stress conditions in underground mining environments. For each Monte Carlo realization, these parameters were combined with the stress orientations obtained by the stress inversion and additional input data to calculate the absolute magnitudes of the principal stresses by the non-Andersonian equations (Pérez-Estay et al., 2023). This approach extends beyond traditional Andersonian faulting theory by incorporating arbitrary stress tensor orientations and variable intermediate stress conditions. This procedure ensures that the variability of mechanical parameters was represented in the simulations, which are summarized schematically in Figure 1.

The fault reactivation criterion (η) was evaluated for each realization in each cell in the grid, which generated a probability distribution of η values in selected sectors. This criterion, based on the Mohr-Coulomb criterion, is defined as the ratio between the distance from the center of Mohr's

circle to the failure envelope and the radius of Mohr's circle (see Figure 2). When η is less than 1, the fault is unstable and considered to be in a state of reactivation, which provides an interpretation linking stress conditions to fault stability and reactivation potential. In particular, the P10, P50, and P90 percentiles were obtained and provide a robust statistical summary of reactivation likelihood, allowing for comparison of fault stability. The P10 value represents the threshold below which 10% of all Monte Carlo realizations fall; this means that there is a 10% probability of obtaining η values lower than the P10 threshold. The P50 value corresponds to the median of the distribution, where exactly 50% of realizations fall below and 50% fall above this threshold. Finally, the P90 value represents the threshold below which 90% of all realizations fall.

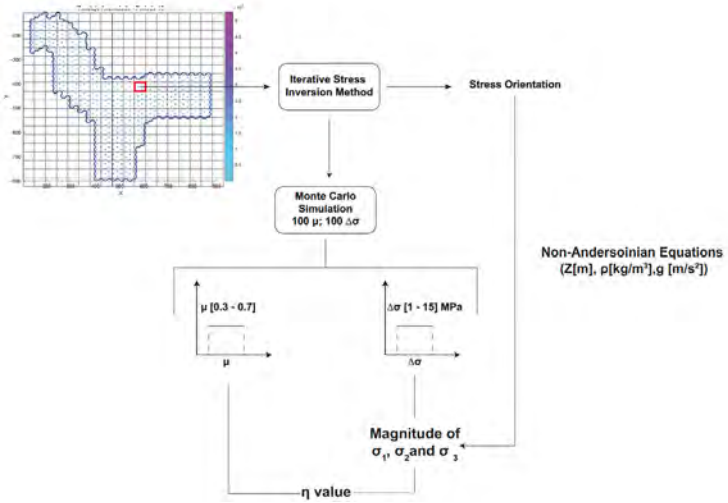

Figure 1. Methodological workflow.

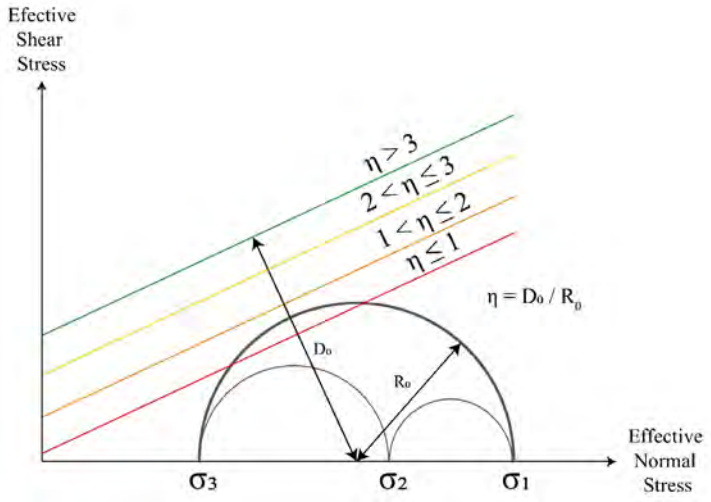

Figure 2. Definition of fault reactivation coefficient η.

Results and Discussions

The analysis of the selected sector reveals consistent spatial and temporal patterns between extraction, stress distribution, and the potential for fault reactivation, which are observed in Figure 3, 4, and 5. By using the stress inversion method combined with Monte Carlo simulations, the study was able to generate a probabilistic assessment of fault stability expressed through the reactivation coefficient η.

Under the P10 scenario (Figure 3), which corresponds to a conservative assessment, consistently highlights regions where faults may exist for reactivation. In these zones, η values less than 1 indicate that stress conditions are sufficient to overcome the frictional resistance along fault planes, and the extent increases markedly as extraction progresses toward the fault. This behaviour illustrates how faults, acting as pre-existing planes of weakness, respond increasingly to stress redistribution induced by mining. These areas represent the least stable conditions and represent the possible potential risk for reactivation. From a methodological perspective, the P10 percentile serves as an early indicator of where slip may be most likely under unfavourable parameter combinations.

The P50 scenario (Figure 4) represents the median or most probable conditions and follows the same trend as the P10 case. In this case, the unstable areas are smaller, but some areas are still almost critical, indicating possible structural instability. As mining periods advance, instability zones persist and become more concentrated near the main fault systems. The persistence of low η values under this intermediate scenario suggests that certain areas are more susceptible to slip, regardless of parameter uncertainty. This reinforces the idea that some areas of the deposit maintain consistently higher potential for instability.

The P90 scenario (Figure 5) corresponds to an optimistic or stable case. In this condition, η values are generally higher, frequently above 3, which indicates that the faults are unlikely to reactivate under stress and frictional conditions. While the P90 provides a useful reference for identifying stable zones, they should not be interpreted independently. Only by comparing it with P10 and P50 can the localized instability zones that persist under less favorable assumptions be fully understood. This comparison highlights the importance of multi-scenario analysis for identifying potential hazards that may not be apparent under optimistic conditions alone.

The combined evaluation of the three percentiles demonstrates the value of incorporating uncertainty into this fault reactivation analysis. Integrating these comparisons of percentiles into mine planning can better evaluate trade-offs between production sequences and seismic hazard, allowing for designs that minimize the probability of fault reactivation without overly compromising extraction efficiency. Traditional deterministic methods often deliver a single solution; meanwhile, this probabilistic approach captures a spectrum of possible outcomes based on distributions of the friction coefficient and differential stress. This assessment is particularly important in geomechanical studies, where parameters would have uncertainty. In this case, the frictional properties of faults and stress magnitudes are normally difficult to constrain precisely, and variations in these properties can significantly influence stability. By incorporating uniform distributions of the parameters, the simulations represent the range of plausible conditions.

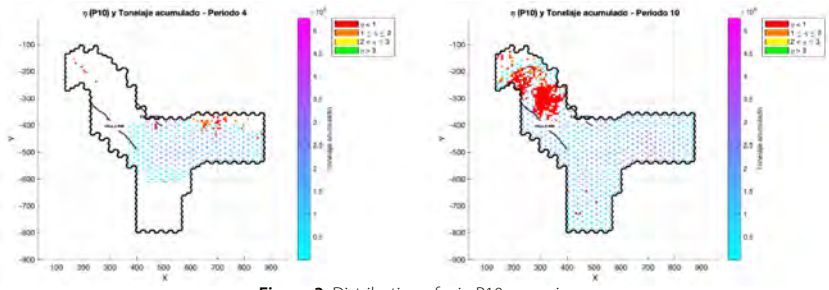

Figure 3. Distribution of η in P10 scenario.

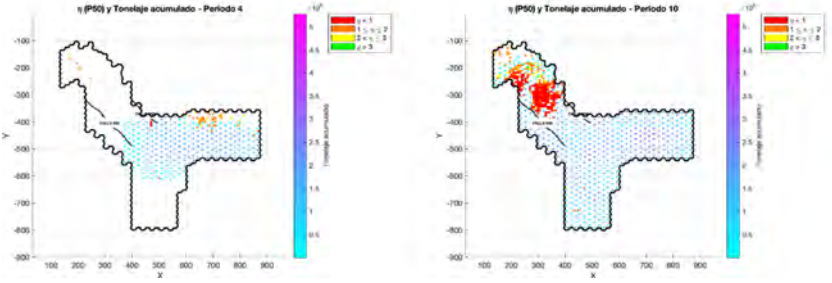

Figure 4. Distribution of η in P50 scenario.

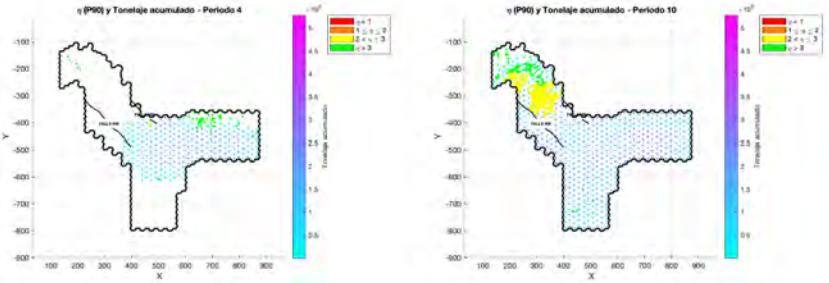

Figure 5. Distribution of η in P90 scenario.

Conclusions

This study applied stress inversion of seismic focal mechanisms combined with Monte Carlo simulations to evaluate fault reactivation potential in a deep mining deposit. The results showed that the reactivation coefficient η provides a useful probabilistic measure for stability, capturing the variability introduced by uncertainties in frictional properties and differential stress. By using different percentiles, it is possible to explore a range of possible scenarios, from conservative to optimistic, and to identify not only the most likely conditions but also the extreme cases that could represent higher risks.

The analysis showed that while most of the sector analysed is stable under optimistic conditions, localized zones with low η values persist under both conservative and intermediate cases. These results highlight the importance of considering multiple scenarios rather than relying on a single

deterministic outcome. Even when the general stability of rock mass is high, the persistence of zones with potential reactivation suggests that the structures can influence the mechanical response of the sector. The classification of η values into four categories provides additional insight, making it possible to detect possible zones for reactivation or with a critical threshold. From a practical perspective, this could be essential for prioritizing monitoring and for developing targeted geomechanical management strategies.

The temporal analysis further highlights how reactivation potential evolves as mining progresses. As production fronts advance toward major fault systems, the extent of unstable zones increases, showing that stress distribution induced by excavation gets faults closer to their reactivation threshold, demonstrating the importance of monitoring over time.

For future work, it is expected to estimate η values in places where we do not have enough focal mechanism data, which is important for the inversion method. This could be done by using an interpolation method or some machine learning tools that combine geological and geomechanical information. Finally, applying this method to other mines with different geological conditions could help to further improve and strengthen the method.

References

Du, K., Bi, R., Khandelwal, M., Li, G. and Zhou, J., 2024. Occurrence mechanism and prevention technology of rockburst, coal bump and mine earthquake in deep mining. Geomechanics and Geophysics for Geo-Energy and Geo-Resources, 10(1), 98. https://doi.org/10.1007/s40948-024-00768-8

Faulkner, D. R., Jackson, C. A. L., Lunn, R. J., Schlische, R. W., Shipton, Z. K., Wibberley, C. A. J. and Withjack, M. O., 2010. A review of recent developments concerning the structure, mechanics and fluid flow properties of fault zones. Journal of Structural Geology, 32(11), 1557-1575. https://doi.org/10.1016/j.jsg.2010.06.009

He, M., Canbulat, I., Suorineni, F. T., Karakus, M., Nie, W., Liu, D., Zhang, C., Nagibin, A. and Rustembek, B., 2025. Definition and classification of rockburst. Rock Mechanics Bulletin, 4(3), 100206. https://doi.org/10.1016/j.rockmb.2025.100206

Levandowski, W., Herrmann, R. B., Briggs, R., Boyd, O. and Gold, R., 2018. An updated stress map of the continental United States reveals heterogeneous intraplate stress. Nature Geoscience, 11(6), 433-437. https://doi.org/10.1038/s41561-018-0120-x

Mitchell, T. M. and Faulkner, D. R., 2009. The nature and origin of off-fault damage surrounding strike-slip fault zones with a wide range of displacements: A field study from the Atacama fault system, northern Chile. Journal of Structural Geology, 31(8), 802-816. https://doi.org/10.1016/j.jsg.2009.05.002

Pérez-Estay, N., Ruz-Ginouves, J., Pérez-Flores, P., Sielfeld, G., Roquer, T., & Cembrano, J., 2023. Decoding the state of stress and fluid pathways along the Andean Southern Volcanic Zone. Communications Earth & Environment, 4(1), 390. https://doi.org/10.1038/s43247-023-01040-9

Ranjith, P. G., Zhao, J., Ju, M., De Silva, R. V. S., Rathnaweera, T. D. and Bandara, A. K. M. S., 2017. Opportunities and Challenges in Deep Mining: A Brief Review. Engineering, 3(4), 546-551. https://doi.org/10.1016/J.ENG.2017.04.024

Sainoki, A., Schwartzkopff, A. K., Jiang, L. and Mitri, H. S., 2021. Numerical Modeling of Complex Stress State in a Fault Damage Zone and Its Implication on Near-Fault Seismic Activity. Journal of Geophysical Research: Solid Earth, 126(7), e2021JB021784. https://doi.org/10.1029/2021JB021784

Witkowski, W. T., Łucka, M., Guzy, A., Sudhaus, H., Barańska, A. and Hejmanowski, R., 2024. Impact of mining-induced seismicity on land subsidence occurrence. Remote Sensing of Environment, 301, 113934. https://doi.org/10.1016/j.rse.2023.113934

Xia, K., Chen, C., Wang, T., Yang, K. and Zhang, C., 2022. Investigation of Mining-Induced Fault Reactivation Associated with Sublevel Caving in Metal Mines. Rock Mechanics and Rock Engineering, 55(10), 5953-5982. https://doi.org/10.1007/s00603-022-02959-9

Solving the Mine Sequencing Problem for Multiple Strip Mining Operations Using Constraint Programming

Jorge L. V. Mariz[1*], Rodrigo L. Peroni[1], Marcel A. A. Bassani[1], Octávio R. A. Guimarães[2], and Flávio H. Tavares[2]

1. Mining Engineering Department, Federal University of Rio Grande do Sul, Brazil
2. Long-term Mine Planning Department, Alcoa, Brazil

**Corresponding author at: Mining Engineering Department, Federal University of Rio Grande do Sul, Brazil, e-mail adress: jorge_valenca@hotmail.com*

ABSTRACT

In the mine planning context, the mine sequencing problem determines, for each portion (mining block) of a mineral deposit, whether and when it will be extracted, its destination (processing plant, dump, or stockpile), and the economic return from that block (Mariz; Soofastaei, 2022). In open-pit mines, the classical mine sequencing optimization model aims to maximize the project's net present value (NPV), subject to constraints related to precedence, reserve, mining equipment and processing capacity, grades, among others, resulting in an NP-hard problem, therefore impractical to be exactly solved in acceptable computational time (Caccetta; Hill, 2003). On the other hand, tabular and sub-horizontal orebodies such as coal, phosphate, and bauxite deposits, present specific geometric conditions that favours to be extracted using strip mining methods. These methods rely on horizontal rather than vertical precedence so that the waste coming from the strip being mined is dumped into the contiguous strip, mined previously (Bassani et al., 2025). Studies addressing the strip mining method and characteristics of the mining equipment and operation can be accessed in some papers like Roberts (1971), Baafi et al. (1997), Silva et al. (2008), Zuckerberg et al. (2011), and Zhao et al. (2022). Also, a comprehensive review on scheduling and design practices related to strip mining can be found at McBrayer and Brickey (2023).

Commercial software tools are not usually designed to deal with the mine sequencing problem in strip mining operations, resulting in a historical gap for mining companies that rely on this approach. An approach especially useful when computers faced severe memory and processing limitations was layer modelling, in which a tabular deposit was modelled in layers rather than using block model, thus reducing the problem size and allowing early computers to tackle mine planning optimization tasks (Mariz et al., 2024). Diverse optimization techniques were employed in this regard, including Chance-Constrained Programming (CCP) (Albach, 1967), Dynamic Programming (DP) (Metz; Jain, 1978), Mixed Integer Non-Linear Programming (MINLP) (Metz; Jain, 1978; Busnach et al., 1985), Linear Programming (LP) (Gershon, 1983), Integer Programming (IP) (Klingman; Phillips, 1988), Linear Goal Programming (LGP) (Chanda; Wilke, 1992), Non-Linear Programming (NLP) (Adadzi; Frimpong, 2013), and Mixed Integer Linear Programming (MILP) (Azzamouri et al., 2018). Mariz et al. (2024) proposed a review of mine sequencing approaches considering layer modeling in tabular deposits.

Recently, Bassani et al. (2025) proposed an LP based-model to sequence panels from a bauxite mine in Brazil, although each period has to be sequenced after the previous one. Furthermore, a routine was

developed to establish the box cut of each panel, which means it will define the first strip to be mined and its mining direction for this panel. This decision also determines the sequence of strips to be mined, in addition to converting the achieved mining sequence to the block level. Later, Mariz et al. (2025) expanded this work by proposing a multi-stage Integer Linear Programming (ILP) approach to tackle the mine sequencing of this bauxite mine over multiple periods simultaneously, also addressing the excavator allocation problem. This solution relies on two distinct mathematical models. The first model optimizes the mining sequence for the panel level and allocates the mining equipment. Then an auxiliary routine determines the box cuts. The second mathematical model converts the optimized mining sequence to the strip level. Both models were solved using Constraint Programming (CP), a flexible and fast approach based on branch-and-bound, chronological backtracking, and constraint propagation.

This study extends the works of Bassani et al. (2025) and Mariz et al. (2025) by proposing a multi-stage approach based on ILP that can simultaneously address the mine sequencing problem and equipment allocation problems of multiple mines operating through the strip mining method. Allowing multiple mines to be optimized simultaneously is important when the ore can come from different mines and goes to the same processing plant. Furthermore, using ore from multiple mines in the optimization significantly contributes to the mine sequencing task, which gains flexibility to satisfy the constraints while aiming at maximizing the economic return of the operation. The models are then solved using Constraint Programming. The remainder of this study is structured as follows: the Methodology section outlines features of the proposed mathematical models and algorithms, the Results and Discussions section describes a case study of a bauxite mine where the proposed methodology was applied, and the Conclusions section summarizes the main findings of this research and proposes directions for further research.

Methodology

The main problem was subdivided into two stages. The first stage schedules the panels of the deposit and allocates the available excavators to each panel. The panels are a set of strips and are defined by the mine planning team before running the algorithm. The mathematical model aims to maximize the net present value of the operation for annual periods. In addition to common mine sequencing constraints such as equipment capacity and reserve, specific constraints have been tailored to prevent excessive movement of excavators. For instance, only one excavator can operate within a panel. In addition, one excavator located in panel A can only move to panel B if panel A has been completely depleted. In this regard, twenty-one constraints were used in this mathematical model.

The second stage aims to convert the panel-based solution to a strip-based solution, maintaining the consistency of the mass moved. In other words, the ore extracted at the first period at the panel scale must be nearly equal to the ore extracted at the first period at the strip scale. The ore extracted at the panel scale comes from the first mathematical model, and the ore extracted at strip scale results from the second mathematical model. First, the box cuts for each panel were determined considering the candidate strips with the least amount of waste. Furthermore, once mining directions were determined based on the box cut selection, it was possible to use a second mathematical model to schedule the strips, also aiming to maximize the net present value of the operation for annual periods. In this stage, the model encompassed six constraints, mainly to force the final mining sequence solution to adhere to the one obtained in the previous stage. A horizontal precedence constraint was also implemented, ensuring that a strip in a panel can only be excavated if the previous neighbouring strips had already been completely mined.

Both ILP-based models were solved through the Constraint Optimization Problem (COP), which is a Constraint Programming (CP) approach that pursues an objective function. COP was chosen

as regular CP approaches may pursue only feasible solutions rather than a local optimum. Two stopping criteria were used simultaneously for both models: (i) 250 iterations and (ii) 24 hours of processing time. The methodology was implemented using the Google OR-tools that allows parallelization; thus, it can efficiently solve complex problems for models with integer variables. Numerical experiments were performed on a computer running the Windows Server 2022, equipped with two Xeon 4214R 2.40 GHz 12-core processors, four solid state drives of 1 TB, 256 GB of RAM and one external hard drive of 4 TB.

Results and Discussions

A case study was developed with two bauxite mines in the Northern region of Brazil, from a dataset combining information of 2D models with XY dimensions of 50 m x 50 m, presenting11,935 and 11,922 blocks of, where these blocks were grouped into 51 and 55 panels, respectively. A heterogeneous fleet with eight excavators was considered: four Liebherr R9200, whose minimum and maximum capacities were assigned as 6.616 Mtpy and 11.027 Mtpy, respectively; and four Liebherr R9250, whose minimum and maximum capacities were assigned as 8.309 Mtpy and 13.849 Mtpy, respectively. Consequently, the fleet maximum capacity was considered as 99.507 Mt/year. The numerical experiments considered ten years of operation.

The results have demonstrated that the strategy of dividing the main mine sequencing problem into two stages allowed the first stage, which is based on panels and also allocates the excavators to these panels, to be solved with 99.49% optimality in 24 hours, after 219 iterations of the COP approach. While the best bound found for this optimization stage was equivalent to 5.352 B$, the best feasible mine sequencing solution reached an NPV of 5.325 B$. Nevertheless, Figure 1 depicts a graph demonstrating the evolution of the best bound found by the Constraint Optimization Problem approach versus the execution time, thus demonstrating that if a stopping criterium of reaching 99% of optimality (1% gap) were employed, roughly 12 hours and 175 iterations would be necessary to deliver this mine sequencing, highlighting the ability of COP approach to efficiently tackle complex and NP-hard problems in acceptable computational time.

Another important aspect to monitor during the first stage is equipment utilization. The optimized mining sequence resulted in the extraction of roughly 995.078 Mt of material over ten years, which is precisely the maximum capacity of the fleet employed. Therefore, the achieved solution not only reached 99.49% of the best bound in terms of economic return, but also reached 100% of equipment utilization, corroborating its quality. Regarding the transition from stage 1 to 2 (from panels to strips), the equipment allocation aspect will not be considered, since it has already been defined which excavator will mine each panel in each period.

In stage two, prior optimization, it is necessary to determine the box cut and mining direction for each panel, as mentioned before. Then, the set of box cuts and mining sequence solution for the panel level, obtained during the first stage, served as input for the second optimization model, reaching a new solution for the strip level with NPV equivalent to 5.109 B$ in 6 seconds, achieving 100% of optimality. Furthermore, an adherence of 95.95% was found between the NPVs from both stages. A difference between the NPVs at the panel and strip scales is expected to the increase in geometric constraints between panel and strip levels. In addition, this solution also determined 995.078 Mt of material to be excavated over ten years, resulting in no loss of productivity, highlighting that the difference between the economic results was due to the difference in support. Figures 2 and 3 display the periods when operation begins at the panel (A) and strip (B) levels for both plateaus, enabling comparison of the results obtained in the two optimization stages. Panels associated with year zero must not be mined. It is worth noting that panels whose mining began in year ten will be completely coloured in the panel sequence, but not necessarily all strips will need to be mined to reach the corresponding mass designated during the first optimization stage. For the same reason,

it is also possible for mining on a panel to begin in one year and continue into the following year, a fact that would only be evident in the strip sequence. Therefore, differences often arise between these mining plans due to change in support.

Conclusions

This study proposed a two-stage optimization-based methodology to solve the mine sequencing and excavator allocation problems in open-pit mines operating through the strip mining method in tabular deposits. The mathematical models were ILP-based and addressed the panel and strip level, being able to simultaneously generate mining sequences for multiple plateaus and deposits, thus increasing the flexibility of the mine planning activities. The models were solved using Constraint Programming, and the numerical experiments of the studied bauxite operation reached more than 99% of optimality in both stages. These results were considered very satisfactory and reached in an acceptable computational time, corroborating the potential of the proposed methodology to increase the level of detail of strategic mine planning in tabular deposits.

Future research should include constraints related to the materials being handled, as the models used in this study solely consider the equipment capacity and total mass in each panel or strip, ignoring the proportion of ore and waste in these masses. Consequently, the actual NPV is expected to be reduced due to the incorporation of these and other necessary constraints, including grade constraints on alumina and reactive silica, as well as processing plant capacity constraints. Furthermore, efforts should also be made to develop a methodology capable of generating a mining sequence at the block level that is consistent with the sequencing and allocation of equipment proposed during the first stage, which operates at the panel scale. This increase in the level of detail in the mining plan would be essential for reconciliation in the short term operation, bringing robustness to the mine sequencing and minimizing risks due to variation in grades in each block.

Graphic Elements

Figure 1. Graph demonstrating the evolution of the best bound found by the Constraint Optimization Problem approach versus the execution time.

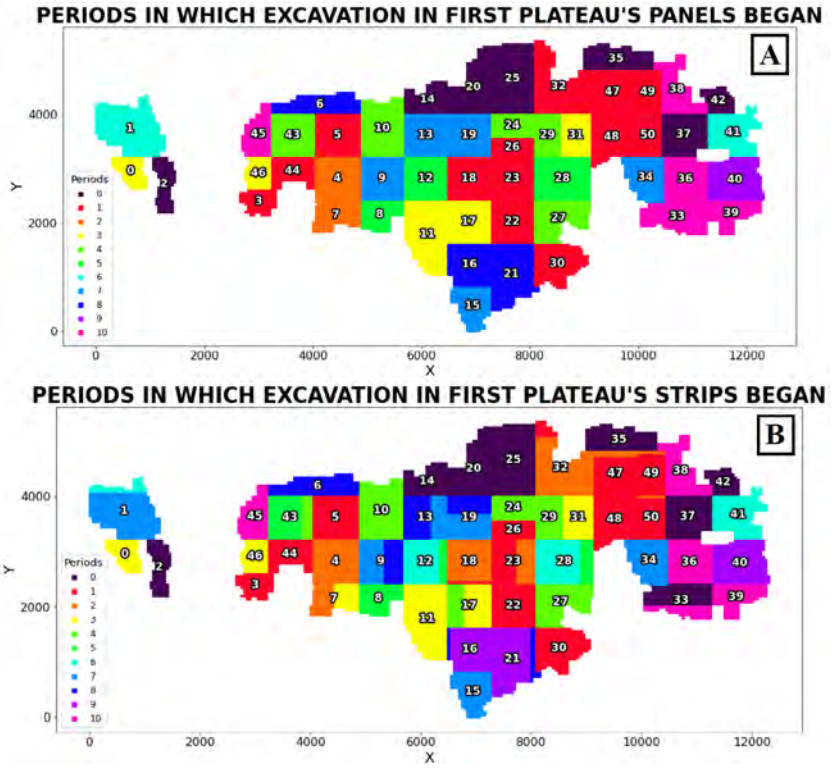

Figure 2. Periods when the operation starts in each panel (A) and strip (B) for the first plateau. The numbers 0-50 identify the 51 panels of the plateau.

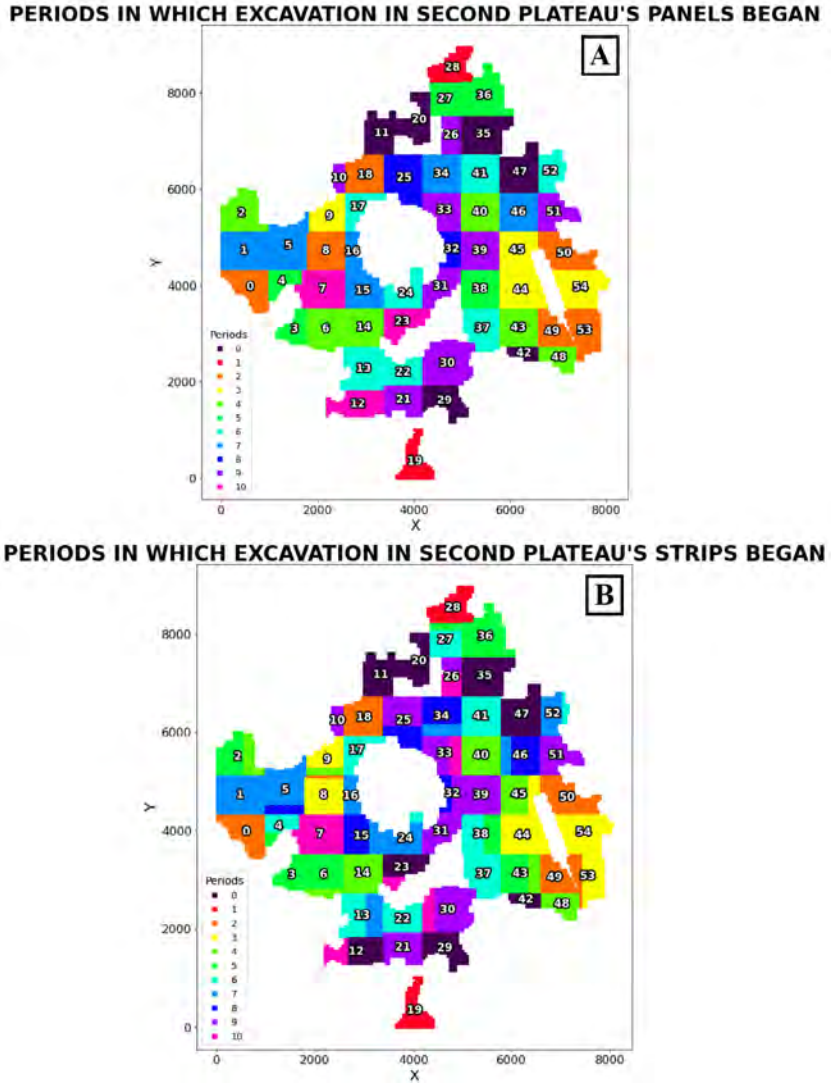

Figure 3. Periods in which operation starts in each panel (A) and strip (B) for the second plateau. The numbers 0-54 identify the 55 panels of the plateau.

References

Adadzi E; Frimpong S, 2013. Stochastic non-linear optimization of equipment productivity in multiseam formations. J. Powder. Metall. Min., S1:001. https://doi.org/10.4172/2168-9806.S1-001.

Azzamouri A; Fénies P; Fontane F; Giard V, 2018. Scheduling of open-pit phosphate mine extraction. Int. J. Prod. Res., 56(23), 7122-7141. https://doi.org/10.1080/00207543.2018.1433341.

Albach H, 1967. Long range planning in open pit mining. Manag. Sci. 13, B549-B568.

Baafi EY; Mirabediny H; Whitchurch K, 1997. Computer simulation of complex dragline operations. Int. J. Surf. Min. Reclamat. Environ., 11(1), 7-13. https://doi.org/10.1080/09208119708944049.

Bassani MAA; Peroni RL; Guimaraes ORA; Cantadori B; Moraes C; Vicenzi R; Alves JL; Mariz JLV; Tavares FH, 2025. Linear Programming model applied to long-term mine planning in strip mining operations. Min. Metall. Explor., 42, 737-750. https://doi.org/10.1007/s42461-025-01185-5.

Busnach E; Mehrez A; Sinuany-Stern Z, 1985. A production problem in phosphate mining. J. Oper. Res. So., 36(4), 285-288. https://doi.org/10.2307/2582414.

Caccetta L; Hill SP, 2003. An application of branch and cut to open pit mine scheduling. J. Glob. Optim., 27, 349-365. https://doi.org/10.1023/A:1024835022186.

Chanda EK; Wilke FL, 1992. An EDP-model of open pit short term production scheduling optimization for stratiform orebodies. In: Proceedings of the 23rd APCOM Conference, 1992, p. 759-768.

Gershon ME, 1983. Optimal mine production scheduling: evaluation of large scale mathematical programming approaches. Int. J. Min. Eng., 1(4), 315-329. https://doi.org/10.1007/BF00881548.

Klingman D; Phillips N, 1988. Integer programming for optimal phosphate-mining strategies. J. Oper. Res. So., 39(9), 805-810. https://doi.org/10.2307/2583523.

Mariz JLV; Soofastaei A, 2022. Advanced analytics for surface mine planning. In: Soofastaei A. Advanced Analytics in Mining Engineering. Springer: Cham, p. 205-306. https://doi.org/10.1007/978-3-030-91589-6_9.

Mariz JLV; Badiozamani MM; Peroni RL; Silva RMA, 2024. A critical review of bench aggregation and mining cut clustering techniques based on optimization and artificial intelligence to enhance the open-pit mine planning. Eng. Appl. Artif. Intell., 133(D), 108334. https://doi.org/10.1016/j.engappai.2024.108334.

Mariz JLV; Bassani MAA; Peroni RL; Guimaraes ORA; Tavares FH, 2025. Solving a multi-stage mine sequencing model encompassing excavator allocation through Constraint Programming in a bauxite strip mining operation. J. Sustain. Min., 24(3), 346-358. https://doi.org/10.46873/2300-3960.1459.

McBrayer A; Brickey A, 2023. A review of current scheduling and design practices in the powder river basin. Min. Metall. Explor., 40, 1059-1080. https://doi.org/10.1007/s42461-023-00754-w.

Metz HJ; Jain SK, 1978. Optimal mining and processing decisions in stratiform phosphate deposits. Interfaces, 9(1), 1-12. https://doi.org/10.1287/inte.9.1.1.

Roberts AL. 1971. Mining of bauxite in Jamaica. In: Proceedings of the Bauxite/Alumina Industry Symposium, 1971, p 41-51. Silva HM; Picanço E; Maurity C; Morais W; Santos HC; Guimarães O, 2008. Geology, mining operation and scheduling of the Paragominas bauxite mine. In: Proceedings of the 8th International Alumina Quality Workshop, 2008, p. 11-16.

Zhao Z; Zhang R; Sun J; Lv S, 2022. Optimization of overcast stripping technology parameters based on discrete event system simulation. Adv. Civ. Eng., 654893. https://doi.org/10.1155/2022/7654893. 7654893.

Zuckerberg M; van der Riet J; Malajczuk W; Stone P, 2011. Optimal life-of-mine scheduling for a bauxite mine. J. Min. Sci., 47, 158-165. https://doi.org/10.1134/S1062739147020031.

The New Advancements in Liquid Oxygen Explosives (LOX) for Blasting in Latin America

E. Munaretti[1], A. F.C. Mesquita[2], L. H. B. Ferreira[3], M. Mavric[4]

1. UFRGS, Porto Alegre, Brazil
2, 3, 4. Blastogas, Santo Antônio do Monte, Brazil

ABSTRACT

Since the early 20th century, Liquid Oxygen Explosives (LOX) have been researched and tested worldwide. The initial LOX compositions utilized cellulose as the primary fuel, liquid oxygen as oxidizer, and a spark or blasting cap for initia-tion. Despite over a century of exploration, the technology failed to gain significant traction due to challenges such as liq-uid oxygen availability, fuel absorption limitations and cost-effectiveness compared to ammonium nitrate based explo-sives. This paper highlights recent advancements by Blastogas, a Brazilian company recognized for its innovative alterna-tives to conventional explosives products. The LOX technique has been significantly improved and is now successfully employed in Latin America. It offers a practical solution in scenarios where conventional explosives are restricted or fail to meet environmental standards. One of the key benefits of this updated LOX technology is its logistical simplicity: liquid oxygen can be easily sourced from third-party suppliers, and the fuel cartridges can be manufactured off-site and delivered to users through standard transportation methods, including postal services. These innovations indicate that LOX technol-ogy has potential to transitioning from niche applications to becoming a viable competitor to ammonium nitrate-based explosives in broader markets.

Keywords: OX, blasting, liquid oxygen, explosives

Introduction

Liquid Oxygen Explosives (LOX) have been explored as an al-ternative to conventional explosives since the late 19th century (Sieder, 1906). Comprising liquid oxygen combined with a compatible fuel, these mixtures form highly energetic com-pounds that were historically employed in mining and con-struction due to their low cost and ease of preparation. Howev-er, concerns regarding their instability, the complexity of liquid oxygen production, and significant safety risks led to a decline in their use after 1947, as more stable and commercially viable alternatives became available. This paper provides an overview of the development of LOX explosives, with a focus on their chemical and physical properties, mechanisms of operation, safety considerations, and recent technological advancements.

Historical development

The explosive properties of LOX mixtures were first explored around 1897 by Carl von Linde, who utilized early air liquefac-tion technology (Sieder, 1906). That same year, a successful field test was conducted in a coal mine crosscut in Penzberg, Germany. In these early experiments, pure oxygen was not yet available; instead, cartridges filled with charcoal were soaked in liquid air. At the time, the necessary machinery for liquefaction was still in its developmental stages. A decade later, the pro-duction of liquid oxygen became economically viable with the introduction of the innovative Claude System (see Figure 1).

LOX explosives offered several advantages, including high en-ergy density, rapid detonation velocity, and ease of preparation. During this period, numerous mining companies worldwide re-lied on LOX as a cost-effective and efficient method for frag-menting rocks. However, the need to establish liquid oxygen production plants for each operation posed a significant logisti-cal challenge. Latin American mining, in particular, became a major field for LOX usage. Companies like Cerro de Pasco Copper Corporation (Peru) and Chile Exploration utilized LOX in large-scale open-pit blasting operations. Chuquicamata, in Chile, was a pioneer in this regard, replacing substantial black powder blasts (250,000 tons) and entirely replacing smaller dynamite blasts (80,000 to 100,000 tons) with LOX. Accord-ing to Perrott & Tolch (1932), at least 1,265,700 tons of rock were blasted using LOX in Chuquicamata alone in 1927.

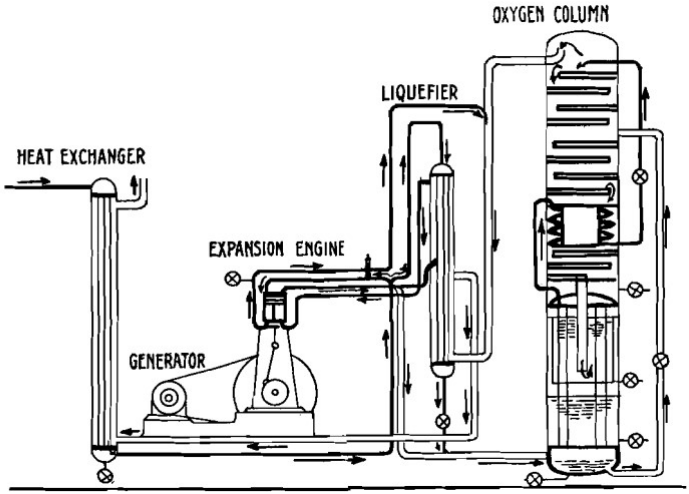

Figure 1. LOX Claude System flow sheet (O'Neil & Van Fleet, 1926).

However, the inherent limitations of LOX—such as the re-quirement for immediate use after mixing and its short effec-tive lifespan—made it impractical for widespread commercial application. In addition, the high volatility of liquid oxygen introduced significant handling and storage risks.

During World War II, LOX saw limited military use. After 1947, the development of ammonium-nitrate-based explosives particularly ANFO (Ammonium Nitrate Fuel Oil) rendered LOX largely obsolete in mainstream blasting operations.

Chemical and physical properties

Liquid oxygen is a cryogenic liquid with a boiling point of −183°C and serves as a potent oxidizer. When combined with a suitable fuel, typically hydrocarbons or cellulose derivatives a highly energetic mixture is formed. Oxygen has a gas density of 0.001429 g/cm^3 (1 ATM; 0 °C), while liquid oxygen has a density of 1.14 g/cm^3 (1 ATM; -183 °C). The amount of 2.67 g of $O2$ is required to burn 1g of carbon to $CO2$ and 1.33 g of carbon to CO. Liquid oxygen acts as a strong oxidizer at its boiling point (-183°C), reacting rapidly with organic materials (Table 1). When liquid oxygen contacts a fuel, such as wood, cotton, coal, hydrocarbons, metal powders or Sulphur, it cre-ates a highly oxygen-rich mixture providing the ideal environ-ment for detonation. The general reaction is as follows (1):

$$\text{Fuel} + O_2 \rightarrow CO_2 + H_2O + \text{Heat} \qquad (1)$$

If the mixture receives sufficient activation energy from a flame, spark, or electrical discharge, rapid combustion can esca-late to detonation under confinement; the detonation velocity may exceed 4,000 m/s, depending on the mixture, blasthole diameter, and the impedance of the surrounding material.

Table 1: Physical Properties of Liquid Oxygen.

Property	Value
Boiling Point	-183 °C / 90.19 K
Density	1.14 g/cm³
Expansion Ratio	1:861
Oxidizing Capability	Strong Oxidizer

LOX (liquid oxygen) mixtures are highly sensitive to shock and friction, and can spontaneously ignite on contact with cer-tain materials (Wicki, 2003). As Wadhwa has noted (1989, 1991), this sensitivity depends on the selection of ingredients and strict control during all manufacturing stages, including cartridge fabrication, soaking, and transport. Here, sensitivity denotes the propensity for explosive behaviour under mechani-cal insult—such as impact from falling weights, compression waves, or friction—which is governed by the molecular con-figuration, required activation energy, and the heat of explo-sion.

When subjected to impact, LOX undergoes viscous flow, which promotes the formation of localized 'hot spots.' These sites are thought to arise from adiabatic compression at the sur-face, thereby creating active centers of decomposition. The crit-ical temperature at which hot spots persist, rather than dissi-pate, can be estimated by equating the heat generated with the heat dissipated through thermal conduction over time.

Perrott and Tolch (1932) reported that the sensitivity of LOX to direct mechanical impact is comparable to that of some com-mercial explosives—specifically, 40% nitroglycerin dynamite. However, LOX is markedly less sensitive to frictional stimuli, and soaked cartridges generally exhibit reduced sensitivity overall.

Operational mechanism

When oxygen is present in its concentrated liquid form approx-imately 800 times denser than the gaseous state—any combustible material immersed in it and exposed to an ignition source will ignite and be rapidly consumed. The reaction releases intense heat, generates high gas pressures, and produces a shock wave. When multiple combustible particles saturated with liquid oxygen lie close together, combustion can propagate rapidly between particles; the accumulated heat and confined-gas pressure further accelerate this propagation. As the reaction progresses, gas expansion and resulting shock waves can be har-nessed for practical applications such as rock blasting.

LOX-based explosives are prepared on site by soaking a porous solid fuel cartridge in liquid oxygen. Because liquid oxygen evaporates rapidly, the charge must be initiated within minutes of soaking to maintain effectiveness. Like other conventional fragmentation explosives, LOX mixtures present significant safety hazards: they are highly sensitive to shock, heat, electrical discharge, and friction, and even slight fuel contamination can trigger detonation. Liquid oxygen can also cause spontaneous combustion on contact with hydrocarbons or organic materials. Consequently, cartridges must not be pre-soaked and stored; mixing and emplacement are performed on site immediately prior to firing. Initiation is commonly achieved with an electrical blasting cap, so precautions to eliminate stray currents and static discharge are essential. Given these risks, strict safety protocols and trained personnel are mandatory when handling LOX explosives.

The **effective life** of a cartridge is the period during which it retains sufficient liquid oxygen (LOX) to achieve the desired blasting performance. It begins at the moment of maximum saturation and ends at the so-called $\mathbf{CO_2\ point}$ — the stage at which only the minimum LOX necessary for complete combustion remains. After this interval the cartridge progressively loses oxygen; once the LOX has fully evaporated the mixture reverts to an inert state and will no longer produce the intended explosive effect.

The effective life of a cartridge is determined by the rates of both absorption and evaporation of the liquid oxygen it contains. The absorption rate is largely governed by the total void space, including both pore and intergranular porosity. In contrast, the evaporation rate depends not only on atmospheric conditions but also on several properties of the absorbent, including its thermal conductivity, surface area, and moisture content:

- The distribution of voids at capillary dimensions,
- The packing density of the absorbent filling,
- Its thermal conductivity, and
- The surface-to-volume ratio of the cartridge.

When the absorbent material is ground into a fine powder, the intergranular spaces shrink to capillary dimensions and become more uniformly distributed. Although higher packing density increases the total pore volume, it simultaneously re-reduces intergranular space. An optimal packing density achieves a balanced ratio between pore and intergranular voids, promoting efficient soaking, high absorption capacity, and slow evaporation—conditions that maximize cartridge performance.

A century ago, O'Neil (1926) established the minimum re-quirements for an effective LOX cartridge. According to his cri-teria, a cartridge should:

- Be made of combustible material,
- Permit ready absorption of liquid oxygen,
- Exhibit high packing density to maximize the oxygen content per unit volume,
- Absorb liquid oxygen in excess of that required for complete combustion, and
- Have filling material and a wrapper with sufficient mechanical strength to maintain structural integrity

Depending on the composition of the combustible materials, LOX combustion can produce hazardous by-products such as carbon monoxide (CO) and sulfur dioxide (SO_2), which present significant safety risks. For example, Wadhwa (1991) reported that in a Loxite (LOX-based) cartridge with a packing density of 325 g/L containing 100 g of liquid oxygen, the expected combustion products are summarized in Table 2.

Table 2: Products of combustion for "Loxite" (Wadhwa 1991).

Constituent	Weight (g)	Product	Weight (g)
H_2O	2.62	H_2O	2.62
C	20.47	CO_2	75.01
H_2	2.43	H_2O	21.78
O_2	17.67		
S	0.03	SO_2	0.06
N_2	0.07	N_2	0.07
SiO_2	0.43	SiO_2	0.43
LOX (inxs)	56.24		

It is generally assumed that the explosive reaction in a LOX cartridge occurs when the mixture reaches an oxygen-balanced, or stoichiometric, condition. In practice, however, this ideal state is rarely achieved in the field. Any excess liquid oxygen must first vaporize and expand adiabatically to attain the reac-tion temperature. During this expansion, the gaseous oxygen is expected to perform useful work, analogous to the behavior of gaseous products in conventional explosives.

As the oxygen content in a cartridge gradually decreases through evaporation, its absorption capacity correspondingly diminishes. Consequently, it is essential to initiate detonation shortly after soaking. Delays can result in a marked reduction in both detonation pressure and velocity, as illustrated in Table 3, which shows maximum, medium, and lower oxygen absorp-tion levels and the resulting transition from full detonation to deflagration.

Table 3: Detonation pressure and velocity according to oxygen absorption, Wadhwa (1991).

LO Absorption	max	medium	lower	deflag.
Detonation Pressure (ATM)	92.847	62.032	37.325	-
Detonation Velocity (m/s)	7.625	6.470	4.182	-

LOX mixtures are strongly oxygen-positive, meaning they con-tain more oxygen at the time of the explosive reaction than is required for the complete combustion of carbon to carbon diox-ide and hydrogen to water vapor, resulting in excess liquid ox-ygen.

A novel technique has recently been investigated with promis-ing results: liquid carbon dioxide explosives $(\mathbf{L\text{-}CO_2})$. Zhang et al. (2022) demonstrated that, similar to conventional explo-sives, $\mathbf{L\text{-}CO_2}$ exhibits two distinct stages during rock fractur-ing: a dynamic loading stage, characterized by stress wave propagation, and a quasi-static loading stage, driven by high-pressure gas. Compared to traditional explosives, $\mathbf{L\text{-}CO_2}$ pro-duces a lower stress wave loading rate, a longer fragmentation duration, and a lower peak stress.

Figure 2 compares the stress waves generated by $\mathbf{L\text{-}CO_2}$ with those produced by conventional explosive blasting, as reported by the authors. Notably, the fragmentation mechanism of $\mathbf{L\text{-}CO_2}$ closely resembles that of LOX-based explosives. This similarity may provide advantages in specific blasting applica-tions, particularly where the rapid release of early energy is un-desirable, such as in the extraction of delicate mineral struc-tures like amethyst geodes (Munaretti & Klippel, 2006).

This insight also highlights the importance of specific geomet-ric relationships among burden, spacing, stemming, and blasthole diameter—relationships that require further investiga-tion to be fully understood and optimized.

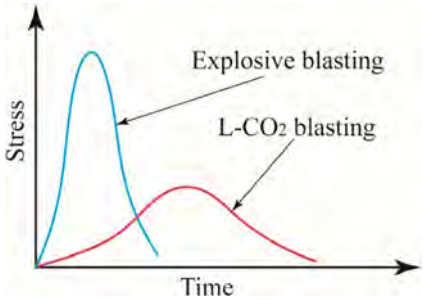

Figure 2. The stress waves generated by "regular explosives" (blue line) and liquid CO_2 blasting by time (Zhang et. all, 2022).

Recently aplications in Latin America

After 78 years of widespread use of ANFO and, subsequently, ammonium nitrate emulsions, LOX has largely fallen out of favor as an explosive, with its applications now mostly limited to demolition and as an oxidizer in rocketry. Nevertheless, LOX remains a critical component of modern space propulsion. When combined with fuels such as methane or liquid hydro-gen, it serves as the basis for high-performance rocket engines employed in launch systems like SpaceX's Falcon 9 and NASA's Space Launch System (SLS).

Despite some isolated initiatives in Brazil, BlastoGas is cur-rently the most advanced and commercially developed LOX-based rock blasting system in Latin America. The company has strategically targeted niche markets where conventional explo-sives are either prohibited or where their transport and storage present significant logistical or financial challenges. According to Oxquímica (2024), BlastoGas is characterized as "a comple-mentary technology to traditional blasting, primarily used in environments where standard explosives are restricted or fail to meet environmental regulations."

One of the principal advantages of this modern LOX technolo-gy is its logistical efficiency. Liquid oxygen can be readily ob-tained from third-party suppliers, and cartridges manufactured off-site can be transported to end users using standard methods, including regular postal services. The drill-and-load process is straightforward, typically involving blastholes with diameters ranging from 64 mm (2½") to 127 mm (5"). Each cartridge re-quires approximately 1.5 liters of liquid oxygen per meter of blasthole (Figure 3). Cartridges are produced in varying diame-ters to match different blasthole sizes and contain a cellulosic absorbent material. They are wrapped in flexible, anti-static plastic coils to ensure safe handling and transport.

Figure 3. Representation of a BlastoGas cartridge (left); and empty cartridges ready for transportation (Oxquímica, 2024).

The BlastoGas cartridge is connected via a flexible stainless-steel hose to a mobile cryogenic oxygen tank mounted on a truck (Figure 4). Once the connection is secured, the cartridge is inserted into the blasthole for loading.

Figure 4. BlastoGas mobile cryogenic O2 tank (Oxquímica, 2024).

The next step involves connecting the activation cables to the stainless-steel hoses, allowing the cartridges to be filled with liquid oxygen. Once filled, the blastholes are prepared for det-onation and linked to a blasting machine using specially de-signed electric detonators compatible with the system (Figure 5). Currently, up to eight blastholes can be fired simultaneous-ly; however, this process could be optimized. Introducing short delays between blasts would likely enhance fragmentation by providing sufficient relief and reducing induced vibrations.

Blastholes are stemmed with crushed stone, typically sized at approximately 10% of the blasthole diameter. Design parame-ters such as burden, spacing, and stemming size are currently determined using guidelines from Olofsson (1990), Konya (1995), and commonly applied 'rules of thumb' developed for conventional packed ammonium nitrate emulsions. These de-sign standards are expected to evolve as LOX-based systems gain broader adoption and a deeper operational understanding. Figure 6 illustrates a typical blast and the resulting crack prop-agation caused by the rapid expansion of oxygen.

Figure 5. BlastoGas blasting machines (Oxquímica, 2024).

Due to its temporary nature, the BlastoGas LOX system pro-vides safety features not typically found in conventional explo-sives, particularly during storage and transportation, as most handling occurs while the cartridge is in a non-explosive state. The cartridges have an effective life of approximately 10 minutes, depending on cartridge size and environmental condi-tions. If detonation does not occur within this period, the car-tridges must be refilled with liquid oxygen to restore their explosive capability.

Figure 6. Phases of a BlastoGas LOX shot. Being an expan-sion of gases, one clearly notices the progressive opening of the natural joint present on the bench face (Oxquímica, 2024).

This modern LOX-based explosive system offers distinct ad-vantages in the following scenarios:

- Remote mining or construction operations, where transporting conventional explosives presents signifi-cant logistical challenges;
- Areas with strict environmental regulations, requiring low-toxicity, low-residue, or biodegradable blasting solutions;
- Jurisdictions where the use, transport, or storage of conventional commercial explosives is legally restrict-ed or subject to stringent supply controls

Field trials have demonstrated the effective use of LOX explo-sives in rock fragmentation and overburden removal. Their streamlined logistics and environmentally favorable profile make LOX-based systems a competitive option in niche, yet expanding, segments of the global explosives market.

Conclusion

Although historically limited by practical and safety concerns, Liquid Oxygen (LOX) explosives are re-emerging as a viable alternative due to recent technological advancements. Histori-cally, LOX explosives played a niche role in the industrial ex-plosives sector, offering cost-effective solutions for specific ap-plications. Today, they are evolving for aerospace applications worldwide and for specialized blasting markets in Latin Ameri-ca. Like any blasting technique, LOX systems have both ad-vantages and limitations. Transportation is simplified, as car-tridges can be shipped via conventional carriers, and liquid ox-ygen can be readily supplied by third-party providers at low cost in populated areas. The system becomes explosive only af-ter the cartridge has been soaked with liquid oxygen for ap-proximately 10 minutes in the field.

Current technological limitations include the need for im-proved delay initiation, adequate relief, and low-vibration blasting. Further research is required to establish optimal geometric relationships among burden, spacing, stemming, and blasthole diameter, as the fragmentation mechanism differs from conventional explosives, rendering classical "rules of thumb" insufficient for general application. While LOX demonstrates significant potential, its adoption requires appro-priate regulations and safety codes to govern handling and use in the region. With continued development, LOX explosives may secure a stable role in the blasting industry, particularly in environments where environmental, logistical, or regulatory considerations necessitate non-conventional approaches.

References

Konya, C. J., 1995. "Blast design". Intercontinental De-velopment, Montville, USA, 230p.

Munaretti, E., Klippel, A. F., 2006. Relatório de atividа-des de engenharia de minas desenvolvimentos em Ametista do Sul, RS, Brazil. CNPq, 108p.

Olofsson, S. O., 1990. Applied explosives technology for construction and mining, Applex, Suécia. 301p.

O'Neil F., Van Fleet H., 1926. Liquid Oxygen as An Ex-plosive. The American Institute of Mining, Metallurgical, and Petroleum Engineers, 42p.

Oxquímica Indústria e Comércio de Produtos Químicos Ltda., 2024. BlastoGas: Boletim Técnico 11. Belo Hori-zonte, MG, Brazil 18p.

Perrott, G. ST. J.; Tolch, N. A., 1932. Liquid Oxygen Ex-plosives. Bulletin 349, U.S. Department of Commerce – Bureau of Mines 108p.

Sieder, L., 1906. Oxyliquit. Ztschr. ges. Schiess u. Sprengs, vol 1.1906, p.87-89.

Wadhwa K., 1989. Development and performance of liquid oxygen explosives. International Society of Explosives En-gineers, 1989 Conference P322, 8 p.

Wadhwa K., 1991. Investigative studies on the explosives characteristics of LOXITE explosives. International Society of Explosives Engineers, 1991 Conference P201, 7 p.

Wicki, R., 2003. Liquid Oxygen – Fire Hazards of Oxy-gen and Oxygen-Enriched Atmospheres. CHIMIA 1. 57(12), 781. https://doi.org/10.2533/000942903777678425.

Zhang Y., Deng H., Ke B., Gao F., 2022. Research on the Explosion Effects and Fracturing Mechanism of Liquid Carbon Dioxide Blasting. Mining, Metallurgy & Explora-tion (2022) 39:521–530. https://doi.org/10.1007/s42461-021-00514-8

Chapter 02

Metallurgical Engineering

Deep Eutectic Solvent: An Alternative to Copper Dissolution From Sulphide Ore

Pía Hernández[1,2,3*], Matías Muñoz[1], Sonia Cortés[3], Yecid Jimenez[1,2,3] and Humberto Estay[3]

1. Departamento de Ingeniería Química y Procesos de Minerales, Universidad de Antofagasta, Antofagasta, Chile
2. Centro de Economía Circular en Procesos Industriales (CECPI) Universidad de Antofagasta, Antofagasta, Chile
3. Advanced Mining Technology Center (AMTC), Universidad de Chile, Santiago, Chile

**Corresponding author at: Universidad de Antofagasta, Av. Angamos 601, Antofagasta, Chile*
pia.hernandez@uantof.cl.

ABSTRACT

Copper is an important resource for technological advancement; therefore, the development of new processes for its recovery should be a focus of research, including sustainable processes. The use of deep eutectic solvents (DES) is an alternative for extracting copper from copper-bearing sulphide minerals using solvometallurgical methods (with low or no water consumption). DES are a mixture of two components that form a liquid with a low melting point. DES is formed by a hydrogen bond donor (HBD) and a hydrogen bond acceptor (HBA). They feature a low synthesis cost compared to ionic liquids, low toxicity, low volatility, high biocompatibility, are biodegradable, easy to synthesize, and exhibit high thermal stability. The objective of this research is to study the dissolution of low-grade copper sulphide minerals (0.83% Cu) using choline chloride (ChCl)-based DES. Laboratory-scale agitated leaching tests were performed using different DES (ChCl + ethylene glycol, ChCl + citric acid, and ChCl + urea) at different temperatures (25, 50, and 60 °C). In some systems, water was added. The highest copper extractions at any of the studied temperatures were for the systems composed of: ChCl + citric acid > ChCl + urea > ChCl + ethylene glycol, reaching 100% copper extraction in some cases.

Introduction

Currently, the mining industry faces a series of challenges, including water scarcity, increasingly complex mineral profiles, climate change, high energy demands, strict legislation, the inclusion of social and environmental considerations, and rising process costs (Ministerio-Minería, 2023). In this context, green mining becomes increasingly relevant (Alta-Ley, 2019; Fundación-Encuentros-del-Futuro, 2023). Green mining focuses on the development of low-emission, low-waste processes that adapt to climate change by reducing the environmental footprint, prioritizing renewable energy, reprocessing waste and materials, and fostering new technologies. This also involves innovations such as waterless mining, hydrometallurgical process technologies (COCHILCO, 2023), novel mining reagents, and the promotion of polymetallic mining (COCHILCO, 2021).
Due to this, the study of new emerging solvents (green solvents) in mining is promoted. These environmentally benign alternatives to traditional solvents are characterized by their stability, low cost, low toxicity, safety, minimal environmental impact, biodegradability, and ease of synthesis. Examples include ionic liquids, amino acids, and deep eutectic solvents (DES) (Tian and Liu, 2024). A DES consists of a mixture of two salts whose combined melting point is lower than that of each

individual component. In hydrometallurgical processes, these solvents present an alternative for waterless operations or for those that require less water (Hansen et al., 2020).

The aim of this work is to study the dissolution of low-grade copper sulphide minerals (0.83% Cu) using choline chloride (ChCl)-based DES at different temperatures of 25, 50 and 60 °C.

Methodology

Ore: Copper sulphide ore samples were obtained from Antofagasta region with particle size < 150 µm. The copper grade of the sample was 0.83 % Cu determined by atomic absorption spectrometry.

Reagents: DES were synthesized using choline chloride (ChCl), ethylene glycol (EG), citric acid (CA) and urea (U). In some test water was added due to high viscosity of solvents, especially at a temperature of 25 °C. Type of DES was studied to determine the copper dissolution in stirring leaching tests at different temperature (25, 50 and 60 °C), solid liquid ratio 1/10, 300 rpm.

Procedure: For DES preparation (ChCl + ethylene glycol in a molar ratio of 1:2, ChCl + citric acid in a molar ratio 2:1, and ChCl + urea in a molar ratio of 1:2), the reagents are mixed in a beaker and placed on a hot plate with magnetic stirring at 80 °C for a period of 2 h. In DES composed by citric acid and urea, water addition was made. Then, 50 mL of jacketed glass beakers were used to leaching tests. The beakers were connected to a thermostatic bath to control the temperature. The solid sample and solvents were added to beaker. The tests were carried out at 300 rpm, 72 h and solid-liquid ratio of 1:10. At the end of the test, the suspension was filtered. The solutions were analysed by atomic absorption spectrometry (AAS) to determine the copper concentration. The tests were performed in duplicate. Figure 1 shows the leaching system and solutions obtained after process.

Figure 1. Left: Leaching system. Right: Solutions obtained.

Results and Discussions

Table 1 show the copper extractions obtained from leaching test with DES at different temperature and addition of water.

Table 1. Copper extraction (%) obtained in leaching tests with different DES.

N°	DES	H_2O (%)	Temperature (°C)	Cu ext. (%)
1	ChCl + EG	0	25	4.7
2	ChCl + EG	0	50	24.8
3	ChCl + EG	0	60	42.4
4	ChCl + CA	20	25	75.2
5	ChCl + CA	20	50	100.0
6	ChCl + CA	20	60	100.0
7	ChCl + U	1	25	38.3
8	ChCl + U	1	50	43.3
9	ChCl + U	1	60	69.4

Figures 2, 3 and 4 show the effect of DES type on the leaching of copper sulphide ore at a constant temperature.

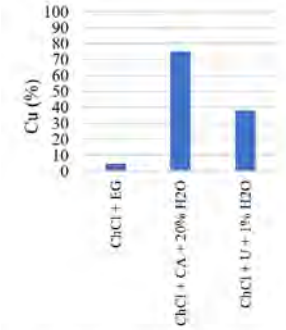

Figure 2. Copper extraction (%) with different DES at 25 °C.

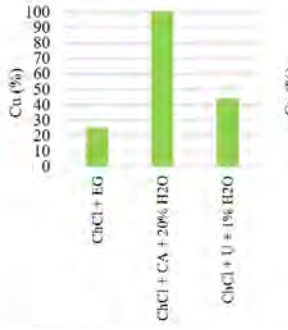

Figure 3. Copper extraction (%) with different DES at 50 °C.

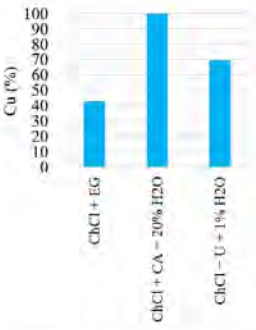

Figure 4. Copper extraction (%) with different DES at 60 °C.

It can be observed from Table 1 and Figures 2, 3 and 4 that the systems with choline chloride and citric acid obtain the best copper extractions, followed by the system with choline chloride and urea and finally, with choline chloride and ethylene glycol. A maximum copper extraction of 100% is obtained with the DES composed of ChCl + citric acid with 20% water at 50 and 60 °C. This DES is viscous therefore the addition of water becomes necessary to improve the mass transfer between solid and solvent. Clearly, in all three DES tested, the effect of increasing the leaching temperature shows positive results.

High copper extractions have been reported using DES composed of ChCl and urea at high temperatures (Topcu et al., 2021; Topçu et al., 2021). The effect of increasing temperature also affects copper dissolutions using ChCl and ethylene glycol (Carlesi et al., 2022).

The challenge is to synthesize a water-free DES, which could suggest mixing different DESs to lower the viscosity in efficient DESs, as is the case with the citric acid-based DES.

Conclusions

Copper extraction from copper sulphide ore was studied with agitated leaching using different DES at temperatures of 25, 50 and 60 °C. The main conclusions were:

- Using acid DES for copper leaching from sulphide ore, extractions of 75% Cu are achieved at 25 °C and 100% Cu at 50 and 60°C under the conditions studied.
- Increasing the leaching temperature increases the dissolution of copper from the ore to the DES.
- It is necessary to synthesize DES without using water and that they have an adequate viscosity for an efficient separation process. This can be achieved by mixing two different DES.
- Viscosity is a challenge that must be addressed to achieve adequate solid-liquid separation in downstream processes.

These results show promising alternatives that can be further investigated.

References

Alta-Ley, 2019. Hoja de Ruta 2.0 de la minería chilena. Actualización y consensos para una mirada renovada.

Carlesi, C., Harris, R.C., Abbott, A.P. and Jenkin, G.R., 2022. Chemical dissolution of chalcopyrite concentrate in choline chloride ethylene glycol deep eutectic solvent. Minerals, 12(1): 65.

COCHILCO, 2021. Chilepolimetálico: Diversificando la minería chilena.

COCHILCO, 2023. Estado actual de la hidrometalurgia de cobre en Chile.

Fundación-Encuentros-del-Futuro, 2023. Chile, líder mundial en minería verde.

Hansen, B.B., Spittle, S., Chen, B., Poe, D., Zhang, Y., Klein, J.M., Horton, A., Adhikari, L., Zelovich, T. and Doherty, B.W., 2020.

Deep eutectic solvents: a review of fundamentals and applications. Chem. Rev., 121(3): 1232-1285.

Ministerio-Minería, 2023. Levantamiento de capacidades académicas en áreas de minería y metalurgia a nivel nacional.

Tian, G. and Liu, H., 2024. Review on the mineral processing in ionic liquids and deep eutectic solvents. Miner. Process. Extr. Metall. Rev., 45(2): 130-153.

Topcu, M.A., Kalem, V. and Rüşen, A., 2021. Processing of anode slime with deep eutectic solvents as a green leachant. Hydrometallurgy, 205: 105732.

Topçu, M.A., Rüşen, A. and Küçük, Ö., 2021. Treatment of copper converter slag with deep eutectic solvent as green chemical. Waste Manage. (Oxford), 132: 64-73.

Effect of Aluminosilicate Concentration on the Rheological Parameters of Thickened Tailings

Christian Escobar E.[1], Julio Valenzuela Elgueta[2]

1,2. Departamento de Minas y Metalurgia, Universidad Católica del Norte, Chile

**Corresponding author at: Departamento de Minas y Metalurgia, Universidad Católica del Norte, Chile*
e-mail adress: escobar.christian@ce.ucn.cl.

ABSTRACT

The rheological behavior of tailings is a critical factor in the design and operation of thickened tailings disposal (ttd) systems. Among their constituents, aluminosilicate clays such as kaolinite and muscovite play a decisive role in controlling sedimentation, viscosity, and flow resistance. Understanding these effects is essential to optimize water recovery, improve thickening performance, and ensure safe and sustainable tailings management.In this study, synthetic mineral mixtures containing different proportions of kaolinite and muscovite were prepared to simulate copper tailings. Sedimentation tests, turbidity measurements, and rheological characterization using an anton paar rheolabqc rheometer were performed. The bingham plastic model was applied to estimate yield stress and plastic viscosity, while focused beam reflectance measurement (fbrm) provided insights into flocculation dynamics and aggregate stability.The results showed that increasing clay content significantly reduced sedimentation rates, increased supernatant turbidity, and led to higher yield stress and viscosity. Kaolinite displayed a stronger effect than muscovite, producing denser aggregates and greater resistance to shear.This study demonstrates the significant influence of aluminosilicate clays on the rheology of thickened tailings, reinforcing the need for mineralogical characterization in ttd design. These findings provide practical insights to optimize water recovery and ensure safer and more efficient tailings management.

Introduction

The mining industry generates large volumes of tailings, which are fine-grained residues resulting from the beneficiation of ores. In copper and molybdenum mining, tailings are typically managed through thickened tailings disposal (TTD), a technology that improves water recovery and reduces the environmental footprint of storage facilities. However, the successful implementation of TTD strongly depends on understanding the rheological behavior of tailings pulps, as it controls thickening efficiency, pumping requirements, and long-term deposit stability.

Among the components of tailings, aluminosilicate clays such as kaolinite and muscovite play a crucial role. Due to their small particle size, high surface area, and structural characteristics, these minerals significantly influence sedimentation, flocculation, and viscosity of suspensions. Even at low concentrations, they can increase yield stress, hinder particle settling, and affect water clarification, thus complicating the management of thickened tailings. This makes their study particularly relevant in Chile, where the large-scale production of copper is directly linked to massive generation of tailings containing significant clay fractions.

From a rheological perspective, tailings with aluminosilicate clays often exhibit non-Newtonian behavior, requiring advanced models such as Bingham plastic or Herschel–Bulkley to describe their flow properties. Parameters such as yield stress and apparent viscosity are critical for predicting transport behavior through pipelines and for designing efficient thickening systems. Understanding how different clay minerals affect these parameters provides valuable insight for improving water recovery, reducing environmental risks, and enhancing operational efficiency.

The motivation for this research lies in the need to bridge the gap between mineralogical composition and rheological response in tailings pulps. Specifically, the study focuses on characterizing how kaolinite- and muscovite-rich suspensions affect sedimentation, turbidity, and rheology, and how these effects can be modeled and interpreted for practical applications in thickened tailings management.

The objective of this work is therefore to evaluate the rheological behavior of aluminosilicate clays in synthetic mineral mixtures representative of copper tailings, using laboratory tests and rheological modeling. By linking clay mineralogy with measurable parameters such as yield stress, viscosity, and sedimentation rate, the study provides a framework for better predicting and managing the performance of thickened tailings systems.

Methodology

Synthetic mineral mixtures representative of copper tailings were prepared with varying proportions of kaolinite and muscovite. Eight different mixtures (M1–M8) were designed to evaluate the effect of increasing clay content on sedimentation, turbidity, and rheological behavior (Table 1). All tests were conducted at room temperature with deionized water to minimize variability due to ionic effects.

Table 1. Mineralogical Composition of the Experimental Mixtures (M1–M8)

Mixture	Kaolinite [%]	Muscovite [%]	Quartz [%]	Pyrite [%]
M1	1	10	84	5
M2	1	20	74	5
M3	3	10	82	5
M4	3	20	72	5
M5	5	10	80	5
M6	5	20	70	5
M7	10	10	75	5
M8	10	20	65	5

Sedimentation tests were performed using graduated cylinders (1000 mL) to monitor the settling rate of suspensions. The interface height between the clear supernatant and the settling pulp was recorded over time, allowing the determination of sedimentation velocity and the evaluation of solid-liquid separation efficiency.

Turbidity measurements of the supernatant were carried out after sedimentation tests using a calibrated turbidimeter, in order to quantify water clarity and the effectiveness of the settling process.

Rheological characterization was conducted with an Anton Paar RheolabQC controlled-stress rheometer. Flow curves were obtained under shear rate ramps, and the Bingham plastic model was applied to estimate yield stress (τ_0) and plastic viscosity (μp). Measurements were performed at 20% solids by weight, with controlled shear rates ranging from low to high values to capture both linear and non-linear responses.

Additionally, **Focused Beam Reflectance Measurement (FBRM)** was employed on 200 mL suspensions to monitor in situ flocculation dynamics (Figure 1). The technique provided real-time data on chord length distribution, allowing the assessment of particle aggregation, breakage, and structural stability under agitation.

This combined experimental methodology enabled the integration of sedimentation, turbidity, and rheological data, providing a comprehensive understanding of the influence of aluminosilicate clays on thickened tailings behavior.

Results and Discussions

Sedimentation behavior

Sedimentation tests revealed a strong influence of clay content on settling performance. Mixtures with higher kaolinite and muscovite fractions exhibited lower sedimentation velocities and greater interface stability, confirming the detrimental role of fine aluminosilicates in hindered settling. Figure 1 illustrates the progressive decrease in settling rate with increasing clay concentration. This effect is consistent with the ability of fine platy particles to increase suspension structuring and water retention, thereby reducing thickening efficiency.

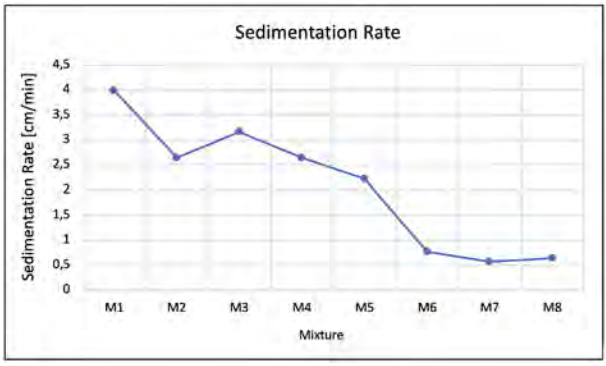

Figure 1. Sedimentation rate of synthetic mixtures (M1–M8) as a function of clay content

Turbidity measurements

The turbidity of the supernatant increased significantly with clay content (Figure 2). High turbidity values indicate that clay-rich suspensions hinder water clarification, which directly impacts water recovery in thickened tailings facilities. This trend reflects the strong colloidal interactions of kaolinite and muscovite, which promote the persistence of fine particles in suspension even after prolonged settling.

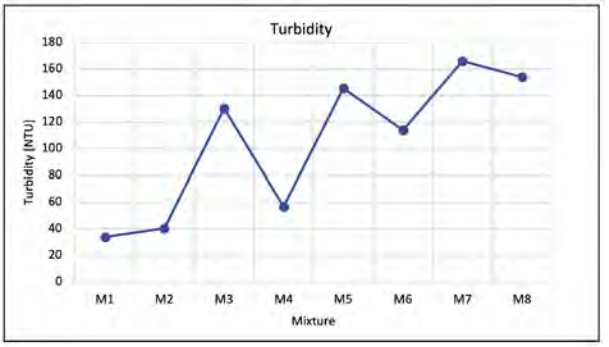

Figure 2. Turbidity of the supernatant in mixtures (M1–M8) with increasing clay proportions

Rheological characterization

Flow curves obtained with the Anton Paar RheolabQC rheometer confirmed non-Newtonian behavior in all mixtures, with Bingham plastic parameters (yield stress and plastic viscosity) increasing systematically with clay content (Figure 3). Kaolinite-rich mixtures displayed higher yield stresses compared to muscovite-rich suspensions, suggesting a stronger interparticle network. These results highlight the need for mineralogical characterization in predicting pipeline transport behavior and pump requirements in tailings systems.

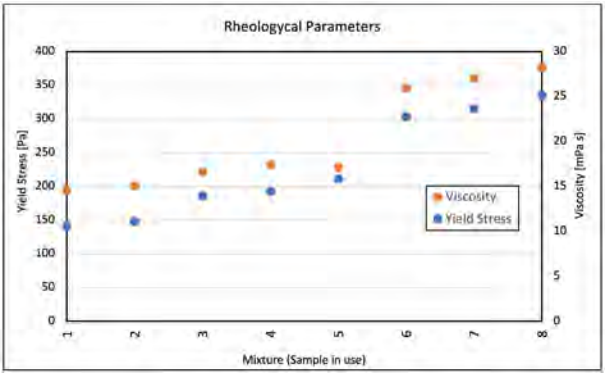

Figure 3. Flow curves fitted with the Bingham plastic model for mixtures (M1–M8)

Flocculation dynamics

FBRM measurements provided real-time information on aggregate stability under agitation. Main results indicated that kaolinite promotes denser and more stable aggregates compared to muscovite in a particle range between 50 -150 [µm] (figure 4), but also contributes to stronger resistance to shear. This observation helps explain the higher yield stresses recorded in kaolinite-rich mixtures, as aggregate restructuring under shear requires greater energy input.

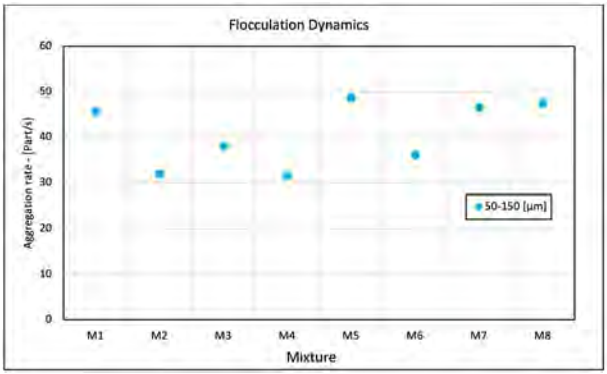

Figure 4. Flocculation dynamics (FBRM): time-evolution of total counts and mean chord length in mixtures (M1–M8), highlighting differences between kaolinite- and muscovite-rich suspensions

Overall discussion

The integration of sedimentation, turbidity, and rheological results demonstrates the central role of aluminosilicate clays in controlling the behavior of thickened tailings. While both kaolinite and muscovite impair sedimentation and water clarification, kaolinite exerts a stronger effect on yield stress and viscosity, making it the most critical mineralogical component influencing thickening and transport performance.

Conclusions

Aluminosilicate clays (kaolinite and muscovite) exert a strong influence on the rheological behavior of thickened tailings, even at relatively low concentrations.

Increasing clay content reduces settling velocity, producing denser suspensions and slower solid-liquid separation.

Supernatant turbidity increases with clay proportion, highlighting the negative impact of clays on water clarification and recovery.

Rheological measurements confirmed a direct correlation between clay content and yield stress, as well as between clay content and plastic viscosity, reinforcing the need to consider mineralogy in process design.

Kaolinite produced a stronger structuring effect than muscovite, reflected in higher yield stress and more stable aggregates, while muscovite showed weaker but still significant influence.

FBRM measurements demonstrated that aggregate stability and restructuring dynamics under shear differ by clay type, providing additional insight into suspension behavior.

These results emphasize the need to integrate mineralogical characterization into the design and optimization of thickened tailings disposal systems, particularly in Chilean copper mining where clay-rich ores are common.

The study contributes practical knowledge for improving water recovery, reducing environmental risk, and enhancing operational efficiency in modern tailings management.

References

Barnes, H. A., Hutton, J. F. and Walters, K.,1989. An Introduction to Rheology. Elsevier.

Bianchini, G., D'Alessandro, W. and Natali, C., 2017. Geochemical behavior of potentially harmful elements in mining tailings and implications for sustainable water management. Environmental Earth Sciences, 76(14), 487. https://doi.org/10.1007/s12665-017-6826-9

Chhabra, R. P. and Richardson, J. F., 2008. Non-Newtonian Flow and Applied Rheology: Engineering Applications. Butterworth-Heinemann.

Sampaio, C. H. and Tavares, L. M., 2005. Rheological behavior of kaolin suspensions: Effects of dispersants and particle size. International Journal of Mineral Processing, 76(1–2), 1–13. https://doi.org/10.1016/j.minpro.2004.09.003

Effect of Curing Time and Ferric Chloride on a Copper Concentrate with a High Arsenic Content

Víctor Quezada*, Stephano Zepeda, Oscar Benavente, María Cecilia Hernández, and Evelyn Melo

Departamento de Ingeniería Metalúrgica y Minas, Universidad Católica del Norte, Antofagasta, Chile;

**Corresponding author at: Departamento de Ingeniería Metalúrgica y Minas, Angamos 0610, Antofagasta, Chile; vquezada@ucn.cl.*

Introduction

According to the Chilean Copper Commission (Cochilco) [1], projections for the period 2022–2034 indicate a significant decline in hydrometallurgical copper production. In 2022, the hydrometallurgical production was 1.38 Mt, and it will decrease to 0.713 Mt by the year 2034, representing a 48.4% reduction in total production. The main factor in this decline is the depletion of copper oxide reserves due to the transition from oxide to sulfide copper reserves. It is worth nothing that 70% of the sulfide copper mineral reserves are attributed to chalcopyrite ($CuFeS_2$). Therefore, the hydrometallurgical treatment of copper concentrates and/or sulfide minerals could represent an increase in copper production using existing hydrometallurgical plants. A problem arises when chalcopyrite is treated via hydrometallurgical processes because it presents slow dissolution kinetics, a consequence of a passivating layer that hinders contact between the mineral and the leaching solution [2].

Further complicating this issue is the presence of enargite (Cu_3AsS_4), a mineral often found in association with chalcopyrite and other sulfur-containing minerals related to copper and arsenic [3]. Enargite and chalcopyrite are classified as refractory minerals under conventional leaching conditions. Moreover, the presence of arsenic in enargite presents a challenge, particularly in copper concentrate treatment. Any copper concentrate with an arsenic content exceeding 0.5% is categorized as a complex concentrate. This leads to penalties for impurities in the commercial value of the copper concentrate [4]. In recent years, several studies have focused on the effect of pretreatment in the leaching of primary copper sulfides, mainly chalcopyrite.

However, there is a notable scarcity of research specifically addressing the effect of pretreatment on enargite. Rivera-Vasquez and Dixon [5] used pyrite as a catalyst in a ferric sulfate acidic media, achieving the highest copper extraction at 80 °C, with a pyrite to enargite ratio (Py:En) of 4 in 24 h. Jahromi et al. [6] conducted a comprehensive investigation into leaching in a chloride media with and without the use of activated carbon (AC) and with a novel carbon-based catalyst called Lanxess Lewatit® AF 5. The results showed a copper extraction of 65%, 92%, and 96% after 96 h. The optimal leaching conditions were achieved at cupric and ferric concentrations of 5 g/L, a concentrate to catalyst ratio of 1:2, and a temperature of 90 °C. This study provides valuable insights into enhancing leaching efficiency through the use of innovative catalysts and conditions. Other studies that evaluated the dissolution kinetics of enargite include Herreros et al. [7], Viñals et al. [8], Riveros and Dutrizac [9], and Hernández et al. [10]. As mentioned earlier, there is currently no available information on this topic for enargite pretreatment studies. Nevertheless, for the purpose

of drawing comparisons, we highlight some relevant studies involving chalcopyrite. Chalcopyrite shares similar characteristics with enargite and serves as a valuable mineral for providing insights and references on the subject. Examples of pretreatment application to chalcopyrite include the following: Cerda et al. [11] used a sample with chalcopyrite (1.21% wt) and bornite (0.54% wt) as the main copper minerals under different types of leaching (flask, reactor, and mini-column). The variables studied for pretreatment were chloride concentration (20, 50, and 90 kg/t), curing time (7, 20, and 40 days), and temperature (20 and 50 °C). A maximum of 93% copper extraction was obtained when treated with 90 kg/t Cl-, 40 days of curing, and 50 °C flask leaching. Hernández et al. [12] studied the effect of agglomeration and pre-leaching curing on a sample composed mainly of chalcopyrite, using mini-columns in acid–chloride–nitrate media. The variables studied were the addition of sodium nitrate $(NaNO3)$ (11.7 and 23.3 kg/t), sodium chloride $(NaCl)$ (2.1 and 19.8 kg/t), curing time (20 and 30 days), and curing temperature (25 and 45 °C). A 58.6% copper extraction was obtained under the conditions of 23.3 kg/t of $NaNO3$, 19.8 kg/t of $NaCl$, and 30 days of curing at 45° without leaching. Subsequently, after the pretreatment stage, leaching in mini-columns was conducted for the samples, varying parameters such as temperature (25 and 45 °C) and chloride concentration (20 and 40 g/L). The optimal copper extraction for the mini-column leaching test was 63.9% at 25 °C, with a chloride concentration of 20 g/L. Quezada et al. [13] worked with a sample consisting mostly of chalcopyrite, aiming to evaluate the effect of pretreatment before leaching using different concentrations of sodium chloride $(NaCl)$, potassium nitrate $(KNO3)$, sulfuric acid $(H2SO4)$, and varying curing times (0 to 15 days). Their optimal extraction was 23% with a $NaCl$ concentration of 25 kg/t, a $H2SO4$ concentration of 15 kg/t, and a curing time of 15 days. According to their ANOVA analysis, parameter A (curing time) had the most significant contribution to variation in the Cu extraction (56.36%), parameter B $(H2SO4)$ had an extremely low contribution (1.78%), and parameter C $(NaCl)$ had a moderate contribution (23.09%). Most of these contributions are statistically significant, according to the p-values obtained (significant A and C at a 99% confidence level). It is worth mentioning that, in the study, the concentration of $KNO3$ did not prove to be a significant parameter in copper extraction. However, a point of comparison in this study, as well as in studies by Cerda et al. [11] and Hernández et al. [12], is observed in the improvement of the copper extraction percentage with increasing chloride concentration (Cl), which proves to be a relevant factor in the search for optimal parameters.

The objective of the current study is to evaluate the impact of curing pretreatment on copper extraction from a concentrate with high arsenic content. The main variables of these curing tests are curing time (days), sulfuric acid $(H2SO4)$, and ferric chloride $(FeCl3)$. The results were subjected to an analysis of variance (ANOVA) to identify the optimal combination of parameters. Interactions between variables were not considered for the analysis. Predictive models support this assumption, but additional tests may be conducted later for confirmation.

Methodology

In this study, the effects of 3 variables were analyzed regarding copper extraction. These variables were curing time, sulfuric acid concentration $(H2SO4)$, and ferric chloride concentration $(FeCl3)$. The ranges of variable values and the number of trials were designed according to an experimental matrix performed with the Taguchi method using the Minitab software (17.1.0, LLC, State College, PA, USA). The Taguchi method involves a set of mathematical procedures aimed at finding improvements in a process through the execution and collection of data, and there are various studies that utilize this optimization method for evaluating the impact of variables involved in the process [14–16]. It is based on the systematic application of the Design of Experiments (DOE) [17]. The designed matrix was an L16 (43) with 3 variables and 4 levels (see Tables 1 and 2).

Table 1. Experimental design with L16 (43) orthogonal array for Taguchi method.

Sample	Matrix L_{16} (4^3)		
	A	B	C
	Curing time (days)	H_2SO_4(kg/t)	$FeCl_3$ (M)
1	1	3	2
2	4	4	4
3	1	2	4
4	2	2	2
5	3	4	2
6	4	3	1
7	3	3	3
8	1	1	1
9	3	2	1
10	4	2	3
11	2	4	1
12	2	3	4
13	2	1	3
14	1	4	3
15	4	1	2
16	3	1	4

Table 2. Variables and levels of the experimental matrix.

	Parameters	Levels			
		1	2	3	4
A	Curing time (days)	0	5	10	15
B	H_2SO_4 (kg/t)	0	70	140	210
C	$FeCl_3$ (M)	0	0.5	1	1.5

The aim of this study is to maximize the performance values of the established variables. To achieve this objective, Equation (1) was employed. In this equation, *'SN'* denotes the characteristic performance to be optimized, **'n'** represents the number of trials conducted for a particular combination, and **'Y_i'** signifies the performance value at the i-th trial [14]. It is worth nothing that all experiments were conducted twice under identical operating conditions.

$$SN = -10Log\left[\frac{1}{n}\sum_{i=1}^{n}\frac{1}{Y_i^2}\right]; \text{ Equation (1)}$$

However, there is the possibility that the optimal values for the trial may not be included in the orthogonal design. In such cases, optimal values can be determined using a balancing feature of the orthogonal matrix. Equation (2) represents the additive model that can be utilized for this purpose. In this equation, 'μ' represents the overall average of the performance value, 'X_i' is the fixed effect of the combination of parameter levels used in the i-th experiment, and 'ei' is the random error of the i-th experiment.

$$Y_i = \mu + X_i + e_i; \text{ Equation (2)}$$

The experiments were conducted with 5 g of the sample to determine the optimal combination of curing time, sulfuric acid concentration (H_2SO_4), and ferric chloride concentration ($FeCl_3$). A solid–liquid ratio of 1/100 (5 g/500 mL) was used to evaluate the samples. The samples were homogenized to form the agglomerate and subsequently covered to prevent evaporation. The samples were kept at room temperature (25 °C) for curing with established times of 0, 5, 10, and 15 days (Figure 1). After the corresponding time period, the samples were washed with a solution consisting of distilled water with 0.5 g/L of sulfuric acid using a digital RW20 mechanical stirrer at 450 rpm for 5 min at room temperature. Finally, this solution was filtered using a vacuum pump, model 1636 Thomas, and the copper concentration in the filtrate was determined by a Varian Atomic Absorption Spectrometer, Model Spectra AA 55B.

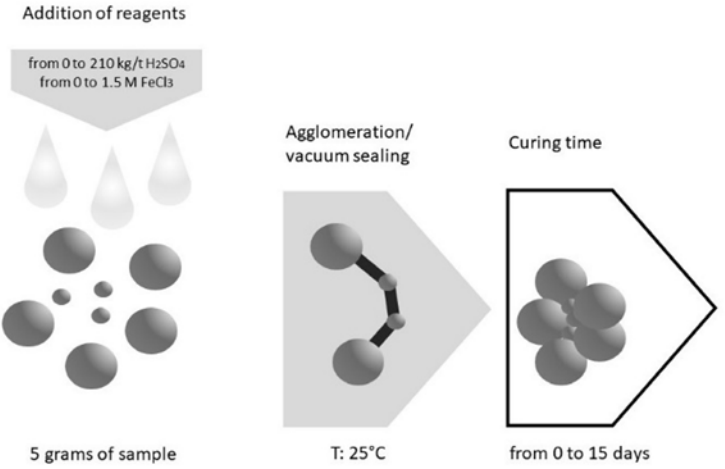

Figure 1. Agglomeration and curing procedure.

Results and Discussions

The results presented in Table 3 correspond to the copper extraction generated by each of the three variable combinations used in the experiments. The combination that achieved the highest copper extraction was sample No. 10 with 20.8%, whose variables consisted of a curing time of 15 days, 70 kg/t of sulfuric acid (H_2SO_4), and 1 M ferric chloride ($FeCl_3$).

Table 3. Percentages of copper extraction from the experiments

No.	Curing time (days)	H_2SO_4 (kg/t)	$FeCl_3$ (kg/t)	Copper extraction (%)	No.	Curing time (days)	H_2SO_4 (kg/t)	$FeCl_3$ (kg/t)	Copper extraction (%)
1	0.00	140	0.50	4.66	9	10.0	70.0	0.00	10.5
2	15.0	210	1.50	9.57	10	15.0	70.0	1.00	20.8
3	0.00	70.0	1.50	6.45	11	5.00	210	0.00	5.05
4	5.00	70.0	0.50	8.22	12	5.00	140	1.50	10.0
5	10.0	210	0.50	6.48	13	5.00	0.00	1.00	8.58
6	15.0	140	0.00	15.4	14	0.00	210	1.00	4.66
7	10.0	140	1.00	6.59	15	15.0	0.00	0.50	6.04
8	0.00	0.00	0.00	3.36	16	10.0	0.00	1.50	12.1

This section may be divided by subheadings. It should provide a concise and precise description of the experimental results, their interpretation, as well as the experimental conclusions that can be drawn. An increase in copper extraction was demonstrated with the increase in curing time of the samples, regardless of the experimental variables [5,11,13].

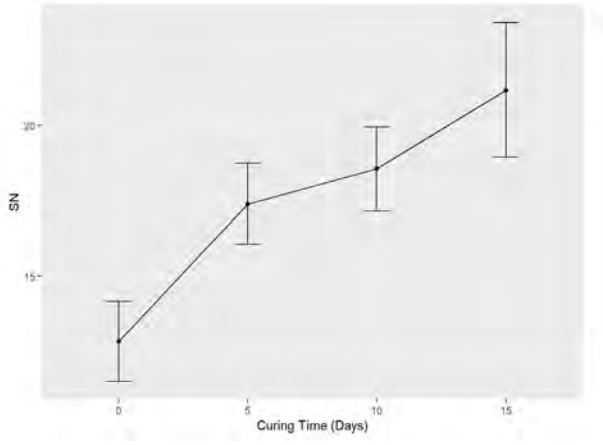

Figure 2. Effect of curing time (days) on the optimization criterion SN for the percentage of Cu extraction.

This effect is observed in Figure 2, which illustrates the behavior of the curing time variable over time. The point of maximum efficiency of the variable may even be at longer times than those evaluated in these experiments. Regarding the impact of the $H2SO4$ and $FeCl3$ concentrations, depicted in Figure 3 and 4, respectively, it is feasible to ascertain optimal concentrations for achieving maximum copper extraction. These findings align with previous research [5,9,18] that demonstrates enhanced copper or arsenic extraction through the addition of these reagents.

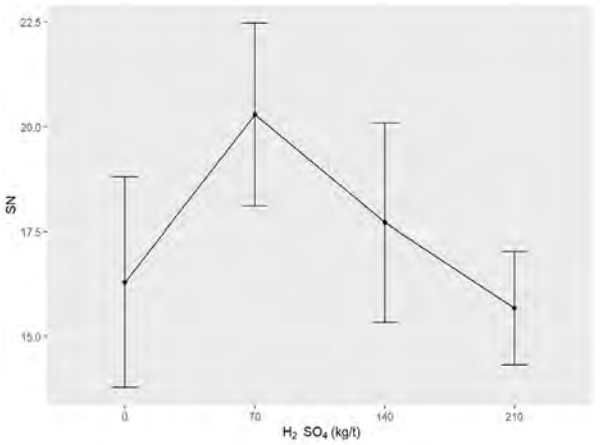

Figure 3. Effect of concentration of H2SO4 on the optimization criterion SN for the percentage of Cu extraction.

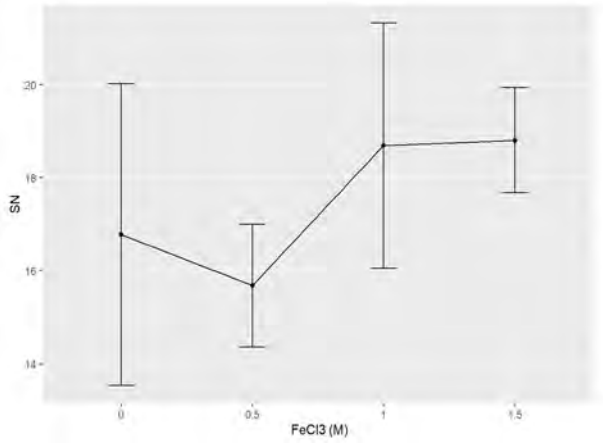

Figure 4. Effect of concentration of FeCl3 on the optimization criterion SN for the percentage of Cu extraction.

In Table 4, it is determined that parameter A (curing time) has the highest contribution (45.76%) among the three parameters to the percentage of extracted **Cu**. Parameter B (acid concentration) has a moderate contribution (20.31%), and parameter **C** (ferric chloride concentration) has a lower contribution (10.08%). All these contributions are statistically significant according to the p-values obtained; A, B, and C are significant variables at a 95% confidence.

Table 4. Influence of parameters on the % of copper extraction (df = Degrees of freedom, SSE = Sum of squares error, MSE = Mean square errors)

	Parameters	df	SSE	MSE	F value	Contribution	p-value
A	Curing time (days)	3	265.349	88.45	14.07	45.76%	0.00002447
B	Acid concentration (kg/t)	3	117.779	39.26	6.245	20.31%	0.00313200
C	Ferric chloride concentration (M)	3	58.446	19.482	3.099	10.08%	0.04764300
	Error	22	138.303				
	Total	31	579.877				

Based on the data obtained in Table 5, it can be seen that the variation in the percentage of copper before and after pretreatment was 7.4% lower, with a 20% decrease in weight, confirming the effect of pretreatment on copper extraction from the concentrate. In analyzing the variation in arsenic before and after pretreatment, we found that it was 0.01% lower. This confirms that the enargite present in the sample was not affected by the pretreatment, and the extracted copper did not originate from it.

Table 5. Percentages of copper and arsenic in the concentrate before pretreatment (BP) and after pretreatment (AP).

Analyzed Element	BP(%)	AP(%)
Copper (Cu)	36.26	28.86
Arsenic (As)	6.44	6.43

Conclusions

According to the analysis of variance (ANOVA), the most effective combination for optimizing copper extraction from an enargite-rich concentrate involves a curing time of 15 days, the addition of 70 kg/t of sulfuric acid (H_2SO_4), and a 1 M concentration of ferric chloride ($FeCl_3$). However, these three parameters do not show a significant impact on enargite and chalcopyrite dissolution at only reaching a percentage of 20.8% of copper extraction. Although the study was limited to the application of a pretreatment process without the implementation of a subsequent leaching stage. Therefore, it is recommended that future research incorporate this additional stage in order to more comprehensively evaluate the effectiveness of the pretreatment process. Subsequently, the analysis suggests that curing time is the most influential factor in the process, accounting for 46% of the overall contribution. In comparison, sulfuric acid and ferric chloride contribute less, with 20% and 10% contributions, respectively. Therefore, it is recommended to extend the curing time and increase the acid concentration to improve the process efficiency.

References

Cochilco. Proyección de la producción de cobre en Chile 2023 – 2034; Comunicaciones Cochilco: Santiago, Chile, 2024.

Quezada, V.; Roca, A.; Benavente, O.; Cruells, M.; Melo, E.; Hernández, M. Pretreatment to Leaching for a Primary Copper Sulphide Ore in Chloride Media. Metals 2021. 11, 1260, doi:10.3390/met11081260.

Lattanzi, P.; Da Pelo, S.; Musu, E.; Atzei, D.; Elsener, B.; Fantauzzi, M.; Rossi, A., 2008. Enargite oxidation: A review. Earth-Science Reviews, 86, 62-88, doi:10.1016/j.earscirev.2007.07.006.

Cochilco. Exportación de concentrados de cobre: caracterización de condiciones comerciales; Comunicaciones Cochilco: Santiago, Chile, 2021.

Rivera-Vasquez, B. F.; Dixon, D., 2015. Rapid atmospheric leaching of enargite in acidic ferric sulfate media. Hydrometallurgy, 152, 149-158, doi:10.1016/j.hydromet.2014.12.012.

Jahromi, F. G.; Cowan, D. H.; Ghahreman, A., 2017. Lanxess Lewatit® AF 5 and activated carbon catalysis of enargite leaching in chloride media; a parameters study. Hydrometallurgy, 174, 184-194, doi:10.1016/j.hydromet.2017.10.012.

Herreros, O.; Quiroz, R.; Hernandez, M. C.; Viñals, J., 2002. Dissolution kinetics of enargite in dilute Cl2/Cl- media. Hydrometallurgy, 64, 153-160, doi:10.1016/S0304-386X(02)00034-8.

Viñals, J.; Roca, A.; Hernández, M. C.; Benavente, O., 2003. Topochemical transformation of enargite into copper oxide by hypo-chlorite leaching. Hydrometallurgy, 68, 183-193, doi:10.1016/S0304-386X(02)00200-1.

Riveros, P. A.; Dutrizac, J. E., 2008. The leaching of tennantite, tetrahedrite and enargite in acidic sulphate and chloride media. Can. Metall. Q., 47, 235-244, doi:10.1179/cmq.2008.47.3.235.

Hernández, M. C.; Benavente, O.; Roca, A.; Melo, E.; Quezada, V., 2023. Selective Leaching of Arsenic from Copper Concentrates in Hypochlorite Medium. Minerals, 13, 1372, doi:10.3390/min13111372.

Cerda, C. P.; Taboada, M. E.; Jamett, N. E.; Ghorbani, Y.; Hernández, P. C., 2018. Effect of pretreatment on leaching primary copper sulfide in acid-chloride media. Minerals, 8, 1, doi:103390/min8010001.

Hernández, P. C.; Dupont, J.; Herreros, O. O.; Jimenez, Y. P.; Torres, C. M., 2019. Accelerating copper leaching from sulfide ores in acid-nitrate-chloride media using agglomeration and curing as pretreatment. Minerals, 9, 250, doi:10.3390/min9040250.

Quezada, V., Roca, A., Benavente, O., Cruells, M., Keith, B., & Melo, E., 2020. Effect of pretreatment prior to leaching on a chalcopyrite mineral in acid media using NaCl and KNO3. J. Mater. Res. Technol., 9, 10316-10324, doi:10.1016/j.jmrt.2020.07.055.

Copur, M.; Kizilca, M.; Kocakerim, M. M., 2015. Determination of the optimum conditions for copper leaching from chalcopyrite concentrate ore using taguchi method. Chem. Eng. Com., 202, 927-935, doi:10.1080/00986445.2014.891506.

Melo, E.; Hernández, M. C.; Benavente, O.; Quezada, V., 2022. Selenium Dissolution from Decopperized Anode Slimes in ClO−/OH− Media. Minerals, 12, 1228, doi:10.3390/min12101228.

Topçu, M.; Rüşen, A.; Yıldızel, S. A., 2023. High efficiency copper recovery from anode slime with 1-butyl-3-methyl imidazolium chloride by hybrid Taguchi/Box–Behnken optimization method. J. Indus. Eng. Chem., 120, 261-270, doi:10.1016/j.jiec.2022.12.033.

Hamzaçebi, C., 2020. Taguchi method as a robust design tool. In Quality Control in Intelligent Manufacturing; IntechOpen: London, UK.

Padilla, R.; Girón, D.; Ruiz, M. C., 2005. Leaching of enargite in H2SO4–NaCl–O2 media. Hydrometallurgy, 80, 272-279, doi:10.1016/j.hydromet.2005.08.006.

Effect of Salts and Ferric in an Acidic Environment on the Leaching of Chalcopyrite: Response Surface Methodology - Box Behnken Design

Cerda Cecilia[1,2], María Elisa Taboada[1], Daniel Calisaya[2] and Julio Valenzuela[2]

1. Department of Chemical Engineering and Mineral Processes, Universidad de Antofagasta, Av, Angamos 601, Antofagasta 1270300, Chile
2. Department Metallurgical and Mining, Universidad Católica del Norte, Av. Angamos 0610, Antofagasta, Chile

**Corresponding author at: Department of Metallurgical and Mining Engineering, Universidad Católica del Norte, Av. Angamos 0610, Antofagasta, Chile, Cecerda@ucn.cl*

ABSTRACT

The continuous operation of the Solvent Extraction and Electrowinning stages in the copper extraction process has prompted the research of innovative alternatives for the leaching of sulfide minerals, particularly chalcopyrite, recognized as the most abundant copper mineral in various deposits. This research focuses on the leaching process of a chalcopyrite ore with a copper grade of 22.7% and an iron grade of 17.7%. The study explores the interactions of several key variables: temperature (20°C, 30°C, and 40°C), the pyrite/chalcopyrite ratio (tested ratios: 0.3:1, 0.5:1, and 1:1), and the ferric chloride dosage (6.9 g/L and 12 g/L). The pyrite ore used in this experiment contains a significant iron content of 27.9%. The results of the experiments are evaluated using an empirical model that considers the interactions between temperature, the pyrite/chalcopyrite ratio, and the ferric chloride concentration. Under optimal conditions of 40 °C, a pyrite/chalcopyrite ratio of 0.5:1, and a ferric chloride dosage of 6 g/L, the experiments yielded copper solution concentrations ranging from 8.78 g/L to 8.96 g/L. This study clearly demonstrates that it is possible to dissolve copper from chalcopyrite and achieve copper solution concentrations above 6 g/L in an acidic medium containing salts and ferric chloride at 40 °C. Therefore, this research offers a practical and efficient method for copper extraction.

Keywords: Pregnant leach solution (P.L.S), temperature, chalcopyrite, pyrite, ferric chloride.

Introduction

In Chile, copper production from copper oxide-based methods is facing significant depletion. This is largely due to processing challenges, which may lead to a drastic reduction in plant output (Cochilco, 2017).

As a response, researchers are actively exploring alternative methods for leaching copper from primary sulphide ores, especially chalcopyrite. A key challenge is that a sulphur layer often forms on chalcopyrite's surface, hindering the effectiveness of leaching solutions (Dutrizac, 1989; Li et al., 2013).

There are many reactive media, such as sulphates, chlorides, iodides, and nitrates, being studied for leaching chalcopyrite at various temperatures and pressures (Liu et al., 2025; Martínez-Bussenius & Videla, 2024; Salinas-Farran et al., 2024; Quezada et al., 2020). Using a chloride-based leaching process offers several advantages, such as faster reaction rates and higher solubility of metals compared to traditional sulphate-based methods. However, challenges like increased corrosion and reduced electrowinning efficiency also arise. Despite this, chloride in acidic environments has shown greater overall benefits. Noteworthy advancements in chalcopyrite leaching technology include processes like the Hydrocopper Process (Hyvärinen & Hämäläinen, 2005), the Cuprex Process (Dalton RF et al., 1991), and others focusing on dissolution in chloride solutions (Velásquez-Yévenes et al., 2010).

In addition to chloride, ferric ions have been studied to understand their effect on chalcopyrite leaching. Research indicates that the concentration of ferric ions significantly affects the rate of chalcopyrite dissolution. Specifically, using ferric chloride in acidic environments can form a protective elemental sulfur layer on chalcopyrite, which may inhibit further leaching unless certain conditions, like elevated temperatures, are met (Hidalgo et al., 2018).

Equations (1), (2), and (3) present the chemical reactions between chalcopyrite and ferric chloride within an acidic environment.

$$CuFeS_2 + 4\,FeCl_3 = CuCl_2 + 5FeCl_2 + 2S^0 \quad (1)$$

$$S^0 + 6FeCl_3 + 4H_2O = 6Fe^{+2} + 8H^+ + 18Cl^- \quad (2)$$

$$CuFeS_2 + 16FeCl_3 + 8H_2O = CuCl_2 + 2H_2SO_4 + 17FeCl_2 + 12HCl \quad (3)$$

Several strategies have been explored to enhance chalcopyrite dissolution rates, such as elevating temperature and pressure, reducing particle size, and introducing various catalysts (Carranza et al., 1997; Bolorunduro et al., 2003). Recent studies since 2012 have highlighted new catalysts, particularly the addition of iodide ions in concentrations between 50 and 200 mg/L, which can significantly improve dissolution even at room temperature (Fukano & Miura, 2021; Granata et al., 2019). Additionally, introducing pyrite in ferric sulphate media has also been shown to enhance dissolution rates, leading to the development of the Galvanox™ process (Nazari et al., 2011). The oxidation of chalcopyrite is particularly favoured when the redox potential is between 0.36 to 0.5 V versus Ag/AgCl, as this facilitates the transformation of chalcopyrite into chalcocite. However, exceeding this potential can lead to the forming of a passive layer that inhibits dissolution.

Most studies conducted thus far have operated at temperatures above 45°C, indicating that temperature control is crucial for optimizing dissolution rates.

The main goal of this study is to generate a copper-rich solution (Pregnant Leach Solution, PLS) with concentrations of at least 6 g/L, suitable for feeding to solvent extraction (SX) plants to produce high-purity copper cathodes (99.999%). To achieve this, standard operating conditions involving chloride, iodide, and sulfuric acid concentrations, along with three main variables—temperature, ferric chloride dosage, and the pyrite/chalcopyrite ratio—are examined. A Box-Behnken design (BBD) model is employed to analyse how these variables influence PLS production, utilizing MATLAB software (version R2022a, MathWorks Inc., Natick, MA, USA) to fit the most relevant interactions and factors (Quezada et al., 2024).

Methodology:

Materials

The minerals used in this analysis are chalcopyrite from Durango, Mexico, and pyrite from Huanzala, Peru, sourced from Ward's Science. The copper grade of chalcopyrite is 22.7%, while the iron grade is 17.7%. Pyrite has a grade of 27.9%. The chemical analyses were conducted using an Agilent Model 55B flame atomic absorption Spectrophotometer. Both minerals were crushed and pulverized to achieve particle sizes under 100 microns.

A sample cutter was utilized to obtain representative samples. The result was 20 samples, each weighing approximately 60 grams of the chalcopyrite and pyrite minerals.

Chalcopyrite and Pyrite particle size distribution

The size distribution of pyrite and chalcopyrite minerals was obtained using a Microtrac S350 with FLEX FBRM software, which provides a particle size distribution ranging from 0.00255 µm to 2000 µm. Figure 1 shows the particle size distribution with a P80 value corresponding to 12.48 µm for chalcopyrite, and Figure 2 shows the particle size distribution with a P80 value for pyrite of 24.43 µm.

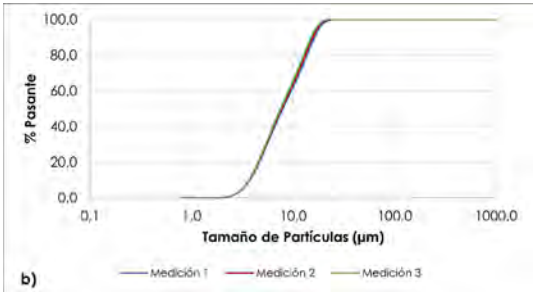

Figure 1 Particle size distribution Chalcopyrite

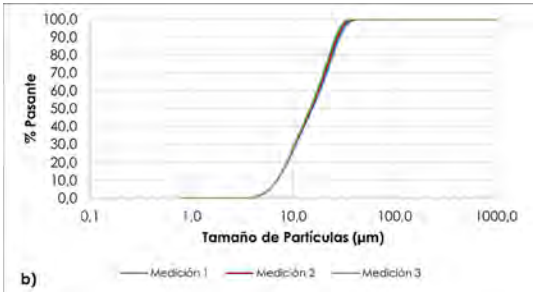

Figure 2 Particle size distribution Pyrite

Stirred leaching methodology

Leaching was conducted using stirred batch processes in 1.5 L jacketed glass reactors (see Figure 3). The jacket surrounding the reactor allows for water circulation to maintain a specific operating temperature, which is regulated by a thermoregulatory bath. Each reactor is equipped with a lid that has holes for periodic sampling of the solution, allowing for analysis of ion concentrations using atomic absorption spectrometry (AAS).

The leaching experiments were carried out with varying mass ratios of pyrite to chalcopyrite of 0.3:1, 0.5:1, and 1:1, along with ferric chloride concentrations of 6, 9, and 12 g/L. A solids to liquid ratio of 1:10 (mass/volume) was consistently maintained across all tests. The reagents used throughout the experiments remained constant and included: 90 g/L of sodium chloride $(NaCl)$, 0.52 g/L of potassium iodide (KI), and 26.3 g/L of sulfuric acid (H_2SO_4).

Mechanical stirring was maintained at 500 rpm, which was sufficient to keep the solids in suspension. The tests were conducted at temperatures of 20°C, 30°C, and 40°C.

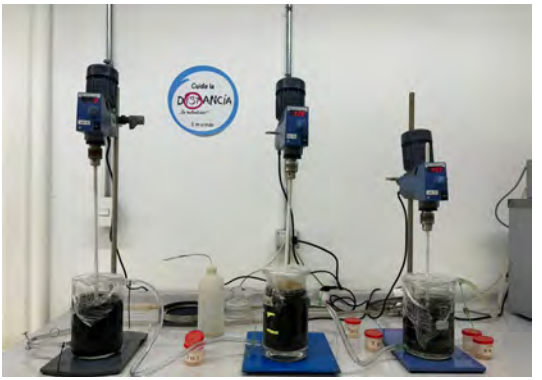

Figure 3 jacketed glass reactors

Box Behnken Experimental Desing and Surface Response Methodology

This study employed a combination of response surface methodology (RSM) to explore how different variables affect the key outcome—specifically, the concentration of cupric ions. RSM is a set of mathematical and statistical techniques used to model and analyse problems where several others influence one variable of interest. The objective was to optimize this key variable, as discussed by (Francisco et al. 2013).

The Box-Behnken design (BBD) was utilized, a well-established experimental approach that simplifies the process by reducing the number of experimental runs compared to traditional full factorial designs. This method ensures a uniform distribution of experimental points and helps minimize testing costs (Amenyeku et al., 2024).

Developed by George E.P. Box and Donald Behnken in 1960, the BBD is particularly useful for establishing cause-and-effect relationships. It combines a three-level factorial design with added center points, which assist in assessing experimental error and validating model accuracy. In each block of the experiment, certain factors are evaluated across all possible combinations, while others remain constant at their center levels (Wang & Wan, 2009).

The study applied Box-Behnken design consisting of 15 experimental tests, including three center points. Three independent variables were examined: temperature, the chalcopyrite to pyrite ratio, and the concentration of ferric chloride. The specific experimental combinations corresponding to this design are detailed in Table 1.

To analyse the results, a response surface methodology was used to develop a model through multivariate polynomial regression. This illustrates how the various parameters influenced the maximum cupric concentration achieved. This model was fitted to a second-order polynomial using Matlab software (ver. R2022a, MathWorks Inc., Natick, MA, USA) (Quezada et al., 2024).

$$Y = \beta_0 + \sum_{i=1}^{k} \beta_i X_i + \sum_{i=1}^{k} \beta_{ii} + X_i^2 + \sum_{i=1}^{k-1} \sum_{j=2}^{k} B_{ij} X_i X_j \quad (4)$$

In this equation, Y represents the response variable (the cupric ion concentration), X_i X_j are the independent variables, and k is the total number of independent variables (K=3). The coefficients β_o,β_i,β_ii and β_ij correspond to the linear, quadratic, and interaction effects.

To evaluate the reliability of the proposed model, the coefficient of determination R2 was calculated to indicate how well the model fits the actual data. The root mean square error (RMSE) was also determined to measure the discrepancy between the observed values and the model predictions, using MATLAB software's average of the squares. This comprehensive approach ensures that the findings are robust and informative.

Table 1. Box Behnken design of experiments

Test	Temperature (°C)	Pyrite/Chalcopyrite	$FeCl_3$ (g/L)
1	20	0.3/1	9
2	40	0.3/1	9
3	20	0.5/1	6
4	20	0.5/1	12
5	40	0.5/1	6
6	40	0.5/1	12
7	20	1/1	9
8	40	1/1	9
9	30	0.3/1	6
10	30	0.3/1	12
11	30	1/1	6
12	30	1/1	12
13	30	0.5/1	9
14	30	0.5/1	9
15	30	0.5/1	9

Results and Discussions

Stirred Leaching

Table 2 shows the results of copper concentrations in solutions. Chemical analyses were performed by atomic absorption spectrometry after 120 hours of leaching. The redox potential was measured on the Ag/AgCl scale.

Table 2. Leaching conditions for 120 hours.

Test	Temperature (°C)	Py/Cpy	$FeCl_3$ (g/L)	$[Cu^{+2}]$ (g/L)	V (volt)
1	20	0.3/1.0	9	3.22	0.40-0.44
2	40	0.3/1.0	9	7.53	0.45-0.46
3	20	0.5/1.0	6	2.29	0.40-0.44
4	20	0.5/1.0	12	2.20	0.39-0.46
5	40	0.5/1.0	6	8.96	0.45-0.46
6	40	0.5/1.0	12	8.78	0.43-0.44
7	20	1.0/1.0	9	2.56	0.42-0.46
8	40	1.0/1.0	9	4.74	0.42-0.45
9	30	0.3/1.0	6	4.28	0.42-0.46
10	30	0.3/1.0	12	4.84	0.42-0.45
11	30	1.0/1.0	6	3.65	0.42-0.45
12	30	1.0/1.0	12	4.34	0.48-0.49
13	30	0.5/1.0	9	4.37	0.46-0.48
14	30	0.5/1.0	9	4.76	0.47-0.48
15	30	0.5/1.0	9	4.57	0.47-0.48

As shown in Table 2, the highest copper concentration in solution after 120 hours was obtained in Experiment 5, reaching a value of 8.96 g/L of Cu^{2+}. This experimental condition corresponds to a temperature of 40°C, a pyrite/chalcopyrite (Py/Cpy) ratio of 0.5:1, and a ferric chloride concentration of 6 g/L. Experiments 2, 5, and 6 showed the highest Cu^{2+} concentrations, ranging from 7.5 to 8.96 g/L, demonstrating that a temperature of 40°C is a determining factor in improving chalcopyrite.
Increasing temperature increases the kinetic energy of molecules, which favors effective collisions between reactive species and, therefore, accelerates oxidation reactions.

From an electrochemical point of view, increasing the temperature can reduce the internal resistance of the system and improve ionic conductivity, allowing for more efficient charge transport of the different ions during the leaching process.

In contrast, Experiment 8, also conducted at 40°C, showed a considerably lower Cu^{2+} concentration (4.74 g/L), despite maintaining a constant temperature. In this case, the Py/Cpy ratio was 1:1, suggesting that an excess of pyrite, and therefore ferric ions in solution, could promote the formation of passive products on the chalcopyrite surface, inhibiting the leaching reaction.

Experiments with a $\mathbf{Py/Cpy}$ ratio of 1:1 and 20°C and 30°C temperatures yielded the lowest $\mathbf{Cu^{2+}}$ concentrations, ranging from 2.56 to 4.84 g/L. This is below the threshold of 7 g/L required to feed solvent extraction plants efficiently.

When analysing the effect of the pyrite/chalcopyrite ratio, it is observed that the highest $\mathbf{Cu^{2+}}$ values at 20°C and 30°C are reached with a ratio of 0.3:1. However, when the temperature is increased to 40°C, the maximum concentration is achieved with a ratio of 0.5:1.

The results regarding the ferric chloride concentration indicate that values of 6 or 9 g/L are sufficient to obtain $\mathbf{Cu^{2+}}$ concentrations suitable for feeding the solvent extraction plant.

Finally, the recorded redox potential values were below 0.5V (Ag/AgCl scale), within the range indicated by Zhao et al. (2016b) as favourable for the transformation of chalcopyrite to chalcocite, a key condition for efficient leaching.

Effect of variables on the concentration of cupric ions in solution

Figures 4, 5, and 6 represent the response surfaces showing the relationships between the cupric ion $\mathbf{[Cu+2]}$ in solution and the effect of these variables on agitation leaching over 120 hours. The model has only three significant factors: temperature, pyrite/chalcopyrite ratio, and ferric chloride concentration.

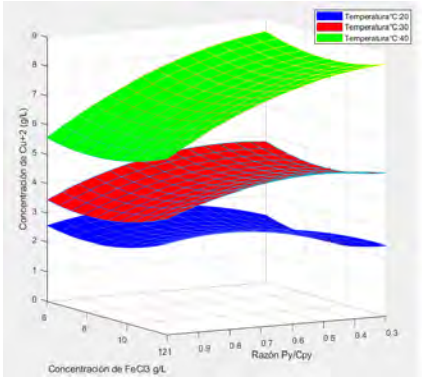

Figura 4 Ratio response Surface $\mathbf{Py/Cpy}$ and $\mathbf{[FeCl3]}$

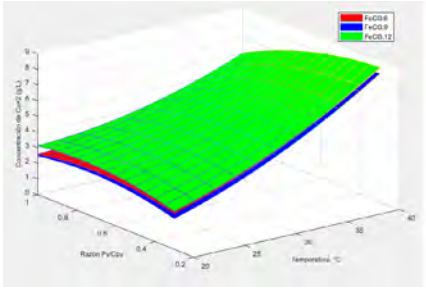

Figura 5 Ratio response Surface Temperature and $\mathbf{Py/Cpy}$

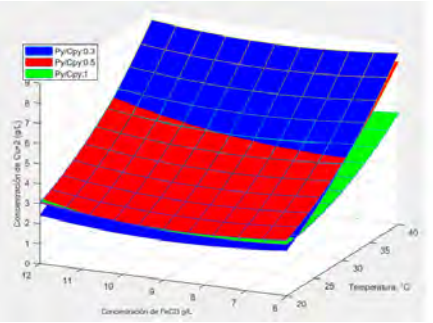

Figura 6 Ratio response Surface Temperature and $[FeCl3]$

Figure 4 shows the combined effect of the pyrite/chalcopyrite (Py/Cpy) ratio and ferric chloride concentration on the copper ion (Cu^{2+}) concentration at different temperatures.

The green surface (40°C) is much higher throughout the range, confirming that temperature is the most determining factor in copper dissolution.

The effect of $FeCl_3$ concentration is analyzed and it is observed that, increasing from 6 to 12 g/L, there is a slight increase in $[Cu^{2+}]$ at 30°C (red surface), while at 20°C and 40°C the impact is minimal. Analyzing the effect of the Py/Cpy ratio, it is evident that Cu^{2+} concentrations are lower at low pyrite concentrations (0.3/1) and (1/1).

However, at the pyrite/chalcopyrite ratio (0.5:1), dissolution is greatest where the highest copper concentrations are observed, especially at 40°C.

Analyzing Figures 5 and 6, as in Figure 4, it is observed that temperature remains the most determining factor in dissolution kinetics. Increasing the ferric chloride concentration offers a marginal benefit; however, the pyrite ratio of 0.5:1 is considered the most optimal, as it maximizes copper release thanks to its role in electrochemical coupling, favoring both the formation and decomposition of passivating layers on the chalcopyrite surface.

Figures 7 and 8 show the confidence level and root mean square error (RMSE).

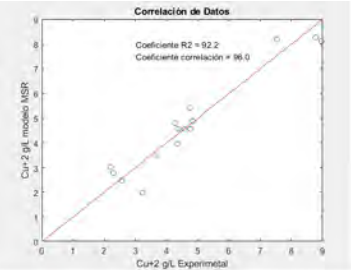

Figure 7 confidence coefficient: real data and model MSR

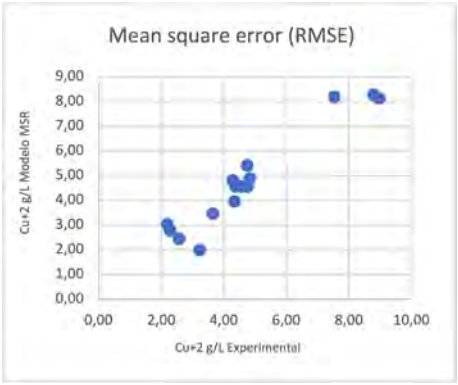

Figure 8 Mean square error RMSE

It can be seen that the predictive model shows high reliability with a correlation coefficient (R2) of 0.922 and a root mean square error (RMSE) of 0.57 g/L, indicating a high prediction of the cupric ion [Cu+2] values obtained in solution for the parameters of temperature, Py/Cpy ratio and ferric dosage used. The RMSE is an important tool for completing the Box-Behnken design (BBD) and making the statistical part more robust with the experimental tests obtained. Adjusting the model with the RMSE produces a reliable estimate of the values obtained from the cupric solutions, concerning the parameters studied in this research.

In a second stage, the proposed model will be validated with experimental tests, where conditions not included in the original set of tests are selected (e.g., T° = 35 °C, Py/Cpy 0.7/1 y $FeCl_3$ = 10 g/L).

Conclusions

This study evaluates the influence of salts and ferric ions in an acidic environment on the leaching of chalcopyrite, leading to several key conclusions. The results indicate that temperature is the most crucial factor influencing the dissolution of copper from chalcopyrite under the tested conditions. The highest copper concentration is achieved at a temperature of 40°C with a pyrite to chalcopyrite ratio of 0.5:1. Additionally, a ferric chloride concentration of 6 g/L at this temperature and ratio yields the most copper-rich solution, measuring 8.96 g/L. Furthermore, the redox potential observed during the experiments was consistently below 0.5 volts on the Ag/AgCl scale, aligning with previous research that suggests this is the range where chalcopyrite converts to chalcocite. The reliability of our model is confirmed by a correlation coefficient (R^2) of 0.922 and a root mean square error (RMSE) of 0.57 g/L, indicating strong predictive accuracy.

References

Amenyeku, G., Cobbina, S. J., Asare, W., & Teye, G. K., 2024. Hydrothermal carbonization of organic waste using faecal sludge as a water source: Response surface methodology-Box Behnken design. Environmental Challenges, 15, 100900. https://doi.org/10.1016/J.ENVC.2024.100900.

Bolorunduro, S. A., Dreisinger, D. B., & Van Weert, G., 2003. Fundamental study of silver deportment during the pressure oxidation of sulphide ores and concentrates. Minerals Engineering, 16(8), 695–708. https://doi.org/10.1016/S0892-6875(03)00164-X.

Box, G. E. P., & Behnken, D. W.,1960. Some New Three Level Designs for the Study of Quantitative Variables. Technometrics, 2(4), 455–475. https://doi.org/10.1080/00401706.1960.10489912.

Carranza, F., Palencia, I. and Romero, R.,1997. Silver catalyzed IBES process: application to a Spanish copper-zinc sulphide concentrate. Hydrometallurgy, 44(1–2), 29–42. https://doi.org/10.1016/S0304-386X(96)00028-X.

Cochilco, 2017. Sulfuros primarios: Desafios y oportunidades.

Dalton RF, Díaz G. and Price R.,1991. El proceso de extracción del metal cuprex : recuperación de cobre a partir de minerales de sulfuro.

Dutrizac, J. E., 1989. Elemental Sulphur Formation During the Ferric Sulphate Leaching of Chalcopyrite. Canadian Metallurgical Quarterly, 28(4), 337–344. https://doi.org/10.1179/cmq.1989.28.4.337.

Francisco, M.-C., Issam, H., Abdellatif, K., Abdallah, J. and Mohamed, B., 2013. Predicción de rugosidad en maquinado de compuestos con base de Peek usando metodología de superficie de respuesta. Ingeniería, Investigación y Tecnología, 14(4), 463–474. https://doi.org/10.1016/S1405-7743(13)72258-3.

Fukano, Y. and Miura, A., 2021. Chalcopyrite leaching with iodine (JX Iodine Process) for various ore types. Hydrometallurgy, 206, 105752. https://doi.org/10.1016/J.HYDROMET.2021.105752.

Granata, G., Miura, A., Liu, W., Pagnanelli, F. and Tokoro, C., 2019. Iodide-assisted leaching of chalcopyrite in acidic ferric sulfate media. Hydrometallurgy, 186, 244–251. https://doi.org/10.1016/J.HYDROMET.2019.04.019.

Hidalgo, T., Kuhar, L., Beinlich, A. and Putnis, A., 2018. Kinetic study of chalcopyrite dissolution with iron(III) chloride in methanesulfonic acid. Minerals Engineering, 125, 66–74. https://doi.org/10.1016/J.MINENG.2018.05.025.

Hyvärinen, O. and Hämäläinen, M., 2005. HydroCopperTM—a new technology producing copper directly from concentrate. Hydrometallurgy, 77(1–2), 61–65. https://doi.org/10.1016/J.HYDROMET.2004.09.011.

Liu, Y., Zhao, S., Wang, G., & Yang, H., 2025. Copper leaching from complex chalcopyrite-rich ores: Utilizing mechanical activation and wastewater-based sulfuric acid system. Separation and Purification Technology, 354, 128631. https://doi.org/10.1016/J.SEPPUR.2024.128631.

Li, Y., Kawashima, N., Li, J., Chandra, A. P., & Gerson, A. R., 2013. A review of the structure, and fundamental mechanisms and kinetics of the leaching of chalcopyrite. In Advances in Colloid and Interface Science (Vols. 197–198, pp. 1–32). Elsevier B.V. https://doi.org/10.1016/j.cis.2013.03.004.

Martínez-Bussenius, C. and Videla, Á., 2024. Iodide-assisted leaching of chalcopyrite concentrate in acidic chloride solution: Effect of different parameters on the copper extraction rate. Minerals Engineering, 213, 108752. https://doi.org/10.1016/J.MINENG.2024.108752

Moraga, G. A., Jamett, N. E., Hernández, P. C., Graber, T. A. and Taboada, M. E., 2021. Chalcopyrite leaching with hydrogen peroxide and iodine species in acidic chloride media at room temperature: Technical and economic evaluation. Metals, 11(10). https://doi.org/10.3390/met11101567.

Nazari, G., Dixon, D. G. and Dreisinger, D. B., 2011. Enhancing the kinetics of chalcopyrite leaching in the GalvanoxTM process. Hydrometallurgy, 105(3–4), 251–258. https://doi.org/10.1016/J.HYDROMET.2010.10.013.

Quezada, V., Roca, A., Benavente, O., Cruells, M., Keith, B. and Melo, E., 2020. Effect of pretreatment prior to leaching on a chalcopyrite mineral in acid media using NaCl and KNO3. Journal of Materials Research and Technology, 9(5), 10316–10324. https://doi.org/10.1016/J.JMRT.2020.07.055.

Quezada, V., Villagrán, G., Calisaya-Azpilcueta, D. and Marín, N., 2024. Effect of Pretreatment on a Copper Concentrate with High Arsenic Content. Minerals, 14(4). https://doi.org/10.3390/min14040419.

Salinas-Farran, L., Brownscombe, W., Iacoviello, F., Shearing, P. R., Brito-Parada, P. and Neethling, S. J., 2024. The impact of chloride ions on chalcopyrite leaching: A multiscale and multimodal assessment. Minerals Engineering, 213, 108762. https://doi.org/10.1016/J.MINENG.2024.108762.

Schmidt P, Backit A. and Jacob J., 2013. Tecnología hidrometalúrgica para la lixiviación de minerales sulfurados en medios clorados.

Velásquez-Yévenes, L., Nicol, M. and Miki, H., 2010. The dissolution of chalcopyrite in chloride solutions: Part 1. The effect of solution potential. Hydrometallurgy, 103(1–4), 108–113. https://doi.org/10.1016/J.HYDROMET.2010.03.001.

Wang, J. and Wan, W., 2009. Experimental design methods for fermentative hydrogen production: A review. International Journal of Hydrogen Energy, 34(1), 235–244. https://doi.org/https://doi.org/10.1016/j.ijhydene.2008.10.008.

Winarko, R., Dreisinger, D. B., Miura, A., Fukano, Y. and Liu, W., 2022. Iodine-assisted chalcopyrite leaching in ferric sulfate media: Kinetic study under fully controlled redox potential and pH. Hydrometallurgy, 208, 105797. https://doi.org/10.1016/J.HYDROMET.2021.105797.

Winarko, R., Dreisinger, D. B., Miura, A., Tokoro, C. and Liu, W., 2020. Kinetic modelling of chalcopyrite leaching assisted by iodine in ferric sulfate media. Hydrometallurgy, 197, 105481. https://doi.org/10.1016/J.HYDROMET.2020.105481.

Zhao, H., Wang, J., Gan, X., Hu, M., Tao, L. and Qiu, G., 2016. Role of pyrite in sulfuric acid leaching of chalcopyrite: An elimination of polysulfide by controlling redox potential. Hydrometallurgy, 164, 159–165. https://doi.org/10.1016/j.hydromet.2016.04.013.

Effect of Temperature on a Chloride Leaching Process of a Pretreated Cu-As Concentrate

Nicolás Emparán Chacana[1*], Víctor Quezada Reyes[1]

1. Departamento de Ingeniería Metalúrgica y Minas, Universidad Católica del Norte, Chile

**Corresponding author at: Departamento de Ingeniería Metalúrgica y Minas, Universidad Católica del Norte, Avenida Angamos 0610, Antofagasta 1270709, Chile, e-mail address: nicolas.emparan@alumnocs.ucn.cl.*

Introduction

Mining stands as a cornerstone of Chile's economic development, with copper production contributing over 40% of the nation's exports and serving as its primary source of income. Refined copper in Chile is obtained through both pyrometallurgical and hydrometallurgical routes. Globally, pyrometallurgy accounts for about 80% of copper production, involving comminution, froth flotation to yield concentrates, followed by drying, smelting to produce matte, slag, and sulfur dioxide (SO2) gases. This matte is then converted to blister copper, fire-refined to anodic copper, and ultimately electrorefined to high-purity copper cathodes. The conventional hydrometallurgical process, in contrast, comprises three main stages: leaching, solvent extraction, and electrowinning, which collectively produce high-purity copper cathodes from a pregnant leach solution (PLS).

A significant shift is underway in the Chilean copper industry. Projections from the Chilean Copper Commission (Cochilco) indicate a marked decrease in the hydrometallurgical copper production, from 25,8% (1,38 Mt) in 2022 to an anticipated 11,1% (0,713 Mt) by 2034, representing a substantial 48,4% reduction. This decline is primarily driven by the depletion of oxidized copper minerals, which have historically been amenable to hydrometallurgical processing. This fundamental, long-term strategic shift in the type of copper ore being exploited necessitates the development and optimization of processing technologies specifically tailored for these complex concentrates, as traditional hydrometallurgical approaches face underutilization.

While concentrate production is projected to increase by 42,2% between 2023 and 2034 (from 4,02 Mt to 5,72 Mt), this product presents a considerable challenge due to its impurity content, with arsenic being the most common. Concentrates containing more than 0,5% arsenic are classified as "complex concentrates". Arsenic-bearing minerals such as enargite (Cu3AsS4), tennantite (Cu12As4S3), and arsenopyrite (FeAsS) are prevalent in Chilean deposits. The presence of arsenic is problematic not only for metallurgical processes, but also for human health and the environment. The combination of declining oxidized ore reserves, increasing concentrate production, and severe economic penalties for arsenic impurities creates a strong economic imperative to find effective and environmentally sound methods for processing these complex concentrates.

Hydrometallurgical processes are considered environmentally benign and require lower capital investment compared to pyrometallurgical methods, positioning them as a promising alternative for treating complex concentrates. However, a significant challenge in the hydrometallurgical

processing of sulfide minerals is the slow dissolution kinetics. This is often caused by the formation of passivating layers, such as polysulfides (CuSn), elemental sulfur (S0), or insoluble sulfates (SO42-), which inhibit contact between the leaching solution and the mineral surface. To overcome these limitations, specific unit operations have been investigated. Acid curing, for instance, has been shown to accelerate copper extraction during leaching, inhibit the dissolution of certain silicates, and promote a homogeneous distribution of acid within the mineral bed. Similarly, the presence of chloride ions (Cl-) in the leaching process of copper sulfide minerals has been observed to enhance dissolution kinetics. This enhancement is attributed to the formation of metal-chloride complexes, morphological modifications of the mineral particles and their passivating layers, and alterations in the process electrochemistry. The existing literature on acid curing for complex copper concentrates is limited, with initial studies suggesting potential benefits but also indicating that early extractions might be linked to oxidized species rather than the primary sulfides. This highlights the need for further investigation into combining these beneficial strategies.

This research aims to address the aforementioned challenges by evaluating the effect of temperature and acid pretreatment (curing) on copper dissolution from a complex copper-arsenic concentrate in a chloride leaching process. The study's general objective is to assess the impact of temperature on copper dissolution from a complex copper concentrate, both with and without acid pretreatment, in a chloride leaching environment. To achieve this, specific objectives include: chemically and mineralogically characterizing the complex copper concentrate using techniques such as atomic absorption spectroscopy (AAS), X-ray diffraction (XRD), scanning electron microscopy (SEM), and Qemscan; analyzing the effect of pretreatment and temperature on copper extraction from the Cu-As concentrate; and quantifying the individual and combined impact of temperature and curing on concentrate leaching through an experimental design.

Methodology

Analytical grade reagents were used throughout the study to maintain purity and minimize experimental variability. Sulfuric acid was employed for both the agglomeration process and the subsequent leaching tests. Sodium chloride was specifically added to the leaching solutions to establish the chloride media. Distilled water served multiple purposes: for preparing all leaching test solutions, for moistening the agglomerates during the curing stage, and as the recirculating heat transfer liquid within the leaching system.

The experimental setup included specialized equipment designed for precise control and measurement. A drying oven was used to maintain a stable and consistent temperature for the formed agglomerates during the curing process. For the leaching experiments, jacketed glass reactors equipped with four-neck lids were employed. Temperature control within these reactors was achieved by recirculating heat transfer liquid from a thermostatic bath. For accurate monitoring of solution chemistry, pH and Eh were measured using research-grade laboratory meters connected to specific glass electrodes. The pH electrode and Eh electrode both featured a double reference cell (Ag/AgCl) and an internal KCl 3,5 M electrolyte. To ensure the solid material remained uniformly suspended within the leaching reactors, mechanical stirrers fitted with polytetrafluoroethylene (PTFE) propellers were utilized.

An initial mass of approximately 1 kg of copper concentrate was used in this study. To ensure sample homogeneity and representativeness, the bulk material was first homogenized and then systematically reduced to a 100 g representative mass. Subsequently, from this 100 g mass, precise 5 g representative samples were obtained using a Quantachrome Instruments micro-rotary splitter. These 5 g samples were then subjected to a comprehensive characterization to establish the baseline properties of the study material.

Five-gram samples of the prepared concentrate were carefully agglomerated. The use of Petri dishes was critical to preventing the evaporation of the liquid reagents during the curing phase. Following agglomeration, these dishes were placed in a drying oven set at a constant temperature of 50 °C for a duration of 15 days. A sulfuric acid concentration of 210 kg/t was applied during agglomeration, maintaining a precise solid-to-liquid ratio of 5:1.

Experiments were performed at four temperatures: 25, 50, 70, and 90 °C (± 1 °C). For each temperature, tests were conducted both with and without the acid pretreatment (curing) to enable direct comparison of its effect. The leaching experiments (Figure 1) were carried out in the 1 L jacketed glass reactors, where the 5 g concentrate samples were submerged in 500 mL of a lixiviant solution. The lixiviant was prepared with concentrations of 0,3 M H2SO4 (equivalent to 29,4 g/L) and 50 g/L Cl-. Agitation within the reactors was maintained at a constant speed of 300 min-1 using mechanical stirrers equipped with PTFE propellers to ensure uniform suspension of the solid material. Temperature within the reactors was precisely controlled by the thermostatic bath. Once the lixiviant solution reached the predetermined test temperature, the 5 g of concentrate (either cured or uncured) were added, marking the start of the 72-hour leaching period. To monitor the progress of copper dissolution, 5 mL aliquots of the solution were periodically extracted throughout the tests. These samples were immediately filtered through 0,2 µm filters, and their copper concentration was subsequently determined using AAS. Concurrently with sample extraction, both the redox potential (Eh) and pH of the solution were measured periodically. All Eh measurements were converted to values relative to the Standard Hydrogen Electrode (SHE) for consistency and comparability.

To quantitatively assess the impact of the studied variables on copper extraction, a significance analysis was performed using Minitab software. A general linear model was applied to the copper extraction data at each specific leaching time point. In this model, temperature and curing were designated as the independent factors, with copper extraction serving as the response variable. This statistical approach allowed for the quantification of the individual and combined contributions of these parameters to the overall copper dissolution.

The elemental chemical composition of the concentrate was determined using AAS. These analyses were conducted at the physical chemistry laboratory of the Biotechnology Center at the Universidad Católica del Norte. The mineralogical composition and characteristics of the concentrate were thoroughly investigated using three distinct analytical techniques, all performed at the MAINI Scientific Equipment Unit located at the Universidad Católica del Norte. XRD analysis was performed to identify the principal crystalline phases present in the concentrate sample. The resulting X-ray diffractograms were then interpreted with the aid of X'pert HighScore Plus software. A Qemscan analysis was conducted to provide a detailed identification and quantitative assessment of the elements and associated mineral species within the particles of the study material. The morphological characteristics of the particles within the concentrate were analyzed using SEM, which was complemented with EDS.

Results and Discussions

The chemical analysis of the concentrate, performed using AAS, provided a critical baseline for the study. The results show a CuT content of 35,57%, CuS of 1,580%, FeT of 12,98%, and a significant AsT content of 5,910%. The arsenic concentration of 5,91% unequivocally classifies this material as a complex concentrate, which is central to the research problem. The presence of 12,98% iron suggests the substantial presence of iron-bearing sulfide minerals, such as pyrite and chalcopyrite, within the concentrate.

Detailed mineralogical characterization, primarily through Qemscan analysis, revealed that the concentrate is predominantly composed of a tetrahedrite/tennantite/enargite group (35,93%), followed by pyrite (22,35%), chalcocite/digenite (16,55%), bornite (6,01%), chalcopyrite (4,66%), and covellite (3,98%). The contribution of copper by these different minerals is significant, with the tetrahedrite/tennantite/enargite group accounting for 43,00% of the total copper in the concentrate, and chalcocite/digenite contributing 34,12%.

XRD analysis corroborated these findings, confirming enargite as the predominant crystalline phase, followed by pyrite, chalcopyrite, digenite, bornite, and tennantite. This alignment between XRD and Qemscan results strengthens the confidence in the identified mineralogy. The arsenic detected in the chemical analysis is primarily associated with enargite, as expected. The presence of digenite might indicate surface oxidation of chalcocite (Cu2S) that occurred during the flotation process.

SEM analysis offered detailed morphological insights into the concentrate particles. At a 250 µm scale, observations revealed particles consistent with bornite, pyrite and enargite. Further magnification to a 25 µm scale confirmed a fully liberated enargite particle, with no other associated mineral elements detected across its composition. At a 50 µm scale, fully liberated pyrite and covellite were identified. Importantly, some enargite particles were observed to be not fully liberated, exhibiting lateral association with silicates and dissemination of aluminosilicates with a composition similar to topaz.

The experimental results for copper extraction from the complex concentrate without acid pretreatment (Figure 2) clearly demonstrated a direct relationship between increasing temperature and enhanced dissolution kinetics, ultimately leading to higher final copper extraction. During the initial hour of leaching, copper extraction ranged between 11% and 14% across all tested temperatures. However, beyond four hours, notable differences in extraction rates became apparent among the various temperatures.

At 25 °C, a final copper extraction of 36,7% was achieved. This value is likely associated with the dissolution of more reactive copper minerals such as chalcocite/digenite and covellite, which collectively contribute approximately 41,03% of the total copper in the concentrate. Observations indicated a passivation of these species between 48 and 52 hours, suggesting a kinetic limitation at this lower temperature.

Increasing the temperature to 50 °C resulted in a final copper extraction of 54,01%. This suggests a near-total dissolution of secondary sulfides, chalcopyrite, and bornite, which together account for 54,48% of the copper content. The rapid dissolution of secondary sulfides occurred between 8 and 24 hours, with chalcopyrite and bornite extraction completing by 72 hours. Passivation in these tests likely initiated between 8 and 24 hours, as evidenced by a clear reduction in the dissolution rate thereafter.

At 70 °C, a final copper extraction of 60,85% was attained. This indicates complete dissolution of copper from secondary sulfides, chalcopyrite, and bornite, along with approximately 6% dissolution of the more refractory enargite. The dissolution rate slowed significantly after 32 hours, a behavior consistent with the high activation energy characteristic of enargite dissolution. The highest copper dissolution without curing was observed at 90 °C, reaching 68,03%, which represents an 8% increase compared to the extraction at 70 °C. This data clearly demonstrates that significant enargite dissolution (6% at 70°C, 14% at 90°C) only occurs at higher temperatures. The observed passivation of even secondary sulfides at lower temperatures and the overall slow kinetics for

enargite suggest that temperature is not merely increasing the reaction rate but is fundamentally overcoming kinetic barriers, likely related to activation energy or the stability of passivation layers. This reinforces the understanding that for complex concentrates containing refractory minerals like enargite, high temperatures are indispensable for achieving commercially viable copper recoveries, even in a chloride medium known to enhance leaching. The study provides quantitative evidence for this necessity.

The results of the leaching tests with acid pretreatment (Figure 3) showed a consistent trend where increasing temperature led to an increase in both the dissolution kinetics and the final copper extraction, similar to the uncured tests. However, the primary differences were evident during the initial 8 hours of leaching, where copper extraction was higher for the acid-cured samples. This enhanced extraction in pretreated samples is mainly attributed to the sulfation of copper minerals, which generates more soluble products.

Specifically, at 25 °C, a copper extraction of 23,77% was achieved in the first hour, representing a 12,38% increase in dissolved copper compared to the uncured test at 25 °C. After 24 hours of leaching, the difference between both tests narrowed to 0.69% in copper dissolution, at which point the trends became practically identical. Similarly, at 50 °C, a copper extraction of 27,27% was reached after the first hour of leaching, which is a 16,45% increase in dissolved copper compared to the uncured test. This difference tended to decrease as the leaching process progressed, being only 2,24% after 24 hours. At 70 °C, copper extraction after the first hour of leaching was 29,12%, showing a 15,74% difference in copper extraction relative to the uncured test. After 32 hours of leaching, the difference in dissolved copper decreased to 0,41%. Finally, a similar trend was found for the tests conducted at 90 °C, where copper dissolution after the first hour of leaching was 30,68%, with an 18,92% difference for that time. The extraction difference also decreased over time, remaining between 2% and 3% from 48 hours onwards.

Regarding the pH and Eh (mV vs. SHE) measurements, at 25 °C, the pH value remained practically constant, suggesting a negligible acid consumption. Conversely, an increase in pH was observed in tests with temperatures above 25 °C, indicating greater copper dissolution during the leaching process. A maximum Eh of 728 mV (SHE) was observed for one test at 24 hours of leaching. The acid-pretreated samples generally exhibited a higher solution potential after the first hour of leaching compared to the uncured samples. This higher redox potential is primarily attributed to the formation of Cu^{2+} ions resulting from the dissociation of copper sulfates produced by acid curing, and the formation of $CuCl^{+}$ complexes.

The percentage contributions of the studied parameters (Figure 4) showed that in the first hour of leaching, copper extraction was predominantly influenced by curing (94,38%) and minimally by temperature (3,59%). This is due to the rapid dissolution of copper sulfates generated during the acid pretreatment stage. After 4 hours of leaching, curing and temperature showed significances of 60,87% and 28,94%, respectively. Thus, curing remained the factor with the greatest impact on copper extraction, although its significance began to decrease. After 8 hours of leaching, the percentage contribution of curing decreased to 31,95%, while that of temperature increased to 62,51%. Therefore, at some point between 4 and 8 hours of leaching, the significance levels in copper extraction inverted, and temperature began to be the factor with the highest percentage contribution compared to curing. This indicates the benefit of the curing stage, as it increases the dissolution kinetics during the initial 8 hours of the process. Finally, after 24 hours of the process, temperature and curing contributed 98,49% and 1,27% to copper dissolution, respectively. Observing subsequent times, it can be noted that curing practically no longer contributes to copper extraction, while temperature becomes the most significant parameter.

Conclusions

This research evaluated the effect of temperature on copper dissolution from a complex concentrate, both with and without acid pretreatment, in a chloride leaching process. The results obtained demonstrated that the leaching process can be a viable alternative for treating complex copper concentrates.

The chemical characterization of the complex concentrate indicated the proportion of Cu (35,57%), Fe (12,98%), and As (5,91%). Mineralogical characterization indicated the presence of enargite (35,93%), pyrite (22,35%), digenite (16,55%), bornite (6,01%), chalcopyrite (4,66%), covellite (3,98%), and other minor elements.

In the leaching tests at 25 °C and 50 °C, final copper extractions of approximately 37% and 54%, respectively, were achieved, so enargite dissolution could not be confirmed. At 70 °C and 90 °C, extractions of 61% and 69% of copper were achieved, respectively, being able to affirm that a proportion close to 6% and 14% of enargite, respectively, dissolved. The increase in temperature produced an increase in the copper dissolution kinetics for all leaching tests, while the curing effect was evident in the first 8 hours of leaching.

The significance analysis for copper extraction indicated that the most influential factor at the beginning of the process was the curing (94,38%), decreasing until 1,27% after 24 hours of leaching, while the temperature, for this same time, reached a contribution percentage of 98,49%, remaining practically invariable until finalizing the test.

Graphic Elements

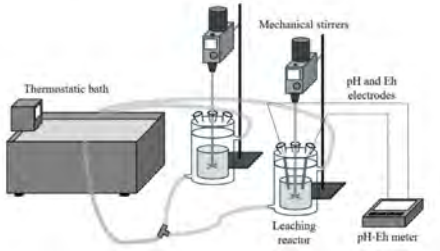

Figure 1. Agitated leaching system diagram.

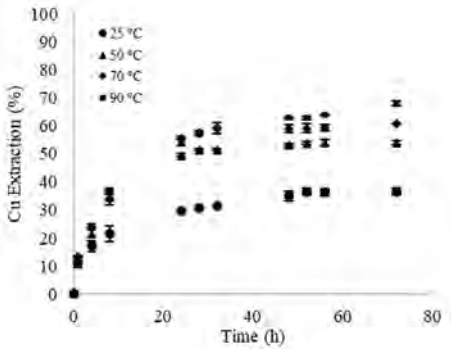

Figure 2. Copper extraction from complex concentrate without acid pretreatment

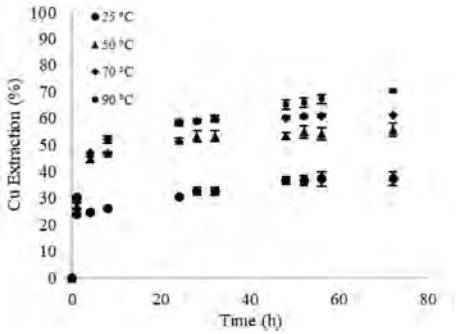

Figure 3. Copper extraction from complex concentrate with acid pretreatment.

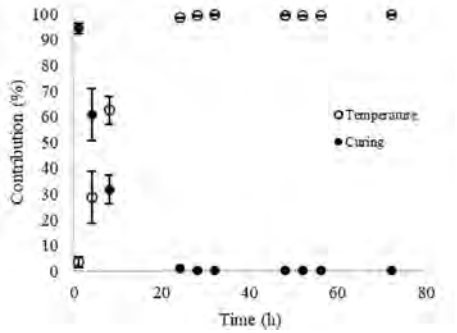

Figure 4. Percent significance of temperature and curing as factors in copper extraction as a response variable over leaching time.

References

Torres, C. M., Ghorbani, Y., Hernández, P. C., Justel, F. J., Aravena, M. I. and Herreros, O. O., 2019. Cupric and chloride ions: Leaching of chalcopyrite concentrate with low chloride concentration media. Minerals. 9 (10), 639.

Quezada, V., Villagrán, G., Calisaya-Azpilcueta, D. and Marín, N., 2024. Effect of Pretreatment on a Copper Concentrate with High Arsenic Content. Minerals. 14 (4), 419.

Abbas, S., Saqib, N. and Shahzad, U., 2024. Global export flow of Chilean copper: The role of environmental innovation and renewable energy transition. Geoscience Frontiers. 15 (3), 101697.

Carneiro, M. F. C. and Leão, V. A., 2017. The role of sodium chloride on surface properties of chalcopyrite leached with ferric sulphate. Hydrometallurgy. 87 (3-4), 73-82.

Fountain, C., 2013. The Whys and Wherefores of Penalty Elements in Copper Concentrates. Metallurgical Plant Design and Operating Strategies.

Gan, Y., Deng, R. and Liu, Q., 2022. Flotation Separation of Covellite and Enargite via Oxidation Treatment. Minerals. 12 (8), 970.

Nicol, M. J., 2017. The use of impedance measurements in the electrochemistry of the dissolution of sulfide minerals. Hydrometallurgy. 169, 99-102.

Zhao, H., Zhang, Y., Zhang, X., Qian, L., Sun, M., Yang, Y., Zhang, Y., Wang, J., Kim, H., & Qiu, G., 2019. The dissolution and passivation mechanism of chalcopyrite in bioleaching: An overview. Minerals Engineering. 136, 140-154.

Alam, M. A., Mukherjee, A., Bhattacharya, P., & Bundschuh, J., 2023. An appraisal of the principal concerns and controlling factors for Arsenic contamination in Chile. Scientific Reports. 13 (1), 11168.

Lu, J., Dreisinger, D., & West-Sells, P., 2017. Acid curing and agglomeration for heap leaching. Hydrometallurgy. 167, 30-35.
Castellón, C. I., & Taboada, M. E., 2023. Leaching of Copper Concentrates with Iodized Salts in a Saline Acid Medium: Part 2—Effect on Chloride Concentration and an Aerated System. Materials. 16 (17), 5940.

Moimane, T., Plackowski, C. and Peng, Y., 2020. The critical degree of mineral surface oxidation in copper sulphide flotation. Minerals Engineering. 145, 106075.

Miki, H., Nicol, M. and Velásquez-Yévenes, L., 2011. The kinetics of dissolution of synthetic covellite, chalcocite and digenite in dilute chloride solutions at ambient temperatures. Hydrometallurgy. 105 (3-4), 321-327.

Velásquez-Yévenes, L., Nicol, M. and Miki, H., 2010. The dissolution of chalcopyrite in chloride solutions: Part 1. the effect of solution potential. Hydrometallurgy. 103 (1-4), 108-113.

Yu, S., Liao, R., Yang, B., Fang, C., Wang, Z., Liu, Y., Wu, B., Wang, J. and Qiu, G., 2022. Chalcocite (bio)hydrometallurgy—current state, mechanism, and future directions: A review. Chinese Journal of Chemical Engineering. 41, 109-120.

Niu, X., Ruan, R., Tan, Q., Jia, Y. and Sun, H., 2015. Study on the second stage of chalcocite leaching in column with redox potential control and its implications. Hydrometallurgy. 155, 141-152.

Castellón, C. I. and Taboada, M. E., 2023. Leaching of Copper Concentrates with Iodized Salts in a Saline Acid Medium: Part 2—Effect on Chloride Concentration and an Aerated System. Materials. 16 (17), 5940.

Quezada, V., Roca, A., Benavente, O., Cruells, M., Keith, B. and Melo, E., 2020. Effect of pretreatment prior to leaching on a chalcopyrite mineral in acid media using NaCl and KNO3. Journal of Materials Research and Technology. 9 (5), 10316-10324.

Cacciuttolo, C. and Atencio, E., 2022. Past, Present, and Future of Copper Mine Tailings Governance in Chile (1905–2022): A Review in One of the Leading Mining Countries in the World. International Journal of Environmental Research and Public Health. 19 (20), 13060.

Martins, F. L. and Leão, V. A., 2023. Chalcopyrite bioleaching in chloride media: A mini-review. Hydrometallurgy. 216, 105995.

Taylor, P. R. and Putra, T. A. R., 2014. Pyrometallurgical Processing Technologies for Treating High Arsenic Copper Concentrates. Celebrating the Megascale. 197-211.

Gaussian Process Models Application to Surface Response Methodology, Analyzing Different Designs of Experiments on Flotation Laboratory Experimentation

Daniel Calisaya-Azpilcueta[1*], Felipe D. Sepúlveda[2,5], Lorena Cortes[3,4]

1. Departamento de Ingeniería Metalúrgica y Minas, Universidad Católica del Norte, Chile.
2. Departamento de Minas, Universidad de Antofagasta, Chile.
3. Departamento de Ingeniería Química y Procesamiento de Minerales, Universidad de Antofagasta, Chile.
4. Departamento de Ingeniería Industrial, Universidad de Antofagasta, Antofagasta, Chile.
5. Centro de Desarrollo Energético Antofagasta, Universidad de Antofagasta, Antofagasta, Chile.

**Corresponding author at: Departamento de Ingeniería Metalúrgica y Minas, Universidad Católica del Norte, Avenida Angamos 0610, Antofagasta, Chile, e-mail address: daniel.calisaya@ucn.cl*

ABSTRACT

This study investigates the empirical modeling of copper recovery from a Chilean ore, highlighting the challenges posed by variability in laboratory flotation tests. The research benchmarks four experimental design methodologies—simple factorial design, Box–Behnken design, central composite design, and full three-level factorial design—recognizing that liberation variability, sampling errors, and operational fluctuations contribute to unpredictable metallurgical responses. The copper ore, characterized by approximately 8 wt% Cu and a dominance of bornite, was subjected to milling and flotation to analyze recovery rates, which ranged between 79% and 91%, reflecting significant experimental scatter. To assess model effectiveness, two statistical approaches were employed: a quadratic response surface methodology (RSM) and a Gaussian-process (GP) surrogate model. The results demonstrated that the Box–Behnken and full factorial designs yielded statistically significant models. In contrast, the simple factorial and central composite designs did not capture effects at the tested noise level. Grind size emerged as the dominant factor influencing recovery rates, with the full factorial design revealing a significant linear relationship and the Box–Behnken design indicating curvature effects. However, the polynomial fits exhibited low predictive performance, suggesting weak generalization ability under prevailing variability, whereas the GP model closely matched observed recoveries with negligible errors for most runs. As such, the study highlights the need for a hybrid modeling approach—utilizing Box–Behnken or full factorial designs to capture nonlinear effects, fitting quadratic models for interpretability, and employing Gaussian processes for precise predictions and uncertainty quantification. This comprehensive strategy aims to provide robust guidance for experimental design and data interpretation in the context of copper flotation, ultimately enhancing the reliability of empirical modeling in metallurgical processes.

Introduction

Design of experiments (DOE) and response surface methodology (RSM) are established tools for building empirical models and guiding optimisation in mineral processing. Classical RSM applications typically presume a largely deterministic process; however, in metallurgical practice, many unit operations exhibit pronounced stochastic behaviour. Variability can arise from latent process fluctuations, sampling error, and analytical uncertainty, and it propagates along comminution–classification–flotation circuits. In laboratory copper flotation, for example, tests conducted at nominally identical setpoints may still yield different particle size distributions (P80), reflecting distinct liberation states; altered bubble–particle collision/attachment probabilities then translate into measurable differences in mass pull, copper recovery, and concentrate grade. In other words, comminution-driven variability introduces first-order uncertainty in flotation outcomes even under apparently controlled conditions.

Recent studies have highlighted the impact of uncertainty and complex spatial trends in the flotation process, particularly through the application of polynomial modeling, for example, in the research conducted by Arancibia-Bravo et al. (Arancibia-Bravo et al., 2021). It was found that when using seawater and kaolinite, there were significant spatial variations in the results compared to those obtained with pure minerals. This finding highlights the considerable impact of material choice on the performance of the flotation process.

In a follow-up study by Arancibia-Bravo et al. (Arancibia-Bravo et al., 2022), two geological units containing low-grade copper minerals with high clay content were assessed using seawater as a leaching agent. The observed spatial changes indicated a need for advanced techniques, such as geostatistics and neural networks, to accurately capture these variations.

Further exploring the theme of uncertainty, Delgado et al. (Delgado et al., 2021) demonstrated that different grinding methods and varying mineral types can lead to discrepancies in results, particularly in terms of uncertainty measures that do not align with the p80 values. This highlights how different conditions can affect the reliability of the results obtained.

Lastly, Sepúlveda et al. (Sepúlveda et al., 2024) examined the combined effects of uncertainty and spatial variability within a flotation cycle test. They utilized polynomial modeling to analyze these complexities, revealing that uncertainty plays a crucial role in shaping the results of response surface methodologies.

Despite the insights gained from these studies, a gap remains in the evaluation of different types of Design of Experiments (DoEs), leaving open the question of whether Bayesian best designs (BBDes) might offer better alternatives for addressing uncertainties in flotation processes.
This study addresses the challenge of modelling copper flotation under such uncertainty by comparing DOE alternatives and estimation approaches that differ in their statistical assumptions and representational capacity. We specifically seek to determine which combinations of design and estimator provide the most reliable empirical descriptions when randomness is non-negligible.

Methodology

The first part involves generating design alternatives. MATLAB® was used to enumerate operational settings for four DOE schemes: the Simple Factorial Design (SFD) (Fisher, 1935), Box–Behnken design (BBD) (G. E. P. Box & Behnken, 1960), Central Composite Design (CCD) (G. E. P. Box & Hunter, 1957), and a full three-factor, three-level factorial (FFD, 3^3) (Fisher, 1935). The controlled factors and levels are summarized in Table 1; levels were coded as −1, 0, and +1 for analysis.

Table 1. Factors and coded levels used in the DOE alternatives.

Parameters (units)	Levels		
	−1	0	+1
Particle size P80 (μm)	150	200	250
Frother dosage (g/t)	25	30	35
Collector dosage (g/t)	25	30	35

The different designs are presented in a 3-D configuration to get a better understanding of each design. Given that the variable with the higher supposed uncertainty is particle size, in the central composite design, it was assigned more repetitions, as shown in Figure 1. In all plots, factors are coded to the interval [−1,1] [−1,1] and mapped to the axes as p80 (particle size), Frother, and Collector. Simple Factorial Design (SFD) occupies only the eight cube. This placement isolates main effects and two-factor interactions at the extremes of the factor space, without intermediate or center levels. The dotted edges of the cube indicate the factorial contrasts along each axis; there are no interior points, so curvature cannot be resolved. Full Factorial Design (FFD, three levels) produces a uniform interior grid. The larger marker at the center highlights potential center-point replication. This dense, evenly spaced structure supports the estimation of linear, interaction, and pure-quadratic terms in all three factors, but at a higher run count than other response surface designs. Box–Behnken Design (BBD) places runs at the midpoints of the cube's edges plus replicated center points. In 3D, these locations trace a cuboctahedral network around the center, deliberately avoiding the eight extreme corners. The red, dotted connections between edge midpoints illustrate how BBD concentrates information in the central region and along pairwise factor planes, allowing for the efficient estimation of curvature without exposing the process to simultaneous extreme settings of all three factors. Finally, Central Composite Design (CCD superimposes a two-level factorial core (the cube vertices), center points, and axial (star) points. In 3D, the axial directions are represented by dotted lines through the center, and connecting the axial points forms an octahedral frame that emphasizes modeling near the center while still allowing for independent probing of curvature along each axis. Because particle size (p80) is the factor with the most significant expected uncertainty, additional replication was assigned along that axis and at the center to stabilize quadratic estimates and improve precision for that factor.

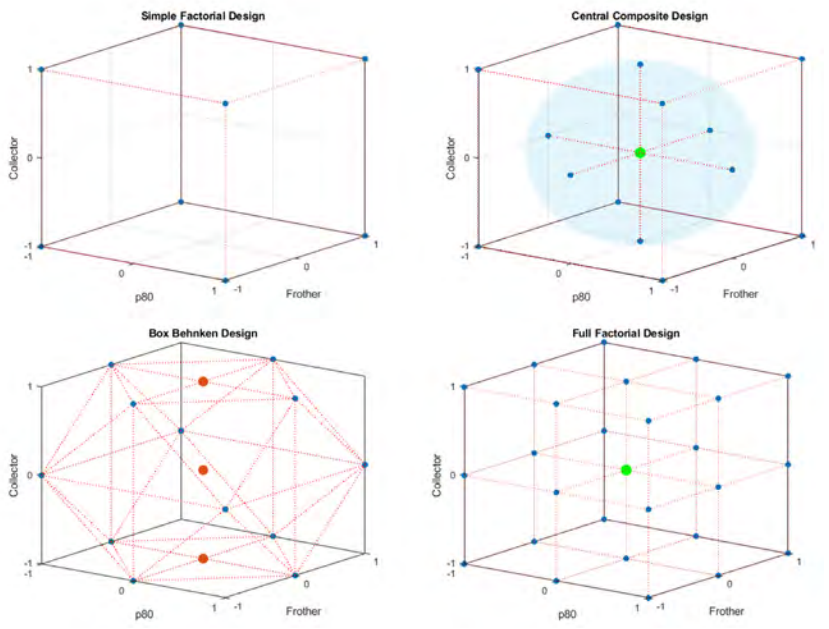

Figure 1. 3D representation of the four Design of Experiments.

After the design of experiments, the experimental campaign continues. Batch laboratory flotation tests were performed on a copper-bearing ore from the Second Region of Chile (feed grade ≈ 8 wt% Cu; F80 ≈ 1 mm), with bornite as the principal Cu mineral. Milling was carried out in a standard Hebro laboratory mill, and flotation was performed in a Metso D-12 mechanical cell. Runs were fully randomised within each design. The response recorded for each test was the copper recovery (%).

Statistical analysis was conducted in Design-Expert® (Anderson & Whitcomb, 2015) and MATLAB®. Two estimators were contrasted: a second-order polynomial (quadratic) RSM model (George. Box & Draper, 1987) and a Gaussian process (GP) model (Rasmussen & Williams, 2006). These alternatives differ fundamentally: the polynomial model provides a parametric mean structure with fixed basis functions (equation 1), whereas the GP specifies a stochastic prior over functions with covariance governed by a kernel (equation 2).

$$\hat{y} = \alpha + \sum_{i=1}^{q} \beta_i X_i + \sum_{i<j}^{q-1} \sum_{j}^{q} \beta_{ij} X_i X_j \qquad \text{Eq1.}$$

$$cov[y_i(x_i), y_j(x_j)] = \sum (x_i, x_j) \qquad \text{Eq2.}$$

Model performance is compared primarily via the coefficient of determination and its adjusted and predictive variants, mathematically represented as follows:

$$R^2 = 1 - \frac{SS_{residual}}{SS_{residual} + SS_{model}} \quad \text{Eq3.}$$

$$R^2_{adj.} = 1 - \frac{SS_{residual}}{df_{residual}\left(\frac{SS_{residual} + SS_{model}}{df_{residual} + df_{model}}\right)} \quad \text{Eq4.}$$

$$R^2_{pred.} = 1 - \left[\frac{PRESS}{SS_{residual} + SS_{model}}\right] \quad \text{Eq5.}$$

$$PRESS = \sum_{i=1}^{n} (e_{-i})^2 \quad \text{Eq6.}$$

$$e_{-i} = y_i - \hat{y}_{-i} = \frac{e_{-i}}{1 - h_{ii}} \quad \text{Eq7.}$$

As a practical diagnostic, R^2 adjusted and R^2 predicted should be in reasonable agreement (often within ≈ 0.20); larger discrepancies may indicate model misspecification or influential data. By juxtaposing DOE schemes of varying resolution (SFD, BBD, CCD, FFD) with both a deterministic quadratic and a stochastic GP-based estimator, this work provides a structured basis for selecting experimental designs and modelling approaches for copper flotation under appreciable process uncertainty.

Results and discussions

Four experimental designs were performed with three factors—collector dosage (A: 25–35 g/t), frother dosage (B: 25–35 g/t), and grind size P80 (C: 150–250 µm)—coded at three levels –1,0,+1-1, 0, +1–1,0,+1. Key descriptive statistics are summarized below:

- Simple factorial design (SFD) – 8 runs covering a 3^2 factorial over A and C (B fixed at its center). Recovery ranged from 79.4 to 90.0 %, with a mean of 84.39 % and a standard deviation of 3.25 %.
- Box–Behnken design (BBD) – 15 runs. Recovery ranged from 78.669 to 89.633 %, mean 85.37 %, SD 3.29.
- Central composite design (CCD) – 17 runs. Recovery ranged from 79.4 to 90.0 %, mean 85.15 %, SD 2.63.
- Full factorial design (FFD) – 32 runs. Recovery ranged from 78.7 to 91.2 %, mean 85.38 %, SD 2.99.

The response variability relative to the experimental range is modest (signal-to-noise ratios ≈1.1–1.2), indicating substantial run-to-run scatter.

An ANOVA test was conducted to determine the differences between the experimental results and the various polynomial models employed. Table 1 shows an ANOVA test that reveals apparent differences among the four designs. The BBD (p-value for the overall model = 0.047) and the FFD (0.048) deliver statistically significant quadratic surfaces, whereas the SFD (0.321) and CCD (0.616) do not. This pattern is consistent with the information content of each design: BBD and FFD provide sufficient support to estimate curvature reliably; SFD is underpowered (linear-only over two factors), and the implemented CCD did not produce a significant lack-of-fit signal or detectable curvature at the tested noise level.

Table 1. Anova for SFD, BBD, CCD, and FFD.

	SFD	BBD	CCD	FFD
Source	**p-value**	**p-value**	**p-value**	**p-value**
Model	0,321	0,047	0,616	0,048
A-col. (x1)	0,318	0,953	0,485	0,530
B-esp.(x2)	0,270	0,089	0,296	0,090
C-p80 (x3)	0,241	0,155	0,153	0,041
AB		0,121	0,489	0,141
AC		0,201	0,498	0,192
BC		0,363	0,299	0,811
A^2		0,031	0,894	0,034
B^2		0,439	0,493	0,601
C^2		0,039	0,795	0,222

Response-surface models of increasing order (Linear, two-factor interaction (2FI), Quadratic, and Cubic) were fitted for each design. Model quality was judged using the coefficient of determination (R^2), the adjusted R^2, and the predicted R^2. The adjusted R^2 penalizes extra terms that do not improve fit, while the predicted R^2 estimates the ability to predict new data.

SFD: The Linear model gave $R^2 = 0.546$, adjusted $R^2 = 0.206$ and predicted $R^2 = –0.816$. Higher-order terms (2FI) increased R^2 but degraded both adjusted and predicted R^2.
BBD: The Quadratic model had $R^2 = 0.609$ but adjusted $R^2 = –0.094$ and predicted $R^2 = –2.982$; adding cubic terms raised R^2 to 0.902 but severely worsened predicted R^2.
CCD: The Linear model performed best ($R^2 = 0.304$, adjusted $R^2 = 0.143$, predicted $R^2 = –0.349$); quadratic and cubic terms overfit the noise.
FFD: The Quadratic model gave $R^2 = 0.491$, adjusted $R^2 = 0.283$, and predicted $R^2 = –0.195$, making it the strongest among the four designs, yet its predictive ability remained poor.

These results indicate that none of the polynomial models demonstrated robust predictive capability; the low and often negative predicted R^2 values reflect the high experimental variability and the limited number of runs.

A non-parametric Gaussian process (GP) model was fitted to the same datasets. By construction, the GP's mean function adapts to pass through the observed data points, and the posterior uncertainty decreases near the observations. The results reveal that for most runs, the GP-predicted recovery equals the measured value to within machine precision. Only a handful of replicated center points show non-zero residuals (ranging from 0.055 to 1.55 percentage points). The Mean Absolute Error, and Root Mean Square Error for each design are:

SFD: MAE $\approx 1.6 \times 10^{-6}$; RMSE $\approx 1.7 \times 10^{-6}$.
BBD: MAE ≈ 0.28; RMSE ≈ 0.50.
CCD: MAE ≈ 0.07; RMSE ≈ 0.19.
FFD: MAE ≈ 0.18; RMSE ≈ 0.40.

These small residuals show that the GP faithfully interpolates the experimental data, except where replicate observations conflict; its in-sample accuracy far surpasses the polynomial models.

Figure 2 represents polynomial and Gaussian surfaces for each design (collector dosage held at its center level). In every surface, recovery decreases as P80 increases. This monotonic decline is smooth in the polynomial surfaces and appears consistently in the GP surfaces, although the latter may show local undulations near data points. Recovery peaks around the mid-level of frother dosage in some polynomial surfaces (reflecting a small positive quadratic term) but shows little systematic trend in others. GP surfaces often display local maxima or saddles aligned with replicate runs rather than genuine trends. Polynomial surfaces are globally smooth, reflecting only the estimated trends. GP surfaces contort to pass through the experimental points, sometimes producing sharp ridges or troughs at replicate locations. For instance, in the FFD GP plot, the surface rises steeply at some central points and dips at others, following measurement noise. This illustrates the difference between trend modeling (polynomials) and data interpolation (GP).

The polynomial models provide interpretability: coefficients for A, B, and C quantify main effects, interactions, and curvature; surfaces are smooth and suitable for optimization. However, in this case, their predictive power is weak due to high process variability and limited runs; negative predicted R^2 values warn against extrapolation. Conversely, the GP model shows excellent in-sample accuracy and can interpolate within the tested space. Yet, the exact fit can be misleading, as it mirrors noise and may imply spurious peaks and valleys. Because the GP lacks a simple summary statistic analogous to R^2, assessing its generalization requires cross-validation or additional experiments.

Conclusions

Polynomial response-surface modeling captures broad trends but exhibits poor predictive power. Linear and quadratic fits indicate that finer grinding (lower P80) consistently increases recovery, and frother and collector dosages have lesser effects. The full factorial quadratic model performs best among the designs but still yields a negative predicted R^2, indicating inadequate generalization.

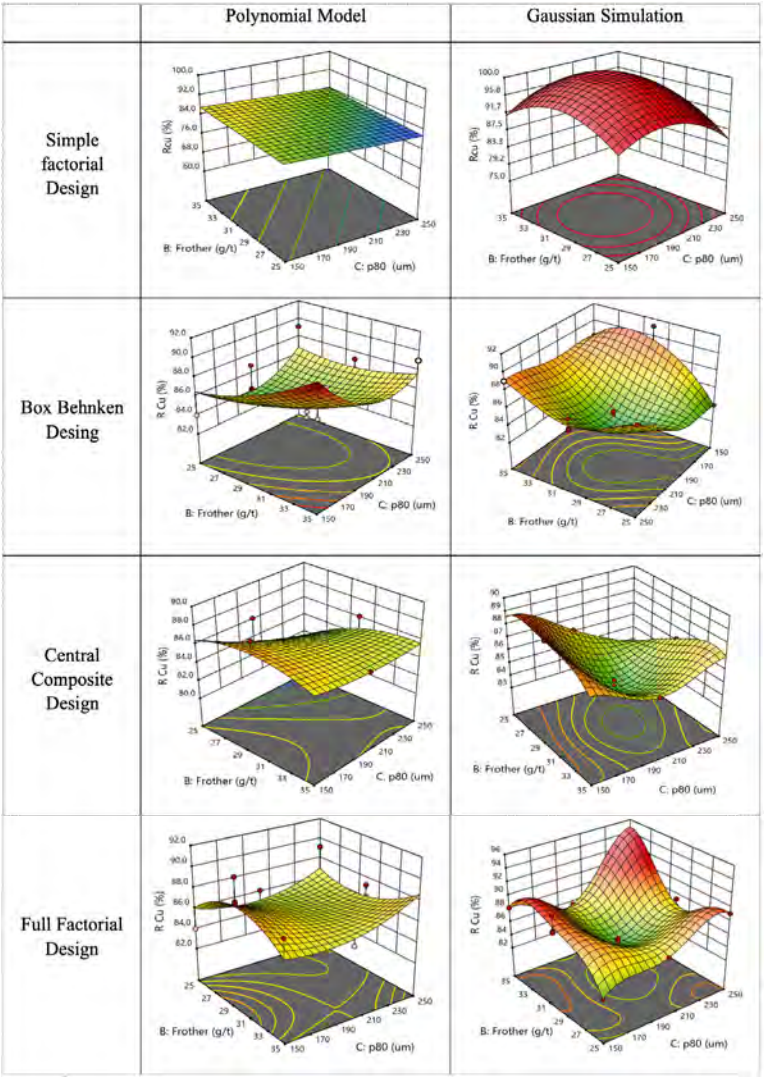

Figure 2. Comparison of polynomial and Gaussian Response surfaces for each DoE.

Gaussian-process modelling provides near-perfect interpolation at observed points, with mean absolute errors below 0.3 percentage points in the larger designs. Its surfaces represent every experimental value (except at conflicting replicates), offering a faithful in-sample representation. However, exact interpolation can be deceptive. By bending to match the data, the GP surfaces exhibit local peaks and troughs reflecting measurement noise rather than underlying process behavior. Without cross-validation or a predictive R^2 analogue, the GP reliability for untested factor combinations.

Practical recommendation: Use polynomial models to understand main effects and interactions and to guide factor screening and optimization, recognizing their limited predictive precision in noisy datasets. Use Gaussian-process models to interpolate between experimental points and to quantify uncertainty, but interpret their surfaces cautiously and complement them with additional replicate runs or cross-validation. A hybrid approach—trend estimation via RSM coupled with local refinement via GP—offers a balanced strategy for modelling flotation processes under uncertainty.

References

Anderson, M. J. and Whitcomb, P. J., 2015. DOE Simplified Practical Tools for Effective Experimentation (Third Edition). Productivity Press.

Arancibia-Bravo, M. P., Lucay, F. A., Sepúlveda, F. D. and Cisternas, L. A., 2021. On the use of Na2SO3 as a pyrite depressant in saline systems and the presence of kaolinite. Physicochemical Problems of Mineral Processing, 57(4), 168–179. https://doi.org/10.37190/ppmp/139511

Arancibia-Bravo, M. P., Lucay, F. A., Sepúlveda, F. D., Cortes, L. and Cisternas, L. A., 2022. Response Surface Methodology for Copper Flotation Optimization in Saline Systems. Minerals, 12(9), 1–20. https://doi.org/10.3390/min12091131

Box, G. E. P. and Behnken, D. W., 1960. Some New Three Level Designs for the Study of Quantitative Variables. Technometrics, 2(4), 455–475.

Box, G. E. P. and Hunter, J. S. 1957. Multi-Factor Experimental Designs for Exploring Response Surfaces. The Annals of Mathematical Statistics, 28(1), 195–241. https://doi.org/10.1214/aoms/1177707047

Box, George. and Draper, N. R. 1987. Empirical Model-Bulding and Response Surfaces (John Wiley & Sons).

Delgado, J., Lucay, F. A. and Sepúlveda, F. D., 2021. Experimental uncertainty analysis for the particle size distribution for better understanding of batch grinding process. Minerals, 11(8), 24. https://doi.org/10.3390/min11080862

Fisher, R. A., 1935. The Design of Experiments (Vol. 1). Oliver and Boyd.

Rasmussen, C. Edward. and Williams, C. K. I., 2006. Gaussian processes for machine learning. MIT Press.

Sepúlveda, F. D., Cortes, L. A., Arancibia-Bravo, M. P., Delgado, J., Lucay, F. A., Chacana, C., Galleguillos, F. and Castellón, C., 2024. Optimizing flotation circuits: A comprehensive approach using design of experiments and stochastic simulation in cycle test validation. Minerals Engineering, 1| – 24. https://doi.org/10.1016/j.mineng.2024.108978.

Microwave Effect on a Refractory Ore of Au With Preg-Robbing

Vanesa L. Bazan[1], Ayelen Lopez[1], Ivana Orozco[2], Luis Rojas[3], Gastón Villafañe[1]

1. CONICET, IIM, F.I. UNSJ. Av. Libertador General San Martín 1109 (O) Capital, San Juan, Argentina
2. IIM, F.I. UNSJ. Av. Libertador General San Martín 1109 (O) Capital, San Juan, Argentina
3. School Of Construction And Transportation Engineering, Pontifical Catholic University Of Valparaíso, Valparaíso 2362804, Chile

bazan@unsj.edu.ar

ABSTRACT

The minerals of gold currently have an increasingly complex chemical composition due to the characteristics of the ores. Species of precious metals in their native state are increasingly scarce. Said mineralogical complexity gives way to refractoriness phenomena; problems arising from refractory gold have the following causes such as the physical encapsulation of disseminated gold particles (usually smaller than a few micrometres in size) within a non-reactive mineral immune to leaching due to chemical interference by one or several of the components in the cyanide leaching process.
In a conventional cyanidation there is a notable reduction in the dissolution of the values of the metals of interest, known as the Preg-Robbing effect, which the granulometry (at a smaller particle size or its equivalent to a higher mesh number) can modify its recovery percentage. using different techniques such as calcination and subsequent extraction of gold by cyanidation, obtaining a positive gradient in the extraction.
This has prompted the study of new technologies or alternatives focused on the treatment of difficult-to-recover minerals, among which is the processing applying microwaves (MW) on refractory minerals. In this case, this type of radiation has potential application in mineral treatment and metal recovery processes.
In this work, it is proposed to treat a refractory-type mineral and submit it to microwave treatment, which will cause micro-fractures due to its electromagnetic vibrations and provide paths for the extraction of desirable metals, thus increasing metalliferous recovery, including those found in extremely low or encapsulated contents.
For the recovery of high value products or the treatment of low tonnage materials, microwave energy can offer a considerable advantage over the conventional process. This also allows taking advantage of the technique to reduce emissions into the environment and increase the performance of the process itself, providing an opportunity for improvement to the extractive metallurgy industry in the country.

Introduction

Gold is a highly stable precious metal and can be obtained from minerals that can be classified as non-refractory grinding ores and those minerals called refractory. The latter are those that are difficult to treat for gold liberation by conventional methods such as cyanidation [1]. The limited

extraction of gold from these minerals occurs due to the preg-robbing effect, which is defined as the adsorption of gold-cyanide complexes formed during leaching [2-4]. The preg-robbing effect depends on the nature of the refractory mineral, and therefore its characterization is essential. The preg-robbing capacity of refractory minerals containing carbonaceous materials has been identified as related to the maturity of the organic carbon structure on a scale from amorphous to graphitic [4, 5].

In this regard, alternative treatment routes that aid cyanidation have been proposed, such as the use of microwave systems. Microwave heating depends on the mineral's composition, and thus elemental substitutions would affect a mineral's behavior in an electric field. The interaction of microwaves with minerals is poorly understood. Therefore, understanding how microwave energy interacts with minerals is key to unlocking the technology for use in the mineral processing industry. Nanthakumar et al. investigated microwave heating of a refractory gold ore as an alternative method and compared the results with those obtained by conventional methods. Indirect microwave heating removed approximately 94% of the organic carbon, resulting in recoveries of over 98% after cyanide leaching. [6]

Walkiewicz et al. demonstrated that rapid heating of ore containing microwave-absorbing minerals in a non-absorbing gangue matrix generates thermal stress. This thermal stress caused microfractures along mineral grain boundaries; as a result, the ore sample became more amenable to leaching. [7]

A literature review reveals Figure 1, which presents an evidence map relating process variables (frequency, power, time, specific energy, additives use, and dielectric behavior) to measure outcomes (improved gold recovery, reduced preg-robbing, improved milling, decreased energy consumption, and reporting of dielectric properties). The colored boxes indicate the intensity of the evidence (0 = not reported; 1 = positive effect).[6-9]

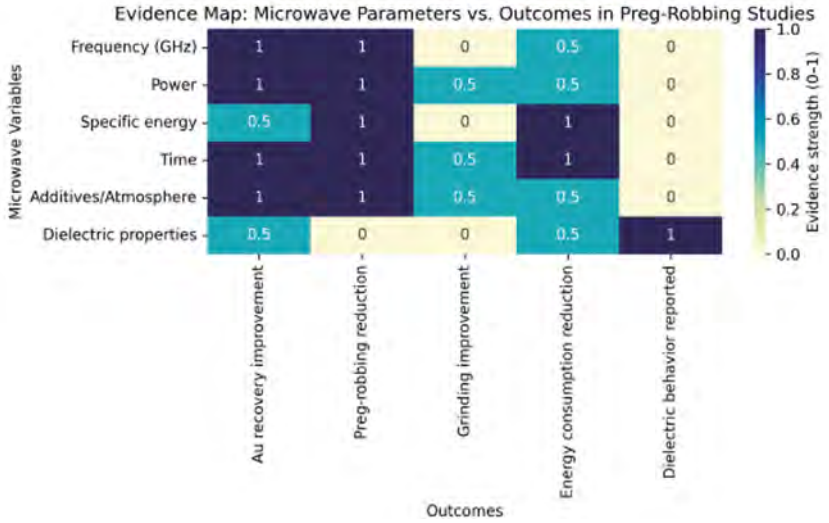

Figure 1: Evidence map linking microwave variables to metallurgical results reported in the literature.

This work proposes the treatment of two gold-bearing ores, which are classified as refractory due to the presence of carbonaceous species in their mineralogy, which prevents high recoveries of Au.

Methodology

Two refractory samples with pre-robbing are being processed. One with the STGO designation and the other with the MO-UG designation. Both samples come from porphyries containing Au and Ag minerals, which have previously been cyanided, resulting in very low Au recoveries.

The following sample treatment scheme is planned:

Mineralogy analysis

Diffractometers were performed on the head samples.A Shimadzu model 6100 X-ray diffractometer was used.

Chemical Analysis

A chemical characterization of the heads is performed to determine the chemical composition of the samples to be studied.

A portion of approximately #100 minerals were prepared for mineral analysis, where the following elements were determined: Au, Ag, Total Carbon, and Organic Carbon.

Au and Ag analyses were performed using the Fire Assay method, while metal analyses were performed by acid digestion and subsequent reading by AA, Perkin Elmer PinaAcle 900T.

Regarding Carbon, the analyte is analyzed by its decomposition product, which volatilizes at an appropriate temperature. The residue is weighed, and the difference is determined by the carbon weight.

Heat Treatment

Both samples were subjected to microwave treatment (MW) in Teflon crucibles. The treatment sample was 10 g with a 10/1 (S/L) H2O ratio.

The samples were subjected to various operating variables within the microwave, such as exposure time of 5 to 30 minutes and wattage of 90 to 900 W.

Cyanide Leaching.

Test (TMW+ Cyanidation): After heat treatment, the Santiago samples performed better at 900 W for 5 min.

While the MO-UG samples performed better at 750 W for 10 min. Based on these values, they were subsequently subjected to cyanide leaching as described.

A 100 g sample was subsequently weighed for the cyanidation process, with the sample being conditioned with lime until reaching a pH of 10.5, with a S/L ratio of 0.5, a concentration of CN:1000 ppm, and a duration of 72 hr. At the end of the test, the Au and Ag concentrations were analyzed by direct reading using the AA, Perkin Elmer PinAcle 900T.

Results and Discussions

In the Figure 2 the characterization of the samples by XRD is shown to MO-UG and STGO, respectively; in the MO-UG sample, the presence of Quartz (SiO2), Berlinite (AlPO4), Graphite (C), Birnshesite ((Na)0.5(Mn)2º4 ·1.5H2O), Calcite (CaCO3), Pyrite (FeS2), and Illite (K0.65Al2.0[Al0.65Si3.35º10](OH)2) was determined.In the STGO sample, the presence of Calcite (CaCO3), Berlinite (AlPO4), Quartz (SiO2), Chalcopyrite (CuFeS2), Illite (K0.65Al2.0[Al0.65Si3.35º10](OH)2), and Calaverite (AuTe2) was determined.

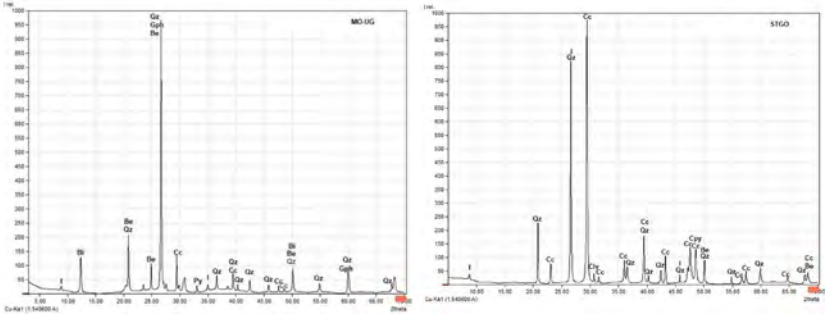

Figure 2: Diffractograms corresponding to the MO-UG and STGO samples

Through chemical analysis we can determine the laws of the noble metals as well as the refractory elements in the mineral, as shown in Table 1.

Table1: Chemical composition of the samples

	Conc.	MO-UG	STGO
Au	g/t	2,10	3,97
Ag	g/t	3,80	19,53
C. Org.	%	6,29	1,35
S	%	3,92	0,34

According to the characterization studies we can observe that the samples have a refractory character both in the presence of S and C.org, which is the cause of the preg-robbing effect.

The samples are subjected to a microwave thermal treatment which demonstrates that as power is applied to the sample, its temperature increases linearly, up to a power at which it reaches an asymptote, as shown in Figure 3.

Once the power levels at which the maximum exposure temperature is reached have been identified, an analysis is made to determine whether the exposure time influences the temperature within the sample, as shown in Figure 4 and Figure 5.

With the data obtained, we proceed to work with two defined parameters: Sample MO-UG at 900W and Sample Stgo at 750W, at a time of 5 minutes in both cases, and then proceed to perform cyanidation leaching tests.

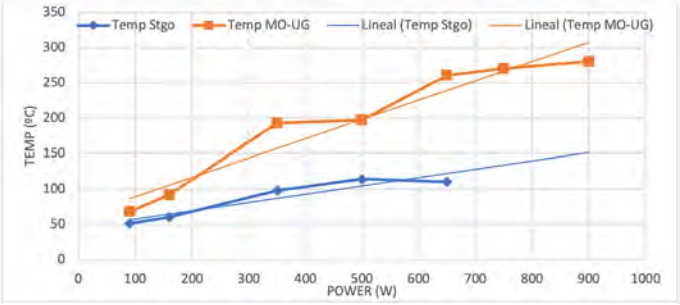

Figure 3- Power – Exposure Temperature Relationship

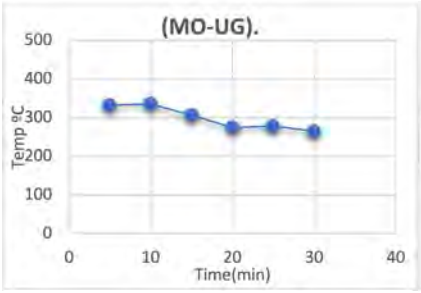

Figure 4- Power ratio 900 W–Exposure time in MO-UG sample

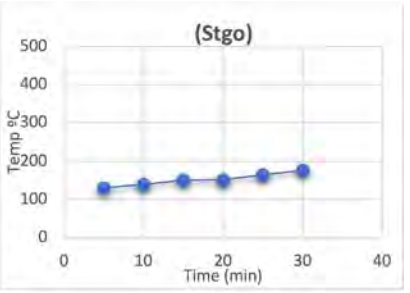

Figure 5- Power ratio 750 W–Exposure time in Stgo sample

The temperature generated during microwave heating is significantly influenced by the mineral types of responses to microwaves. The refractory gold ore used in this study consists primarily of quartz, berlinite, and graphite, with minor amounts of pyrite. Previous research reported that pyrite and chalcopyrite minerals generated temperatures of 670°C and 780°C when heated at 900 W for 1 min [10]. Therefore, the MOUG sample was subjected to a power of 900 W in 5 minutes. According to Lovas et al [10]., during the roasting process, the transformation of sulfide minerals into oxide minerals altered their response to microwaves. In the current work, it was observed that heating at 900 W generated temperatures no greater than 350°C. The generated temperature was related to the decomposition of sulfide minerals into oxides, especially the change in pyrite.

While the Santiago Sample according to figures 3 and 5, it can be determined that the exposure temperature reached does not exceed 150°C. Therefore, it is decided to use a power lower than 750 W.

The study by Díaz et al. (2016), measured the complex permittivity of pyrite samples as a function of temperature and found that both the real part ϵ' and the imaginary part ϵ'' (or tan δ) follow a Gaussian correlation with a coefficient of determination R2 > 0.995.[9] This behavior implies maximum energy absorption at intermediate temperatures and explains why microwave roasting drastically reduces processing time and energy consumption. Figure 6 illustrates a representative trend based on these results, showing that both samples reach their maximum absorption temperature with the effect of microcracking.

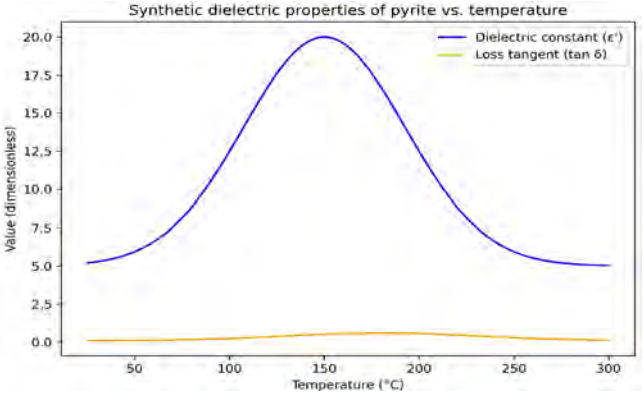

Figure 6: Synthetic dielectric landscape showing the variation of the actual permittivity ϵ' and the loss factor tan δ of pyrite with temperature. The maxima indicate temperatures where microwave absorption is most efficient

The mechanisms that explain the observed effects are summarized in Figure 7. Selective irradiation of sulfides and carbonaceous matter generates localized heating and thermal gradients that induce microcracks, increase porosity, and facilitate the diffusion of leaching solutions. In doubly refractory ores with carbonaceous matter,.

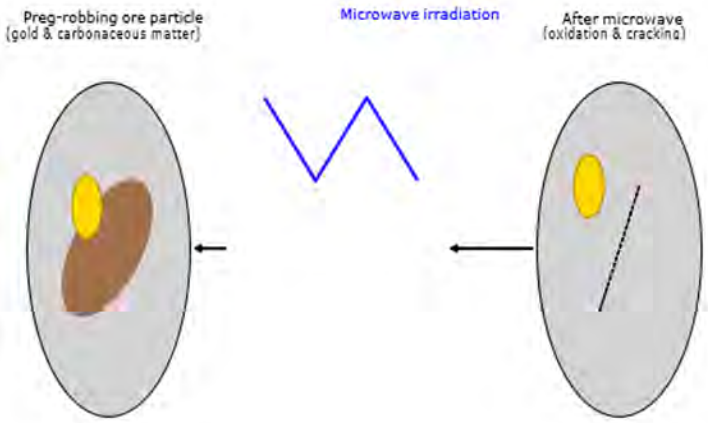

Figure. 7 Conceptual diagram of the mechanisms associated with microwave treatment of preg-robbing ores. Irradiation generates microcracks, oxidizes or passivates the carbonaceous material, and releases the encapsulated gold.

The structural study is completed by scanning electron microscopy (SEM) including EDS analysis. In Figure 8a , multiphase particles (white, light gray and dark gray phases) are identified. The white phase particles show considerable disintegration and stratification, giving rise to the formation of fibers that constitute the most abundant proportions of fines in the sample. In Figure 8b, at higher magnification, the appearance of the particles presents in the sample subjected to heat treatment can be observed. It is verified that the white phase particles present internal microcracks and decohesion (which justify the disintegration mechanism and stratification observed in previous images. This possibly gives rise to the formation of fibers that constitute the fines in the sample.

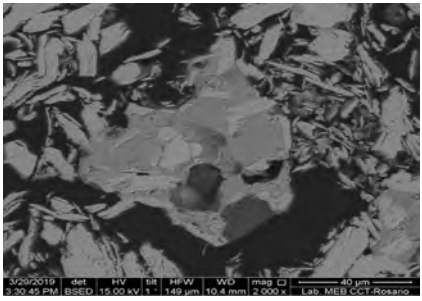

Figure 8a. Appearance of the particles at high magnifications.

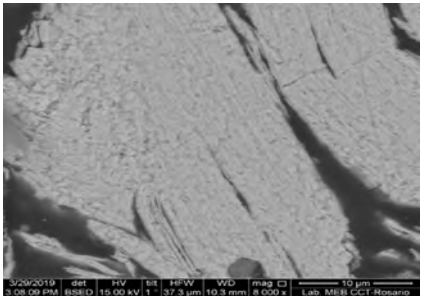

Figure 8b. Appearance of cracked and stratified white phase particles

The cyanidation recovery results for Au are described in Figure 9. Where the cyanidation treatment (CONV) and the sample subjected to microwave treatment plus the cyanidation process (TMW+Lix) can be observed.

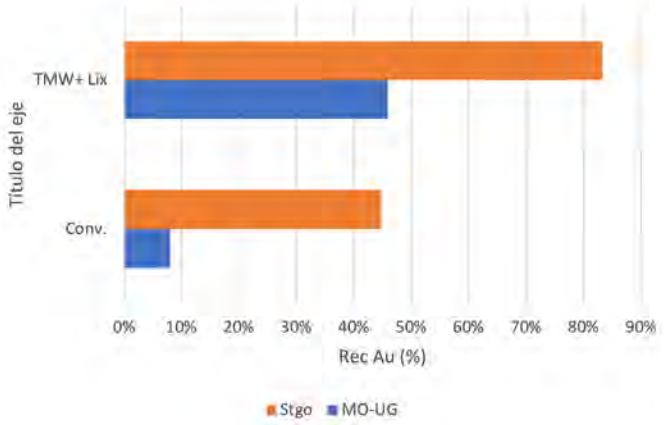

Figure 9: Au recovery by cyanidation , microwave treatment(TMW)+cyanidation

A mineral leaching process was performed with thermal pretreatment and a substantial improvement in gold extraction was found, Figure 9. It can be inferred how the reaction of sulfur with oxygen generates a change in the structure of the ore allowing metal values to be reached by the leaching reagent. The trend of the leaching process indicates that with enough time it is possible to achieve the extraction of the gold in the sample.

It is important to note that, as a relatively simple infrastructure, its implementation in small-scale mining processes would be a cost-effective option for these producers.[11] As can be seen in the results of the leaching process, Figure 9, a good part of the gold is encapsulated(CONV), which makes it a limitation for its extraction.[12 -14]

Microwave treatment is not a gold recovery method, but rather a concentrating agent. Its purpose is to break down the physical and chemical barriers that cause refractory gold to be released, and through a conventional chemical process such as cyanidation, achieve improved recoveries ranging from 8% to 45% in the same time period for the MOUG sample due to its dual refractoriness. Meanwhile, for the STGO sample, improved recoveries range from 45% to 83%, attributed to the microfracture studies presented.

Finally, additional studies are required from a chemical engineering perspective to analyze other factors such as the effect of ore agitation, residence times, and particle size, among others.

Conclusions

The microwave effect is an effective pretreatment for gold extraction in refractory minerals. With sufficient exposure time for each type of gold ore in the microwave, it is possible to reach an energy absorption temperature, which subsequently creates microfractures. This facilitates gold leaching with cyanidation, achieving the extraction of 45% gold in the MO-UG sample and 83% in the Stgo sample.

The results of this study demonstrate the effectiveness of microwave thermal treatment, making it a more cost-effective option for gold production from refractory minerals.

The applicability of the treatment is because, even in difficult-to-access conditions, where fuels, furnaces, and robust equipment are unavailable, obtaining electrical energy from other sources (solar energy) and applying microwave treatment to the ore on a small scale would be sufficient.

Additional analyses are required from a chemical engineering perspective to complement the results of this initial approach to the problem in small-scale metallurgical mining projects.

References

M. Helm, J. Vaughan, W. Staunton and J. Avraamides. 2009. "An investigation of the carbonaceous component of preg-robbing gold ores," in World gold conference,pp. 139-144.

P. Afenya.1991. "Treatment of carbonaceous refractory gold ores," Minerals Engineering, vol. 4, no. 7-11, pp. 1043-1055.

O. P. Karthikeyan, A. Rajasekar, and R. Balasubramanian. 2015. "Bio-oxidation and biocyanidation of refractory mineral ores for gold extraction: a review," Critical Reviews in Environmental Science and Technology, vol. 45, no. 15, pp. 1611-1643.

W. S. Ng, Q. Wang and M. Chen. 2020. "A review of Preg-robbing and the impact of chloride ions in the pressure oxidation of double refractory ores," Mineral Processing and Extractive Metallurgy Review, pp. 1-28.

R. Santiago and A. Ladeira. 2019. "Reduction of preg-robbing activity of carbonaceous gold ores with the utilization of surface blinding additives," Minerals Engineering, vol. 131, pp. 313-320.

Nanthakumar, B., Pickles, C. A. and Kelebek. 2007. Microwave pretreatment of a double refractory gold ore.Minerals Engineering, 20(11):1109–1119.

J.W. Walkiewicz, G. Kazonich, S.L. McGill. 1988. Microwave heating characteristics of selected minerals and compounds. Mineral and Metallurgical Processing, 5 (1), 39–42.

Amankwah, R. K., Pickles, C. A. and Yen, W. T. 2005. Improved grindability and gold liberation by microwave pretreatment of a free-milling gold ore. Mining Technology (Trans. Inst. Min. Metall. A), 114(2):79–88.

Díaz, M., Amaya, I. and Correa, R. 2016. Microwave enhanced roasting for pyrite ore samples with dielectric properties strongly dependent on temperature. Ingeniería y Universidad, 20(1):63–84.

Lovás, M., Znamenáčková, I., Zubrik, A., Kováčová, M. and Dolinská, S. 2011. The application of microwave energy inmineral processing–a review. Acta Montanistica Slovaca, 16(2),137-148.

Zhang, X., Kou, J., & Sun, C. 2019. A comparative study of thethermal decomposition of pyrite under microwave and conventional heating with different temperatures. Journal ofAnalytical and Applied Pyrolysis, 138, 41-53.

Uslu, T., Atalay, Ü. and Arol, A. I. 2003. Effect of microwaveheating on magnetic separation of pyrite. Colloids andSurfaces A: Physicochemical and Engineering Aspects, 225(1-3),161-167.https://doi.org/10.1016/S0927-7757(03)00362

Eymery, J. P. and Ylli, F. 2000. Study of a mechanochemicaltransformation in iron pyrite. Journal of alloys andcompounds, 298(1-2), 306-309.

Baláž, P., Achimovičová, M., Bastl, Z., Ohtani, T. and Sanchez, M. 2000. Influence of mechanical activation on the alkaline leachingof enargite concentrate. Hydrometallurgy, 54(2-3)

Roasting with Carbothermal Reduction of Molybdenum-Rhenium Sulfide Ore

Orozco, Ivana[1*], Bazan Vanesa[1], Brandaleze, Elena[2], Oieni Martin[1]

1. Mining Research Institute (IIM), Faculty of Engineering, National University of San Juan, Argentina.
2. Department of Metallurgy, Faculty of Engineering, National Technological University of San Nicolás, Argentina.

**1Mining Research Institute (IIM), Faculty of Engineering, National University of San Juan, Argentina.*
iorozco@unsj.edu.ar.

ABSTRACT

Carbothermal reduction is an alternative method for treating sulfide concentrates that prevents air pollution with SO_2. *It involves the direct reduction of sulfides with appropriate reducing agents in the presence of a desulfurizing agent such as* CaO, $CaCO_3$, *or* Na_2CO_3. *Rhenium is a very rare element found alongside molybdenum in molybdenite. Due to the limited literature on the study of roasting with carbothermal reduction applied to molybdenum sulfide ore accompanied by rhenium, this work studies the behavior of the roasting process with carbothermal reduction applied to molybdenum-rhenium sulfide ore.*

During the carbothermal reduction process, CaO *is used as a sulfur scavenger and* C *as a reducing agent. Therefore, the optimal molar ratio of* CaO *and* C *with respect to* Mo-Re*, required to accelerate the reduction rate and control the emission of* S *into the atmosphere, was studied. The data obtained showed that there is a dependence on several factors, such as the nature of the metal sulfide, the reduction temperature, the molar concentrations, and the roasting times, among others. Based on the results obtained, the optimal operating conditions for* Mo-Re *recovery were determined.*

The initial plan is to characterize the concentrates by determining their chemical compositions using various analytical and instrumental techniques, as well as their mineralogical composition. Subsequently, the samples will be subjected to carbon thermal reduction roasting and analyzed to determine their behavior at different temperatures and roasting times. Once the optimal conditions have been defined, the application of carbon thermal reduction roasting under the aforementioned conditions will be designed, adding the operational parameters of the aforementioned process, thereby defining its virtues and strengths when non-traditional processes such as carbon thermal reduction are used. This latter roasting process falls within the scope of processes known as clean technologies.

Methodology

Initially, chemical and mineralogical analyses were performed on the sample under study, which was a sulfide concentrate called M3, obtained from differential flotation. The mineralogical composition was determined using X-ray diffraction techniques, identifying the main crystalline phases present. The equipment used was a Philips X'Pert WP 1011 diffractometer. The structural study was carried out by optical microscopy using an Olympus GX 51 microscope with a Leco IA32 image analyzer and the Olympus GX 51 optical microscopy equipment used. The structural study was carried out by scanning electron microscopy (SEM) and EDS analysis with FEI Quanta 200 equipment.

The chemical composition was quantified using volumetric techniques with acid digestion and subsequent reading with atomic absorption spectrophotometry on Perkin Elmer PinAAcle 900T equipment and ICP-OES spectroscopic techniques on Perkin Elmer 7300 DV equipment. Total sulfur was determined by gravimetric precipitation for sulfide minerals.
Based on the results obtained from the chemical and mineralogical analyses, the following carbon thermal reduction roasting tests were scheduled: temperature variations from 300°C to 600°C; reaction time variations: 10, 20, 30, 45, 60, and up to 180 min. Work was also carried out on the variation of the molar ratio of CaO to the element Me (Me:CaO:C), equal to: 1:0,5:1; 1:1:1; 1:2:1; 1:3:1.

Results and Discussions

Characterization of samples

Determination of the chemical composition of the original samples "M"

The data obtained from the chemical composition of the concentrate called M3 are detailed in Table 1.

Table 1. Chemical composition of M3 sulfide concentrates.

	Cu	Fe	Na	K	Mo	Mn	Ca	Mg	Re	S	As
	(%wt)	(%wt.)	(%wt.)	(%wt.)	(%wt.)	(%wt.)	(%wt.)	(%wt.)	(%wt.)	(%wt.)	(%wt.)
M3	0,91	1,32	0,04	0,05	52,17	0,01	0,26	0,16	0,10	28,89	0,05

Given that the samples studied are concentrates from roughing and differential flotation processes, the chemical compositions determined are consistent with the results obtained from the aforementioned processes. In other words, chemical characterization allows the sample to be classified. This would indicate that the values obtained from the chemical characterization of M3 is a molybdenum sulfide concentrate, which will be corroborated in the mineralogical characterization.

Mineralogical characterization

The results obtained from the mineralogical composition by X-ray diffraction for the M3 samples are detailed in Figures 1, indicating the composition with the following designation: $CuFeS_2$ = Chalcopyrite, MoS_2 = Molybdenite, and Re = Rhenium. In addition, the study is completed with observation using scanning electron microscopy (SEM), including semi-quantitative chemical analysis using the EDS technique. The results obtained are detailed in Figure 2.

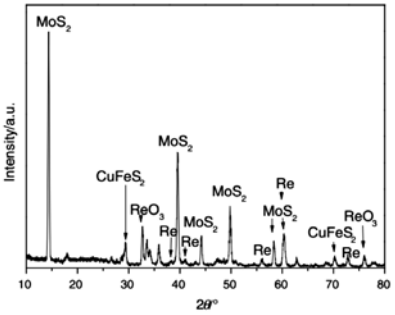

Figure 1. Diffractogram of sample M3.

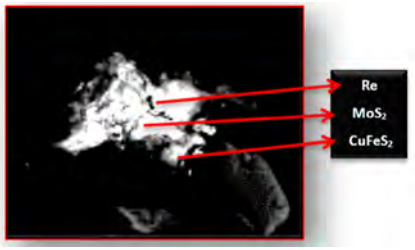

Figure 2. Sample M3. Molybdenite (MoS_2) and chalcopyrite $CuFeS_2$ sample containing Re.

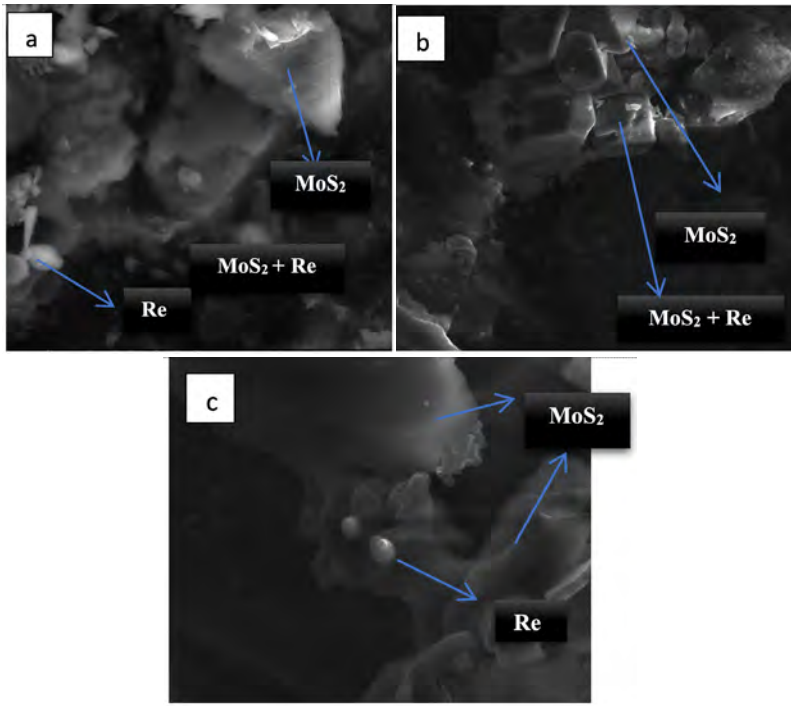

Figure 3. Electron microscopy images with SEM-EDS analysis of sample M3.

SEM and EDS analysis determines the chemical composition of all phases. Both molybdenite (MoS2) and chalcopyrite (CuFeS2) are phases commonly associated with the presence of other minerals and trace elements. Therefore, the Re content is also detected within the particles combined with molybdenite (MoS2) and chalcopyrite (CuFeS2). In summary, for each of Figures 2 and 3, flat, opaque edges with flat sheets characteristic of molybdenite and chalcopyrite minerals with significant rhenium incrustations can be observed.

Through SEM and EDS analysis, the chemical composition of all phases is determined, and the presence of molybdenite, chalcopyrite, and rhenium particles is confirmed. In conclusion, practically all the figures indicate that the constituent minerals of the samples studied are found with adjacent minerals joined by curved edges and with a significant degree of particle release or exposure.

Variation of molar ratios for CaO (Re:CaO:C)

The variations in the stoichiometric ratios for CaO are shown in Figures 4 to 7, respectively, with the effects obtained from the tests for M3 shown graphically. Each of the stoichiometric variations of CaO. The study conditions are Me:CaO:C = 1:0,5:1; 1:1:1; 1:2:1; 1:3:1 at temperatures of 300°C, 400°C, 500°C, and 600°C.

In the case of copper, the same molar ratio as rhenium is used because it is in the same concentration range as rhenium, which is not the case with molybdenum. The results for rhenium and molybdenum are detailed below.

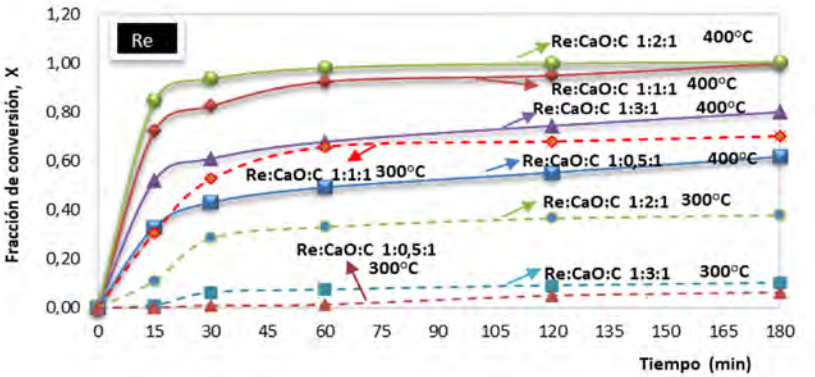

Figure 4. Effect of the CaO molar ratio on the sulfide reduction rate in the presence of C at 300°C and 400°C for M3, for Re.

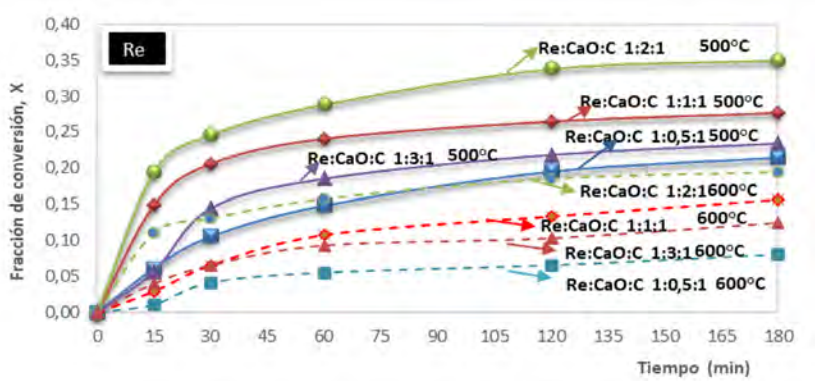

Figure 5. Effect of the CaO molar ratio on the sulfide reduction rate in the presence of C at 500°C and 600°C for M3, for Re.

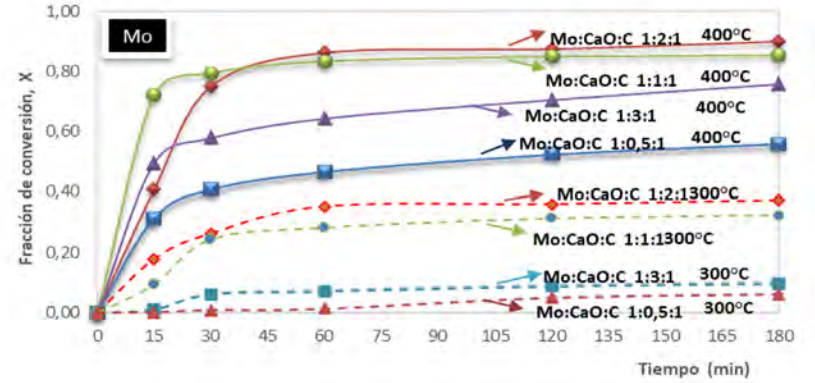

Figure 6. Effect of the CaO molar ratio on the sulfide reduction rate in the presence of C at 300°C and 400°C for M3, for Mo.

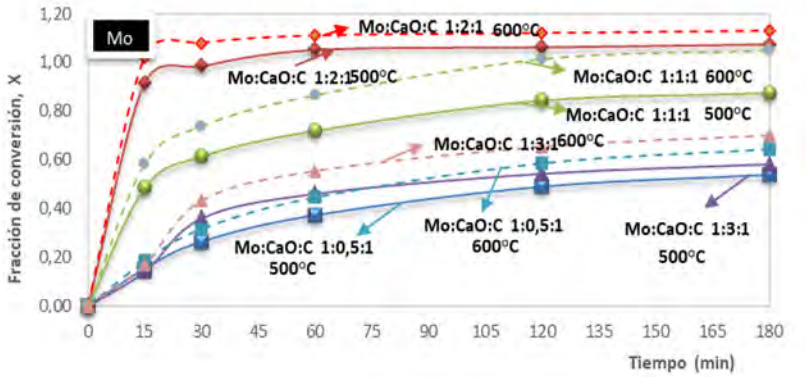

Figure 7. Effect of the CaO molar ratio on the sulfide reduction rate in the presence of C at 500°C and 600°C for M3, for Mo.

Based on the figures shown for each stoichiometric molar ratio studied for Me:CaO:C, the optimum working concentration of CaO at which the highest percentage of rhenium retention in calcite is obtained is Re:CaO:C=1:2:1 at 400°C, achieving recoveries of 82.50%. For molybdenum, it is considered that the highest conversion percentage is achieved for a stoichiometric molar ratio of Me:CaO:C of Mo:CaO:C 1:2:1 at 600°C, reaching recoveries of 89.05%. In the case of copper, it is established that the stoichiometric molar ratio for Me:CaO:C can use the same conversion as for Re, given that the percentage of copper in sample M3 is of the same order as rhenium. Therefore, the behavior can be analyzed for the same molar ratios. In the particular case of copper, a better response is obtained for the condition of Re:CaO: C=1:2:1 at 600°C.

Tables 2 and 3 summarize the percentage recovery values of rhenium and molybdenum in calcite when the molar ratio of CaO is modified in the reduction rate of sulfide in the presence of C at 300°C, 400°C, 500°C, and 600°C for M3, for rhenium and molybdenum.

Table 2. Summary of the effect of the CaO molar ratio on the sulfide reduction rate in the presence of C at different temperatures for rhenium

Samples	300°C $\%Re_{calcite}$	400°C $\%Re_{calcite}$	500°C $\%Re_{calcite}$	600°C $\%Re_{calcite}$
Re:CaO:C=1:0,5:1	9,87	67,15	3,71	1,86
Re:CaO:C=1:1:1	12,98	70,50	5,58	1,98
Re:CaO:C=1:2:1	11,03	82,50	7,10	3,02
Re:CaO:C=1:3:1	10,23	75,32	2,89	1,50

Table 3. Summary of the effect of the CaO molar ratio on the sulfide reduction rate in the presence of C at different temperatures for molybdenum.

Sample	300°C $\%Mo_{calcite}$	400°C $\%Mo_{calcite}$	500°C $\%Mo_{calcite}$	600°C $\%Mo_{calcite}$
Re:CaO:C=1:0,5:1	10,10	37,25	75,05	78,80
Re:CaO:C=1:1:1	12,55	45,90	80,35	85,95
Re:CaO:C=1:2:1	15,45	48,50	83,45	89,05
Re:CaO:C=1:3:1	13,25	43,32	79,80	83,10

This paper proposes a study based on the theoretical analysis outlined above, evaluating the typical variables of the oxidative roasting and carbothermal reduction roasting processes. Traditional pyrometallurgical methods are not suitable for treating most of these metal sulfides when they are found in the form of low-grade concentrates, or when they form small mineral deposits or polymetallic sulfide deposits.

To determine whether this development is feasible, the thermodynamic conditions of the process must be analyzed together with the reaction mechanism accompanied by the kinetics of the overall reaction, applied to rhenium sulfide (ReS_2).

For the particular case of rhenium, the possible chemical reactions involved in a carbothermal reduction roasting process are detailed below, using HSC 6.0 software:

$ReS_2 + C + 2CaO + 4O_{2(g)} \rightarrow Re + 2CaSO_4 + CO_{2(g)}$	$\Delta H^0_{(400°C)} = -431kcal$	(1)
$ReS_2 + C + 2CaO + 5O_{2(g)} \rightarrow ReO_2 + 2\,CaSO_4 + CO_{2\,(g)}$	$\Delta H^0_{(400°C)} = -535kcal$	(2)
$ReS_2 + C + 2CaO + 5{,}5O_{2(g)} \rightarrow ReO_3 + 2CaSO_4 + 2CO_{2(g)}$	$\Delta H^0_{(400°C)} = -570kcal$	(3)
$2ReS_2 + 2C + 4CaO + 11{,}5O_{2\,(g)} \rightarrow Re_2O_7 + 4CaSO_4 + 2CO_{2\,(g)}$	$\Delta H^0_{(400°C)} = -1143kcal$	(4)

Thermodynamic analysis is also performed by analyzing whether a chemical reaction is spontaneously possible. Figure 8 shows the values of standard Gibbs free energy as a function of temperature for reactions 1 to 4 in the range from 25°C to 1000°C, bearing in mind that the more negative ΔG^o is, the more spontaneous the chemical reaction is. Based on the chemical reactions expressed above (1 to 4), a phase equilibrium of the **Me-S-Ca-O** systems is proposed, which can be analyzed in detail through stability diagrams. From these, the different areas of predominance and the possible compounds that are generated for different pressure conditions of S_2 and O_2 gases are obtained. Figure 9 shows the respective phases for rhenium: $ReS_2/Re/ReO_2/ReO_3/ReO_4$ / Re_2O_7 in the presence of CaO. The presence of different phases indicates that thermodynamic phase equilibrium will not be achieved for the **Re-S-Ca-O** system. Since Re comes from a sulfide mineral ReS_2, when it is subjected to a roasting process, the appearance of intermediate oxides is expected, which suggests a possible reaction mechanism for the working atmosphere. On the other hand, the phases produced by roasting in the presence of CaO coexist, giving rise to calcium sulfates and sulfides, as shown in the chemical reactions developed above (1 to 4).

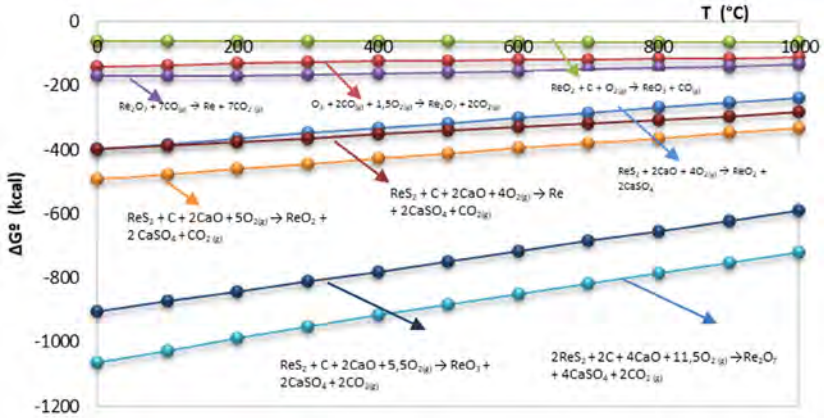

Figure 8. Gibbs free energy of reactions versus temperature for rhenium.

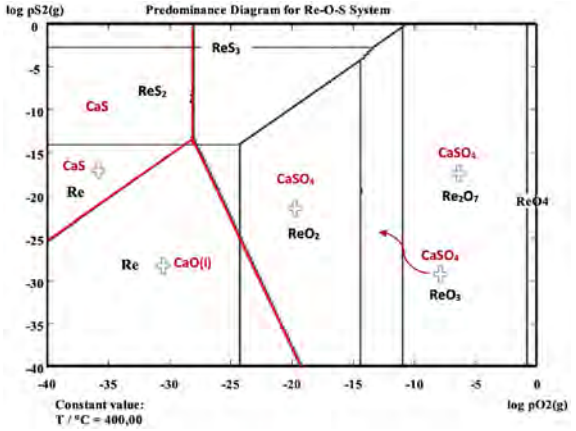

Figure 9. Stability diagram of the Re-S-Ca-O system at 400°C.

Since the mineral under study has significant concentrations of molybdenite, the role of molybdenum during the roasting process must be taken into account. With this in mind, and based on thermodynamic studies of carbothermal reduction, the general equation (5) is formulated. This global equation governs the carbothermal reduction process for molybdenum, which is described below:

$$MoS2 + C + 2CaO + 1{,}5O2\ (g) \rightarrow MoO3 + 2CaS + CO2\ (g) \qquad (5)$$

One of the most important variables to consider is the roasting temperature, where temperature control must be very strict. The stability diagram studies the possible chemical species that form as a result of changes in the PS2 and PO2, conditions involved in carbothermal roasting, which is why the conditions outlined above are closely linked to the formation of different compounds expressed in the respective chemical reactions that occur. However, the compounds involved in carbothermal reduction, such as CaO and C, must also be taken into account. Thus, a phase diagram is presented in Figure 10.

Next, the phase equilibrium of the Me-Ca-S-O-C systems (Figure 11) can be analyzed in detail through the diagrams of the different areas of predominance and the possible compounds that are generated.

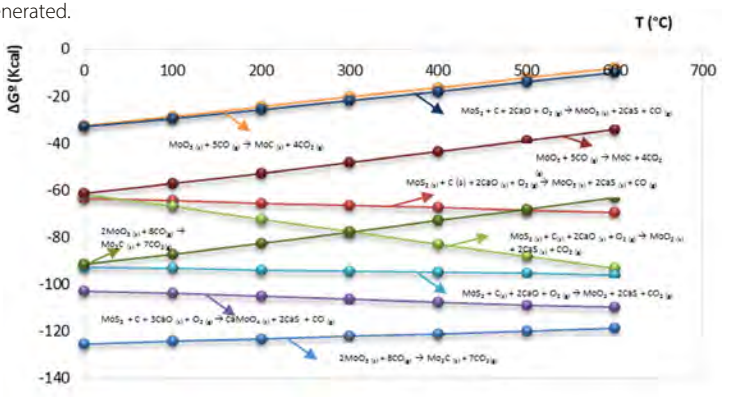

Figure 10. Gibbs free energy of reactions versus temperature for molybdenum.

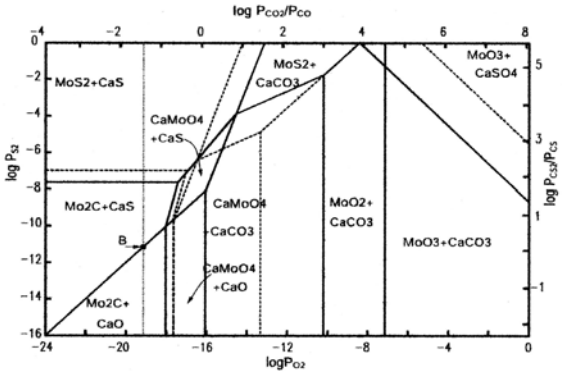

Figure 11. Stability diagram for the Mo-Ca-S-O-C system at 600°C for the metal fraction $0<Mo/Mo+Ca<0,5$.

The functionality that presents Gibbs free energy as a function of reaction temperature is shown in Figure 10, as a function of temperature, calculated using the HSC 6.0 calculation program. Figure 10 shows that the governing chemical reaction is equation 5. This is considered to be the predominant chemical equation in the carbothermal reduction process. This is justified as the most exothermic reaction $(\Delta G° < 0)$ compared to the other chemical equations, which becomes equation 5 in the case of molybdenum.

Conclusions

Based on thermodynamic analysis, it is determined that an increase in temperature is the least effective way to increase the percentage of rhenium recovery, but it is more beneficial for obtaining molybdenum.

It is determined that the highest percentage of recovery is a function of temperature variation, where rhenium (Re) recoveries of up to 70.50% are observed at 400°C. In contrast, for molybdenum (Mo), recoveries of 85.95% are obtained at 600°C. For this analysis, a molar ratio of calcium oxide (CaO) and carbon (C) of $Re:CaO:C= 1:1:1$ was set, and the temperature was run from 300°C to 700°C.

The optimal operating conditions for calcination with carbothermal reduction were obtained at a temperature of 400°C, a time of 30 min, and a molar ratio of calcium oxide (CaO) to carbon (C) of $Re:CaO:C= 1:2:1$. Under these conditions, higher values of rhenium (Re) were obtained, with up to 82.50% recovery of molybdenum at 48.50%.

The most controllable reagent in the variation of molar ratios when carbothermal reduction roasting is applied is calcium oxide (CaO) and not carbon (C). This is because calcium oxide (CaO) plays a very important role as a sulfur scavenger. Together, this causes increases in the reacting fraction.

References

Padilla R., Ramírez G, Ruiz M., 2010. "High-Temperature Volatilization Mechanism of Stibnite in Nitrogen-Oxygen Atmospheres". The Minerals, Metals & Materials Society and ASM International.

Padilla, R., Ramírez, G. & Ruiz, M.C., 2010. Metall and Materi Trans B 41: 1284. https://doi.org/10.1007/s11663-010-9429-6.

Padilla R., Ruiz M.C., 2015. Behavior of Arsenic, Antimony and Bismuth at Roasting Temperatures. In: Battle T.P. et al. (eds) Drying, Roasting, and Calcining of Minerals. Springer, Cham.

Moscoso, I., 2016. "Cloruración de antimonita (Sb2S3) a altas temperaturas en ambiente oxidante". Memoria de título, Departamento de Ingeniería Metalúrgica, Universidad de Concepción.

R. Padilla, M. C. Ruiz and H. Y. Sohn, 1997. "Reduction of molybdenite with carbon in the presence of lime" Metall Mater. Trans., 28B: 265-274.

Safarzadeh, M et al. 2014. "Recent trends in the processing of enargite concentrates" in Mineral Processing & Extractive Metall. Rev., 35: 283–367.

Ebrahimi K., Hasan M., Saidi A., 2006. "Mechanochemical effects on the molybdenite roasting kinetics". Chemical Engineering Journal, pp 86-93.

Smith H. and E. Paredes, 1988. Arsenic Metallurgy: Fundamentals and applications, R.G. Reddy et al., eds., TMS, Warrendale, PA, pp. 145-160.

Roger J., Audubert F., Petitcorps Y., 2009. "Thermal reaction of SiC films with Mo, Re and Mo–Re alloy", Journal of Alloys and Compounds, v. 475, n. 2, pp 635-642.

Graham Long, Yongjun Peng, Dee Bradshaw, 2012. A review of copper–arsenic mineral removal from copper concentrates Minerals Engineering 36–38, 179–186.

Daventport G.W., King M., Schlesinger M. and Biswas A.K., 2002. Extractive Metallurgy of copper, Ed.: Pergamon, Chap.4, 4th Edition, pp 57- 72.

Use of Pretreatments to Improve Gold Recovery From Refractory Auriferous Ores in Colombia: A Proposal for Responsible Mining

Restrepo Baena, Oscar Jaime[1]*, Chaverra Arias Dairo Ernesto[1]

1. Facultad de Minas, Universidad Nacional de Colombia, sede Medellín, Av. 80 #65-223 Medellín, Antioquia, Colombia

**Corresponding author: ojrestre@unal.edu.co*

ABSTRACT

The growing presence of refractory gold ores in Colombia has posed a considerable challenge for conventional cyanidation processes, particularly in regions where copper- and iron-bearing minerals directly interfere with extraction efficiency. These ores exhibit complex mineralogical characteristics that require innovative and adaptable approaches to achieve effective gold recovery.

This work presents the results of an experimental study focused on chemical pretreatments using sulfuric acid and hydrogen peroxide applied to gold ores with high contents of copper, iron, and tellurium minerals. The objective was to increase gold recovery and reduce cyanide consumption through the partial removal of species that act as cyanicides and passivating agents. Tests were conducted on representative samples from real beneficiation processes in Colombia, with mineralogical characterization performed by X-ray diffraction (XRD), X-ray fluorescence (XRF), and chemical analyses using atomic absorption spectrometry.

These improvements not only optimize metallurgical efficiency but also represent a significant step forward in terms of environmental sustainability by reducing contaminant loads and the costs associated with cyanide waste management.

Beyond the technical impact, the project has also served as an academic platform for the training of undergraduate and graduate students, who actively participated in the experimental design, testing, and results analysis, thereby strengthening scientific and practical competencies around responsible mining.

In conclusion, the acid–oxidative pretreatment represents an effective, economical, and environmentally appropriate option for the processing of refractory gold ores. Its application can contribute to improving the competitiveness of Colombia's gold sector while promoting sound technical and environmental practices in socially and ecologically sensitive contexts.

Keywords: Refractory ores, Gold recovery, Chemical pretreatment, Cyanidation, Mining sustainability

Introduction

Gold continues to be a critical mineral resource for the global economy, valued not only for its monetary and technological applications but also for its strategic importance in emerging clean technologies and the electronics industry. Colombia, recognized for its geological wealth, has a long-standing gold mining tradition. However, many of the deposits currently under development present complex mineralogy that significantly limits gold recovery through conventional hydrometallurgical methods. In particular, refractory ores—those in which gold cannot be efficiently dissolved due to encapsulation in sulfides or association with deleterious elements—represent a growing technical challenge for both artisanal and industrial operations.

Refractoriness in gold ores is often associated with a high presence of sulfide minerals, such as pyrite and arsenopyrite, or with gangue phases that block cyanide access to gold particles. In Colombia, it is increasingly common to find ores with elevated contents of iron, copper, arsenic, and tellurium, which makes conventional cyanidation inefficient or environmentally risky. In such cases, gold recoveries are often below 60–70%, a level that is economically unviable and environmentally concerning due to excessive cyanide consumption and inadequate tailings management.

In response to this problem, the objective of this research is to evaluate the effectiveness of different pretreatment strategies (ultrafine grinding, oxidative chemical pretreatment, thermal pretreatment, and sequential acid leaching) for improving gold and silver recovery from Colombian refractory ores, while reducing cyanide consumption and providing technically and environmentally sustainable processing alternatives.

Each technique was applied to ore samples classified according to their dominant refractory mineral phases (e.g., iron-rich ores, copper–arsenic ores, or telluride-associated ores). Mineralogical characterization before and after each treatment was performed using XRD, SEM-EDS, and ICP-OES, while gold recovery was evaluated through standardized cyanidation tests.

The results show that certain combinations of chemical and mechanical treatments can increase gold recovery by as much as 30–40 percentage points, depending on the ore type. These findings provide valuable insights for the design of tailored processing routes for Colombian gold ores, particularly in regions where complex mineralogy prevents efficient recovery. The study supports the development of low-cost, scalable, and environmentally responsible alternatives for refractory ore processing, aligned with the principles of sustainable mining.

Methodology

This study was structured in three successive experimental phases: mineralogical characterization, application of pretreatments, and metallurgical evaluation of gold recovery, with the objective of establishing effective processing routes for different types of Colombian refractory ores.

Samples and mineralogical characterization

Representative samples of three types of refractory gold ores were selected:

- **Ore type A:** high presence of pyrite and arsenopyrite. **Au** = 7.8 g/t; **Ag** = 12.5 g/t
- **Ore type B:** association with tellurides and silicate gangue. **Au** = 6.2 g/t; **Ag** = 18.9 g/t
- **Ore type C:** high concentration of iron and copper oxides. **Au** = 8.5 g/t; **Ag** = 9.7 g/t

The main impurities identified were **Fe** (25–32 wt%), **Cu** (1.8–2.6 wt%), **As** (0.8–1.4 wt%), and **Te** (0.2–0.5 wt%), depending on ore type.

Each sample was crushed and classified to a particle size below 150 µm. Physicochemical and mineralogical characterization was performed using the following techniques:

- X-ray diffraction (XRD) for mineral phase identification,
- Scanning electron microscopy with EDS analysis (SEM-EDS) to determine the distribution and mode of occurrence of gold,
- Inductively coupled plasma optical emission spectrometry (ICP-OES) for quantification of associated elements (Fe, Cu, As, Sb, Te).

Application of pretreatments

The samples were subjected to different pretreatments aimed at breaking the refractory mineralogical structure and increasing the exposure of gold to leaching reagents:

- Ultrafine grinding: Wet ball milling was applied to reduce the D80 to values below 45 µm, seeking to increase particle surface area.
- Advanced chemical oxidation: Mixtures of H_2O_2 and H_2SO_4 in aqueous medium were tested at different concentrations, residence times (2, 4, and 6 h), and temperatures (25, 50, and 70 °C) under constant agitation. The objective was to oxidize sulfides and remove detrimental metals.
- Thermal pretreatment: Samples were heated in an electric furnace at temperatures between 400 and 650 °C for 1–3 h to induce partial decomposition of sulfide phases without significant formation of non-leachable secondary oxides.
- Sequential acid leaching: An acid leach stage using diluted HCl or H_2SO_4 was followed by washing and alkaline conditioning as a strategy to remove soluble metallic phases prior to cyanidation.

Cyanidation tests

After pretreatments, the samples were subjected to cyanide leaching tests under standardized conditions:

- Sodium cyanide $(NaCN)$ concentration: 500–1000 ppm,
- Solid/liquid ratio: 1:3,
- Contact time: 24 h,
- pH controlled between 10.5 and 11.5.

Gold and silver recoveries were measured through solution analysis by AAS and ICP, while reagent consumption was also assessed. Tailings were analyzed to determine residual gold content using fire assay and residual mineralogy.

Comparative analysis and efficiency criteria

The results were compared against each other and against a control test without pretreatment, using the following key indicators:

- Increase in metallurgical gold and silver recovery,
- Reduction in specific cyanide consumption,
- Modification of post-leaching mineralogy,
- Qualitative assessment of the technical and environmental feasibility of each route.

This methodological approach enabled the establishment of relationships between ore mineralogy and pretreatment response, providing a basis for industrial application recommendations.

Results and discussion

The results clearly demonstrate the significant impact of the applied pretreatments on gold recovery from refractory ores, with variations directly associated with the specific mineralogy of each sample type.

Effect of pretreatments on mineralogy

Post-pretreatment mineralogical analyses revealed important transformations in the gold-bearing phases:

- In Ore type A (high pyrite and arsenopyrite content), chemical treatment with H_2O_2–H_2SO_4 generated partial oxidation of sulfides, facilitating the release of trapped gold. Thermal pretreatment, although effective in decomposing sulfides, produced less leachable secondary phases when temperatures exceeded 600 °C.
- Ore type B, associated with tellurides, showed limited response to conventional acid treatments. However, ultrafine grinding (D80 ~10 µm) substantially improved the surface exposure of tellurides, enabling subsequent cyanidation recoveries above 70%.
- For Ore type C, rich in iron and copper oxides, acid prewashing reduced copper interference in cyanide consumption and prevented the formation of undesirable complexes, allowing for more efficient gold recovery.

Metallurgical recoveries

Cyanidation tests revealed significant improvements in gold and silver recovery compared to the control test without pretreatment:

Type of ore	Essay	Recovery of Au (%)	Recovery of Ag (%)	NaCN consumption (kg/t)
A	White	43,2	27,5	1,15
A	Chemical Ox.	78,6	41,3	0,98
B	Blanco	39,5	33,2	1,25
B	Ultrafine grinding	72,4	45,9	1,10
C	White	45,1	29,7	1,38
C	acid leaching + cyanidation	80,3	52,1	0,87

These results confirm that the proper selection of pretreatment allows for increased leaching efficiency, both in terms of recovery and reagent consumption. In particular, the sequential acid–alkaline strategy proved to be highly effective in ores with significant amounts of metallic oxides.

Comparative analysis of pretreatment routes

From a technical and operational standpoint, the following observations were made:

- Advanced chemical oxidation delivers outstanding results, with controllable operating conditions and without the generation of hazardous gases as in roasting.
- Ultrafine grinding, while effective, entails considerable energy consumption and may cause filtration or sedimentation issues in subsequent stages.
- Sequential acid leaching is versatile, relatively low-cost, and can be integrated into various plant configurations without major capital investments.
- Thermal treatments must be managed carefully, as overheating can lead to the formation of phases such as scorodite or crystalline iron oxides, which are poorly reactive toward cyanide.

Industrial implications

The results suggest that the pretreatments analyzed not only improve metallurgical recoveries but also enhance process sustainability by reducing cyanide consumption and minimizing environmental risks associated with highly reactive residues.

This work provides a solid experimental foundation for the design of processing routes tailored to the mineralogical conditions of Colombian gold ores. Such advances represent a key step toward more efficient and responsible mining practices, aligned with the principles of environmental sustainability.

Conclusions

- Gold recovery from Colombian refractory ores can be substantially increased through the application of specific pretreatments, selected according to the mineralogy and geochemistry of the material. This study demonstrated that recoveries can be improved from below 50% to over 80%, depending on ore type and treatment applied.

- Pretreatments based on advanced chemical oxidation, sequential acid leaching, and ultrafine grinding proved to be the most effective strategies for decomposing or altering gold-bearing phases and liberating the metal for subsequent cyanidation. In particular, chemical oxidation emerged as a viable alternative compared to capital-intensive processes such as roasting or pressure oxidation.

- Proper mineralogical characterization before and after pretreatment is essential to understand ore transformations and to optimize operating conditions. Correlating cyanide consumption, pretreatment type, and metallurgical recovery enables the development of more efficient and sustainable processing routes.

- From an industrial perspective, the proposed pretreatments represent a real opportunity to improve the efficiency of existing processing plants or to design new plants with greater capacity to handle refractory ores. Additionally, by reducing reagent consumption and minimizing the generation of hazardous waste, these approaches foster more environmentally responsible operations.

- Finally, this work helps to close technological gaps in Colombian gold mining by providing an experimental and methodological basis for companies, research centers, and universities seeking to advance toward more profitable, cleaner, and sustainable gold extraction.

References

Marsden, J.O. and House, C.I., 2006. The Chemistry of Gold Extraction (2nd ed.). Society for Mining, Metallurgy, and Exploration (SME).

Aylmore, M.G., 2016. Alternative lixiviants to cyanide for leaching gold ores. In Gold Ore Processing (2nd ed., pp. 447–484). Elsevier.

Ubaldini, S., Massidda, R. and Veglió, F., 2000. Biooxidation of arsenopyritic gold ore: Kinetic study and process comparison. Hydrometallurgy, 57(2), 113–124.

Wang, J., Chen, W., Qin, W. and Lu, Z., 2020. Effect of ultrafine grinding on the physicochemical properties and leaching behavior of gold in a refractory gold ore. Minerals Engineering, 146, 106120.

Sayilgan, E., Kukrer, T. and Civelekoglu, G., 2021. Improvement of Gold Recovery from Refractory Gold-Bearing Pyrite by Nitric Acid Pretreatment. Minerals, 11(2), 153.

Nazari, S., Yazdani-Chamzini, A. and Hossaini, M., 2015. A new approach for evaluating and ranking gold ore pre-treatment processes. Journal of the Southern African Institute of Mining and Metallurgy, 115(5), 417–428.

Restrepo-Baena, O.J., Chaverra-Arias, D.E. and Ariza-González, J.S., 2023. Evaluación de alternativas para mejorar la recuperación de oro en minerales refractarios colombianos. Revista Facultad de Minas UNAL, (en preparación).

Habashi, F., 1999. Textbook of Hydrometallurgy. Metallurgie Extractive Québec.

Wang, H., Zhou, Y., Li, Q. and Zhang, J., 2019. Pretreatment process on refractory gold ores with as high content as 1.24% arsenic. Metals, 9(1), 22.

Ghorbani, Y. and Petersen, J., 2021. Advances in the use of X-ray computed tomography for ore characterization and process optimization: A review. Minerals Engineering, 160, 106678.

Chapter 03

Green Mining

Assessing Circularity Loops in Solid Waste Management to Improve Efficiency and Sustainability in Copper Concentration Plants

Marco A. Vargas[1], Luis A. Cisternas[2,3], Daniel Calisaya-Azpilcueta[2] and Yendery Ramirez[4]

1. Department of Chemical Engineering and Mineral Processes, University of Antofagasta, Chile
2. Department of Metallurgical and Mining Engineering, Universidad Católica del Norte, Chile
3. Advanced Mining Technology Center, AMTC, Chile
4. Sustainable Minerals Institute- International Centre of Excellence Chile (SMI-ICE-Chile), The University of Queensland, Las Condes, Chile

**Corresponding author at: Department of Chemical Engineering and Mineral Processes, University of Antofagasta, Chile: marco.vargas.suarez@ua.cl*

ABSTRACT

The mining industry has been fundamental to human development, driven by a growing demand for raw materials that is expected to increase with technological advancements, posing significant environmental and resource management challenges. The circular economy emerges as a solution through practices such as the reuse of waste rock and tailings, although uncertainty remains regarding which strategies best balance operational efficiency and sustainability. This study analyzed circularity loops in mining waste management through MATLAB simulations and material flow analysis, validated with sensitivity and uncertainty assessments. The multicriteria methods TOPSIS and AHP established key relationships between objectives and cycle performance: the Medium Loop is the optimal strategy when the priority is to maximize copper production and recovery; the Short Loop is the most effective for improving solid waste management or ensuring overall sustainability; while the Long Loop, although reducing tailings deposition, presents limitations that make it the least favorable alternative in terms of circularity and sustainability. These findings provide a decision-making framework for implementing circular economy practices in mining, allowing the selection of strategies from the outset of operations based on specific priorities, production maximization, waste management, or sustainability, to reduce negative externalities.

Introduction

Mining has been fundamental to human development, supplying essential resources such as copper, lithium, and nickel that support technological, industrial, and social progress (Shavina & Prokofev, 2020). However, its extractive nature generates profound challenges. The industry processes vast quantities of rock and soil to obtain small amounts of valuable metals, resulting in declining ore grades, resource depletion, and immense waste production (Balanay & Halog, 2016). Globally, mining generates over 80 billion tons of waste rock and tailings each year, making it one of the largest contributors to industrial waste (Kotarska et al., 2018; Pappu et al., 2007). These by-products pose long-term environmental risks, including land degradation, water contamination, and the formation of Acid Mine Drainage, which threaten ecosystems, communities, and economic stability.

The persistence of the linear "take–make–use–waste" model further intensifies these issues. This consumption pattern emphasizes short-term extraction while overlooking sustainability, leaving significant ecological and social liabilities (Velenturf et al., 2021). As the demand for critical raw materials grows, mining faces the dual challenge of meeting global needs while aligning with

sustainability goals.
The Circular Economy (CE) offers a promising alternative by rethinking resource flows and extending material lifecycles (Born, 2025). CE promotes strategies such as reducing demand, reusing by-products, and recovering value from waste, guided by the principles of the 5Rs: Reduce, Reuse, Repurpose, Recycle, and Recover(Mukherjee et al., 2023). In mining, CE is operationalized through circularity loops. Short loops focus on reintegrating materials within the same process, medium loops enable repurposing across interconnected industries, and long loops transform waste into inputs for entirely new sectors (Stahel & MacArthur, 2019). Tailings and waste rock represent critical opportunities for these strategies, with potential applications in construction, cement production, and mine backfilling (O'Hara & Kakovitch, 2023; Villachica et al., 2021).
Despite its potential, CE adoption in mining remains limited due to technological barriers, high costs, regulatory gaps, and the absence of standardized frameworks to evaluate performance. These challenges reflect the sector's traditionally conservative approach and underline the need for innovative solutions supported by clear evaluation metrics.
This study addresses these gaps by examining the role of circularity loops in managing tailings and waste rock within mineral processing. The objective is to determine which approaches improve plant efficiency, resource recovery, and sustainability. By integrating CE principles, sustainability metrics, and multi-criteria evaluation methods, the research proposes a framework to support decision-making and foster the transition toward a circular and sustainable mining sector.

Methodology

The framework for circular solid waste assessment involves problem definition, indicator development, Monte Carlo simulation, and evaluating circularity and sustainability. It addresses uncertainty and data limitations on an industrial scale. Validation and decision synthesis convert analysis into strategies, linking technical assessment and resource management (Figure 1).

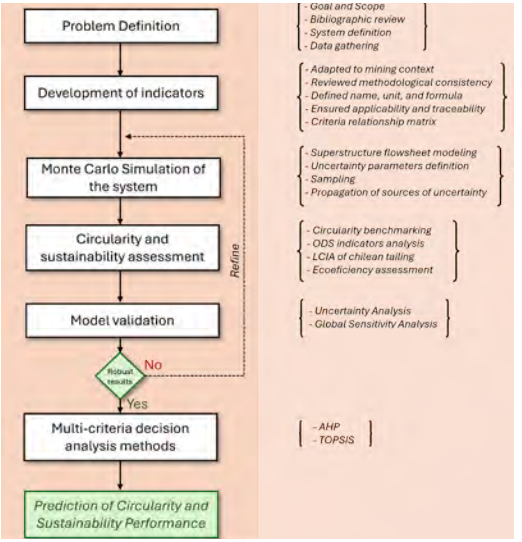

Figure 1. Overview of the proposed methodology for assessing the impact of circularity loops in solid waste management in mineral processing

1.1. Problem Definition

This phase establishes the foundation of the framework by defining the goal and scope: comparing circularity loops and their effects on solid waste management in a copper concentration plant. It requires clear system boundaries, identification of relevant processes, and characterization of critical resource flows in terms of nature, direction, and magnitude. A literature review was conducted using Scopus, Science Direct, and Google Scholar. General searches on "circular economy," "circularity loops," "indicators," and "sustainability" were complemented by focused searches on "tailings," "waste rock," and "mining" to assess circular economy applications in waste management. Priority was given to studies published in the last five years, while older works provided contextual grounding. Special attention was placed on research from northern Chile due to its distinct climatic and geographic conditions. Finally, data requirements, collection methods, and quality assurance measures were defined to ensure methodological coherence, analytical rigor, and reliability throughout the framework's application.

1.2. Development of Indicators

The development of indicators was based on extensive bibliographic research and the theoretical framework of the study, with a focus on circularity loops tailored to the management of tailings and waste rock in mineral processing. Unlike traditional approaches, this framework integrates operational efficiency, waste management, and sustainability indicators to evaluate circular economy performance.

A set of 10 operational KPIs was defined to measure efficiency (e.g., copper recovery rate, energy and water consumption) and solid waste management (e.g., tailings stability, waste-to-product ratios, recycling indexes). These indicators capture how circular strategies affect both material flows and process performance. To align with global sustainability objectives, 11 environmental indicators were selected and linked to the Sustainable Development Goals (SDGs 6, 7, 12, 13, 14, and 15). They address water consumption, greenhouse gas emissions, acid mine drainage risks, and ecosystem impacts, allowing regular monitoring of environmental performance under circular strategies (Figure 2). Additionally, one economic indicator, net sales derived from enhanced copper recovery, was included to capture the financial benefits of CE practices. All indicators were normalized through simulation-based maximum and minimum ranges, using direct or inverse normalization formulas depending on whether higher or lower values represented optimal outcomes. This ensures comparability across metrics and supports a robust multi-criteria evaluation framework.

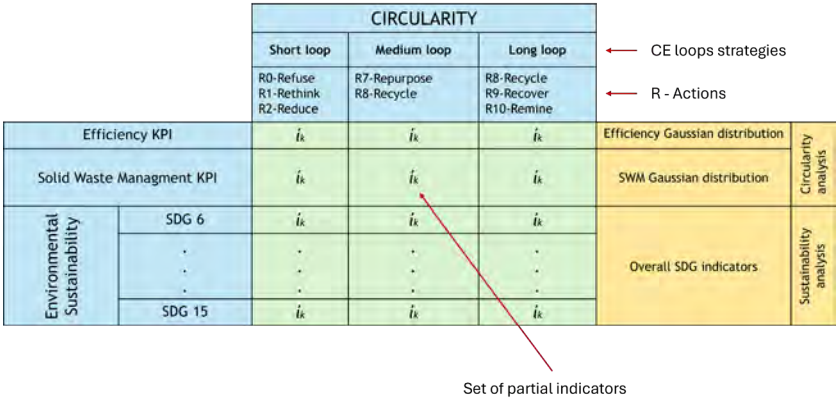

Figure 2. Overview of the indicators and their role in this research

1.3. Simulation step

Once the circularity KPIs and sustainability indicators were defined, the study advanced to the simulation phase to quantify their performance. A Material Flow Analysis (MFA) was conducted for the case study, using literature-based operational parameters and stage-specific models to ensure contextual accuracy. This step translated qualitative indicators into scenario-driven insights for decision-making. The model integrated the role of particle size distribution across grinding, classification, and flotation, recognizing its influence on mineral liberation, recovery efficiency, and waste generation. In grinding, fragmentation models predicted particle size ranges; in classification, efficiency curves for hydrocyclones and separators optimized fines and coarse fractions; and in flotation, size-based responses were modeled to capture the relationship between liberation, kinetics, and copper recovery. This approach emphasized the sensitivity of flotation performance to energy input in prior stages. Additionally, particle size distributions were linked to tailing formation, assessing how fines and coarse fractions contribute to solid waste management challenges. To address variability, 250,000 Monte Carlo simulations were executed per case, introducing normally distributed variations to critical parameters. This provided a robust framework for testing uncertainty and optimizing operational strategies. Overall, the simulation step reflects the interdependence of processes, connecting circuit efficiency with sustainability outcomes in copper concentration.

1.4. Validation tools

The uniform distribution function characterizes epistemic uncertainty in process stages, reflecting gaps in understanding their dynamics. By integrating Monte Carlo simulations with Global Sensitivity Analysis (GSA), the model identifies the most sensitive input variables, allowing them to be refined and thereby reducing model uncertainty and increasing the empirical reliability of results. By highlighting which parameters most influence system behavior, this approach validates model robustness and supports adaptive operational decisions. In this way, uncertainty becomes a structured factor for process optimization, ensuring that technical and economic strategies align with operational realities and circularity objectives in resource-intensive environments.

1.5. Circularity KPIs Benchmarking

Circularity indicators in the mineral processing plant were evaluated through two complementary approaches: operational efficiency KPIs, measuring the optimization of water, energy, and mineral use across classification, milling, and flotation stages; and solid waste management KPIs, quantifying the reduction, valorization, or reintegration of waste rock and tailings into productive cycles. Metrics such as metallurgical recovery, specific energy consumption, waste diversion, and material reintegration were analyzed to identify synergies between industrial productivity and environmental sustainability. This benchmarking provides a quantitative basis for prioritizing circular strategies that balance technical feasibility and economic viability in mining operations.

1.6. SDGs in Sustainability Metrics

The sustainability impact assessment integrates environmental, economic, and social dimensions. Environmental performance is evaluated using normalized indicators linked to SDGs, producing a profile of the plant under short, medium, and long circularity loops. These results are reinforced through a gate-to-gate Life Cycle Assessment (LCA) using SimaPro and the ReCiPe 2016 method, identifying environmental hotspots and validating impact categories. To capture the economic dimension, a net sales-based performance indicator is combined with weighted environmental impacts, producing an eco-efficiency metric that reflects the integration of economic and environmental outcomes and assesses contribution to SDG 8.

1.7. Multicriteria Analysis Methods

Multicriteria Decision Analysis (MCDA) provides systematic and transparent guidance for complex decision-making. In this study, the Analytic Hierarchy Process (AHP) was first applied to assign relative weights to criteria and sub-criteria, enabling hierarchical prioritization and incorporating qualitative

factors often overlooked due to measurement challenges. Criteria were weighed according to the research objectives, establishing a structured framework for evaluating alternatives.

Next, the TOPSIS method was used to rank the proposed alternatives based on key circularity and sustainability indicators. This approach identifies the most desirable and least favorable options while providing a structured comparison of different technologies. By integrating weighted criteria, the methodology highlights the solutions that best support circularity and sustainability goals, ensuring informed decision-making in complex, multi-dimensional scenarios.

1.8. Study Case

This case study illustrates the proposed methodology in a copper processing plant supplied with desalinated water from a coastal plant 170 km away at 316 m above sea level. Pipeline and geographic data, along with production rates, were used to calculate circularity indicators, ensuring operational feasibility and alignment with sustainability goals. The processing facility operates at a capacity of 1,400 tons of mineral per hour. The process begins with the Run-of-Mine (ROM) material, which is fed into a classifier that segregates particles by size. Embeds the base-case flowsheet within a superstructure that branches into three mutually exclusive ("OR") circularity loops scenarios. The baseline scenario involves particle classification, grinding, and conventional flotation, resulting in a concentrate stream and tailings being sent to a storage dam. The short loop scenario integrates sensor-based sorting at classification to reject coarse sterile particles early, reducing downstream energy use and unnecessary processing. The medium loop scenario incorporates a secondary flotation stage to recover coarse particles that are typically lost in conventional methods. The long loop scenario valorizes tailings post-processing, transforming inert waste into construction aggregates or secondary raw materials for industries like ceramics (Figure 3). Each scenario is color-coded to reflect its temporal and spatial integration within the processing chain. Controlled input parameters, including feed rate and particle size distribution, prioritize mass balance accuracy and mineral recovery. Circularity and sustainability indicators are applied to evaluate the performance of each alternative.

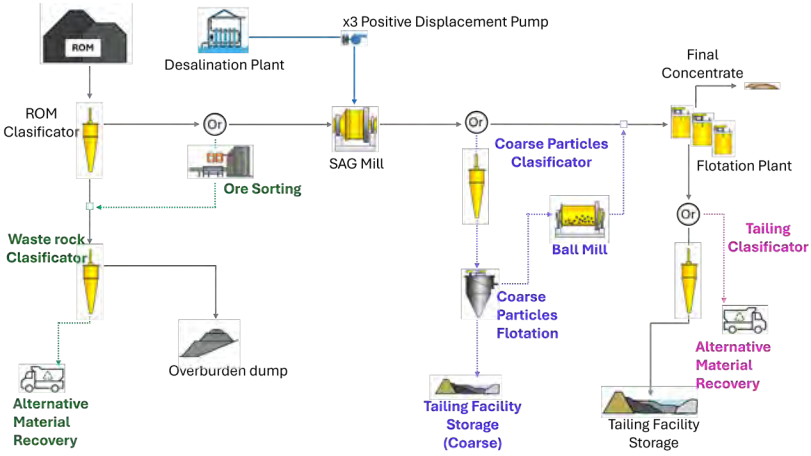

Figure 3. Flowchart of the system under study

Results and Discussions

The Results and Discussion section assesses circular loop strategies that improve both plant efficiency and sustainability in mining waste management using three circularity loops aligned with the SDGs. Model reliability and the identification of key influencing factors are ensured through Global Sensitivity Analysis (GSA) and uncertainty analysis (UA). Each set of results is followed by a focused discussion, with a comprehensive overview presented at the end. The following subsections provide a detailed examination of these evaluations.

Circularity KPI Measurement

In this section, efficiency and waste management KPIs for each circularity loop were evaluated to provide a quantitative assessment of system performance and identify opportunities for improvement. The measurements were based on simulation data, enabling a comprehensive analysis of operational efficiency and resource utilization. Standard distribution plots, derived from a probabilistic Monte Carlo uncertainty analysis with 250,000 simulations, evaluate the robustness of normalized efficiency KPIs under varying operational conditions. Within this framework, the medium loop, which incorporates coarse flotation technology, exhibits the highest throughput efficiency.

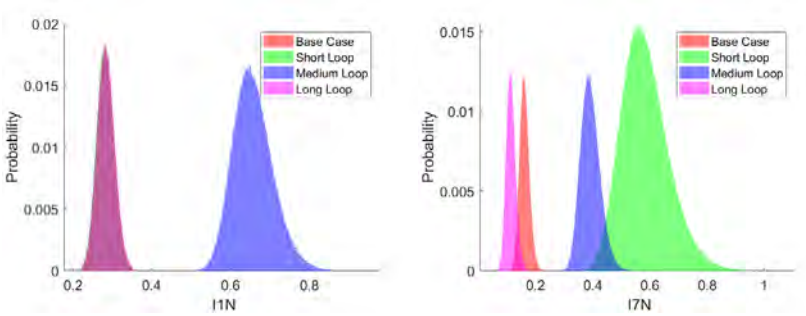

Figure 4. Gaussian distribution of efficiency (A) and waste management (B) KPIs under circular strategies.

Figure 4 presents examples of two of the analyses performed for the normalized indicators. For I1N, representing Concentrate Recovery Efficiency (Ore to be milled / Final concentrate), and I7N, representing the Disposed Waste-to-Product Ratio (Σ of solid waste final deposit/ Final concentrate), the performance of the three circularity loops is compared against the base case. The circularity of each loop is evaluated for two perspectives: operational efficiency (A) and solid waste management (B).

In case A, the medium loop shows the best performance because the coarse flotation stage increases the amount of floatable material, improving concentrate recovery. In case B, the short loop exhibits superior results due to the application of sensor-based sorting, which reduces the volume of material entering the plant and consequently decreases tailings deposition, while maintaining competitive concentrate levels. This comparison highlights how different circularity strategies can optimize distinct aspects of plant performance depending on the operational focus.

Sustainability Assessment

This section evaluates the environmental performance of each circularity loop, focusing on tailings' contribution to acid mine drainage (AMD) and overall eco-efficiency, aligned with relevant SDGs.

Environmental Assessment

Environmental Assessment metrics analyze the influence of circularity loops on environmental sustainability, emphasizing their alignment with SDGs. By integrating circular economy practices, these metrics evaluate reductions in resource exploitation, pollution, and climate-related risks, while fostering regenerative systems (Figure 5).

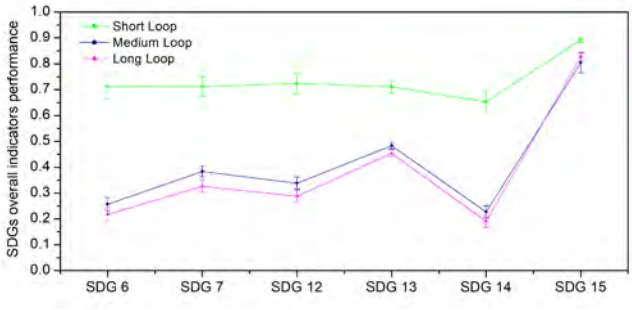

Figure 5. Environmental sustainability analysis for the various proposed SDGs. The highest values represent the most sustainable overall indicators.

Figure 5 compares the environmental performance of three circularity loops in a copper concentrator plant, evaluating their impact on SDGs. The short loop, which utilizes early sorting technology to remove non-valuable material, demonstrates the highest sustainability, as it significantly reduces water use, energy demand, and GHG emissions (SDGs 6, 7, 12, 13, and 14) by avoiding the processing of waste rock. Although it produces larger volumes of sterile rock, these wastes have coarser particles, which lowers the risk of AMD by limiting pyrite oxidation, contrasting with the fine tailings of the traditional process that increase this risk. The medium loop offers balanced performance, improving energy efficiency and reducing GHG emissions compared to the long loop, as it allows flotation at larger particle sizes and reduces the need for mineral regrinding. This alignment benefits SDGs 7 and 13, and it also improves several other indicators. However, coarse particle flotation produces finer tailings, which raises AMD risk and causes a relative decline in SDG 15 performance. This trade-off underscores the importance of considering both process efficiency and the long-term stability of waste disposal sites. The long loop, although designed to maximize tailings recycling, does not provide enough resource savings to justify its operational complexity. These findings highlight that sustainable mining relies not only on technical efficiency but also on process designs that emphasize critical risk mitigation, such as controlling waste particle size to meet global goals like the SDGs.

Life Cycle Impact Assessment

Building on findings related to SDG 15, where the amount of tailings deposited emerged as a key variable influencing the likelihood of AMD generation, an environmental impact assessment was carried out to evaluate the implications of tailings disposal (Figure 6).

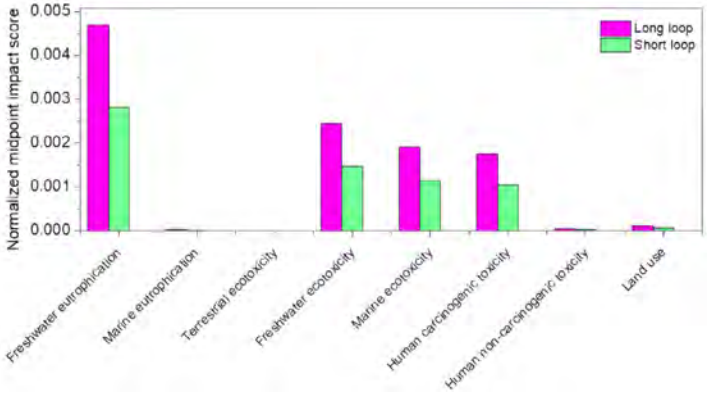

Figure 6. Life Cycle Impact Assessment of Sulfidic tailings, from copper mine operation {CL}

A gate-to-gate LCA for sulfidic tailings shows that the short loop consistently outperforms the long loop in impacted environmental categories such as freshwater ecotoxicity, marine ecotoxicity, and human carcinogenic toxicity, indicating its superior environmental performance. These significant reductions in toxic emissions suggest that the short loop is more effective in preserving biodiversity and maintaining the health of aquatic life, as well as reducing the release of carcinogenic substances harmful to human health. Figure 6 shows that the short loop also holds a slight advantage in other categories, reflecting a reduced contribution to nutrient loading in marine environments, diminished toxic effects on terrestrial ecosystems, and more efficient land utilization. In conclusion, these findings demonstrate that the short-loop strategy is more effective in minimizing environmental impacts, thereby supporting ecosystem conservation and human health within the evaluated context.

Eco-efficiency Analysis

Eco-efficiency analysis plays a crucial role in the overarching framework of sustainability assessment by integrating environmental performance with economic efficiency. By organizing specific sustainability indicators into broader categories associated with the circularity loops, depicted as a square (short), circle (medium), and triangle (long) in Figure 7.

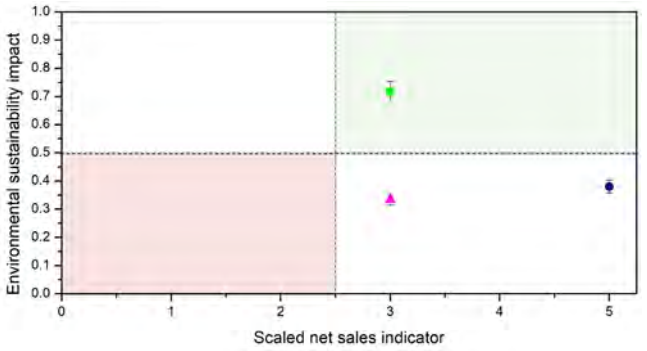

Figure 7. Eco-efficiency graph: Environmental sustainability impact vs. Scaled net sales indicator

Figure 7 evaluates the eco-efficiency of three circularity loops using a scaled net sales indicator and a sustainability impact metric. The short loop strategy (green square) stands out in the upper-right quadrant, combining high environmental sustainability with moderate economic performance, confirming its effectiveness in reducing ecological burdens while remaining economically viable. The medium loop strategy (blue circle) achieves the highest financial performance, as indicated by its position on the x-axis, while also outperforming the long loop in terms of environmental sustainability. However, its sustainability impact remains lower than that of the short loop, reflecting trade-offs associated with this approach. The long loop strategy (magenta triangle), centered on tailings recycling, shows modest outcomes in both dimensions, limited by operational complexity. Overall, the short loop emerges as the most eco-efficient option. In contrast, the medium loop highlights the economic potential of coarse particle flotation when coupled with improved environmental performance compared to traditional recycling approaches.

Multicriteria Analysis Method

The multicriteria analysis (AHP to weight criteria and TOPSIS to rank alternatives) yields consistent results depending on the prioritized objective. When the plant's priority is to maximize copper recovery, the Medium Loop is optimal: incorporating stages such as coarse-particle flotation and reprocessing increases the recoverable fraction and improves metallurgical performance.

If the objective is to improve solid waste management, the Short Loop is most suitable because early sorting reduces the volume of waste rock entering the circuit, thereby decreasing tailings generation. Likewise, when the priority is sustainability (lower resource consumption, reduced emissions, and lower acid mine drainage risk), the Short Loop also offers the best impact–benefit balance, even if it may sacrifice some production performance.

Conclusions

The implementation of circularity loops in mineral processing enables a comprehensive evaluation that integrates operational efficiency, environmental sustainability, and economic viability. The analysis showed that the Medium Loop is optimal when the main objective is to maximize copper recovery and sales, thanks to stages such as coarse flotation that increase the recoverable material fraction. However, Short Loop, through early sorting techniques, stands out for its ability to reduce the generation of fines and non-valuable material, significantly lowering environmental risks, including the probability of acid mine drainage, while also reducing resource consumption and emissions. This strategy maintains economic competitiveness by avoiding energy-intensive processes. From a sustainability perspective, the Short Loop provides the best balance between environmental performance and operational efficiency, demonstrating that waste prevention and optimization strategies can simultaneously deliver economic and ecological benefits. Overall, the results suggest that decision-making in mining should rely on multicriteria approaches, prioritizing holistic designs that integrate efficiency, waste management, and environmental sustainability. Strategies such as the Short Loop represent a replicable model for more sustainable mineral processing, aiming to minimize ecological impacts without compromising profitability, and provide a solid foundation for advancing toward circular and resilient operations.

References

Balanay, R. and Halog, A., 2016. Charting Policy Directions for Mining's Sustainability with Circular Economy. Recycling, 1(2), 219–231. https://doi.org/10.3390/recycling1020219

Born, K., 2025. Adoption of circular economy practices in the mining sector: Evidence from Chile. Resources Policy, 102, 105514. https://doi.org/10.1016/j.resourpol.2025.105514

Kotarska, I., Mizera, B. and Stefanek, P., 2018. Mining Waste in the Circular Economy - Idea Versus Reality. E3S Web of

Conferences, 41, 1–7. https://doi.org/10.1051/e3sconf/20184102013

Mukherjee, P. K., Das, B., Bhardwaj, P. K., Tampha, S., Singh, H. K., Chanu, L. D., Sharma, N. and Devi, S. I., 2023. Socio-economic sustainability with circular economy — An alternative approach. Science of the Total Environment, 904(August), 166630. https://doi.org/10.1016/j.scitotenv.2023.166630

O'Hara, S. and Kakovitch, T. S., 2023. Water as driver of economic capacity: Introducing a physical economic model. Ecological Economics, 208, 107811. https://doi.org/10.1016/j.ecolecon.2023.107811

Pappu, A., Saxena, M. and Asolekar, S. R., 2007. Solid wastes generation in India and their recycling potential in building materials. Building and Environment, 42(6), 2311–2320. https://doi.org/10.1016/j.buildenv.2006.04.015

Shavina, E. and Prokofev, V., 2020. Implementation of environmental principles of sustainable development in the mining region. E3S Web of Conferences, 174, 02014. https://doi.org/10.1051/e3sconf/202017402014

Stahel, W. R. and MacArthur, E., 2019. The Circular Economy. Routledge. https://doi.org/10.4324/9780429259203

Velenturf, A. P. M., Purnell, P. and Jensen, P. D., 2021. Reducing material criticality through circular business models: Challenges in renewable energy. One Earth, 4(3), 350–352. https://doi.org/10.1016/j.oneear.2021.02.016

Villachica, C., Clemente-Jul, C., Villachica, J., Villachica, L. and Llamosas, J., 2021. Circular Economy in Tailings Management. Mine Water and the Environment, 40(1), 23–35. https://doi.org/10.1007/s10230-020-00740-4

Assessment of Cobalt Recovery from Copper Tailings by Leaching with Acid Deep Eutectic Solvent

Yahaira Barrueto[1*], Juan Patricio Ibañez[1], Miguel Veliz[1], Matias Santana[1], José Ojeda [2], Carlos Carlesi[3]

1. Departamento de Ingeniería Metalúrgica y Materiales, Universidad Técnica Federico Santa María, Valparaíso 2340000, Chile.
2. Sustainable Minerals Institute–International Centre of Excellence Chile (SMI-ICE-Chile), The University of Queensland, Australia, Las Condes, Santiago, Chile.
3. Department/Division/Institute, Organization, Country
**Corresponding author at: Departamento de Ingeniería Metalúrgica y Materiales, Universidad Técnica Federico Santa María, Valparaíso 2340000, Chile, e-mail adress: yahaira.barrueto@usm.cl*

ABSTRACT

The increasing global demand for cobalt, driven primarily by its application in lithium-ion batteries, has intensified the search for alternative sources of supply. mine tailings represent a promising secondary resource, especially in regions with extensive mining histories such as Chile. this work evaluates cobalt leaching from copper tailings using a single deep eutectic solvent (DES), choline chloride–citric acid (chcl–ca), under controlled addition of hydrogen peroxide. the tailings were subjected to various pre-treatment strategies including froth flotation, chlorination, and thermal roasting, prior to leaching with choline chloride–citric acid-based des or H_2SO_4*. parameters such as temperature, leaching time, and solid–liquid ratio were evaluated. results show that roasting significantly enhanced cobalt recovery when followed by citric acid or des leaching, achieving up to 100% recovery. des-based leaching proved highly effective and selective in the polymetallic matrix, achieving similar or superior recoveries compared to acid leaching under optimized conditions, without the generation of toxic emissions. despite the limited effect of flotation and chlorination on overall recovery, this study demonstrates the viability of integrated and cleaner technologies for the valorization of tailings containing critical metals like cobalt.*

Introduction

The global energy transition has significantly increased the demand for critical raw materials, with cobalt (Co) playing a key role due to its use in rechargeable batteries, specialty alloys, and catalysts [1]. By 2024, EV batteries already accounted for ~43% of cobalt demand and their share is expected to keep rising toward 2030 [2], [3]. This increasing demand, combined with limited primary sources and geopolitical supply risks, has prompted the search for alternative, sustainable sources of cobalt [4], [5].

In this context, mine tailings have emerged as a promising secondary resource. These finely ground residues, generated after the extraction and concentration of valuable metals, often contain non-negligible amounts of strategic elements such as cobalt and copper. Although traditionally discarded, tailings have the advantage of being pre-mined and comminuted, which reduces the energy input required for further processing [6].

In Chile, one of the world's largest copper producers, the mining industry is facing growing challenges related to environmental management, social responsibility, and energy efficiency. Tailings management has become a focal point, as these materials represent not only a long-term environmental liability but also a potential source of critical metals [7], [8]. The valorization of these wastes aligns with both circular economy principles and the country's strategic interest in adding value to its mining sector [9], [10], [11]. At a representative cobalt grade for our study material of ~33.3 ppm, the resource potential is non-trivial: every 100 Mt of tailings would contain on the order of ~3.3 kt of Co in place, underscoring the industrial relevance of recovery routes from this matrix.

Beyond mineral acids, deep eutectic solvents (DES) have attracted attention as low-volatility, designer lixiviants with tunable acidity and coordination chemistry. In choline chloride–citric acid (ChCl–CA)—an "acidic" DES—the citrate functions as a complexing agent for Co(II), while controlled hydration mitigates viscosity and mass-transfer limitations inherent to many DES systems. These features enable selective leaching under moderate operating conditions and with a lower off-gas burden compared with strong mineral acids [12], [13]. Against this backdrop, the benchmark routes for cobalt recovery from tailings remain sulfuric acid (H_2SO_4) leaching and physical/thermal pretreatments such as froth flotation, chlorination, and roasting, which can alter mineral speciation and improve solubility of target metals.

This study presents a comparative assessment of cobalt recovery from polymetallic tailings using a combination of froth flotation, roasting, and leaching with sulfuric acid and deep eutectic solvents (DES) based on choline chloride and citric acid [12], [13]. The influence of key operational parameters such as temperature, leaching time, and solid–liquid ratio is evaluated. In addition, pre-treatment methods are analyzed for their potential to enhance metal solubility and leaching efficiency. The results contribute to the development of integrated and cleaner strategies for cobalt recovery from mining residues, particularly within the Chilean context.

Methodology

Tailings origin and characterization: The investigated tailings originate from a copper flotation circuit processing a sulphide ore from Coquimbo, Chile. Bulk tailings were sampled at the thickener underflow; composite samples were homogenized, riffle-split, and characterized by XRD and particle size analysis. The tailing used was homogenized and for specific test, it was classified using standard stainless steel laboratory sieves. This were: S1 (+335 µm), S2 (-335 + 250 µm), S3 (-250 + 150 µm), S4 (-150 + 75 µm), S5 (-75 + 45 µm), S6 (-45 + 32 µm) and S7 (-32 µm). For the test in which unclassified tailings were used (full size range), they will be assumed to be S0 (+335 – 32 µm).

For the characterization of the tailings, Inductively Coupled Plasma (ICP) was used to identify what elements are present, and to quantify the cobalt. The most abundant elements present in the tailings are in Table 1:

Table 1: Concentration of elements in the tailings.

Metals Concentration	Co (ppm)	Cu (ppm)	Al %	Ca %	Fe %	K %	Mg %	Na %	S %
	33.3	3145.1	6.88	4.47	8.56	1.52	1.71	3.05	0.58

Reagents and DES preparation: For leaching, choline chloride from Sigma Aldritch, citric acid (CA) from Merck, sulfuric acid (H2SO4) from Winkler, and hydrogen peroxide 30 wt% (H2O2) from Vimaroni were used. All these reagents were analytical grades. The solutions preparation was carried out utilizing deionized water and all the chemicals were used without further purification.

For froth flotation, a polyglycol–alkyl alcohol frother (MatFroth 355; Mathiesen Company, used as received) and a thionocarbamate collector (Matcol D-101; Mathiesen Company, Chile; commercial

grade, used as received) were employed. Slurry pH was adjusted with calcium hydroxide, $Ca(OH)_2$ (analytical grade, ≥95% purity).

Sodium chloride (NaCl, ≥99% purity, anhydrous) was used in the chlorination pretreatment was crushed in a mortar until a fine and homogenized product size was generated.

Two deep eutectic solvent (DES) were developed, with different citric acid concentration. These solutions were formed by adding 20% w/w of deionized water and 80% w/w choline chloride (CC) & citric acid (CA) 1:1 and 1:2 molar (M) ratio and agitated in an ultrasonic bath at 80 ºc until the solution was synthesized. The addition of deionized water accelerates the synthesis of the solution, since the first solutions were prepared with the same proportions of CC & CA without the addition of water, then the solution was agitated for more than 16 hours at 80 ºC but the synthesis was not achieved.

Tailing pre-leaching procedures

Froth flotation: The tailings were froth-floated to further concentrate cobalt and copper. Given the frequent association of Co with pyrite (as Fe↔Co substitution) in tailings and ores, operating conditions were selected within typical pyrite/copper–pyrite flotation ranges [14], [15]. Accordingly, pH was set to 10, which lies at the upper limit of the pyrite flotation window with thiol collectors and is commonly applied around 9.5–10 in Cu–FeS_2 systems. Air flow was fixed at 7 L·min^{-1}, a value used in laboratory Denver-type cells for sulphide flotation, and frother/collector dosages were 30 and 35 g·t^{-1}, respectively—within published laboratory/plant ranges for polyglycol–alcohol frothers and thionocarbamate collectors in Cu-bearing sulphides [16], [17]. Agitation was 600 rpm during conditioning and 750 rpm during flotation, consistent with guidance to use lower impeller speeds. Conditioning and flotation times were 3 and 12 min, respectively, aligning with common laboratory practices (2–3 min reagent conditioning; 10–12 min batch flotation) [18].

Chlorination: The tailings underwent an acid–chloride agglomeration and humid-curing pretreatment (80 °C, 6 h) designed with cobalt as the primary target. In chloride media, Co(II) forms stable chloro-complexes (e.g., $CoCl^+$, $CoCl_2{}^0$, $CoCl_3{}^-$, $CoCl_4{}^{2-}$), which facilitates cobalt solubilization during the subsequent oxidative leach. This strategy follows agglomeration-and-curing practices widely reported for sulphide ores, adapted here to increase chloride activity in the solid bed while preserving moisture for low-temperature reactions [19], [20].

Sodium chloride dosage was set at 70% of the stoichiometric requirement for in-situ HCl generation according to reaction: $H_2SO_4 + 2\ NaCl \rightarrow 2\ HCl + Na_2SO_4$ (via $NaHSO_4$). The stoichiometric amount was computed from the measured sulphuric-acid consumption of the tailings. Once the agglomerates had formed, they were transferred to a sealed glass reactor equipped with a gas inlet and outlet. Saturated steam was introduced through the inlet to maintain a humid atmosphere during curing, while the outlet stream was bubbled through a trap containing a sulfuric acid solution (pH 1.5) to suppress the release of chlorinated gases. The reactor was immersed in a thermostated water bath at 80 °C for 6 h [21], [22].

Cobalt in our material is expected to occur either in discrete Cu–Co sulphides (e.g., carrollite) or isomorphically substituted in pyrite; both modes benefit from chloride–oxidant systems that either form soluble Cu/Co chlorides or prevent sulphur passivation, thereby enhancing Co release [23].

Roasting: To evaluate a thermal activation route, the tailings were oxidatively roasted at 600 °C for 2 h under flowing air (100 mL min^{-1}) to ensure an oxygen-rich atmosphere. For cobalt, laboratory and thermodynamic studies show that cobalt-bearing sulphides (e.g., cobaltite; Co hosted in pyrite) undergo structural/phase changes from ~550–650 °C, forming Co–As oxides and ultimately cobalt oxides at higher temperatures, which facilitates dissolution of Co^{2+} in acid leach. Additionally,

selective sulphation-roasting routes used on Cu–Co concentrates transform Cu/Co into water/acid-soluble sulphates while iron is fixed as hematite—an established rationale for testing thermal pretreatments prior to leaching even when the present work uses oxidative (air) rather than sulphating conditions [24].

Leaching test: DES leaching. Leaching tests with the hydrated ChCl–citric acid DES were carried out in a jacketed glass reactor at 30 or 60 °C for 8 h, with temperature controlled by a thermostatic water bath. The reactor was charged with 2.5 g of tailings, 20 mL of DES solution and 10 mL of deionized water (solid–liquid ratio S/L ≈ 83 g L^{-1}). Hydrogen peroxide (30 wt%) was dosed at 5.0 mL h^{-1} throughout the test. The slurry was continuously stirred to maintain all particles in suspension.

Acid leaching (citric acid and sulfuric acid). Three acidic media were evaluated: citric acid (CA) at 1 M and 5 M, and sulfuric acid at 2 M. CA leaching was performed in a jacketed reactor at 60 °C for 4 h, using 2.5 g of tailings and 40 mL of CA solution (S/L ≈ 62.5 g L^{-1}); H_2O_2 (30 wt%) was added at 2.5 mL h^{-1}. Sulfuric-acid leaching was conducted at 60 °C for 4 h on seven particle-size fractions; reactors were loaded with 15 g of tailings and 90 mL of 2 M H_2SO_4 (S/L ≈ 167 g L^{-1}), and H_2O_2 (30 wt%) was dosed at 2.5 mL h^{-1}.

Leaching of chlorination-pretreated tailings. Tests were carried out in an 800 mL reactor at 25 °C for 4 h, charging 100 g of tailings and 300 mL of an H_2SO_4-adjusted solution at pH 1.5 containing 70 g L^{-1} Cl^- (added as mineral salt, NaCl) (S/L ≈ 333 g L^{-1}). Hydrogen peroxide (30 wt%) was added at 2.5 mL h^{-1}.

Leaching of flotation products. Concentrate or tailings obtained from froth flotation were leached in a 100 mL reactor at 25 °C for 4 h, using 10 g of solids and 30 mL of 2 M H_2SO_4 (S/L ≈ 333 g L^{-1}); H_2O_2 (30 wt%) was dosed at 2.5 mL h^{-1}.

Sampling and analysis. Liquid samples were collected at the end of each test (and, for selected experiments, at predetermined times), filtered through 0.22 µm syringe filters to remove suspended solids, and analyzed by AAS.

Results and Discussions

Tailing characterization:

The powder X-ray diffraction pattern (Cu Kα, 20–90° 2θ, step 0.020°), Figure 1, is dominated by framework silicates consistent with zeolitic phases. The most intense reflection at 28.07° 2θ (d = 3.179 Å) matches zeolite Beta (BEA), while additional reflections in the 21–32° 2θ window are accounted for by BEA and ferrierite (FER) (e.g., 21.00–21.02° [Qz+BEA], 23.19° [FER+BEA], 23.71° [FER], 24.44° [FER]). Quartz (α-SiO_2) is evident at 26.77° 2θ (101) and contributes, together with BEA/FER, to medium-angle overlaps such as 39.58° and 42.57° 2θ. Metallic copper (fcc Cu) is identified by its characteristic triplet at 43.31° (111), 50.25° (200) and 74.23° (220). Weak lines compatible with $Co(OH)_2$ (e.g., near 33°, 38°, 51° 2θ) are at trace level. Low-angle BEA/FER features (<15–20° 2θ) are not captured by the present scan range. Overall, the pattern points to a zeolite-rich matrix with quartz, minor fcc-Cu, and traces of Co-bearing phase(s).

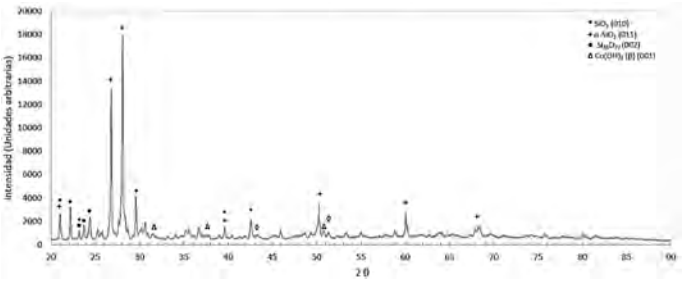

Figure 1. Powder X-ray diffraction (XRD) pattern of the head sample (Cu Kα, 20–90° 2θ; intensity in arbitrary units).

SEM imaging reveals angular to sub-angular particles with abundant platy fragments and widespread fines coating coarser grains. High-magnification views show stepped surfaces and microfractures, indicating high specific surface area and potential mass-transfer advantages during leaching, but also a propensity for slime entrainment in flotation.

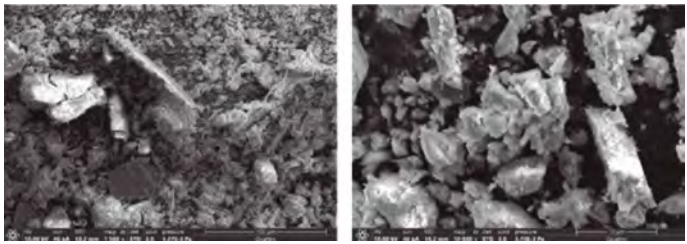

Figure 2. SEM micrographs of the head sample. (a) Low-magnification view (10 kV, 1,500X). (b) High-magnification view (30 kV, 10,000X).

Leaching test: Initially, various leaching test were carried out with sulfuric acid, to form reference points for future experiments in this work. The results of this leaching are in Table 2.

Table 2: Summary of no pretreatment acid leaching results.

Particle Size (μm)	Experimental Conditions	%Co Recovery
S_0	T° = 25 °C, t = 4 h, H_2SO_4 = 1 M	42%
S_0	T° = 60 °C, t = 4 h, H_2SO_4 = 1 M	42%
S_0	T° = 25 °C, t = 4 h, H_2SO_4 = 2 M	31%
S_0	T° = 60 °C, t = 4 h, H_2SO_4 = 2 M	73%
S_1	T° = 60 °C, t = 4 h, H_2SO_4 = 2 M	89%
S_2	T° = 60 °C, t = 4 h, H_2SO_4 = 2 M	61%
S_3	T° = 60 °C, t = 4 h, H_2SO_4 = 2 M	73%
S_4	T° = 60 °C, t = 4 h, H_2SO_4 = 2 M	73%
S_5	T° = 60 °C, t = 4 h, H_2SO_4 = 2 M	91%
S_6	T° = 60 °C, t = 4 h, H_2SO_4 = 2 M	91%
S_7	T° = 60 °C, t = 4 h, H_2SO_4 = 2 M	100%

Some leaching was carried out utilizing classified sizes to determine whether there is a fraction with higher proportion of cobalt concentration within the tailings. No significant differences in concentration were found, but the effect of particle size can be seen, which is directly related to particle liberation.

Because the tailings have a very low concentration of cobalt, it was proposed to carry out different pretreatments to tailings, utilizing the full particle size range (S0), to increase the concentration of cobalt phases or transform the possible insoluble phases for subsequent leaching, results are show in Table 3.

Table 3: Summary of pretreated tailing leaching with acid.

Pretreatment	Leaching Agent	Experimental Conditions	%Co Recovery	% Cu Recovery
Roasting	CA	T° = 60 °C, t = 4 h, CA = 1 M	100	73
Roasting	CA	T° = 60 °C, t = 4 h, CA = 5 M	100	100
Roasting	H_2SO_4	T° = 25 °C, t = 4 h, H_2SO_4 = 2 M	43	46
Chlorination	H_2SO_4	T° = 25 °C, t = 4 h, H_2SO_4 = pH 3,5	17	38
Chlorination	H_2SO_4	T° = 25 °C, t = 4 h, H_2SO_4 = pH 1,5	25	37
Froth flotation	H_2SO_4	T° = 25 °C, t = 4 h, H_2SO_4 = 2 M, Tailing	40	41
Froth flotation	H_2SO_4	T° = 25 °C, t = 4 h, H_2SO_4 = 2 M, Concentrate	48	99
Froth flotation & chlorination	H_2SO_4	T° = 25 °C, t = 4 h, H_2SO_4 = pH 1,5, Tailing	23	36
Froth flotation & chlorination	H_2SO_4	T° = 25 °C, t = 4 h, H_2SO_4 = pH 1,5, Concentrate	41	75

From the pretreated tailing leaching, roasting was the best overall, but because of the gas production and the high energy cost, and low treatment capacity, is not a viable option. The other procedures did not achieve the expected results; therefore, it was decided to continue working with the tailings without pretreatment.

The last leaching tests were carried out utilizing deep eutectic solvent, based on the previous works which indicate that cobalt (specifically the oxides) can be leached reaching good efficiencies.

In the first tries, the leaching was carried out with just tailings and DES, but the high viscosity of the solution plus the mineral caused problems with the agitation, since the mineral was not mixed homogeneously, and made sampling complex. Therefore, it was decided to add water to reduce the viscosity of the solution and allow proper leaching and sampling. The results of these experiments are shown in Table 4.

Table 4: Summary of no pretreatment DES leaching results. Condition: Particle Size: S0

Leaching Agent	Experimental Conditions	% Co Recovery	% Cu Recovery
DES 1:2	T° = 25 °C, t = 4h, S/L = 300 g/L	18	44
DES 1:1	T° = 25 °C, t = 4 h, S/L = 300 g/L	18	62
DES 1:2	T° = 25 °C, t = 4h S/L = 50 g/L	36	48
DES 1:1	T = 60° C, t = 4 h, S/L = 50 g/L	55	100
DES 1:1	T° = 25 °C, t = 8 h, S/L = 50 g/L	66	80
DES 1:1	T° = 60 °C, t = 8 h, S/L = 50 g/L	100	100
DES 1:2	T° = 25 °C, t = 8 h, S/L = 50 g/L	73	80
DES 1:2	T° = 60 °C, t = 8 h, S/L = 50 g/L	100	100

Cobalt recovery exhibited a marked dependence on operating conditions across both leaching systems. In sulfuric media $(1–2\ \mathrm{M}\ H_2SO_4)$, increasing temperature from 25 to 60 °C raised extraction in the multigranular feed $(S0)$ from 31–42% to 73% at 2 M, with values approaching ~100% for the finest size classes, consistent with prior reports on polymetallic matrices and with the expected acceleration of chemically controlled dissolution at elevated temperature [25], [26]. Increasing acid strength likewise improved dissolution (e.g., Co from 42% to 73% and Cu from 40% to 60%), in line with greater stability of solvated ionic species at lower pH and with oxidative assistance when H_2O_2 was present [27], [28], [29]. Mechanistically, proton-promoted dissolution of oxyhydroxides/carbonates and oxidant-assisted opening of sulfide or mixed matrices favor the formation of soluble sulfate species, releasing Co^{2+} into solution. The response, however, is sensitive to particle size and liberation: near-quantitative extractions within short times required very fine fractions. From an environment, heal EHS/operability standpoint, the sulfuric route entails acid consumption, corrosion control, and potential acid mist/off-gas management—considerations that may weigh against deployment in processes with stringent environmental constraints [26].

Deep eutectic solvent (DES) leaching based on choline chloride–citric acid (CC:CA = 1:1–1:2) delivered high selectivity in the polymetallic matrix and, after addressing viscosity limitations, enabled complete dissolution under optimized conditions. Raising temperature from 25 to 60 °C and extending contact time from 4 h to 8 h increased Co recovery from 18–36% (at S/L = 50–300 g

L^{-1}) to 100% (at S/L = 50 g L^{-1}). This behavior reflects the concurrence of (i) faster interfacial reaction kinetics with temperature and (ii) reduced medium viscosity—further improved by ~20 wt% water addition—which thins the hydrodynamic boundary layer, enhances wettability/particle–liquor contact, and increases diffusive flux. Beyond acidity, citrate acts as a complexing ligand that stabilizes Co(II) in solution, suppressing secondary re-precipitation; accordingly, increasing the citrate fraction (CC:CA from 1:1 to 1:2) modestly improved recovery at 25 °C and sustained the attainment of 100% at 60 °C (8 h), consistent with greater ligand availability. The S/L ratio also proved influential: decreasing S/L from 300 to 50 g L^{-1} increased Co recovery (e.g., 18% → 36% at 25 °C/4 h), both by increasing active reagent per unit solid and by mitigating film formation/plugging by fines. Practically, the DES route trades lower gaseous emissions for requirements on viscosity management and recycle to avoid solvent dilution losses [30], [31].

Pretreatments produced mixed outcomes. Chlorination intended to "activate" sulfides by forming more leachable chlorinated phases was ineffective at 80 °C: with H_2SO_4 at pH 3.5–1.5, only 17–25% Co and ~37–38% Cu were obtained, and combining flotation with chlorination yielded lower extractions in the concentrate (41% Co; 75% Cu) than direct leaching without chlorination (48% Co; 99% Cu). These results suggest insufficient solid-state chlorination and possible formation of passivating surface layers that dissolve poorly in sulfate media [19]. Roasting (600 °C, oxidizing atmosphere) transformed the matrix and markedly favored the citric-acid/DES systems (up to 100% Co and 73–100% Cu), whereas cold sulfate media remained kinetically limited (e.g., 43% Co and 46% Cu at 2 M H_2SO_4, 25 °C) [24], [32]. Flotation met its principal aim for Cu (99% in the concentrate) but not for Co (48% in the concentrate; ~40% in tailings), consistent with low Co grade, probable dissemination in fines, operation at pH 10 without sulfidization, and the use of a generic collector more selective for sulfides than for oxidized Co phases; slimes (−32 µm) likely promoted entrainment and compromised selectivity[15], [33], [34] .

Together, both systems can achieve high extractions, but under different "envelopes." In H_2SO_4, dissolution becomes rapid and almost quantitative when release is high and fractions are fine, especially with oxidants, as shown by studies on sulfide tailings and fine sulfide concentrates (accelerated kinetics with T and smaller particle size) [13], [26], [28]. On the other hand, DES ChCl–citric acid (ChCl:CA ratios of 1:1–1:2) achieves 100% under optimized conditions after managing viscosity (↑T and controlled addition of water) and adjusting S/L, also benefiting from citrate–Co(II) complexation that stabilizes dissolved Co and favors selectivity [35]. This contrast suggests that, for fine polymetallic tailings, DES emerges as a selective and environmentally friendly (low volatility) alternative to strong acid, provided that the process diagram incorporates viscosity control and solvent recycling (limitations and scaling) [12], [30].

Conclusions

The results obtained in this study demonstrate that sulfuric acid leaching has good results for cobalt recovery, especially when temperature and time conditions are optimized. However, the environmental drawbacks associated with the generation of toxic gases limit its applicability in sustainable processes. Conversely, the use of DES showed promising selectivity and recovery efficiency, with the benefit of not generating gases during the process, ensuring its applicability in environmentally friendly process. Key operational parameters such as temperature, leaching time, leaching agent concentration and solid-liquid ratio, had a significant influence on metal recovery, highlighting the importance of process optimization. In this framework the best conditions parameters were 60 °C, 8 h, 1:2 (DES) and 50 g/L respectively. Although pretreatment steps like froth flotation and chloration did not enhance cobalt recovery, the consistent solubility of cobalt phases suggest that direct leaching strategies remain viable. Overall, DES-based leaching presents itself

as a cleaner and potentially more selective alternative to conventional acid leaching, warranting further exploration and scale-up in future studies.

References

[1] U. Geological Survey, "mcs2025.pdf - Mineral Commodity Summaries 2025," 2025.

[2] "Cobalt Market Report 2024," 2025.

[3] "Outlook for key minerals – Global Critical Minerals Outlook 2024 – Analysis - IEA." Accessed: Aug. 21, 2025. [Online]. Available: https://www.iea.org/reports/global-critical-minerals-outlook-2024/outlook-for-key-minerals?utm_source=chatgpt.com

[4] G. S. Seck, E. Hache, and C. Barnet, "Potential bottleneck in the energy transition: The case of cobalt in an accelerating electro-mobility world," Resources Policy, vol. 75, p. 102516, Mar. 2022, doi: 10.1016/J.RESOURPOL.2021.102516.

[5] C. Church and A. Crawford, "Minerals and the metals for the energy transition: Exploring the conflict implications for mineral-rich, fragile states," Lecture Notes in Energy, vol. 73, pp. 279–304, 2020, doi: 10.1007/978-3-030-39066-2_12/FIGURES/5.

[6] A. S. Maest, "minerals Remining for Renewable Energy Metals: A Review of Characterization Needs, Resource Estimates, and Potential Environmental Effects," 2023, doi: 10.3390/min13111454.

[7] P. DE Nacional Depósitos De Relaves, "Depósitos de Relaves para una Minería Sostenible", Accessed: Aug. 21, 2025. [Online]. Available: www.minmineria.gob.cl/

[8] "Datos Públicos Depósito de Relaves - SERNAGEOMIN." Accessed: Aug. 21, 2025. [Online]. Available: https://www.sernageomin.cl/datos-publicos-deposito-de-relaves/?utm_source=chatgpt.com

[9] J. Leiva González and I. Onederra, "Environmental Management Strategies in the Copper Mining Industry in Chile to Address Water and Energy Challenges—Review," Mining 2022, Vol. 2, Pages 197-232, vol. 2, no. 2, pp. 197–232, Apr. 2022, doi: 10.3390/MINING2020012.

[10] R. Álvarez, E. De Miguel, C. Cacciuttolo, and E. Atencio, "Past, Present, and Future of Copper Mine Tailings Governance in Chile (1905–2022): A Review in One of the Leading Mining Countries in the World," International Journal of Environmental Research and Public Health 2022, Vol. 19, Page 13060, vol. 19, no. 20, p. 13060, Oct. 2022, doi: 10.3390/IJERPH192013060.

[11] N. Araya, A. Kraslawski, and L. A. Cisternas, "Towards mine tailings valorization: Recovery of critical materials from Chilean mine tailings," J Clean Prod, vol. 263, p. 121555, Aug. 2020, doi: 10.1016/J.JCLEPRO.2020.121555.

[12] K. Binnemans and P. T. Jones, "Ionic Liquids and Deep-Eutectic Solvents in Extractive Metallurgy: Mismatch Between Academic Research and Industrial Applicability," Journal of Sustainable Metallurgy 2023 9:2, vol. 9, no. 2, pp. 423–438, Apr. 2023, doi: 10.1007/S40831-023-00681-6.

[13] N. Peeters, K. Binnemans, and S. Riaño, "Solvometallurgical recovery of cobalt from lithium-ion battery cathode materials using deep-eutectic solvents," Green Chemistry, vol. 22, no. 13, pp. 4210–4221, Jul. 2020, doi: 10.1039/D0GC00940G.

[14] G. Velásquez, D. Carrizo, S. Salvi, I. Vela, M. Pablo, and A. Pérez, "Tracking Cobalt, REE and Gold from a Porphyry-Type Deposit by LA-ICP-MS: A Geological Approach towards Metal-Selective Mining in Tailings," Minerals 2020, Vol. 10, Page 109, vol. 10, no. 2, p. 109, Jan. 2020, doi: 10.3390/MIN10020109.

[15] Q. Dehaine, L. T. Tijsseling, H. J. Glass, T. Törmänen, and A. R. Butcher, "Geometallurgy of cobalt ores: A review," Miner Eng, vol. 160, p. 106656, Jan. 2021, doi: 10.1016/J.MINENG.2020.106656.

[16] Z. Štirbanović et al., "Application of Thionocarbamates in Copper Slag Flotation," Metals 2022, Vol. 12, Page 832, vol. 12, no. 5, p. 832, May 2022, doi: 10.3390/MET12050832.

[17] K. K. Brest, M. M. Henock, N. Guellord, M. Kimpiab, and K. F. Kapiamba, "Statistical investigation of flotation parameters for copper recovery from sulfide flotation tailings," Results in Engineering, vol. 9, p. 100207, Mar. 2021, doi: 10.1016/J.RINENG.2021.100207.

[18] X. Yang, X. Bu, G. Xie, and S. Chehreh Chelgani, "A comparative study on the influence of mono, di, and trivalent cations on the chalcopyrite and pyrite flotation," Journal of Materials Research and Technology, vol. 11, pp. 1112–1122, Mar. 2021, doi: 10.1016/J.JMRT.2021.01.086.

[19] V. Quezada, A. Roca, O. Benavente, M. Cruells, and E. Melo, "The Effects of Sulphuric Acid and Sodium Chloride Agglomeration and Curing on Chalcopyrite Leaching," Metals 2021, Vol. 11, Page 873, vol. 11, no. 6, p. 873, May 2021, doi: 10.3390/MET11060873.

[20] E. ; Urtnasan et al., "Correlation between Thermodynamic Studies and Experimental Process for Roasting Cobalt-Bearing Pyrite," Metals 2024, Vol. 14, Page 777, vol. 14, no. 7, p. 777, Jun. 2024, doi: 10.3390/MET14070777.

[21] P. Altinkaya, J. Liipo, E. Kolehmainen, M. Haapalainen, M. Leikola and M. Lundström, "Leaching of Trace Amounts of Metals from Flotation Tailings in Cupric Chloride Solutions," Min Metall Explor, vol. 36, no. 2, pp. 335–342, Apr. 2019, doi: 10.1007/S42461-018-0015-9/FIGURES/8.

[22] J. P. Ibáñez, Y. Barrueto, J. Ipinza and N. Quispe, "Solid reaction products from NaCl+H2SO4 chemical pre-treatment of chalcopyrite," Canadian Metallurgical Quarterly, pp. 1–12, Aug. 2025, doi: 10.1080/00084433.2025.2545618.

[23] N. Toro, C. Moraga, D. Torres, M. Saldaña, K. Pérez and E. Gálvez, "Leaching Chalcocite in Chloride Media—A Review," Minerals 2021, Vol. 11, Page 1197, vol. 11, no. 11, p. 1197, Oct. 2021, doi: 10.3390/MIN11111197.

[24] G. Atesoglu and İ. Atilgan, "Effect of Roasting Temperature on the Leaching of Chalcopyrite Concentrate in Sulphuric Acid," Min Metall Explor, vol. 39, no. 5, pp. 2199–2208, Oct. 2022, doi: 10.1007/S42461-022-00669-Y/FIGURES/5.

[25] E. A. Oke, H. Potgieter, F. Mondlane, N. P. Skosana, S. Teimouri and J. K. Nyembwe, "Concurrent leaching of copper and cobalt from a copper–cobalt ore using sulfuric and organic acids," Miner Eng, vol. 216, p. 108853, Sep. 2024, doi: 10.1016/J.MINENG.2024.108853.

[26] A. Karppinen, S. Seisko and M. Lundström, "Atmospheric leaching of Ni, Co, Cu, and Zn from sulfide tailings using various oxidants," Miner Eng, vol. 207, p. 108576, Feb. 2024, doi: 10.1016/J.MINENG.2024.108576.

[27] M. Thomas, "Understanding gangue acid consumption in copper sulfide heap leaching: Predicting the impact of carbonates, silicates and secondary precipitates," Miner Eng, vol. 171, p. 107090, Sep. 2021, doi: 10.1016/J.MINENG.2021.107090.

[28] M. Sokić et al., "Kinetics of Chalcopyrite Leaching by Hydrogen Peroxide in Sulfuric Acid," Metals 2019, Vol. 9, Page 1173, vol. 9, no. 11, p. 1173, Oct. 2019, doi: 10.3390/MET9111173.

[29] H. A. Phyo et al., "Effect of particle size on chalcocite dissolution kinetics in column leaching under controlled Eh and its implications," Physicochemical Problems of Mineral Processing, vol. Vol. 56, iss. 4, no. 4, pp. 676–692, 2020, doi: 10.37190/PPMP/124399.

[30] M. J. Khuduwe, A. Shemi and S. Ndlovu, "Extraction of Gold from Tailings Using Ethaline Deep Eutectic Solvent," Minerals 2024, Vol. 14, Page 1239, vol. 14, no. 12, p. 1239, Dec. 2024, doi: 10.3390/MIN14121239.

[31] F. J. Alguacil, "Utilizing Deep Eutectic Solvents in the Recycle, Recovery, Purification and Miscellaneous Uses of Rare Earth Elements," Molecules, vol. 29, no. 6, p. 1356, Mar. 2024, doi: 10.3390/MOLECULES29061356.

[32] İ. Sönmez, K. Şahbudak, L. Kartal and B. Alkan, "Optimization of sulfuric acid leaching of roasted chalcopyrite concentrate with Box–Wilson experimental design," SN Appl Sci, vol. 2, no. 9, pp. 1–8, Sep. 2020, doi: 10.1007/S42452-020-03341-6/FIGURES/3.

[33] M. Zanin, H. Lambert and C. A. du Plessis, "Lime use and functionality in sulphide mineral flotation: A review," Miner Eng, vol. 143, p. 105922, Nov. 2019, doi: 10.1016/J.MINENG.2019.105922.

[34] G. Zhang, Y. Gao and M. Wang, "Effect of sulfidization on the surface property and flotation behavior of heterogenite," Miner Eng, vol. 204, p. 108375, Dec. 2023, doi: 10.1016/J.MINENG.2023.108375.

[35] R. Ninayan et al. "Water-induced changes in choline chloride-carboxylic acid deep eutectic solvents properties," Colloids Surf A Physicochem Eng Asp, vol. 679, p. 132543, Dec. 2023, doi: 10.1016/J.COLSURFA.2023.132543.

Assisted Evaporation Technology for Replacing Solar Ponds, Recovering Water and Integrating Energy

Claudio Acuña-Pérez1, Elías Fernández1, Paula Guerra-Pinto1*

1. Chemical and Environmental Engineering Department, Universidad Técnica Federico Santa María, Chile

**Corresponding author at: Chemical and Environmental Engineering Department, Vicuña Mackenna 3939, San Joaquin, Santiago, Chile, e-mail adress: paula.guerra@usm.cl.*

Introduction

The global transition to electromobility has intensified the demand for lithium-ion batteries, driving the development of more sustainable extraction and concentration processes. In the Salar de Atacama, Chile, lithium (Li) is obtained from natural brines containing about 0.2% Li. The conventional baseline technology relies on large solar evaporation ponds, which operate with irreversible evaporation rates of 6–8 L/m^2/day and require 14–18 months to reach target concentrations. These ponds demand high capital expenditures—representing 30–50% of total investment (about USD 2 million per pond)—yet achieve only limited efficiency, with average lithium recoveries of 40–50% and additional losses caused by infiltration and salt impregnation. Moreover, the scale of the operation exacerbates water scarcity: an area of 56 km^2 of ponds, with an average evaporation rate of 6 L/m^2/day, translates into a daily water loss of approximately 336,000 m^3, equivalent to a continuous flow of 6,450 L/s. In one of the driest regions of the planet, this irreversible loss of water raises major environmental concerns, even though brine evaporation still offers advantages compared to mineral-based extraction routes (Euronews, 2022).

Overcoming the challenge of water recovery from brines remains critical. Conventional technologies face severe limitations: reverse osmosis is restricted to salinities below 70 g/L; ion exchange and solvent extraction are feasible only under conductivities below 10 mS/cm; membrane-based processes become inefficient and costly above 200 g/L; and thermal evaporation or crystallization require significant thermal energy. Although alternatives such as electrodialysis, pervaporation, and forward osmosis are under active development, their applicability to highly concentrated brines containing clays and impurities remains limited (Xu et al., 2021; Butt et al., 2022; Khalil et al., 2022).

As an alternative, a patented technology developed at UTFSM, which introduces a novel system based on the injection of dry microbubbles for simultaneous brine concentration and water recovery (Guerra Pinto & Acuña Perez, 2021). The process relies on supplying extremely dry air—previously dehumidified to near 0% relative humidity in an adsorption tower and conditioned through heat exchangers—into an evaporation tank via porous injectors or impinging jet systems, producing bubbles with controlled diameter distribution. Inside the tank, evaporation is intensified by multiple energy reintegration steps designed to increase solution temperature and accelerate mass transfer. Operating at 80 °C, the air becomes saturated with water vapor, which is subsequently condensed and recovered as distillate, in a process analogous to humidification–dehumidification cycles. Importantly, this approach requires neither high pressure nor chemical additives, while condensation enables partial energy recovery, improving overall efficiency (Figure 1).

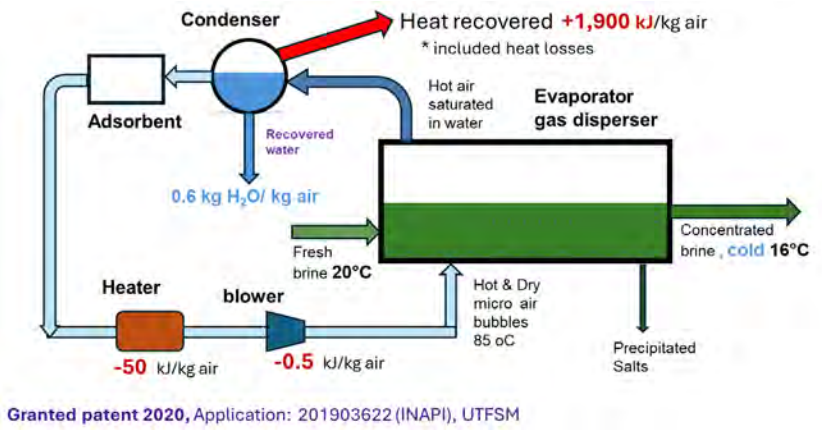

Figure 1. Schematic representation of the patented UTFSM dry-bubble injection technology (201903622, INAPI), developed as an alternative system for simultaneous brine concentration and water recovery.

This innovation directly addresses the limitations of conventional pond systems and emerging membrane or thermal technologies, offering a scalable pathway toward efficient lithium recovery with simultaneous water reuse. In this context, the main objective of this work is to validate the patented dry-bubble evaporation technology under real operating conditions, demonstrating its feasibility at Technology Readiness Level 5 (TRL5). The specific objectives of this work are (i) to design and implement a 15 L pilot unit for assessing evaporation rates and projecting the industrial mechanical design, (ii) to experimentally evaluate the effect of operational conditions—specifically superficial gas velocity and brine temperature—on the evaporation rate in the pilot unit, and (iii) to assess the economic feasibility of the proposed system through CAPEX estimation, cash flow projection, and profitability indicators (NPV, IRR, payback).

Methodology

At the beginning of the prototype testing, it was necessary to characterize the brine extracted from one of the evaporation ponds of the Salar de Atacama used in the experiment. For this purpose, a multiparameter meter (Hanna HI5522) was employed.

The patented dry-bubble evaporation technology was validated under real operating conditions through the design and implementation of a 15 L prototype. The system was constructed in a stainless-steel cell with temperature control (29 × 50 cm cross-sectional area) and equipped with eight porous bubblers (2 cm Ø × 3 cm length), airflow regulation, and temperature monitoring. Gas injection was provided through a drying column system composed of three acrylic adsorption towers (5 cm Ø), packed with commercial silica gel (2.7 mm Ø). The experimental validation followed a factorial design with two solution temperatures (20 and 40 °C) and three superficial gas velocities (0.6, 1.7, and 2.9 cm/s). Figure 2 presents the flow diagram of the laboratory-scale prototype, highlighting the two main stages of the system.

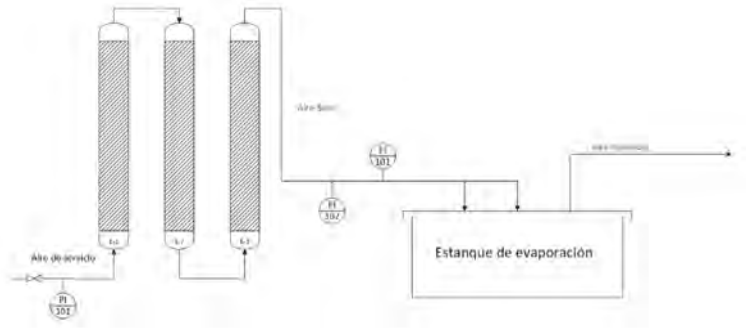

Figure 2. Flow diagram of the laboratory-scale prototype, highlighting the two main stages of the system: the air-drying columns and the evaporation tank.

Desiccant tower system:
Three acrylic adsorption columns were employed to reduce air humidity to ~0.1% relative humidity. The design, previously validated through simulation, divided a 1.5 m tower into three columns of 0.5 m height and 2 inches in diameter, with an L:D ratio of 10 (Figure 3a).

Evaporation tank:
The assisted brine evaporation tank was designed with hermetic sealing, precise temperature control, and porous-tip lances for dry-air injection. Its dimensions were determined by the thermostatic bath, with a transparent acrylic cover allowing injector installation and controlled evaporation while enabling visualization of gas hold-up (Figure 3b). Fusion 360 software was used to generate a 3D design. The effective evaporation area was 0.145 m^2, and eight porous-tip lances were installed with hermetic sealing. The tank was connected to the desiccant stage through a rotameter to regulate airflow.

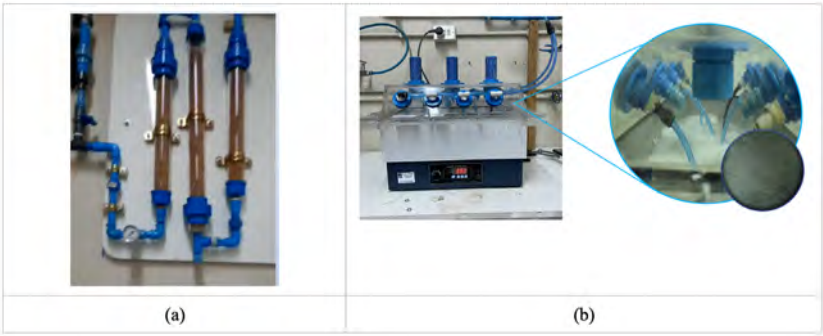

Figure 3. Main components of the laboratory-scale prototype: (a) acrylic adsorption columns packed with silica gel, and (b) assisted brine evaporation tank with hermetic sealing, temperature control, and porous-tip lances for dry-air injection.

Operating procedure: The experimental protocol began by drying the silica gel in a muffle furnace at 120 °C for 90 minutes, after which the adsorption columns were filled with the dry adsorbent. The tank was then filled with brine up to a height of 10 cm, and the solution temperature was set and stabilized using the thermostatic bath. Once ready, the purge valve (V-2, Figure 1) was opened and closed to remove condensate, followed by gradual opening of valve (V-1, Figure 1) up to 6 bar. Air was directed through the desiccant system via valve (V-3, Figure 1) and adjusted to the desired flow. Pressure drops and airflow were continuously monitored and regulated throughout

the operation. Each experimental run lasted 90 minutes, after which the change in brine level was recorded. The procedure was repeated across the defined operating conditions.

Performance evaluation:
The prototype was used to assess the moisture transfer capacity from brine to dry bubbles under controlled conditions (Table 1). The evaporation rate (E) was quantified by measuring the difference in brine level before and after operation, using a millimeter scale attached to the tank wall. The evaporation rate was calculated according to Equation 1:

$$E = \frac{\Delta h}{A_{tank} t_{exp}} \qquad \text{(Equation 1)}$$

where Δh is the difference in brine height, Atank is the tank surface area, and texp is the experimental operation time. This evaluation was performed considering the two main parameters: solution temperature and dry air flow.

Comparison with baseline:
The results obtained from the pilot prototype were compared with the conventional lithium brine concentration process (8 L/m^2/day). This comparison demonstrated the advantages and potential limitations of the proposed design, providing robust evidence of its technical feasibility and added value.

Table 1. Experimental conditions for technological validation

Air flow (Lpm)	Velocity (cm/s)	Solution temperature
50	0.8	20
		40
150	1.7	20
		40
250	2.9	20
		40

Moisture transport capacity:
Finally, the performance of dry bubbles was analyzed up to experimental saturation and compared with the theoretical capacity predicted by the psychrometric chart, which relates air properties to dry-bulb temperature and relative humidity at sea level. The theoretical evaporation rate was calculated according to Equation 2:

$$V_{exp} = \frac{m_{air}}{V_{specific}} \frac{(HA_{max} - HA_{min})}{\rho_{H2O}} \qquad \text{(Equation 2)}$$

where mair is the air mass flow rate, Vspecific is the specific volume of air, HAmax and HAmin correspond to the maximum and minimum absolute humidity, and ρH2O is the density of water, all under the defined operational conditions.

Economic feasibility:

The economic assessment comprised three main steps:
(i) Cost-performance analysis, where the key performance indicator (KPI) was defined as the cost per cubic meter of evaporated and recovered water; (ii) CAPEX estimation, based on equipment quotations; and (iii) cash flow modeling, including key profitability indicators such as Net Present Value (NPV), Internal Rate of Return (IRR) and payback period under different implementation scenarios.

(i) Cost-Performance Analysis: The process flow diagram (Figure 4a) served as the basis for system modeling, which considers an evaporation tank with a top surface area of 12 m^2 (Figure 4b). The design prioritizes energy efficiency by heating the brine and air through four crossflow heat exchangers (HX) and two heat pipes, supplemented by a centrifugal pump, rotary blower, adsorption dryer, and a final condenser to maximize water recovery. A simulator was developed in Microsoft Excel 365 to minimize heat pipe energy demand by adjusting inlet and outlet temperatures (ΔT_1, ΔT_2) of the HX units, assuming equal heat exchange between streams (Equation 3):

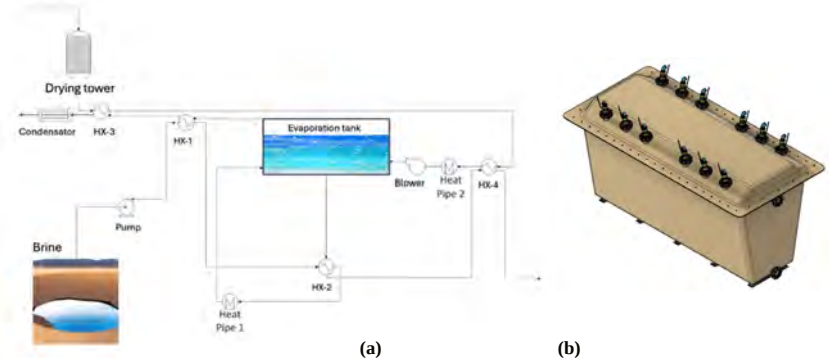

Figure 4. Industrial-scale prototype design: **(a)** process flow diagram and **(b)** evaporation tank.

$$F_1 * Cp_1 * \Delta T_1 = F_2 * Cp_2 * \Delta T_2 \qquad \text{(Equation 3)}$$

where Fn and Cpn (n = 1,2) are the mass flow rate and specific heat capacity of each stream, respectively. The required heat transfer area (Atrans) was determined for each HX using Equation 4:

$$A_{trans} = Q / U * LMTD \qquad \text{(Equation 4)}$$

where Q is the heat duty, U the overall heat transfer coefficient, and LMTD the log-mean temperature difference.

Energy losses due to phase change (ΔH_{evap}) were included following Fan et al. (2018) to maintain thermal stability. The simulator generated brine inlet temperature profiles and quantified energy contributions for air pressure drop (ΔP) at 20 °C and 40 °C, defining operational ranges (Table 2) and a maximum brine inlet temperature of 70 °C. These ranges, together with blower and pump energy consumption and a reference electricity price of 0.0031 USD kWh^{-1} (CNE, Chile), were used to calculate the final KPI.

Table 2. Operational ranges of brine flow in the proposed industrial-scale prototype

Operation temperature [°C]	Air velocity [cm/s]	Operational range of brine volumetric flowrate [m3/h]
20	0.6	[0.1 - 5]
	1.7	[0.2 - 5]
	2.9	[0.75 - 5]
40	0.6	[0.2 - 5]
	1.7	[0.75 - 5]
	2.9	[1 - 5]

(ii) CAPEX Estimation. A detailed quotation was prepared for key equipment, i.e., adsorption column, rotary blower, fiberglass tank, steel beams, air injectors, and centrifugal pump, to derive a reference capital expenditure per tank.

(iii) Cash Flow and Profitability Analysis. A cash flow model was built for a system processing 1 m^3 h^{-1} of brine at 40 °C with an air injection velocity of 1.5 cm s^{-1}. OPEX was estimated at 10 USD m^{-3} of evaporated water. Lithium production was projected from 2022 data (39 kt) using a quadratic growth function (R^2 = 0.96), with a lithium price of 45 000 USD t^{-1} (50 % of 2022 peak), increasing by 5 % annually. Fixed costs included annual electricity consumption (USD 2500 per tank), while variable costs covered annual maintenance (1 % of CAPEX). The total investment per tank comprised equipment plus USD 10000 for construction, depreciated linearly over 15 years with no residual value. The cash flow was evaluated under discount rates of 12 % (typical for mining projects) and 30 % (reflecting TRL 5 risk), incorporating a 25 % mining tax rate. Sensitivity analysis was conducted for scenarios with 100, 200, and 400 tanks (12 m^2 each) to assess how profitability scales with capacity.

Results and Discussions

Brine quality:

The brine had a pH of 7.56, a specific conductivity of 105 mS/cm and a salinity of 354 parts per thousand.

Validation of the Prototype: Figure 5 shows the evaporated volume measured after 90 minutes of operation, clearly showing the thermal effect of the solution: as brine temperature increases, the evaporation rate improves significantly.

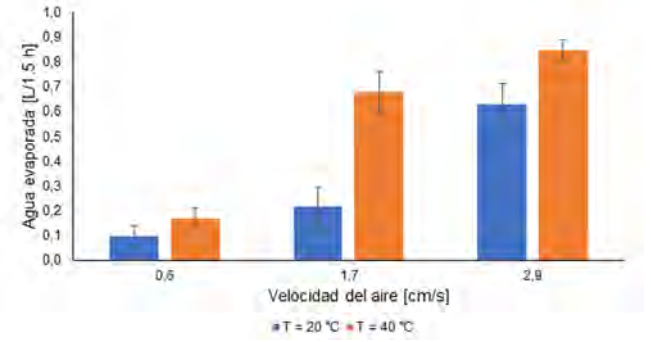

Figure 5. Evaporated volume measured after 90 minutes of operation, evidencing the thermal effect of the solution: higher brine temperatures significantly enhance the evaporation rate.

Comparison with Baseline Process:

The performance of the pilot prototype was benchmarked against the conventional method of lithium brine concentration in solar evaporation ponds. Figure 6 presents the experimental results, highlighting a substantial improvement in evaporation capacity: the prototype achieved evaporation rates 2 to 9 times higher than the baseline, reaching values up to 93 L/m^2 per day. These results confirm the patented principle of dry-bubble injection for intensifying brine evaporation (Guerra Pinto & Acuña Perez, 2021).

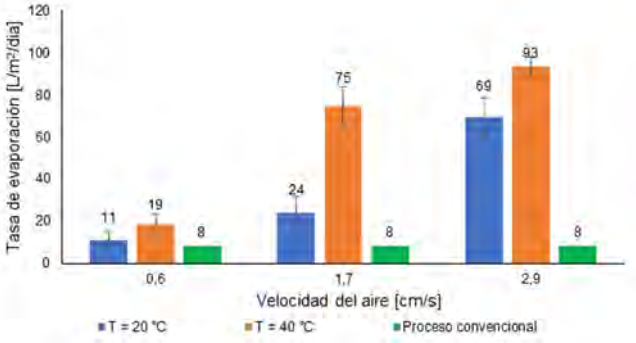

Figure 6. Experimental results showing the improvement in evaporation capacity: the prototype achieved rates 2 to 9 times higher than the baseline, reaching up to 93 L/m^2 per day.

Performance Evaluation:

Prototype performance was also compared against the theoretical moisture transport capacity defined by the psychrometric chart, considering superficial gas velocity as the main sensitized parameter. Figure 7a shows the results at 20 °C, where higher gas velocities enhanced evaporation rates. This effect is attributed to increased gas hold-up, turbulence, and mixing within the bubble column, consistent with previous findings (Letzel et al., 1999; Devakumar et al., 2010). At the highest velocities, over-performance was observed, likely due to bubble-bed disruption and additional evaporation caused by entrainment.

The impact of temperature was then analyzed at 40 °C. Figure 7b illustrates that, as in the 20 °C case, higher superficial velocities increased the evaporation rate. However, efficiency declined at the highest flows, with values remaining below the saturation limit predicted by psychrometric theory. This loss of efficiency can be explained by reduced interfacial viscosity, greater bubble coalescence, and the formation of a thicker gas hold-up layer at the tank surface, which limits bubble saturation.

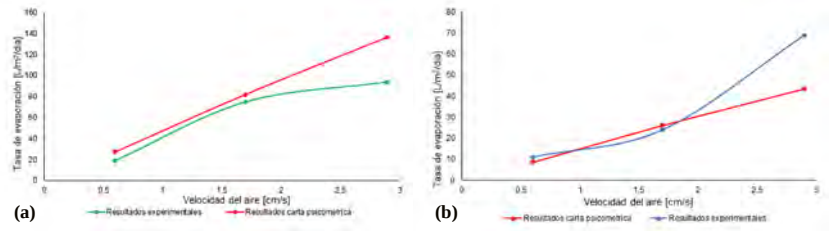

Figure 7. Prototype performance compared with the theoretical moisture transport capacity defined by the psychrometric chart, using superficial gas velocity as the sensitized parameter: (a) results at 20 °C, showing enhanced evaporation rates at higher velocities due to increased gas hold-up, turbulence, and mixing; and (b) results at 40 °C, where higher velocities also increased evaporation but efficiency declined at the highest flows, remaining below the saturation limit predicted by psychrometric theory.

Economic feasibility:

(i) Cost-Performance Results: Operational cost curves were developed for the prototype under different air injection velocities and operating temperatures (Figures 8a y 8b). The most economical operation was achieved at 1.7 cm s^{-1} and 40 °C, with costs ranging between 3–9 USD m^{-3} for evaporated water and 5–11 USD m^{-3} for recovered water, depending on brine flow rate. Using the operational range from Table 2, a brine flow of 1 m^3 h^{-1} was selected as it meets all design scenarios. Figure 9 shows the variation of operational cost per cubic meter of water evaporated or recovered at constant brine flow and different air injection velocities. Overall, the optimal operating point was identified as 1 m^3 h^{-1} brine flow, 40 °C brine temperature, and 1.5 cm s^{-1} air injection velocity, resulting in a final operating cost of approximately 10 USD m^{-3} of evaporated water.

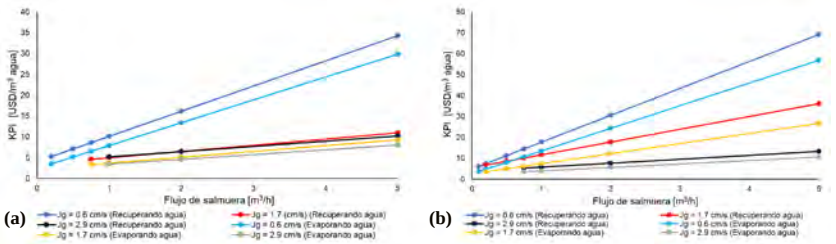

Figure 9. Operating cost of the proposed industrial-scale prototype at 20 °C and 40 °C, with a brine flow rate of 1 m^3 h^{-1} and different air injection velocities.

(ii) CAPEX Estimation: A detailed equipment quotation was carried out to estimate the reference capital cost (Table 2). The total equipment cost per tank was USD 30 163, with the largest contribution coming from the adsorption column (≈ 50 % of CAPEX). Including construction, the total capital cost per unit is approximately USD 40 000. This value may vary depending on equipment specifications, particularly the centrifugal pump, which must handle highly saline brines without scaling or fouling.

Table 2. Capital investment estimate for the industrial-scale evaporation technology, based on detailed equipment quotations.

Equipment	Units	Unit Price (USD)	Total (USD)
Adsorption column	1	14,950	14,950
Blower	1	1,902	1,902
Fiberglass tank	1	6,800	6,800
Steel beams	5	340	1,700
Air injectors	6	780	4,680
Centrifugal pump	1	130	130.79
Total			**30,163**

(iii) Cash Flow and Profitability Analysis: The cash flow model was used to compute NPV, IRR and Payback Period under three implementation scenarios (100, 200, 400 tanks). Results are summarized in Table 3. At a 12 % discount rate, the project yields a positive NPV and a 15-year payback period, with profitability increasing proportionally to the number of tanks. At a 30 % discount rate, the NPV remains negative for all scenarios, indicating the project would not recover its investment under high-risk assumptions.

Table 3. Cash flow analysis results showing NPV, IRR, and payback period for different numbers of evaporation tanks under two discount rate scenarios (12 % and 30 %).

Discount Rate	Tanks	NPV (kUSD)	IRR	Payback
12%	100	2,588	16%	Year 15
	200	5,176	16%	Year 15
	400	10,351	16%	Year 15
30%	100	–2,867	16%	–
	200	–5,734	16%	–
	400	–11,469	16%	–

Conclusions

The results obtained with the implemented prototype demonstrate that effective mass transfer occurs from the humid medium across the bubble interface to the dry medium, significantly increasing the evaporation rate of lithium brines. This validates the proposed method as a promising alternative to accelerate lithium production, positioning it as a transitional technology compared to emerging direct extraction methods such as adsorption, reverse osmosis, and electrolysis.

At laboratory scale, the system successfully combined an evaporation tank with dry-air injection through a desiccant stage, operating between 2 and 12 hours while maintaining control of key variables such as solution temperature and superficial air velocity. This configuration met the requirements for concentration testing and provided reliable operational performance.

The experimental validation confirmed the feasibility of the proposed technology, achieving Technology Readiness Level 5 (TRL5) and evaporation rates up to nine times higher than those of conventional solar pond concentration. These findings highlight the potential of this design to move beyond laboratory implementation and advance toward industrial-scale application.

The economic feasibility assessment shows that the proposed accelerated evaporation system is economically viable under conventional mining discount rates (≈ 12 %). Nevertheless, pilot-scale implementation in real operating conditions is necessary to confirm process efficiency, operational stability, and economic performance before full-scale deployment.

References

Butt, F.S., Lewis, A., Chen, T., Mazlan, N.A., Wei, X., Hayer, J., Chen, S., Han, J., Yang, Y., Yang, S. and Huang, Y., 2022. Lithium harvesting from the most abundant primary and secondary sources: A comparative study on conventional and membrane technologies. Membranes, 12(4), 373.

Devakumar, D., Saravanan, K., Kannadasan, T. and Meenakshipriya, B., 2010. Mass transfer coefficient studies in bubble column reactor. Modern Applied Science, 4(7), 65–72.

Euronews, 2022. South America's 'lithium fields' reveal the dark side of our electric future. Euronews Green Chapter (date), Pages not applicable.

Guerra Pinto, P. and Acuña Perez, C., 2021. Método y sistema para evaporar agua desde piscinas de salmueras que comprende: Suministrar aire a poza de evaporación; secar hasta HR 0% en columnas empacadas con sílice gel; ajustar y controlar T° del aire seco y alimentación de agua; suministrar aire a través de un inyector; y retirar la salmuera concentrada. Patent 62821.

Khalil, A., Mohammed, S., Hashaikeh, R. and Hilal, N., 2022. Lithium recovery from brine: Recent developments and challenges. Desalination, 528, 115611.

Letzel, H.M., Schouten, J.C., Krishna, R. and Van Den Bleek, C.M., 1999. Gas holdup and mass transfer in bubble column reactors operated at elevated pressure. Chemical Engineering Science, 54(13–14), 2237–2246.

Xu, S., Song, J., Bi, Q., Chen, Q., Zhang, W.-M., Qian, Z., Zhang, L., Xu, S., Tang, N. and He, T., 2021. Extraction of lithium from Chinese salt-lake brines by membranes: Design and practice. Journal of Membrane Science, 635, 119441.

CO_2 Capture in Copper Mining: Adsorbents and Tailings Carbonation for Net-Zero Emissions Operations

G. Córdova1*, C. Reinao[1], G. Núñez[1] and I. Cornejo[1]

1. Department of Chemical and Environmental Engineering, Universidad Técnica Federico Santa María, Valparaíso, Chile.

**Corresponding author at: Department of Chemical and Environmental Engineering, Universidad Técnica Federico Santa María, Avenida España 1680, Valparaíso, Chile. Email: guillermo.cordovac@usm.cl.*

ABSTRACT

Copper industry is a significant economic pillar in Chile but also a major source of CO_2 *emissions, particularly from high-temperature processes such as calcination and smelting. Calcination furnaces, including rotary kilns, fluidized beds, and flash furnaces, release* CO_2 *through both fossil fuel combustion and thermal decomposition of carbonate minerals, with dolomitic limestone producing the highest emissions. This study evaluates the technical and economic feasibility of capturing* CO_2 *using modular monolithic activated carbon contactors combined with mineral carbonation of mine tailings for permanent storage. A validated 1D model of a monolithic bed simulated* CO_2 *adsorption under cyclic Temperature–Vacuum Swing Adsorption (TVSA) conditions. According to the results, the scaled system can capture ~69.830 t*CO_2*/year (~70% of furnace emissions) per facility for a furnace emitting ~104.000 t*CO_2*/year. An economic analysis gives a levelized cost of capture of USD 57/t*CO_2 *over 20 years, with activated carbon as the main cost. A sensitivity analysis shows capture efficiency and cost improve at larger scales. Integration with tailings carbonation at sites such as Talabre can sequester 35–241 Mt*CO_2 *over 20 years, providing an in-situ carbon sink. Overall, the combination of adsorption-based capture with tailings mineralization presents a cost-effective and scalable strategy to mitigate* CO_2 *emissions in Chilean copper mining, supporting the transition to net-zero operations.*

Introduction

Copper production is one of the cornerstones of Chile's economy, yet it remains among the most emission-intensive industries, particularly due to the high-temperature operations required. Achieving net-zero goals therefore demands targeted mitigation of CO_2 released in smelting and calcination stages. In the case of Chilean mining, calcination furnaces such as rotary kilns, fluidized beds, and flash systems stand out as major point sources of these emissions (Reuters, 2025). These units operate at temperatures exceeding 800°C and release CO_2 through two main pathways: (i) combustion of fossil fuels such as diesel, natural gas, or petroleum coke, and (ii) the thermal decomposition of carbonate minerals. This latter process is particularly relevant in lime production for metallurgical operations, where high-purity limestone (≥50% $CaCO_3$) is heated in rotary kilns to produce quicklime (CaO) (Greco-Coppi, Hofmann, Walter, Ströhle, & Epple, 2023). The chemical reaction is as follows.

$$CaCO_3 + heat \rightarrow CaO + CO_2 \quad (1)$$

When dolomitic limestone (30–45% $MgCO_3$) is used, the reaction releases even more CO_2.

$$CaCO_3 \cdot MgCO_3 + heat \rightarrow CaO \cdot MgO + 2CO_2 \quad (2)$$

The calcined lime is then processed by screening, grinding, or hydration ($Ca(OH)_2$ production) according to market specifications, but the majority of CO_2 emissions occur during the calcination stage itself. Evidence from analogous industries, such as cement and lime manufacturing, shows that calcination reactions alone account for 60–75% of total direct CO_2 emissions, with the remainder from fuel combustion (Ezekiel, Vandi, & Desai, 2024). Recent studies indicate that a single calcination furnace in copper mining can emit between 20.000 and 60.000 tonnes of CO_2 per year, depending on throughput, operating conditions, and fuel mix. Large facilities like Ministro Hales and Chuquicamata divisions from CODELCO, which operate flash smelting units processing over 500,000 tonnes of concentrate annually, are therefore priority candidates for carbon capture integration (Sonami, 1989). To address these emissions, solid-based CO_2 capture using monolithic contactors filled with activated carbon presents a potentially cost-effective and modular solution. These systems operate at moderate temperatures (50–80 °C) and pressures, making them suitable for remote mining locations such as those in the Antofagasta region. Liquid-based capture methods, such as amine scrubbing, are less suitable for remote mining environments due to their higher operational complexity, corrosion issues, and significant water requirements, making solid adsorbents a more practical alternative (Lai, Ngu, & Hashim, 2021). Biomass-derived activated carbons particularly from coconut shells activated with KOH have shown adsorption capacities above 4.8 mmol CO_2/g at 25 °C and 1 bar, with surface areas exceeding 1.300 m^2/g, making them attractive for industrial-scale deployment (Gayathiri, 2022). Captured CO_2 can be permanently sequestered via mineral carbonation by injecting it into mine tailings rich in calcium and magnesium silicates, forming stable carbonates. This coupling of adsorption and mineral sequestration leverages existing waste streams, providing a long-term in-situ carbon sink. Such integration could significantly reduce net emissions from calcination furnaces in copper mining and align with Chile's long-term climate neutrality goals (Guo et al, 2016).

In that context this research evaluates a dual strategy: (i) adsorption-based capture using activated carbon monolithic contactors, and (ii) permanent storage through mineral carbonation in mine tailings. Together, these approaches provide a pathway to align copper operations with net-zero goals.

Methodology

Development of the 1D Monolithic Bed Model

A one-dimensional model for an activated carbon monolithic bed was first developed in software MATLAB v2024. The representative domain consisted of a single rectangular channel, discretized along the axial direction into nodes as shown in Figure 1. The parameters of the model are listed in Table 1. The model assumes dispersed plug flow, isothermal conditions, and negligible nitrogen adsorption (Ahn & Brandani, 2005).

The mass balance for CO_2 in the gas phase within the porous bed is described by:

$$\frac{\partial C}{\partial t} = \frac{\partial}{\partial z}\left(D_g \frac{\partial C}{\partial z}\right) - v_{ch}\frac{\partial C}{\partial t} - \frac{1-\varepsilon}{\varepsilon}\frac{\partial q}{\partial t} \qquad (3)$$

Where C is the gas-phase CO_2 concentration, v_{ch} the channel velocity, D_g the gas-phase diffusivity, ε the void fraction, and q the adsorbed CO_2 concentration.

The Linear Driving Force (LDF) model was applied to simulate adsorption kinetics:

$$\frac{\partial \bar{q}}{\partial t} = k_{LDF}(q^* - \bar{q}) \qquad (4)$$

Where $q*$is the equilibrium concentration obtained from the Langmuir isotherm:

$$q^* = \frac{q_s bC}{1 + bC} \quad (5)$$

The monolith geometry was represented using Gaussian distributions for channel heights and wall thicknesses, considering both mean values and standard deviations to reflect the variability of the manufactured substrate. This approach allowed the computation of effective void fraction, cross-sectional area, and number of channels, reducing the computational complexity while maintaining accuracy. The adsorption process was simulated at 298 K (25 °C). Desorption, in contrast, would typically be carried out via temperature swing adsorption (TSA) or vacuum swing adsorption (VSA), requiring regeneration temperatures in the range of 80–120 °C.

Table 1. Parameters and values for the monolithic column model (Ahn & Brandani, 2005).

Parameter	Value	Unit
Total length of monolithic column, L	0.5	m
Length of each column section	0.1	m
Cross-sectional area	660	mm²
Average void fraction, ε	0,6827	–
Height of central channels, $h_{ave,l}$ (std. dev. σ_l	0,007	mm
Height of side channels, $h_{ave,s}$ (std. dev. σ_s)	0,008	mm
Mean wall thickness, w_{ave} (std. dev. σ_w)	0,0015	mm
Gas-phase diffusivity, D_g	1.7×10^{-5}	m²/s
Solid-phase diffusivity, D_s	3.3×10^{-9}	m²/s
Langmuir isotherm parameter, q_s	11.532	mmol/cm³
Langmuir isotherm parameter, b	38.503	cm³/mmol

Figure 1. Internal structure of sintered monolithic carbons.

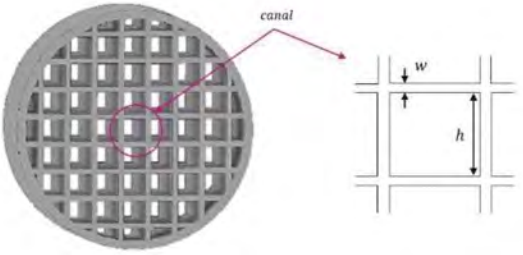

Model Validation

The model was validated by comparing simulated CO_2 breakthrough curves with experimental data reported in the literature (Ahn & Brandani, 2005). In the base comparison, the model underestimated the breakthrough time by roughly 250 s, which can be attributed to uncertainties in bed properties and inlet flow conditions. After applying an empirical adjustment to the channel velocity, the agreement between simulation and experimental data improved significantly shown as Figure 2. Although minor discrepancies remained, the model was able to reproduce the general adsorption trend with reasonable accuracy, supporting its applicability for scaling studies. It is noted that an adjustment factor was employed to match the experimental asymptotic value.

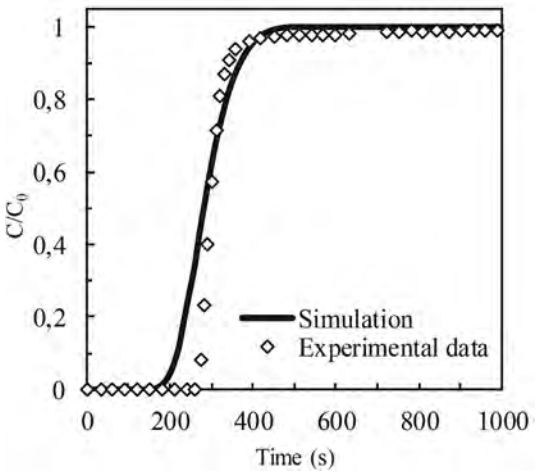

Figure 2. Comparison between experimental data (Ahn & Brandani, 2005) and simulation results.

Scale-Up to Industrial TVSA System

The one-dimensional model of a monolithic activated carbon bed was scaled up to design a modular Temperature–Vacuum Swing Adsorption (TVSA) system adapted to the operating conditions of a flash smelting furnace. These furnaces typically release off-gas streams with CO2 concentrations between 10–14% and flow rates exceeding 50.000 Nm^3/h per unit. The scaling procedure consisted in defining the number and size of parallel adsorption columns required to process the total gas throughput. Each column was modeled as a packed assembly of 12.614 activated carbon monolithic blocks, each block corresponding to a single extruded monolith with regular parallel channels (rather than pellets). These structural units provide the low pressure drop and high contact area required for industrial deployment. Adsorption and desorption steps were defined under cyclic TVSA operation at 293 K and 1 atm, ensuring continuous treatment of the flue gas stream. Column & emission parameters are shown in Table 2.

Table 2. Parameters and values for the monolithic column escalated model.

Parameter	Value	Unit
Colum parameters		
Total length of column	7,00	m
Cross-sectional area	4,91	m^2
Units per industrial column	12.614	–
Emission parameters		
Superficial gas velocity	0,25	m/s
CO_2 concentration	13	%
TVSA operation		
Adsorption time	83,33	min
Desorption time	111,11	min
Operating temperature	293	K
Operating pressure	1	atm

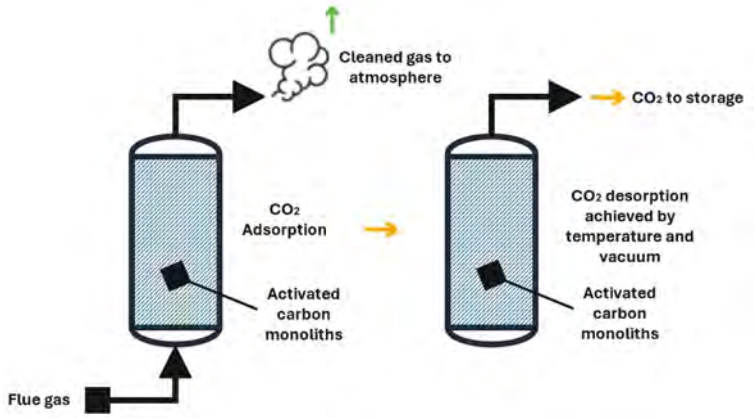

Figure 3. Schematic diagram of the adsorption–desorption capture process using an activated carbon bed.

The proposed scaling ensures that the designed TVSA system can process emissions from a typical industrial calcination furnace, capturing CO2 continuously under cyclic adsorption/desorption conditions, shown in Figure 3. The system can be expanded by increasing the number of parallel columns to accommodate the total annual CO2 emissions of a mining facility. The modular design ensures high capture efficiency while remaining compatible with existing calcination infrastructure.

Results and discussion

Base Assumptions

A base case was established considering a calcination furnace emitting 104.196 tCO_2/year, consistent with typical values reported for flash smelting or rotary kilns in large-scale copper operations (e.g., Chuquicamata or Ministro Hales Division from Codelco) (Sonami, 1989). That number aligns with emission studies from similar processes in the copper industry and was used as the central scenario for scaling the TVSA system. Table 3 summarizes the key operating parameters and performance indicators for the base case of the proposed carbon capture system, including furnace CO_2 emissions, adsorption column requirements, capture efficiency, and sorbent productivity.

Table 3. Parameters and values for the base case of carbon capture.

Parameter	Value	Unit
Furnace CO_2 emissions (base case)	104.196	tCO_2/year
Number of adsorption columns	10	–
CO_2 captured per cycle (per column	2.733	kg CO_2/cycle
Annual manutention time	20	days
Annual operation time	345	days
Cycles per year	2.555	–
Total CO_2 removed (10 columns)	69.830	tCO_2/year
Capture efficiency	~70	%
Specific productivity (realistic)	115	kg CO_2/kg AC/year
Specific productivity (optimistic)	200	kg CO_2/kg AC/year

Detailed operational records from the flash furnace at Chuquicamata provide additional context. Between 2015 and 2020, Codelco implemented a series of projects to upgrade the flash Furnace and improve compliance with environmental regulations, increasing its throughput from 825 ktpa to 1.170 ktpa. These upgrades included enhanced gas capture systems, new acid plants for dual absorption of SO_2, replacement of drying equipment, and improved control of particulate and sulfur emissions. By 2020, the facility achieved a capture efficiency of 97–98% for arsenic and sulfur emissions, demonstrating the effectiveness of emission control measures (Pavez & Álvarez, 2021).

Based on these operational improvements, furnace throughput, and typical CO_2 concentrations in post-combustion gases, it is reasonable to estimate annual CO_2 emissions from the Flash Furnace on the order of 100.000 tCO2/year. This estimate aligns with reported values for large copper operations and provides a realistic baseline for scaling CO_2 capture systems such as TVSA.

Techno-Economic Evaluation

The economic evaluation of the base case, assuming a furnace emitting approximately 100,000 tCO2/year, was conducted under two scenarios: an equipment-only scenario and a full investment scenario. In the equipment-only scenario, the analysis is restricted to the purchase of core process components activated carbon monoliths, adsorption columns, vacuum and heating systems required for thermal swing adsorption (TSA/TVSA) as well as auxiliary equipment such as blowers, piping, instrumentation, silencers, and valves. CAPEX estimation followed a bottom-up approach:

first, equipment costs were derived from the number of adsorption monoliths required (12.614 per column, USD 20–50 per unit), stainless steel columns, blowers, heating and vacuum systems, and auxiliary items, using vendor quotations and cost data from similar PSA/TSA plants. Under this scenario, the total capital expenditure (CAPEX) amounts to USD 7,22 million, with activated carbon monoliths dominating the cost structure by nearly 90% (see Figure 4). By contrast, the full investment scenario expands the scope to include all costs necessary for complete system deployment, covering installation, auxiliary systems, buildings, piping, electrical systems, instrumentation, engineering, supervision, contingency, and working capital. Here, direct costs total approximately USD 11,7 million, while indirect costs including engineering, supervision, legal fees, and contingencies, add another USD 9,1 million, bringing the total CAPEX to USD 20,8 million. When working capital is added, the final capital investment reaches USD 23,9 million (see Figure 5). This stepwise methodology, with explicit reporting of unit costs, scaling factors, and cost allocations, ensures transparency and replicability of the economic assessment.

Figure 4. Equipment-Only CAPEX.

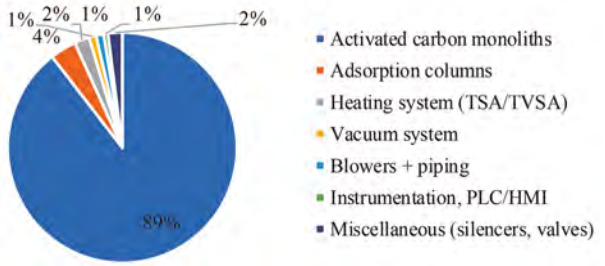

Figure 5. Full Investment CAPEX.

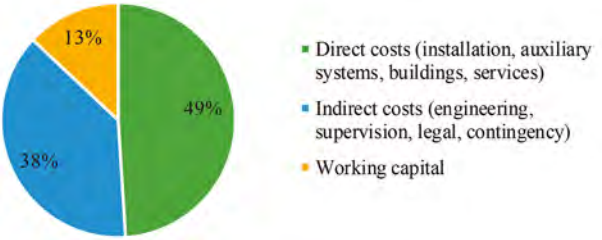

Annual operating expenditure (OPEX) in the full investment scenario is estimated at USD 2,75 million (~11,5% of capital expenditure, CAPEX), which is consistent with the typical range of 8–15% of CAPEX per year for carbon capture systems (Lai, Ngu, & Hashim, 2021). The main operating expenses include energy consumption for heating and gas handling (3–6%), maintenance and periodic replacement of activated carbon monoliths (5–10%), and labor, valves, and other minor services (1–3%). For this design, the dominant contributors are energy use and adsorbent maintenance, while labor and auxiliary costs play a smaller role (see Figure 6).

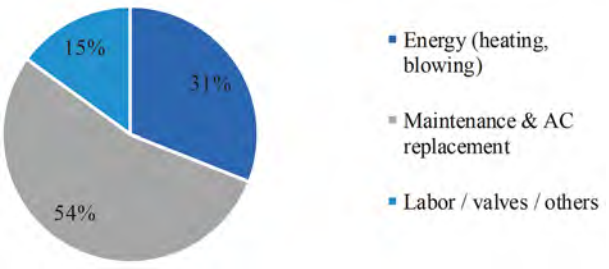

Figure 6. Annual OPEX.

Economies of scale, combined with optimized operations and maintenance, reduce the Levelized Cost of Capture (LCOC) to about USD 57 per tonne of CO_2. This KPI represents the average cost of capturing one tonne of CO_2 over the entire lifetime of the project, accounting for both upfront capital expenditures and recurring operating expenditures. The undiscounted LCOC is calculated as:

$$LCOC = \frac{CAPEX + n \cdot OPEX}{n \cdot Anual\ capture} \quad (6)$$

Where n is the project lifetime (years). In this study, a 20-year horizon was selected, consistent with typical industrial equipment lifetimes and financial evaluation practices in the energy and process industries. A shorter horizon would increase the LCOC, as CAPEX would be distributed over fewer years, while a significantly longer horizon is less realistic due to equipment degradation, adsorbent replacement cycles, and regulatory uncertainty. Thus, 20 years provides a balanced assumption between technical durability, economic relevance, and comparability with similar carbon capture cost assessments reported (Lai, Ngu, & Hashim, 2021), while also aligning with typical lifespans of industrial equipment, financing horizons of large-scale projects, and the long-term planning cycles of mining operations.

Analysis of cost distribution highlights that activated carbon monoliths remain the dominant contributor to CAPEX, accounting for roughly 27% of the total full investment scenario, while the remaining costs are associated with installation, auxiliary equipment, and engineering services. Investing in these additional components enhances system reliability, operational efficiency, and safety, ultimately lowering the levelized cost of capture compared to the equipment-only scenario.

Integration with Mine Tailings Carbonation

Coupling the captured CO_2 stream with mineral carbonation in mine tailings provides an additional and permanent sequestration pathway, particularly relevant for Chilean copper operations such as Talabre (Codelco). Based on available inventory data, Talabre contains approximately 452 Mt of tailings, with a conservative reactive fraction of 3–6% CaO + MgO, which are the main mineral phases capable of forming stable carbonates (SERNAGEOMIN, 2025). Using stoichiometric conversion factors, this corresponds to a carbonation potential of 35–241 $MtCO_2$ over 20 years, equivalent to 7.8–53.3% of current annual furnace emissions (see Figure 7).

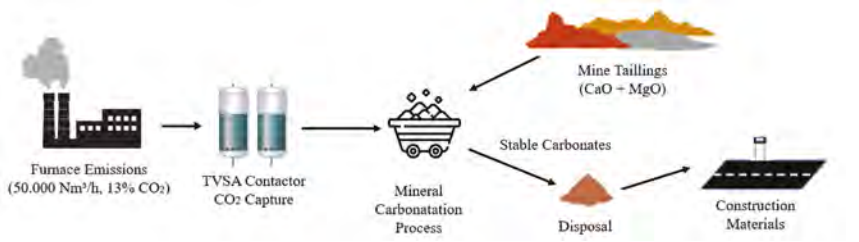

Figure 7. Mine Tailings Carbonation Process.

At the operational scale, the TVSA system considered in this study captures about 69.830 tCO_2/year, which can then be directed to carbonation. The amount of tailings required to mineralize this stream ranges between 1.27 and 2.96 Mt/year, depending on mineral reactivity (7%, 5%, or 3% CaO + MgO, respectively). Over two decades, this represents the mobilization of ~35 Mt of tailings, less than 10% of Talabre's total inventory, highlighting the feasibility of the approach. The 20-year timeframe is consistent with both the expected lifetime of capture units and the long-term mine planning horizon, ensuring comparability with other industrial carbon management strategies. By combining adsorption-based capture with mineral carbonation in existing waste streams, the system not only delivers significant reductions in net emissions but also transforms mining residues into a long-term in-situ carbon sink.

Sensitivity Analysis

A sensitivity analysis was performed across three operational scenarios (Low, Medium, High) to assess the impact of flue gas flowrate and CO2 concentration on capture performance and cost. The preferred visualization is a stacked-bar (cascade-style) chart that separates the annual emitted CO2 into the fraction captured and the fraction remaining uncaptured for each scenario, annotated with capture efficiency, number of adsorption towers, and levelized capture cost (USD/tCO_2).

In low scenario (10 kNm^3/h, 2 towers), the system captures 13.966 tCO_2/yr out of 20.839 tCO_2/yr emitted, achieving 67% capture efficiency. The levelized cost of capture (LCOC) is USD 23.4/tCO_2 for equipment-only but rises to USD 64/tCO_2 when full project costs are considered, reflecting the limited scale and the dominance of fixed costs. In the medium scenario (30 kNm^3/h, 4 towers), capture increases to 27.932 tCO_2/yr, but efficiency decreases to 45% due to the higher baseline emissions (62.517 tCO_2/yr). Here, the LCOC drops slightly to USD 22/tCO_2 (equipment-only) and USD 59.3/tCO_2 (full project), showing partial economies of scale despite efficiency losses. In the high scenario (50 kNm^3/h, 10 towers), the system captures 69.830 tCO_2/yr out of 104.196 tCO_2/yr emitted (67% capture efficiency). Because of the larger throughput and improved scale utilization, costs decrease further: USD 21/tCO_2 (equipment-only) and USD 57/tCO_2 (full project) (see Figure 8 & 9).

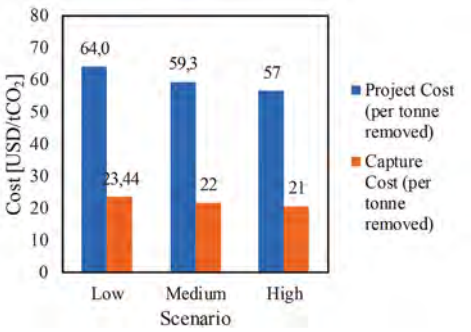

Figure 8. Sensitivity analysis of capture cost (n = 20 years).

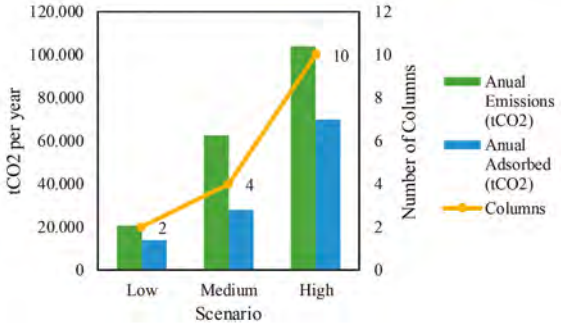

Figure 9. CO2 balance and number of columns per scenario.

This comparative assessment reveals two key insights: (i) capture efficiency is not monotonic with scale, as shown by the dip in the medium case, but absolute CO_2 removal capacity increases significantly with throughput; and (ii) the levelized capture cost consistently decreases with scale, from USD 64/tCO_2 in the low case to USD 57/tCO_2 in the high case, confirming the importance of economies of scale. Additionally, long-term mineral carbonation of tailings offers modest mitigation (0.08–0.39% of annual emissions, 1.6–7.8% over 20 years), reinforcing that direct capture remains the dominant pathway in all scenarios. The apparent drop in capture efficiency in the medium case (45% vs. 67% in the low and high scenarios) is explained by the interaction between flue gas flowrate and adsorption cycle time. At the intermediate throughput (30 kNm^3/h), the fixed cycle duration leads to earlier CO_2 breakthrough in the adsorption columns, meaning that part of the flue gas bypasses capture before regeneration occurs. In contrast, at the low flowrate the residence time is sufficient to fully utilize sorbent capacity, while at the high flowrate the larger number of towers increases effective contact area and balances the shorter mass transfer window. This highlights the importance of cycle optimization for each operating scale: without adjusting cycle time and regeneration scheduling, intermediate flowrates may appear less efficient despite having more towers installed.

Conclusions

This study concludes the technical and economic feasibility of implementing a CO_2 capture and storage system in Chile's copper mining industry, specifically in flash smelting and calcination furnaces. Through the modeling and scaling of a modular temperature and vacuum swing adsorption (TVSA) system using monolithic activated carbons, it was projected that up to 69.830 tCO2/year could be captured, equivalent to an efficiency of nearly 70% of the direct emissions from a large-scale furnace (~100.000 tCO2/year). The economic analysis estimated a levelized cost of capture of 57 USD/tCO2, consistent with reported values for emerging technologies, with economies of scale identified as a key driver for cost reduction. Integration with mineral carbonation of tailings, particularly in Talabre, with a potential of 35–241 MtCO2 over 20 years provides an additional pathway for permanent and on-site storage, leveraging existing waste streams while strengthening alignment with national carbon neutrality goals. Operational sensitivity analysis confirmed that, although relative efficiency may vary with gas flow rate and the number of towers, absolute capture and economic competitiveness improve at larger scales. Overall, the results show that combining activated carbon-based capture with tailings mineralization constitutes a robust, replicable, and infrastructure-compatible strategy, providing a concrete solution to mitigate emissions in one of the country's most carbon-intensive industries. A future pilot-scale validation is recommended to confirm these model projections under real operating conditions.

References

[1] Ahn, H. and Brandani, S. 2005. Dynamics of Carbon Dioxide Breakthrough in a Carbon Monolith Over a Wide Concentration Range. Chemical Engineering Science. 60(4), pp. 1151-1161.

[2] Ezekiel, O., Vandi, D. and Desai, D. 2024. Carbon emissions mitigation methods for cement industry using a systems dynamics model. Clean Technologies and Environmental Policy. 26(3), pp. 845-860.

[3] Gayathiri, M. et al. 2022. Activated carbon from biomass waste precursors: Factors affecting production and adsorption mechanism. Malaysia: Elsevier.

[4] Greco Coppi, M., Hofmann, C., Walter, D., Ströhle, J. and Epple, B. 2023. Negative CO2 emissions in the lime production using an indirectly heated carbonate looping process. Mitigation and Adaptation Strategies for Global Change. 28(3), p. 20.

[5] Guo, L., Yang, J., Hu, G., Hu, X., Wang, L., Dong, Y., DaCosta, H. and Fan, M. 2016. Role of hydrogen peroxide preoxidizing on CO2 adsorption of nitrogen-doped carbons produced from coconut shell. ACS Sustainable Chemistry & Engineering. 4(5), pp. 2806–2813.

[6] Lai, J., Ngu, L. and Hashim, S. 2021. A review of CO2 adsorbents performance for different carbon capture technology processes conditions. Greenhouse Gases: Science and Technology. 11(5), pp. 1076-1117.

[7] Nilsson, E. et al. 2017. A review of the carbon footprint of Cu and Zn production from primary and secondary sources. Minerals, 7(9), 168.

[8] Pavez, I. and Álvarez, J. 2021. Potenciamiento del Horno Flash, Fundición Chuquicamata. PYA Consultores Report. Available from: https://pya.cl/potenciamiento-del-horno-flash-fundicion-chuquicamata/ [Accessed 20 May 2025].

[9] Reuters. 2025. Chilean miner Codelco plans 25% cut in indirect emissions by 2030. Reuters. Available from: https://www.reuters.com/sustainability/chilean-miner-codelco-plans-25-cut-indirect-emissions-by-2030-2025-01-28/ [Accessed 20 May 2025].

[10] SERNAGEOMIN. 2025. Depósitos de relaves identificados en el territorio nacional. Servicio Nacional de Geología y Minería. Reporte Anual.

[11] Sociedad Nacional de Minería (SONAMI). 1989. Horno Flash: causa y efecto de una explosión. Boletín Minero. CXI(32), pp. 5–6.

eDME As a Low-Carbon Alternative in Chilean Copper Mining

Rodrigo Unzueta1*, Ivan Cornejo[1]

1. Departamento de Ingenieria Quimica y Ambiental, Universidad Tecnica Federico Santa Maria, Valparaiso, Chile

**Corresponding author at: Departamento de Ingenieria Quimica y Ambiental, Universidad Tecnica Federico Santa Maria, Valparaiso, Chile, e-mail adress: rodrigo.unzueta@usm.cl.*

ABSTRACT

As Chile's copper mining sector seeks to reduce its carbon footprint, attention has turned to low-carbon alternatives to conventional fossil fuels used across various operations. Among these, diesel remains the dominant source of direct emissions, especially in thermal processes, off-grid power generation, and large-scale haulage. This study examines the potential of renewable dimethyl ether (rDME), with particular emphasis on electro-DME (eDME), as a substitute for conventional fuels in mining, analyzing its technical characteristics, environmental performance, and implementation prospects in the Chilean context.

DME exhibits thermophysical properties compatible with fossil fuels such as diesel and liquefied petroleum gas, which allows its use in certain systems with limited modifications. It can be synthesized from renewable methanol or syngas derived from renewable hydrogen and captured carbon dioxide, or alternatively from biogenic feedstocks. Both routes yield a carbon-neutral fuel, although they differ in terms of cost and scalability. Compared with diesel, DME offers a cleaner combustion profile, significantly reducing soot and nitrogen oxide emissions due to its simple molecular structure and high cetane number. When produced from renewable hydrogen and carbon dioxide, it can reach near-zero or even net-negative carbon intensities.

The Chilean mining sector consumes more than two million tons of fossil fuels annually. Replacing part of this demand with eDME represents a significant opportunity for emissions reduction. The most immediate applications are found in high-temperature thermal processes such as smelting support burners, steam and hot water generation for electrowinning, and drying of non-metallic minerals. In the longer term, there is also potential for use in ultra-class mining trucks, although technical barriers remain for mobile applications. Bio-DME is currently more economical at about 500 USD per ton, but its availability is limited. In contrast, eDME produced from renewable hydrogen and carbon dioxide, while more expensive at present at around 2,000 USD per ton, offers greater scalability and aligns with Chile's Green Hydrogen Strategy. These factors position eDME as a promising candidate to decarbonize fuel use in copper mining.

Introduction

Chile is the world's leading copper producer, and the mining sector represents both a cornerstone of the national economy and a significant contributor to greenhouse gas emissions. Mining activities account for more than 30% of national energy demand, with diesel dominating fuel use in stationary heat processes, off-grid power generation, and large-scale haulage.[1] This reliance on fossil fuels translates into over six million tons of CO2 emissions annually in Chile's mining sector, positioning diesel substitution as a central lever for sectoral decarbonization.

National strategies to accelerate the energy transition, such as the National Strategy of Green Hydrogen, seek to leverage Chile's exceptional solar and wind resources to develop scalable hydrogen derivatives.[2] These efforts respond not only to domestic climate objectives but also to the growing importance of carbon intensity in international trade and investment. Within this framework, renewable dimethyl ether (rDME) emerges as a promising low-carbon alternative fuel.

DME exhibits thermophysical and combustion properties favorable for clean energy conversion. It ignites readily, burns with minimal soot formation, and enables lower nitrogen oxide emissions compared with diesel. It can be synthesized either from biomass residues (bio-DME) or through power-to-X routes that combine renewable hydrogen with captured CO_2 (PtX eDME). Its physical similarity to liquefied petroleum gas also allows partial compatibility with existing storage and distribution infrastructure, reducing barriers to adoption in certain applications.[3-5]

This study evaluates the potential role of eDME in Chilean copper mining as part of a broader decarbonization pathway. The analysis addresses technical properties, substitution opportunities across mining operations, production routes and costs, infrastructure compatibility, life-cycle environmental performance, and policy drivers. By integrating global literature with Chile-specific data, the work aims to identify realistic niches where eDME can complement electrification and hydrogen in reducing the carbon footprint of copper production.

Methodology

This research was conducted through a structured review of the scientific and technical literature combined with an analysis of energy and mining data specific to Chile. The review included searches in databases such as Scopus, Web of Science, and ScienceDirect, as well as institutional repositories and international energy reports (IEA, IEA-AMF, European Commission). Chilean sources, including official energy statistics from the Ministry of Energy, reports from the Superintendence of Electricity and Fuels (SEC), and publications from Cochilco and Consejo Minero, were also incorporated. Keywords used in the search included "dimethyl ether", "renewable DME", "bio-DME", "PtX DME", "CO_2 hydrogenation to DME", "life cycle assessment DME", and "DME mining applications". More than fifty publications were screened during the review, covering both peer-reviewed literature and technical reports.

Academic publications, international reports, and industrial case studies were examined to compile evidence on DME's combustion properties, emission profiles, and performance in engines and industrial systems. Sources covering production technologies were reviewed to compare bio-based and electro-based pathways, with particular attention to techno-economic analyses and advances in catalysts for direct CO_2 hydrogenation. Life-cycle assessments were included to evaluate environmental performance across production routes, with emphasis on carbon intensity, air quality co-benefits, and resource trade-offs such as water and land use.

Chilean energy statistics from the government and mining sector reports were used to quantify current diesel consumption, emissions, and the segmentation of energy demand across stationary and mobile applications. This information provided the baseline for estimating substitution potential with renewable DME in processes such as smelting support burners, electrowinning, off-grid power generation, and heavy-duty transport. Cost data for bio-DME and PtX eDME were drawn from comparative techno-economic evaluations and analyzed in the context of Chile's renewable energy resources, biomass availability, and infrastructure constraints.

The integration of combustion studies, production cost scenarios, life-cycle assessments, and sectoral energy data enabled a comprehensive evaluation of the potential role of renewable DME

in copper mining. The discussion highlights how technical properties, production pathways, and environmental trade-offs intersect with the operational realities of the Chilean mining sector, underscoring both immediate opportunities and the technological gaps that remain for large-scale adoption.

Results and Discussions:

This section examines the role of renewable dimethyl ether in Chilean copper mining from multiple perspectives. It begins with an analysis of thermophysical and combustion properties in comparison with incumbent fuels, establishing the technical basis for substitution. It then reviews diesel consumption in the mining sector to identify priority segments where eDME could achieve the greatest impact. The following subsections address production pathways and techno-economic aspects, infrastructure compatibility and safety considerations, life-cycle environmental performance, and the policy and sectoral drivers that condition adoption prospects.

Technical Properties and Combustion

Dimethyl ether (DME, $CH3OCH3$) is the simplest ether, a colorless and chemically stable compound with approximately 35% oxygen by mass and no carbon-carbon bonds. These structural characteristics explain its distinctive combustion behavior: virtually soot-free burning, very short ignition delays, and strong responsiveness to exhaust gas recirculation for nitrogen oxide control. Its cetane number, typically between 55 and 60, surpasses that of conventional diesel, which usually ranges from 40 to 55. This represents an increase of approximately 10% to 50%, depending on diesel grade, and ensures reliable auto-ignition and enabling compression ignition without the need for pilot fuels when injection systems are appropriately designed.[4,6]

At ambient conditions, DME is gaseous, but it liquefies at moderate pressures of 5–6 bar, making its handling comparable to liquefied petroleum gas (LPG) and enabling storage and distribution in LPG-type tanks and tankers.[3,7] Its low viscosity and limited lubricity require the use of suitable additives when conventional diesel injection systems are employed, providing a practical pathway to ensure durability without major hardware modifications. Alternatively, dedicated injection designs can be implemented to fully optimize performance in commercial applications.[9]

Controlled engine tests have consistently shown that neat DME reduces particulate matter emissions to levels close to the measurement floor (<0.01 g kWh^{-1}) and enables nitrogen oxide reductions of up to 40% with optimized calibration.[5,9,10] Commercial heavy-duty road engines operating exclusively on DME have demonstrated compliance with Euro VI and even anticipated Euro VII standards without exhaust gas particulate filters, while maintaining efficiency comparable to diesel.[6] Full-vehicle prototypes, including buses and freight trucks, confirm the feasibility of DME in demanding duty cycles, with tailpipe emissions of soot, CO, and unburned hydrocarbons significantly lower than those of diesel benchmarks.[5,9]

To position DME relative to incumbent liquid fuels, three properties are particularly relevant. First, the density of liquid DME at room temperature and moderate pressure is approximately 0.66 g cm^{-3}, compared with 0.83–0.85 for diesel and about 0.50–0.56 for LPG. This means larger tanks are required than for diesel to store the same mass of fuel, although volumes remain more manageable than those of LPG. Second, the lower heating value of DME is about 28.9 MJ kg^{-1}, compared with ~42.5 for diesel and ~46 for LPG, which results in a significant penalty in volumetric energy density for mobile applications. Third, DME's ignition quality is excellent, with cetane numbers consistently above 55.[3,6]

Table 1 summarizes these properties, comparing DME with diesel and LPG across key physical, combustion, and emission indicators.

Table 1. Comparative overview of diesel, LPG, and DME properties.[3-10]

Property	Diesel	LPG	DME
Liquified density (g cm^{-3})	0.83-0.85	0.50-0.56	0.66
Lower heating value (MJ/kg)	~42.5	~46	~28.9
Cetane number	40-50	Not applicable	>55
Oxygen content (wt%)	0	0	~35
PM emissions (g kWh^{-1})	0.05-0.1	Very low	<0.01
NOx emissions	Significant	Moderate	~40% with EGR
Storage pressure (bar)	Ambient liquid	7-10	~5

The comparison in Table 1 highlights a clear trade-off: DME offers superior ignition quality, soot-free combustion, and partial compatibility with LPG infrastructure, yet its lower volumetric energy density poses challenges for large-scale mobile applications. These trade-offs are central when assessing substitution opportunities in Chilean copper mining, where fuel logistics and energy intensity vary widely across stationary and mobile uses.

Fuel consumption profile and substitution potential in Chilean copper mining

Diesel remains the dominant fuel in Chilean copper mining, and consequently the principal source of direct emissions. In 2023, the sector consumed approximately 192 petajoules of energy, split almost evenly between electricity and fuels, with diesel representing nearly 90% of total fuel consumption.[1] As illustrated in Figure 1, this predominance underscores its central role in the sector's direct emissions and the strategic importance of targeting it for substitution.

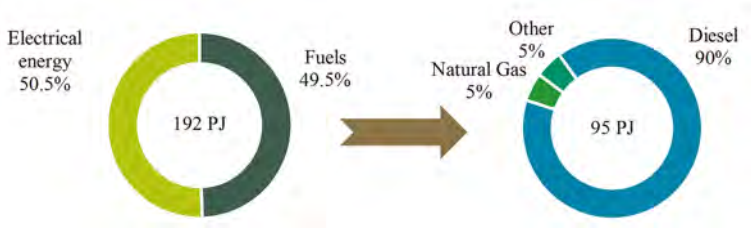

Figure 1. Energy consumption in Chilean copper mining (2023). Data from Cochilco show an almost even split between electricity and fuels, with diesel accounting for nearly 90% of fuel use.[1]

Energy demand is distributed across multiple uses. Open-pit haulage constitutes the most energy-intensive fuel use in mining, but significant amounts of diesel are also consumed in stationary thermal applications such as concentrate drying, smelting support burners, and steam generation for electrowinning[11]. In addition, off-grid and backup power generation represents a smaller yet relevant share, particularly in remote mines located far from the main grid.

This segmentation has direct implications for the substitution potential of renewable DME. Stationary and centralized applications are the most accessible near-term targets, since they can accommodate fuels with lower volumetric energy density without major operational penalties. In these systems, eDME can be introduced through either direct substitution or co-firing with diesel, options already discussed in studies of industrial burners and boilers.[5,12] Remote diesel generator

sets also constitute a promising niche, as their reliance on liquid fuels makes them compatible with DME while offering immediate local air quality benefits.

By contrast, application in ultra-class mining trucks (400-ton class) remains more complex. These vehicles demand very high fuel mass flow rates and are strongly constrained by onboard storage capacity. While international demonstrations in buses and medium-duty trucks have proven the feasibility of DME in compression ignition engines, no trials have yet been conducted at this scale. [5,9] This technological gap represents both a barrier and a research opportunity for the mining sector. While near-term adoption is most feasible in stationary and distributed applications, extending eDME to ultra-class haulage will require large-scale demonstrations before broader deployment in this energy-intensive segment of copper mining.

Production Pathways and Techno-Economics

Two renewable pathways are particularly relevant for DME production. Bio-derived DME can be synthesized through biomass gasification followed by catalytic conversion. Techno-economic studies report production costs of approximately 500 USD/t under favorable feedstock conditions. [5,12] However, scalability is constrained by the limited availability of sustainable biomass in Chile's northern and central regions, where most residues are concentrated in the south and already committed to forestry and bioenergy industries.

The second pathway is electro-based power-to-X (PtX) eDME, in which renewable hydrogen from electrolysis is combined with captured CO_2. This route can follow two alternatives: (i) indirect synthesis via renewable methanol as an intermediate, or (ii) direct hydrogenation of CO_2 to DME in bifunctional catalytic reactors. Recent techno-economic evaluations estimate current production costs in the range of 1,800–2,100 USD/t, depending on renewable electricity prices, electrolyzer costs, and the source of CO_2.[13,14] Figure 2 summarizes these two production pathways, showing their feedstocks and main conversion steps.

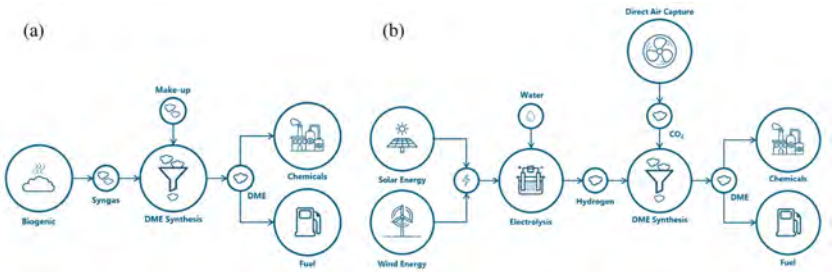

Figure 2. Schematic of renewable DME production pathways: (a) bio-DME via biomass gasification and catalytic synthesis; (b) PtX eDME via renewable hydrogen and CO2 through direct conversion. Adapted from Blue World Technologies[15].

Advances in process intensification aim to improve this outlook. One-step CO_2-to-DME synthesis in membrane-assisted reactors increases conversion efficiency by removing water in situ, thereby reducing hydrogen demand and catalyst inventories.[13] In parallel, significant efforts are focused on catalyst design. Hybrid Cu/ZnO–zeolite systems remain the state of the art, but novel approaches such as core–shell structures and bifunctional catalysts with optimized acid–metal interfaces have demonstrated higher selectivity, greater stability, and improved resistance to deactivation.[16,17] These innovations are critical to achieving commercially viable PtX production routes.

From a climate perspective, the distinction between fossil and renewable DME is fundamental. Fossil DME exhibits life-cycle carbon intensities comparable to conventional diesel and thus does not deliver climate benefits. By contrast, PtX eDME produced with renewable electricity and captured CO_2 can achieve 0–10 gCO2/MJ, while bio-DME from residues may reach 10–30 gCO2/MJ if sustainability criteria are satisfied.[13]

In the Chilean context, bio-DME is limited to small-scale opportunities in the biomass-rich south, while its deployment in northern mining regions would require long-distance transport, adding logistical complexity and costs. By contrast, PtX eDME offers larger-scale potential directly aligned with renewable resources near the mining centers, particularly solar in the north and wind in the south. As summarized in Table 2, these two pathways differ significantly in production costs, scalability, and competitiveness horizons. All those factors must be considered when evaluating their role in the energy transition of the mining sector.

Table 2. Techno-economic and environmental indicators of renewable DME pathways[13,14].

Route	Current cost (USD/t)	Scalability in Chile	Carbon intensity (gCO_2/MJ)
Bio-DME	~500	Limited	10-30
eDME	1,800-2,100	High	0-10

Infrastructure compatibility and safety considerations

As mentioned, DME's physical similarity to LPG provides a pragmatic basis for infrastructure integration. It liquefies at moderate pressures of about 6 bar at room temperature, enabling the use of pressurized storage tanks, piping, and road tankers already familiar to Chilean operators handling propane and butane.[3] International experience shows that blends of up to 12% DME in LPG can be accommodated within existing logistics, offering a low-barrier pathway for pilot projects in boilers and industrial burners.[18] Beyond this range, or when using neat DME, material compatibility becomes critical due to its solvent properties. Elastomers and seals in contact with DME must be replaced with resistant materials such as PTFE, FKM, or EPDM, introducing modest but relevant adaptation costs in pumps and valves.[5,12]

From a safety perspective, DME is classified under UN 1033 as a Class 2.1 flammable gas, the same category as LPG, which allows established handling and emergency protocols to be applied. [19] International assessments indicate that DME is non-carcinogenic and less hazardous than conventional diesel exhaust, although its wider flammability range compared with liquid diesel requires careful leak detection and adequate ventilation in confined environments.[3,5]

Domestic adoption, taken as reference, must align with Chilean regulatory frameworks. The storage and handling of pressurized flammable gases are currently regulated by the Superintendence of Electricity and Fuels (SEC) and by the Ministry of Health's DS 160 on hazardous substances. LPG infrastructure norms would serve as the immediate reference for DME, with certification of tanks, piping, and transfer systems following established procedures. Nevertheless, regulatory updates may be required to explicitly recognize DME as a stationary fuel in industrial combustion systems. [20,21]

Environmental life cycle assessment insights

Life-cycle assessments emphasize that the climate performance of dimethyl ether is highly dependent on the production pathway and the boundary conditions considered. Renewable

options such as bio-DME and PtX eDME can achieve near-zero life-cycle CO2-equivalent emissions, whereas fossil-based DME remains comparable to conventional diesel. In Chile, the most relevant factors are the interplay between resource availability and potential environmental trade-offs.

A first critical factor is the electricity supply. Although fossil-based generation is declining, it still represents a significant share of national production, which raises the carbon intensity of electrolysis-based eDME when connected to the grid.[21] By contrast, direct coupling with dedicated renewable sources such as solar and wind, resources in which Chile holds exceptional potential, would allow life-cycle intensities to approach net-zero CO_2-equivalent emissions and underscores the importance of accelerating renewable deployment for large scale PtX production.

Air quality improvements constitute another consistent advantage across renewable DME pathways. The absence of sulfur oxides, the near elimination of particulate matter, and the potential for deep reductions in nitrogen oxides when combined with exhaust gas recirculation and modern aftertreatment translate into tangible occupational health and safety benefits. These gains are particularly relevant for mining operations at high altitude and in confined underground environments, where exposure levels and ventilation demands are critical concerns.

Resource requirements also play a decisive role. Electrolysis for hydrogen production entails substantial electricity and water inputs, a significant challenge in the arid regions of northern Chile. Scaling PtX eDME in this context will require integration with desalination capacity alongside the expansion of renewable energy. By contrast, bio-DME can deliver favorable carbon performance when derived from certified residues, but its contribution is limited by the low availability of biomass near major copper mining operations.

Policy alignment and drivers for adoption

The aforementioned Chile's National Green Hydrogen Strategy sets an ambitious trajectory that explicitly includes hydrogen derivatives and aims to position the country among the world's leading producers within the next decade. The strategy frames green hydrogen as both a vector for industrial decarbonization and a basis for new export markets, directly supporting power-to-X products such as renewable DME.[2] Operationally, DME extends the hydrogen value chain into a liquid form with easier storage and transport than gaseous hydrogen, while also offering direct compatibility with burners and certain engines.

Domestic price signals still remain weak. Chile currently applies a carbon tax of five USD per ton of CO2 for large stationary sources, yet this level is far from sufficient to close the cost gap between diesel and renewable DME.[21] To accelerate cost discovery and technology learning, stronger policy instruments are needed, including contracts for difference, blending mandates, or concessional financing for early production plants.

External regulatory pressure is increasing. The European Union's Carbon Border Adjustment Mechanism, currently in a transitional phase and scheduled for full implementation in 2026, will expose carbon-intensive exports to a price linked to the European Emissions Trading System. [22] Although copper cathodes are not included in the initial scope, the policy direction is clear: reducing the embedded carbon footprint of copper will be critical for market access. In this context, renewable DME can contribute to lowering stationary combustion emissions in smelters and mining operations.

Corporate and sectoral commitments also shape adoption pathways. The Chilean large-scale mining industry, through Consejo Minero, was the first productive sector to voluntarily commit to

reducing its greenhouse gas emissions. At COP26, member companies of the International Council on Mining and Metals (ICMM), including those operating in Chile, pledged to achieve net-zero Scope 1 and 2 emissions by 2050.[11] These commitments underscore the urgency of reducing diesel use in mining, particularly in haulage, which accounts for nearly 80% of the sector's direct emissions.

Conclusions

Renewable dimethyl ether represents a technically viable and environmentally meaningful option to reduce diesel-related emissions in Chilean copper mining. Its high cetane number, soot-free combustion, and capacity for nitrogen oxide control makes it particularly suited for stationary thermal processes and off-grid power, where adoption requires limited infrastructure adjustments and delivers immediate environmental and health benefits. Applications in ultra-class haulage remain a longer-term prospect, limited by lower volumetric energy density, demanding fuel requirements, and the absence of large-scale demonstrations.

The evidence shows that eDME can complement electrification and direct hydrogen usage within a diversified decarbonization pathway for the sector. Its role is clearer in stationary and distributed applications, while expansion to mobile uses will depend on technological progress and demonstration at scale. In this defined scope, eDME contributes to reducing the carbon footprint of copper production and supporting the sustainability of Chilean mining.

References

1] Comisión Chilena del Cobre, 2024. Consumo energético de la minería del cobre al año 2023 (DEPP N° 17/2024).

[2] Ministerio de Energía, Gobierno de Chile, 2020. Estrategia Nacional de Hidrogeno Verde.

[3] IEA AMF. Fuel information: DME. IEA AMF. https://iea-amf.org/content/fuel_information/dme

[4] Putrasari, Y. and Lim, O., 2022. Dimethyl Ether as the Next Generation Fuel to Control Nitrogen Oxides and Particulate Matter Emissions from Internal Combustion Engines: A Review. ACS Omega, 7(1), 32-37.

[5] Thomas, G. A., Durbin, S. E. and Webb, H. A., 2014. Dimethyl Ether (DME) as a Fuel for Compression Ignition Engines (ORNL/TM-2014/59). Oak Ridge National Laboratory.

[6] Motola, V., Buffi, M., Scarlat, N., Hurtig, O., Georgakaki, A., Letout, S., Mountraki, A., Tattini, J. and Schmitz, A., 2023. Clean Energy Technology Observatory: Renewable fuels of non-biological origin in the European Union 2023 Status Report on Technology Development, Trends, Value Chains and Markets. Publications Office of the European Union.

[7] Marchionna, M., Patrini, R., Sanfilippo, D. and Migliavacca, G., 2008. Fundamental investigations on di-methyl ether (DME) as LPG substitute or make-up for domestic uses. Fuel Processing Technology, 89(12), 1255-1261.

[8] Thomas, G., Feng, B., Veeraragavan, A., Cleary, M. J. and Drinnan, N., 2014. Emissions from DME combustion in diesel engines and their implications on meeting future emission norms: A review. Fuel processing technology, 119, 286-304.

[9] Soltic, P., Hilfiker, T., Wright, Y., Hardy, G., Fröhlich, B. and Klein, D., 2024. The potential of dimethyl ether (DME) to meet current and future emissions standards in heavy-duty compression-ignition engines. Fuel, 355, 129357.

[10] Youn, I. and Jeon, J., 2022. Combustion performance and low NOx emissions of a dimethyl ether compression-ignition engine at high injection pressure and high exhaust gas recirculation rate. Energies, 15(5), 1912.

[11] Consejo Minero, 2025. Towards Net Zero in Chilean Mining.

[12] Azizi, Z., Rezaeimanesh, M., Tohidian, T. and Rahimpour, M. R., 2014. Dimethyl ether: A review of technologies and production challenges. Chemical Engineering and Processing: Process Intensification, 82, 150-172.

[13] Poto, S., Vink, T., Oliver, P. and Gallucci, F., 2023. Techno-economic assessment of the one-step CO2 conversion to dimethyl ether in a membrane-assisted process. Journal of CO2 utilization, 69, 102419.

[14] Im-orb, K. and Piroonlerkgul, P., 2023. Sustainability analysis of the bio-dimethyl ether (bio-DME) production via integrated biomass gasification and direct DME Synthesis Process. Renewable Energy, 208, 324-330.

[15] Blue World Technologies. Renewable Methanol. https://www.blue.world/renewable-methanol/

[16] Mota, N., Millán Ordoñez, E., Pawelec, B., Fierro, J. L. G. and Navarro, R. M., 2021. Direct synthesis of dimethyl ether from CO2: Recent advances in bifunctional/hybrid catalytic systems. Catalysts, 11(4), 411.

[17] Mohamud, M. Y., Abdullah, T. A. T., Ahmad, A., Ikram, M., Alir, A., Phey, M. L. P. and Nabgan, W., 2023. Direct synthesis of dimethyl ether from CO2 hydrogenation over core-shell nanotube Bi-functional catalyst. Catalysts, 13(2), 408.

[18] Fedeli, M., Di Pretoro, A., Montastruc, L. and Manenti, F., 2024. Life Cycle Assessment (LCA) of Dimethyl Ether (DME) Production: Fossil Fuels vs. Biogas. In Computer Aided Chemical Engineering (Vol. 53, pp. 2425-2430). Elsevier.

[19] United Nations, Secretariat, 2024. Present and future products in the liquefied petroleum gas (LPG) industry - Addition of a new special provision to UN 1075 and UN 1965 - Supporting information, research and testing (ST/SG/AC.10/C.3/2024/49).

[20] Ministerio de Economía, Fomento y Reconstrucción, 2009. Aprueba Reglamento de Seguridad para las Instalaciones y Operaciones de Producción y Refinación, Transporte, Almacenamiento, Distribución y Abastecimiento de Combustibles Líquidos. (Decreto Nº 160).

[21] Ministerio de Energía, Gobierno de Chile, 2024. Reporte Público 2024: Avances en los Sistemas de Gestión de Energía.

[22] European Commission. Carbon Border Adjustment Mechanism. https://taxation-customs.ec.europa.eu/carbon-border-adjustment-mechanism_en

Fabrication of Composite Materials for Structural Applications Using Polymeric and Mining Waste From Northern Chile

Felipe Torres Larenas[1], Javiera Vega Acayaga[1], Adriana C. Mera[2], Alexander Alfonso Avarez[1*]

1. Departamento de Ingeniería Mecánica, Universidad de La Serena, La Serena, Chile
2. Unidad de Cambio Climático y Medio Ambiente (UCCMA), Instituto Iberoamericano de Desarrollo Sostenible (IIDS), Universidad Autónoma de Chile, Temuco, Chile

**alexander.alfonso@userena.cl*

ABSTRACT

This work addresses the valorization of polymeric and mining waste through the development of a composite material based on recycled expanded polyethylene (PE) and fine mining tailings. The methodology was structured in two phases: the experimental evaluation of the PE matrix using a factorial design considering thickness, temperature, drying time, and compression condition, and a second phase in which tailings were incorporated in proportions ranging from 10% to 40%. The results showed that the best-performing matrix reached 3.6 MPa, while the composite material with 10% tailings reached 10.6 MPa. It is concluded that reinforcement proportions of 10% and 20% significantly improve the mechanical performance.

Introduction

The accumulation of industrial waste constitutes one of the main environmental challenges in Chile, particularly in the northern region of the country, where mining residues and plastics with low degradability converge. Among these, mining tailings stand out as by-products of mineral extraction that contain heavy metals and toxic compounds capable of contaminating soils, surface, and groundwater, as well as emitting fine particulate matter under dry conditions (Morales, 2022). It is estimated that there are more than seven hundred tailings deposits in Chile, a significant portion of which are inactive or abandoned, representing a latent risk to human health and ecosystems.

Adding to this scenario is the impact of expanded polyethylene (PE), widely used in packaging due to its low cost and versatility, but with extremely low biodegradability. Its inadequate disposal leads to persistent accumulation in landfills and marine ecosystems, contributing to the global problem of plastic pollution (Velazquez, 2017). The combination of mining and plastic waste thus poses a dual environmental challenge: the management of large volumes of waste and the mitigation of their negative effects on health and the environment.

Considering this scenario, it becomes imperative to explore valorization alternatives that can transform these wastes into useful resources. The integration of recycled PE with fine mining tailings into composite materials offers an innovative and necessary proposal, as it simultaneously addresses two critical sources of pollution.

This approach not only contributes to reducing the environmental impact of both wastes but also

aligns with the principles of circular economy and industrial symbiosis, promoting sustainable and regionally applicable solutions.

Methodology

The work was structured in two stages. The first consisted of the experimental evaluation of the recycled expanded polyethylene (PE) matrix through a factorial design, followed by the fabrication of composite materials reinforced with fine mining tailing. The first stage was conducted to identify the most favorable processing conditions for consolidating a recycled expanded polyethylene (PE) matrix. For this purpose, D-Limonene (D-L) was employed as a green solvent to dissolve the polymer, facilitating its handling and enabling its function as a binding matrix, which will be necessary for the subsequent stage. A factorial experimental design was applied, considering four independent variables (Table 1).

Table 1. Processing conditions for the PE matrix.

Variable	Levels
Thickness [mm]	5, 10, 15
Drying temperature [°C]	120 & 180
Drying time [h]	1 & 3
Material condition	Compressed & Uncompressed

From the combination of these variables, 24 test runs were obtained, which were coded to facilitate their reference and to organize the information in groups (Table 2). For each of the combinations (Table 2), five Type V specimens were fabricated in accordance with ASTM D638 for plastics and composite materials, to ensure adequate statistical representativeness of the results.

The fabrication process consisted of the initial dissolution of PE in d-limonene, using 40% of the saturation point at controlled temperature, followed by placing the mixture into molds (Petri dishes). Under compressed conditions, the PE was pre-compacted to reduce its volume and eliminate trapped air before adding the solvent, whereas in the uncompressed condition, d-limonene was incorporated directly into PE in its original state. Subsequently, the matrices were subjected to drying under the previously defined conditions. To ensure the efficiency of the compression process, a study was conducted to characterize the behavior of PE under compression. For this purpose, a fixed volume of 800 ml of PE was used in a cylindrical press, and its response was evaluated at different time intervals under a constant load. The variable analyzed was the remaining height of the material (ht), from which the compressibility ratio was defined (Eq. 1), with h0 = 95 mm.

$$RC = \frac{h_t}{h_0} \qquad \text{(Eq.1)}$$

After drying, the samples were left to cool at room temperature for 48 hours and were subsequently cut using a CNC laser cutter (Aeon Nova14) to obtain five specimens from each, dimensioned in accordance with the standard. The mechanical tests were conducted by means of uniaxial tension using a universal testing machine (Zwick Roell Z100, 100-ton capacity). For each specimen, the maximum stress and elastic modulus were recorded.

Table 2. Coding of the experimental configurations.

Material	Temperature [°C]	Thickness [mm]	Time [h]	Condition
A	120	5	1	Uncompressed
B	120	5	3	Uncompressed
C	120	10	1	Uncompressed
D	120	10	3	Uncompressed
E	120	15	1	Uncompressed
F	120	15	3	Uncompressed
G	180	5	1	Uncompressed
H	180	5	3	Uncompressed
I	180	10	1	Uncompressed
J	180	10	3	Uncompressed
K	180	15	1	Uncompressed
L	180	15	3	Uncompressed
M	120	5	1	Compressed
N	120	5	3	Compressed
O	120	10	1	Compressed
P	120	10	3	Compressed
Q	120	15	1	Compressed
R	120	15	3	Compressed
S	180	5	1	Compressed
T	180	5	3	Compressed
U	180	10	1	Compressed
V	180	10	3	Compressed
W	180	15	1	Compressed
X	180	15	3	Compressed

Using the configuration that achieved the highest ultimate stress (Sut) and elastic modulus (E) in the previous stage corresponding to series H (180 °C, 3 hours of drying, 5 mm thickness, and uncompressed PE) composite materials reinforced with mining tailings were fabricated. The tailings used came from the "El Culebrón" deposit (Coquimbo, Chile), which were previously dried and sieved through a 100 mesh (W.S. Tayler) to obtain fine particles suitable for incorporation into the polymeric matrix. Four composite materials (CM) were prepared by varying the weight ratio of matrix to tailings (Table 3).

Table 3. PE–Tailings Composites.

Composition	Weight ratio
MC-0	100% PE – 0% Tailings
MC-1	90% PE – 10% Tailings
MC-2	80% PE – 20% Tailings
MC-3	70% PE – 30% Tailings
MC-4	60% PE – 40% Tailings

the PE dissolved in d-limonene for 3 hours at 180 °C, the tailings were incorporated hot into the mixture and homogenized by manual stirring. Once the drying process was completed, specimens were prepared in accordance with the standard, allowing them to cool at room temperature for 48 hours. The tensile tests were performed following the same protocol described in the previous stage, comparing the results of the different reinforcement proportions with those obtained for the base matrix (CM-0).

Once the results from both stages were obtained, they were statistically processed by calculating means, standard deviations, and coefficients of variation. The quantitative evaluation of the data was complemented with stress–strain graphs and tables of average results.

Results and discussions

The experimental values of remaining height (ht) and the corresponding compressibility ratio (CR) as a function of the pressure application time are presented in Table 4.

Table 4: Values corresponding to the compressibility ratio.

Time [min]	Remaining height [mm]	Compressibility ratio
2	79.3	0.834
5	87.4	0.919
15	90.75	0.919
30	90.8	0.955
45	91.6	0.964
60	91.9	0.967

Subsequently, the evolution of CR is shown in Figure 1, where an initial significant reduction is observed during the first minutes of compression, followed by a tendency toward progressive stabilization. The analysis of the curve indicates that, although most of the compaction is achieved after 5 minutes, the optimal value is established at 15 minutes, from which point no significant variations in the compression ratio are observed.

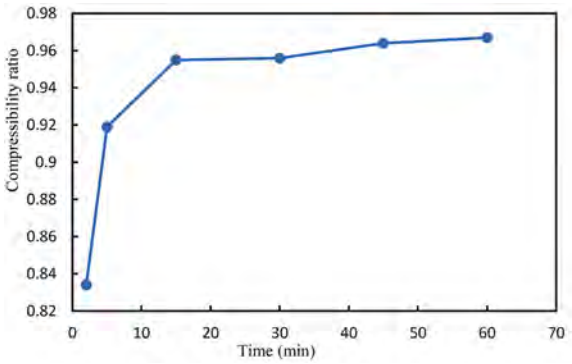

Figure 1: Evolution of compressibility ratio over time.

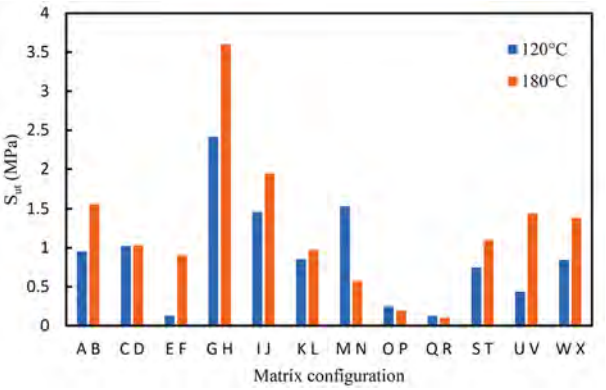

Figure 2. Influence of drying temperature on the ultimate tensile strength of the PE matrix.

The results shown in Figure 2 indicate that the configurations with a drying temperature of 180 °C reached higher ultimate stress values than those at 120 °C in most cases, demonstrating that drying temperature is a determining factor in the mechanical performance of the material. This is consistent with the assumption that part of the D-limonene used for the dissolution of PE remains inside the specimens, thereby affecting the mechanical properties of the material. Therefore, temperatures above the evaporation point of D-limonene are necessary to ensure adequate drying.

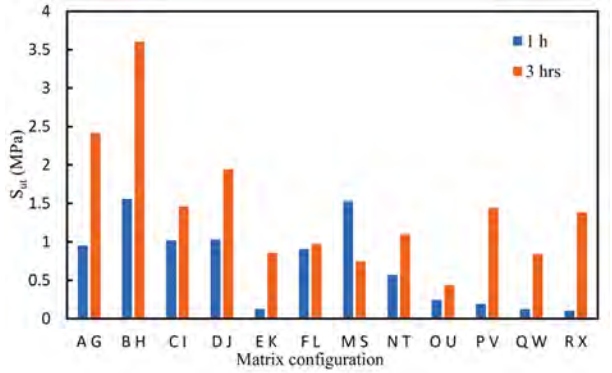

Figure 3. Influence of drying time on the ultimate tensile strength of the PE matrix.

The results shown in Figure 3 indicate that the configurations with a drying time of 3 hours reached higher ultimate stress values than those at 1 hour in most cases, demonstrating that drying time is a determining factor in the mechanical performance of the material. This is consistent with the assumption that part of the D-limonene used for the dissolution of PE remains inside the specimens, thereby affecting the mechanical properties of the material. Thus, longer drying times combined with an optimal temperature ensure the partial or total removal of the residual D-limonene.

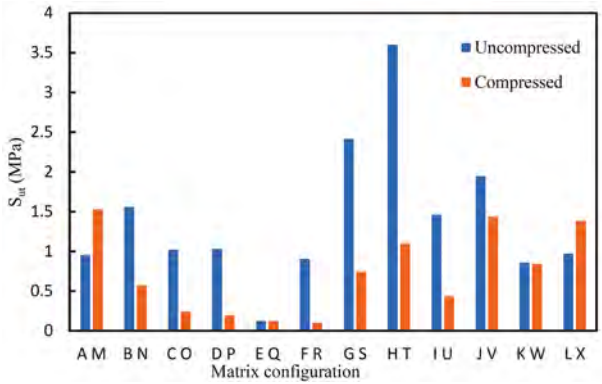

Figure 4. Influence of compression conditions on the ultimate tensile strength of the PE matrix.

The results shown in Figure 4 indicate that the configurations with the uncompressed material condition reached higher ultimate stress values than the compressed ones in most cases, although not by a significant difference in many cases. Therefore, it can be concluded that the uncompressed PE condition is preferable, but not definitive, to ensure higher ultimate stress values.

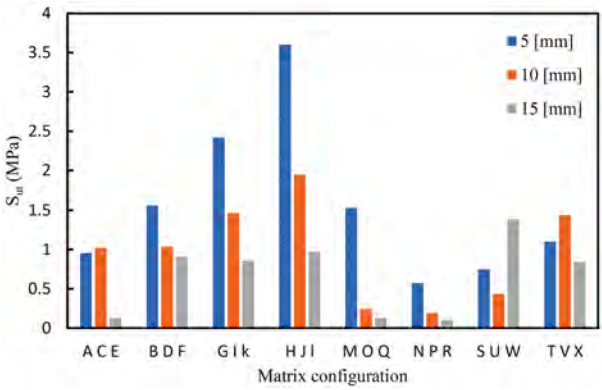

Figure 5. Influence of thickness on the ultimate tensile strength of the PE matrix.

The results shown in Figure 5 indicate that the configurations with a thickness of 5 mm reached higher ultimate stress values than the other cases. This further confirms the assumption that, with a smaller volume, the combined temperature and time conditions allow the evaporation of the D-limonene contained in the specimen.

As a final analysis, the most favorable configuration corresponded to series H (180 °C, 3 hours of drying, 5 mm thickness, and uncompressed condition), reaching an average ultimate stress of 3.6 MPa and an elastic modulus of 856 MPa, values higher than those of the other evaluated conditions. On the other hand, series R (120 °C, 1 hour of drying, 15 mm thickness, and compressed condition) reached an average ultimate stress of 0.104 MPa and an elastic modulus of 1.5 MPa, representing the lowest values obtained.

It is worth saying that the uncompressed specimens showed a performance like those subjected to compression, indicating that it is not necessary to apply an additional compression process to the PE to achieve higher ultimate stress values. This represents a practical advantage, as it simplifies the fabrication process and reduces costs without compromising strength.

The results obtained from the composite material tests (Table 5) indicated that the formulation corresponding to 90% PE – 10% tailings (CM-1) achieved the highest ultimate stress, with a value of 10.6 MPa, significantly surpassing the unreinforced matrix. This increase, equivalent to nearly three times the initial strength, demonstrates that a 10% proportion of tailings as reinforcement enhances the mechanical properties of the composite material. This behavior is clearly observed in the stress–strain curve presented in Figure 6.

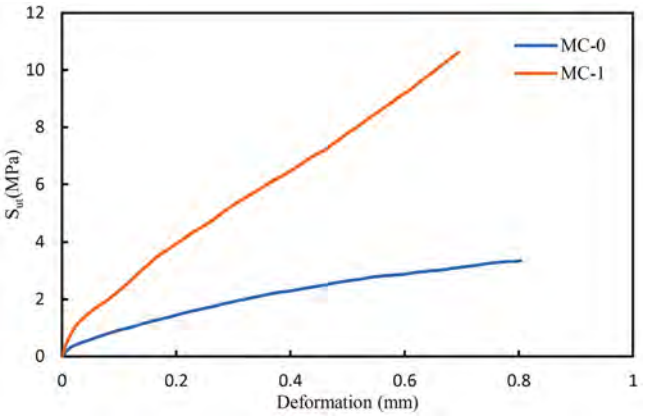

Figure 6. Stress–strain curve of the formulation (10% mining tailings – 90% PE), showing the highest ultimate tensile strength compared with the matrix (0% mining tailings – 100% PE).

The composition CM-2 showed an intermediate performance, reaching an ultimate stress of 8.39 MPa. Although lower than the formulation with 10% reinforcement, it maintained a significant improvement compared to the base matrix, confirming a positive effect of tailings at low and moderate concentrations.

In contrast, the formulations with compositions CM-3 and CM-4 showed a decrease in their mechanical properties compared to the previous compositions. This behavior is attributed to the agglomeration of mineral particles and the loss of homogeneity in the polymeric matrix, which generates weak zones and structural defects that compromise the overall performance of the material. This behavior is consistent with what has been reported in the literature on polymer composites with particulate reinforcements, where low and moderate concentrations lead to improvements in strength, while higher levels tend to cause a loss of properties.

Table 5: Results of tensile tests on composite material specimens.

Material	S_{ut} (MPa)	E (MPa)
MC-0	3.6	856
MC-1	10.6	361
MC-2	8.39	921
MC-3	2.47	656
MC-4	6.90	194

The results obtained support the potential of this approach as a technically and environmentally viable alternative for the fabrication of materials intended for low-demand structural applications, contributing to the valorization of polymeric and mining waste.

Conclusions

From the analysis of the results, it can be deduced that the use of d-limonene, while facilitating the dissolution and initial handling of expanded polyethylene, did not generate a direct improvement in the structural properties of the material. On the contrary, the results suggest that D-L acts mainly as a softening agent and integration medium, rather than as a reinforcing factor. Its contribution should be understood from a processability and sustainability perspective, as it is a natural solvent and less polluting than conventional ones, but not as a component that increases the mechanical strength of the matrix.

In the matrix optimization stage, the most favorable combination corresponded to a drying temperature of 180 °C, 3 hours of duration, 5 mm thickness, and an uncompressed condition. This configuration reached an ultimate stress of 3.6 MPa and an elastic modulus of 856 MPa, while the poorest matrix results were obtained with the configuration of 120 °C drying temperature, 1 hour of duration, 15 mm thickness, and compressed condition, which reached an ultimate stress of 0.104 MPa and an elastic modulus of 1.5 MPa. Furthermore, the finding that the uncompressed specimens did not show a significant improvement in the mechanical performance of the material implies that it is not necessary to incorporate an additional compression process, which simplifies manufacturing and reduces costs. Likewise, the study of the compressibility ratio yielded relevant results, as it was concluded that the optimal value for compressing PE is 15 minutes, which may be crucial for other investigations where it is required.

In the fabrication stage of the PE–tailings composite material, the results evidenced the existence of an optimal reinforcement range. The formulation with 10% tailings reached the highest ultimate stress with 10.6 MPa, followed by the 20% formulation with 8.39 MPa. As the tailings proportion increased to 30% and 40%, the mechanical properties decreased significantly, as shown in the results where composite material 3 reached an ultimate stress of 2.7 MPa and an elastic modulus of 656 MPa, which are lower than the values of the unreinforced matrix. This behavior is attributed to dispersion and cohesion problems between the matrix and the mineral particles.

These results demonstrate that it is possible to obtain composite material with improved mechanical properties through the incorporation of mining tailings as reinforcement. The applied

methodology is adaptable and scalable and aligns with the principles of circular economy and industrial symbiosis. This approach constitutes a technically and environmentally viable alternative for the valorization of polymeric and mining waste, with potential application in low-demand structural elements.

References

Velazquez, J., 2017. Solubility/Insolubility: A possible option for recycling polystyrene. ResearchGate. https://www.researchgate.net/publication/383843966_SolubilityInsolubility_A_Possible_Option_for_Recycling_Polystyrene

Morales, R., Cortés, J. and Muñoz, M., 2022. Emisión de polvo desde depósitos de relaves en el norte de Chile. Información Tecnológica, 33(2), 45–54. https://www.scielo.cl/scielo.php?pid=S0718-07642022000200129&script=sci_arttext

Tangram Technology Ltd., 2021. Design guides for plastics. Tangram Technology. https://tangram.co.uk/wp-content/uploads/Plastics-Topics-Design-guides-for-plastics.pdf

Mustafa Kurt, O. Saban Kamber, Yusuf Kaynak, Gurcan Atakok, Oguz Girit., 2009. Experimental investigation of plastic injection molding: Assessment of the effects of cavity pressure and mold temperature on the quality of the final products.

ASTM D638, Standard Test Method for Tensile Properties of Plastics, ASTM International, West Conshohocken, PA.

Influence of Operational Parameters on Valuable Metal Liberation From Spent Lithium-Ion Batteries Via Cryogenic and Dry Grinding

F. Mulet-Mery[1,2] and J. Valenzuela-Elgueta[1,2*]

1. Department of Metallurgical and Mining Engineering, Universidad Católica del Norte, Av. Angamos 0610, Antofagasta, Chile
2. Lithium I+D+i Research Center, Universidad Católica del Norte, Av. Angamos 0610, Antofagasta, Chile

**Corresponding author at: Department of Metallurgical and Mining Engineering, Universidad Católica del Norte, Av. Angamos 0610, Antofagasta, Chile, jvalenzuela01@ucn.cl.*

ABSTRACT

The increasing production of lithium-ion batteries (LIBs) demands sustainable end-of-life solutions, particularly within recycling processes such as Mechanical Activation, which is essential for the liberation of valuable metals. This study assesses the influence of operational parameters, specifically grinding frequency and time, on both cryogenic and Dry grinding methods, and their impact on particle size reduction and metal liberation from a mixed black mass composed of NMC, LCO, *and* LMO *chemistries. A total of 18 samples underwent controlled Cryogenic grinding. Both grinding methods were tested under frequencies of 10, 20, and 30 Hz and durations of 3, 5, and 7 minutes. A* 3^2 *randomized factorial design was employed for both approaches, allowing the development of a predictive statistical model through second-order polynomial regression. Design of Experiments (DoE) was also used to identify the operational variables with the greatest influence on the* D_{80} *response variable. Characterization was first performed using X-ray diffraction, which revealed distinct associations between crystalline compounds. QEMSCAN and SEM-EDS analyses showed that cobalt-bearing particles (*$LiCoO_2$ *and* Co_3O_4*) tended to be liberated at coarser size fractions (250–450 µm), maintaining a spatial distribution distinct from other phases. In contrast, Ni–Mn-bearing particles,* $(Li_{0.65}Ni_{0.05})(NiO_2)$ *and* $Li_{1.27}Mn_{1.73}O_4$*, were liberated primarily at finer particle sizes, although only ~1% of these were fully liberated. Microtextural features revealed the co-localization of* Co, Ni, *and* Mn *in composite particles, suggesting the presence of layered or spinel-type cathode phases rather than isolated metal oxides. These micrometric particles exhibited plate-like and blocky morphologies typical of metal oxide agglomerate and remain partially liberated at lower grinding intensities. These findings emphasize the key role of grinding frequency in controlling both particle size and the degree of metal liberation, providing valuable insights for optimizing pre-treatment conditions in the efficient recycling of spent LIBs within a circular economy framework.*

Keywords: Lithium-ion batteries, Cryogenic grinding, Dry grinding, Characterization, Mechanical Activation.

Introduction

Lithium-ion batteries (LIBs) have played a crucial role in modern society's growing demand for energy storage due to their excellent electrochemical performance in various electronic devices. Strategies for recycling these batteries have gained interest in recent years, driven by the rising demand for valuable metals and the adverse environmental effects resulting from irresponsible battery disposal. Therefore, the sustainable recovery of metals from these batteries provides not only an economic incentive but also an opportunity to generate greener recycling processes.

Mechanical activation methods for spent lithium-ion batteries (LIBs) include dry, wet, and cryogenic crushing, each with distinct advantages. Dry crushing enables efficient separation of electrodes and separators without chemicals, while wet crushing employs liquid solutions to inactivate lithium and suppress dust, heat, and fire risks. Cryogenic comminution, using liquid nitrogen at extremely low temperatures, enhances brittleness, facilitates fine particle production, and ensures operational safety without prior deactivation.

On the other hand, size conditioning is essential to release target elements by reducing particle size and increasing surface area for subsequent refining. The process depends on operational variables such as frequency and duration, which influence abrasion mechanisms and compound concentration. Studies have shown that comminution followed by screening promotes selective liberation of elements, with **Li, Co, Ni, Mn,** and graphite typically concentrating in the fine fraction (<250 µm), while **Cu, Al,** and **Fe** remain in coarser fractions (Widijatmoko., et al 2020; Zhang et al., 2013; Granata et al., 2012; Mulet-Mery et al., 2025).

The objective of this study is to optimize the reduction of particle size fraction through the frequency-time operational variables, aiming to develop a statistical regression model that represents both processes. Ultimately, evaluate the effect that these milling processes have on critical metal liberation **(Co, Ni, Mn)** through physicochemical characterization.

Methodology

As shown in Figure. 1, the spent LIBs from laptop battery packs were manually extracted and classified according to cathode chemistry. The batteries were deactivated by immersion in a 2 M **NaCl** solution for 24 h [31, 32] and then dismantled using a Dremel 3000 rotary tool (Bosch, Germany) to separate electrodes, separators, and casings. Cathode materials deposited on Al foils were dried at 110 °C for 24 h (Binder, Germany), cut into 0.5–1 cm^2 pieces, and subjected to granulometric separation using an RX-29-10 Sieve Shaker (Gilson, USA). The active material was subsequently calcined at 700 °C for 2 h in a RHF1400 muffle furnace (Carbolite, UK) to remove graphite and organic binders, and homogenized into uniform 25 g samples with a Rotary Micro Riffler (Quantachrome, Germany).

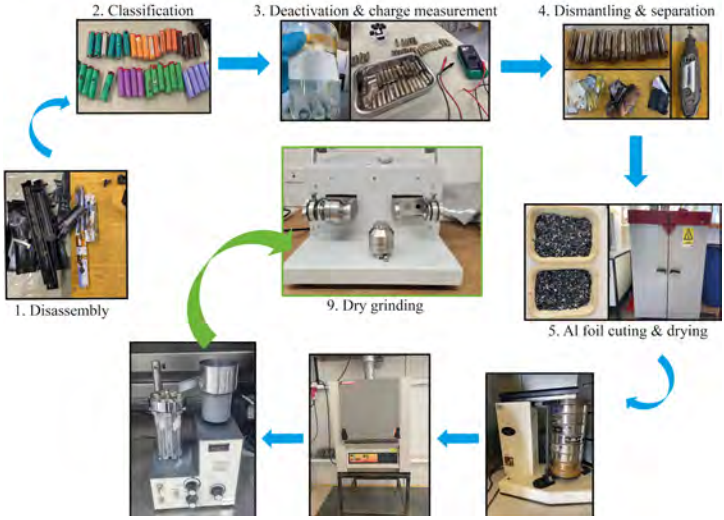

Figure 1. Pretreatment flowchart for the Spent LIBs

Two grinding methodologies were then applied: Dry grinding and Cryogenic grinding. In both cases, a total of 9 samples with a replica each (weight: 25 g each sample), were processed in a BM500 ball mill (Anton Paar, Austria) with a 12 mm iron ball under controlled conditions of frequency (10, 20, and 30 Hz) and time (3, 5, and 7 min). For the cryogenic process, each jar containing the cathodic material and the grinding ball was pre-cooled by immersion in liquid nitrogen for 30 s before milling, ensuring brittle fracture and safe handling of the samples (See Figure 2(a-b)). In contrast, the Dry grinding samples were directly subjected to milling under the same operating conditions.

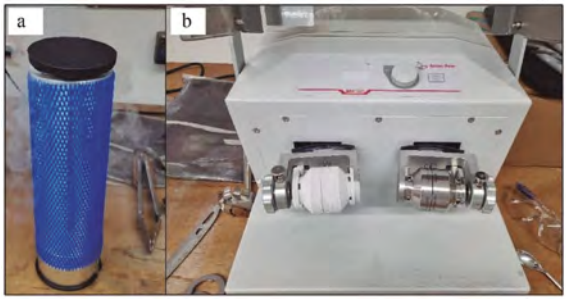

Figure 2. (a) Cryogenic jar containing iron container immersed in liquid nitrogen.
(b) Frozen iron container prepared for grinding.

The experimental design followed a 3^2 factorial scheme with randomized runs, one replica per condition, and statistical analysis performed through Response Surface Methodology (RSM) using MATLAB 2018 for Dry grinding and Minitab 2018 for Cryogenic grinding. The independent factors were grinding frequency and time, while the response variable was the characteristic particle size (D_{80}), determined using a S3500 particle size analyser (Microtrac, USA). A full quadratic model was applied to evaluate both main and interaction effects, with a 95% confidence level (Table 1).

Table 1. Factorial levels used in both experimental designs.

Factors	Coded variable	Unit of measurment	Levels		
			Low (-1)	Standard (0)	High (+1)
Frequency	X_1	Hz	10	20	30
Time	$X2$	min	3	5	7

The characterization of the processed samples was carried out using SEM-EDS, XRD, and QEMSCAN techniques. A Scanning Electron Microscope U5000 (Hitachi, Japan) was employed to obtain both morphological images from SE signals and elemental distribution maps of valuable metals such as **Co**, **Ni**, and **Mn**, with semiquantification performed via EDS using BSE intensities. Structural composition and crystalline changes were assessed through X-ray diffraction (XRD) using a D8 Advance diffractometer (Bruker, Germany). The analysis was conducted with **Cu Kα$_1$** radiation (λ = 1.5406 Å), at 40 kV and 30 mA, with a scan range of 5–70° (2θ) and a step time of 1 s, enabling the identification of metal oxides and quantification of valuable phases. In addition, Quantitative Evaluation of Minerals by Scanning Electron Microscopy (QEMSCAN) was performed using a QEMSCAN Evo 50 (Zeiss, Germany). This non-destructive technique, which integrates EDS and BSE through a pre-defined database, provided high-quality quantification of polished samples and was used to determine the degree of liberation of **Co**, **Ni**, and **Mn** across different particle size distributions.

Results and Discussions

The ANOVA results for both grinding methodologies confirm that frequency is the dominant factor influencing the reduction of particle size (D_{80}). In both dry and Cryogenic grinding, frequency exhibits extremely high F-values (209.6 and 584.4, respectively), indicating that higher grinding frequencies strongly promote particle size reduction. Time also has a significant effect in both cases, although to a lesser extent, while the interaction between frequency and time further contributes to the response. Interestingly, only frequency^2 shows a statistically relevant effect, with stronger significance in the cryogenic case (p-value < 0.001). In contrast, time^2 is not significant for either methodology, confirming that extended time variable alone does not notably affect the D_{80}. Overall, Cryogenic grinding enhances the impact of frequency and its quadratic component, supporting the conclusion that the brittle fracture induced by liquid nitrogen could improve particle liberation efficiency compared to conventional Dry grinding.

Table 2. ANOVA analysis for Dry and Cryogenic grinding.

Source	df	F-value (Dry)	p-value (Dry)	F-value (Cryo)	p-value (Cryo)
Frequency (linear)	1	209.62	5.82×10^{-9}	584.41	1.51×10^{-11}
Time (linear)	1	43.54	2.54×10^{-5}	52.77	9.95×10^{-6}
Frequency^2	1	5.80	0.033	21.18	6.09×10^{-4}
Time^2	1	0.97	0.34	0.28	0.606
Frequency × Time	1	24.55	3.34×10^{-4}	29.95	1.42×10^{-4}
Residual (Error)	12	–	–	–	–

The results presented in Figure 3 clearly demonstrate the effect of the frequency and time variables on the particle size distribution (D_{80} value) for both Cryogenic and Dry grinding. In Figure 3(a–c), corresponding to Cryogenic grinding, a marked decrease in D_{80} value is observed as the frequency increases, highlighting frequency variable as the dominant factor influencing particle size reduction. The time variable also contributes to the response, but its effect is comparatively weaker and becomes more evident at higher frequencies. The interaction plots indicate that while time exerts some influence, the overall reduction in D_{80} value is largely governed by the increase in frequency, consistent with the ANOVA results.

As shown in Figure 3(d–f), which represent Dry grinding, show a similar trend: higher frequencies consistently yield smaller particle sizes, while milling time alone has limited impact. The contour plots for both grinding processes confirm that the smallest D_{80} values are achieved at the highest frequency levels (30 Hz), regardless of grinding time. Notably, Cryogenic grinding tends to produce finer particles overall compared to Dry grinding.

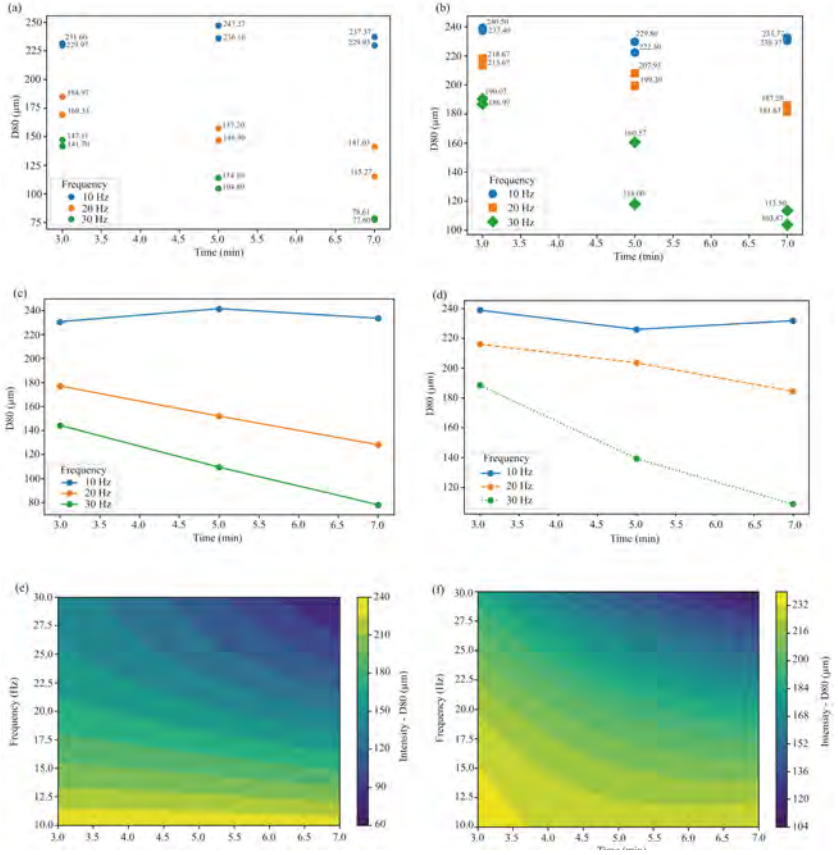

Figure 3. Resulting D_{80} values for each sample and its respective replica, main factor interactions of frequency and time on D_{80} value, and contour plots for cryogenic (a,c,e) and Dry grinding (b,d,f).

The regression equation from the RSM is a second-order polynomial model that describes the empirical relationship between the response and the factors by estimating the regression coefficients, where y is the predicted D_{80} value, X1 is the frequency, and X2 is the time. An optimization model using this equation predicts D_{80} values based on the input factors with accuracy dependent on the model's fit to the original data. This approach was done for both grinding processes, allowing us to use our empirical results to predict how size fraction would react with higher grinding frequencies. This is the equation for Cryogenic grinding:

$$y = 306.70 - 10.14X_1 + 13.80X_2 + 0.21X_1^2 - 0.59X_2^2 - 0.86X_1X_2 \qquad (1)$$

The regression equation shows a good fit, with a coefficient of determination, R2 = 0.98, based on the fit between the experimental data and the predicted data. The predicted D_{80} values indicate that the smallest size fraction D_{80} value equal to 55.82 µm can be obtained at a frequency of 39 Hz and a grinding time of 7 min. On the other hand, the following equation represents Dry grinding:

$$y = 196.9878 - 16.6171X_2 - 36.4605X_1^2 + 3.6129X_2^2 - 8.8282X_1X_2 \qquad (2)$$

The regression model obtained a coefficient of determination, R2 = 0.96, based on the fit between the experimental data and the predicted data. Furthermore, the optimal conditions for obtaining the lowest D_{80} value were found to correspond to a frequency of 35 Hz and a grinding time of 7 minutes. Substituting these values into the regression equation yields a predicted D_{80} value of 62.81 µm, representing the optimal condition for reducing size fraction within the evaluated model.

Based on the results obtained from the diffraction patterns, Table 3 shows the presence of lithium metal oxides such as $LiCoO_2$, $Li_{1.27}Mn_{1.73}O_4$, and $(Li_{0.65}Ni_{0.05})(NiO_2)$, as well as a metallic oxide, Co_3O_4, along with graphite in samples chosen for advanced characterization: M3 (from Dry grinding) and M18 (from Cryogenic grinding). Furthermore, as dismantling was done manually, the samples contain only electrode material, which underwent significant changes due to pretreatment. Cobalt oxide (Co_3O_4) is a common product during the calcination of $LiCoO_2$ at ~ 700 °C, decomposing to form Co_3O_4, which can be easily leached with organic and inorganic acids. Additionally, $LiNiO_2$ is formed from the calcination of NMC cathodic material at approximately 700 °C, which could explain the detection of $(Li_{0.65}Ni_{0.05})(NiO_2)$ in the samples.

Table 3. Identifyied compounds through XRD analysis.

Compounds in M3	Mass percentage (%)	Compounds in M18	Mass percentage (%)
C	50.10	C	22.80
$Li_{0.79}Ni_{1.21}O_2$	30.05	$(Li_{0.65}Ni_{0.05})(NiO_2)$	42.10
$Li(Li_{0.406}Mn_{1.592})O_4$	1.68	$Li_{1.27}Mn_{1.73}O_4$	5.2
$LiCoO_2$	14.81	$LiCoO_2$	20.40
Co_3O_4	3.36	Co_3O_4	9.50

SEM-EDS elemental mapping (Figures 4 and 5) highlights the strong influence of grinding frequency on particle morphology and elemental distribution. At low frequency (M1 and M2, ~10 Hz), **Co**, **Ni**, and **Mn** appear in coarser, more aggregated particles with less homogeneous spatial distribution, consistent with their larger D_{80} values (~233–237 µm). In contrast, high-frequency grinding (M3 and M18, 30 Hz) produces finer, more uniformly dispersed particles (D_{80} ~113 and 77 µm), reflecting enhanced liberation and reduced aggregation due to higher mechanical energy transfer. Notably, Co-rich phases remain thicker than **Ni**- and **Mn**-containing particles across all samples, suggesting that cobalt-bearing oxides tend to be liberated at larger particle sizes.

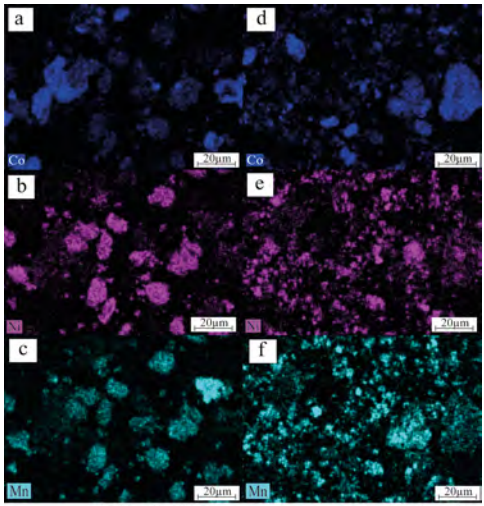

	Mass (%)	Mass Norm. (%)
Cobalt	9.60	52.34
Nickel	5.33	29.06
Manganese	3.41	18.59
Sum	18.34	100.00

	Mass (%)	Mass Norm. (%)
Cobalt	9.82	53.54
Nickel	5.15	28.08
Manganese	3.38	18.43
Sum	18.35	100.00

Figure 4. Co, Ni, and Mn elemental mapping for (a-c) M2 (10 Hz – 7 min – 237.37 µm) and (d-f) M18 (30 Hz – 7 min – 77.60 µm).

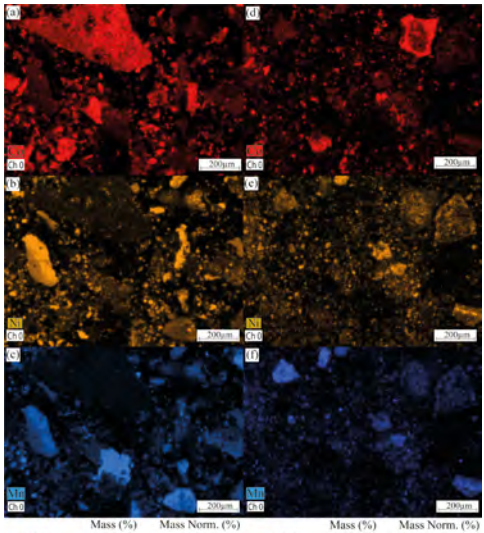

	Mass (%)	Mass Norm. (%)
Cobalt	24.13	62.81
Nickel	8.52	22.18
Manganese	5.77	15.02
Sum	38.42	100.01

	Mass (%)	Mass Norm. (%)
Cobalt	10.50	50.24
Nickel	6.37	30.48
Manganese	4.03	19.28
Sum	20.90	100.00

Figure 5. Co, Ni and Mn elemental mapping for (a-c) M1 (10 Hz – 7 min – 233.37 µm) and (d-f) M3 (30 Hz – 7 min – 113.50 µm). "Ch 0" refers to a channel associated with the Secondary Electron Image.

The liberation analysis (Figures 6 and 7) reveals a distinct behavior for cobalt compared to nickel and manganese. Cobalt shows the highest liberation in coarse fractions (300–425 µm and ≥425 µm), which is consistent with the brittle fracture of $LiCoO_2$ particles during grinding, facilitating the release of Co-rich phases in this range. However, cobalt is also enriched in the fine fractions (<38 µm), where it remains significantly higher than Ni and Mn. This dual distribution suggests that while a portion of cobalt-bearing particles breaks down efficiently into fines, another fraction of $LiCoO_2/Co3O4$ particles is more resistant to fragmentation and persists as larger aggregates. The stronger crystallinity and bonding of $LiCoO_2$ compared to Ni- and Mn-bearing oxides likely explain its persistence in coarser size classes. In contrast, Ni and Mn are more evenly distributed across intermediate fractions, rarely exceeding 35%, indicating that their associated oxides (e.g., layered Ni oxides and spinel-type Mn oxides) are more effectively comminuted into medium size ranges under mechanical stress. Increasing the grinding frequency (M3 and M18) accentuates these trends by producing finer particles overall, enhancing Co liberation in small fractions while still leaving a residual portion in the coarse size classes.

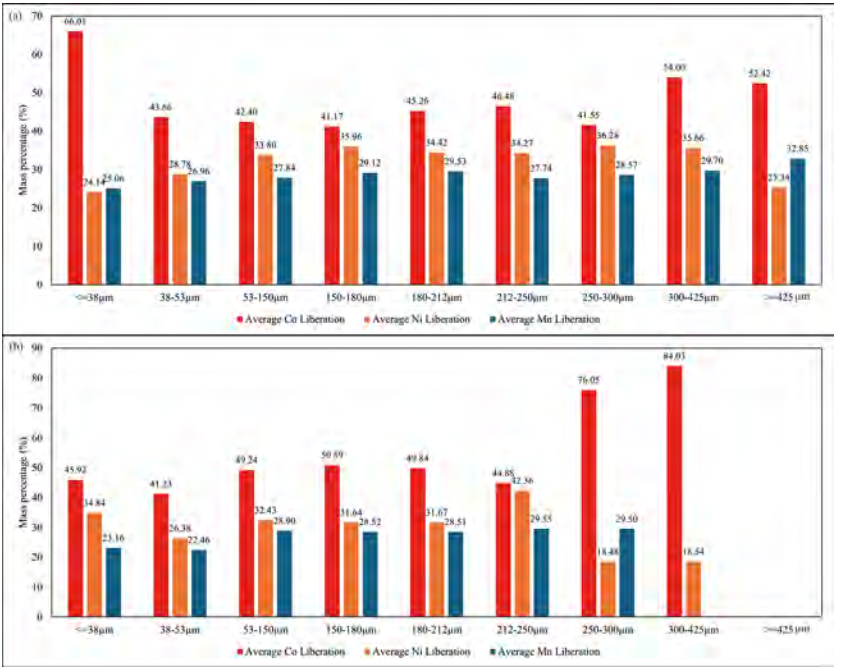

Figure 6. Co, Ni, and Mn average liberation at different size fractions for (a) M2 (10 Hz – 7 min – 237.37 µm) and (b) M18 (30 Hz – 7 min – 77.60 µm) samples.

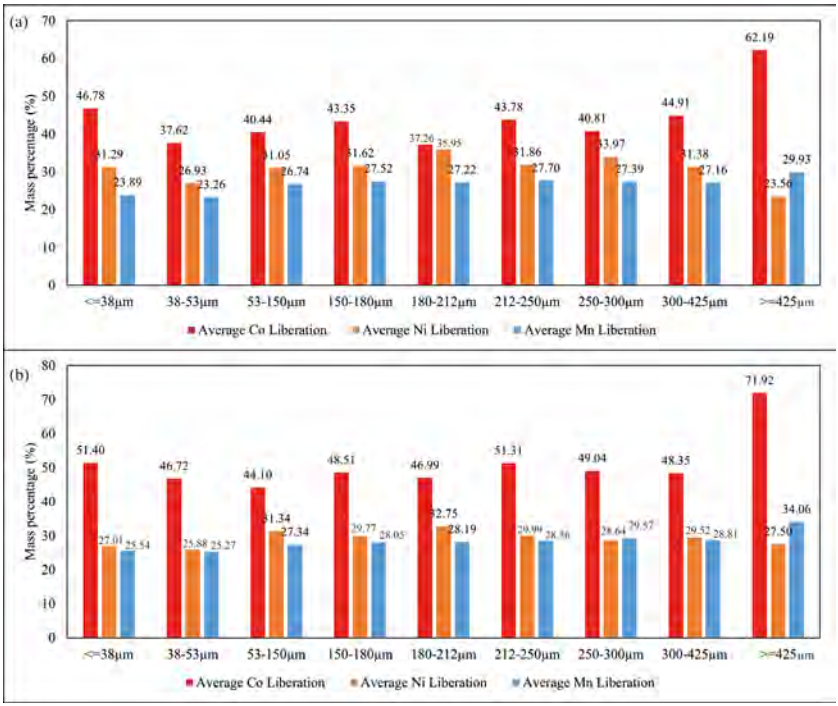

Figure 7. Co, Ni, and Mn average liberation at different size fractions for (a) M1 (10 Hz – 7 min – 233.37 μm) and (b) M3 (30 Hz – 7 min – 113.50 μm) samples.

SEM-EDS micrometric images highlighting differences in particle morphology and elemental composition at varying grinding frequencies. In sample M18 (30 Hz – 7 min – 77.60 μm), a liberated $LiCoO_2/Co3O4$ grain is observed (Figure 8a–b), characterized by a high cobalt content (27.23 wt%) and only minor contributions from **Ni** and **Mn**. In contrast, sample M12 (20 Hz – 7 min – 141.03 μm) shows aggregated particles containing a mixed composition of **Co** (20.27 wt%), **Ni** (21.75 wt%), and **Mn** (13.11 wt%) (Figure 8c–d). These results suggest that higher grinding frequencies favor the liberation of discrete Co-rich particles, while intermediate conditions promote aggregation and coexistence of **Co**, **Ni**, and **Mn** phases within larger composite grains.

Conclusions

This work confirmed that grinding frequency is the dominant parameter influencing the reduction of particle size (D_{80}) and metal liberation in both dry and Cryogenic grinding of spent LIBs. ANOVA results showed very high F-values for frequency (209.6 dry; 584.4 cryogenic), compared to lower but still significant values for time (43.5 and 52.8, respectively), while time^2 was not significant. The regression models predicted minimum D_{80} values of 62.81 μm at 35 Hz and 55.82 μm at 39 Hz, respectively. XRD analyses revealed the presence of $LiCoO_2$, $(Li_{0.65}Ni_{0.05})(NiO_2)$, $Li_{1.27}Mn_{1.73}O_4$, Co_3O_4, and residual graphite, while SEM-EDS elemental mapping showed that high frequencies (M3 = 113.5 μm; M18 = 77.6 μm) produced finer and more homogeneous particles than low-frequency samples (M1 = 233.4 μm; M2 = 237.4 μm). Liberation analysis demonstrated a bimodal behaviour for cobalt, highly enriched both in fine (<38 μm, >45–65%) and coarse (>300 μm,

>50%) fractions, whereas **Ni** and **Mn** remained below ~35% and concentrated in intermediate sizes. Micrometric SEM-EDS images further confirmed that high-frequency grinding promotes the liberation of discrete Co-rich particles, while lower and intermediate frequencies yield **Co-Ni-Mn** aggregates. Overall, the results demonstrate that Cryogenic grinding maximizes particle size reduction and selective liberation, providing critical insights for optimizing LIB recycling processes under a circular economy approach.

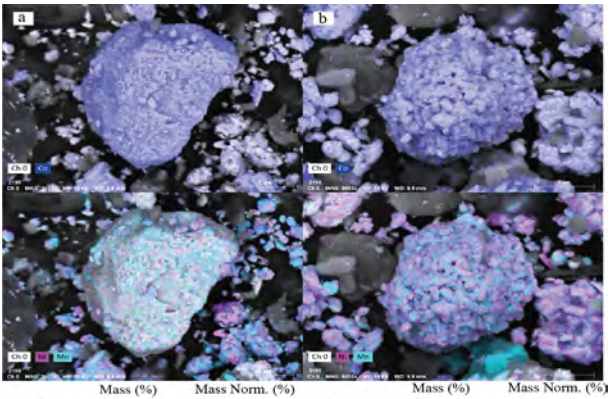

	Mass (%)	Mass Norm. (%)		Mass (%)	Mass Norm. (%)
Cobalt	27.23	72.52	Cobalt	20.27	36.76
Nickel	6.48	17.26	Nickel	21.75	39.45
Manganese	3.84	10.22	Manganese	13.11	23.79
Sum	37.55	100.00	Sum	37.55	100.00

Figure 8. Micrometric images from SEM-EDS. (a-b) Liberated LiCoO2 grain from M18 (30 Hz – 7 min – 77.60 µm) containing 27.23 wt% Co and fewer Ni-Mn content. (c-d) Aggregated Co-Ni-Mn particles from M12 (20 Hz – 7 min – 141.03 µm) exhibiting a content of 20.27 wt% Co, 21.75 wt% Ni and 13.11 wt% Mn. "Ch 0"is a channel associated with the" Secondary Electron Image ", a grayscale morphological image.

References

Widijatmoko. S.. Gu. F.. Wang. Z.. and Hall. P., 2020. Selective liberation in dry milled spent lithium-ion batteries. Sustainable materials and technologies. 23. doi:https://doi.org/10.1016/j.susmat.2019.e00134

Zhang, X., Xie, Y., Lin, X., Li, H., and Cao, H., 2013. An overview on the processes and technologies for recycling cathodic active materials from spent lithium-ion batteries. Journal of Material Cycles and Waste Management, 15, 420-430. https://doi.org/10.1007/s10163 013-0140-y

Granata, G., Pagnanelli, F., Moscardini, E., Takacova, Z., Havlik, T., and Toro, L., 2012. Simultaneous recycling of nickel metal hydride, lithium ion and primary lithium batteries: Accomplishment of European Guidelines by optimizing mechanical pre-treatment and solvent extraction operations. Journal https://doi.org/10.1016/j.jpowsour.2012.04.016

Mulet-Mery, F., Uribe, J., Valenzuela-Elgueta, J., and Serrano, C., 2025. Evaluating Cryogenic grinding variables to maximize valuable metal liberation from spent lithium-ion batteries. Minerals Engineering, 223, 109193. https://doi.org/10.1016/j.mineng.2025.109193

Optimization of the Use of Electric Trucks in Underground Mining Through Renewable Energy Sources

Fernando Soto Naranjo[1,2*], Gonzalo Monsalve[3], Marcos E. Orchard[1,4], Javier Ruiz-del-Solar[1,2], Luis Felipe Orellana[2,5], Ángela Flores[1,6], and Pierre Nancel-Penard[2]

1 Department of Electrical Engineering, University of Chile, Chile
2 Advanced Mining Technology Center (AMTC), University of Chile, Chile
3 Corporate Management of Innovation and Technology, CODELCO, Chile
4 Centro de Aceleración Sostenible de Electromovilidad (CASE), Universidad de Chile, Chile
5 Department of Mining Engineering, University of Chile, Chile
6 Instituto Sistemas Complejos de Ingeniería (ISCI), Universidad de Chile, Chile

**Corresponding author at: Department of Electrical Engineering, University of Chile, Av. Tupper 2007, Santiago, Chile, e-mail address: fernando.soto.n@ug.uchile.cl*

Introduction

Mining operations are among the most energy-intensive industrial activities [Aramendia et al., 2023] and are under increasing pressure to substantially reduce greenhouse gas emissions while advancing toward more sustainable practices [Hernández et al., 2024]. In response to stringent environmental regulations and global decarbonization targets, the industry is actively exploring alternatives to conventional diesel-powered haulage vehicles, which represent a significant share of operational emissions [Bao et al., 2023].

Battery-electric haulage vehicles have emerged as a promising pathway to support this transition [Assimi et al., 2024]. However, large-scale adoption faces uncertainties regarding operational efficiency and cost-effectiveness under real mining conditions [Assimi et al., 2024].

This study addresses these challenges by developing an optimization-based decision-support approach that integrates the operation of battery-electric vehicles (EVs) in underground mining with renewable energy sources. The proposed approach leverages electricity price fluctuations driven by renewable generation availability to strategically schedule EV charging and fleet operations. By aligning energy demand with renewable generation, it is possible to achieve lower operational costs without compromising productivity or reliability [Zhao et al., 2024].

The main objective is to provide a practical tool that supports informed decision-making, enabling mining operators to achieve both environmental sustainability and economic efficiency. By incorporating energy management strategies into daily operations, this work contributes to the industry's transition toward low-carbon, cost-effective haulage solutions.

The remainder of this writing is organized as follows: Section 2 describes the methodology, Section 3 presents the results under different operational and cost scenarios, and Section 4 summarizes the key conclusions.

Methodology

The proposed optimization-based decision-support approach model underground haulage operations at the fleet level, considering both battery-electric and diesel-powered trucks operating under identical production targets considering a one-week operational horizon. The analysis integrates key operational elements, including vehicle activity schedules, energy demand, battery logistics, and associated costs.

The objective function seeks to minimize the total operational costs, expressed as:

$$\text{Total costs} = \min \sum_t^T \sum_i^I c_t \cdot P_{i,t}\, \Delta t \quad (1)$$

where ct represents the electricity cost at time t and Pi,t the power consumption of truck. The metrics used to compare the different technologies were: (1) total operational cost, (2) total material transported, and (3) utilization. Total material transported was defined as:

$$\text{Total Material} = \sum_t^T \sum_i^I \sum_j^J M_{i,j,t} \quad (2)$$

Where Mi,j,t denotes the material moved by truck i from ore pass j at time t. Fleet utilization was expressed as:

$$\text{Utilization} = \frac{T_{use}}{T_{use}+T_{available}} \quad (3)$$

In this expression, $Tuse$ corresponds to the time spent in productive activities (travel, loading, and discharging), while $Tavailable$ represents the remaining available time, excluding charging periods or breaks between shifts.

This study evaluates battery-electric trucks equipped with battery swapping technology. Each battery swap is modeled as a 15-minute process, which includes traveling to the nearest swapping station, executing the battery exchange, and returning to the operation level. This approach eliminates charging downtime at the production front and allows for more effective fleet utilization. The case study assumes haulage distances between 1.5 km and 2 km from the ore passes to the dump point. Ore pass operations are incorporated with explicit constraints on storage capacity and minimum/maximum material levels, ensuring operational feasibility by avoiding overflow or depletion while maintaining coordination with production. Four ore passes are considered in this case, and any vehicle can load ore into any ore pass and discharge it at a single common dump point. Five vehicles are evaluated under three operational configurations.

The first configuration involves EVs with variable electricity costs, supplied by a solar energy source. In this case, electricity prices depend on the time of day — higher at night and lower at noon.

The second configuration also uses EVs, but with fixed electricity costs, meaning a constant cost per kWh consumed. The third configuration, which serves as the base case, considers the use of diesel trucks. The optimization determines the optimal allocation of tasks, charging schedules, and ore pass usage, aiming to minimize total operational costs. Comparative analyses evaluate cost savings, effective fleet utilization, and operational performance for both technologies under equivalent ore transport requirements.

It should be noted that the current model assumes deterministic operating conditions and does

not explicitly incorporate probabilistic events such as equipment failures, variable travel times, or unexpected production delays.

Results and Discussions

Table 1 presents the optimization results for the three operational configurations: battery-electric haulage with variable costs, battery-electric haulage with fixed costs, and conventional diesel trucks. The findings show a clear cost advantage for battery-electric haulage. Under the variable-cost scenario, total operational costs amount to 3,492.67 $, which represents a reduction of nearly 88% compared to diesel operations (29,237.6 $). Even when fixed costs are considered, the electric alternative remains substantially more cost-effective at 6,991.12 $, corresponding to a 76.09% reduction relative to diesel. These results emphasize the potential competitiveness of battery-electric fleets, particularly when their operation is synchronized with electricity price fluctuations driven by renewable energy availability.

Operation	Total operational costs	Total material transported	Utilization
Electric with variable costs	3,492.67 [$]	197,720 [ton]	73.00 %
Electric with fix costs	6,991.12 [$]	197,720 [ton]	75.46 %
Diesel	29,237.6 [$]	197,720 [ton]	71.14 %

Table 1. Summary optimization-results for one week operation.

The total material transported in one week is constant at 197,720 tons across all scenarios, ensuring that production targets are met regardless of the haulage technology. This confirms that the proposed optimization framework achieves operational feasibility without compromising productivity, while enabling a fair comparison between technologies.

In terms of utilization, battery-electric trucks slightly outperform diesel units, reaching 73.00% in the variable-cost case and 75.46% when fixed costs are considered, compared to 71.14% for diesel. Although the differences are modest, the results suggest that battery swapping can be integrated into haulage operations without compromising efficiency, allowing the electric fleet to achieve utilization levels comparable to or slightly higher than diesel. This improvement is partly attributed to the way available time is measured: in the case of electric trucks, battery swapping events reduce the total available time ($Tavilable$) considered in the utilization metric. Consequently, even though each swap takes 15 minutes, the proportional effect is to increase the ratio of productive time relative to total time, slightly boosting utilization compared to diesel. The results confirm that explicitly modeling the 15-minute battery swapping events does not hinder operational performance and instead validates the feasibility of incorporating this process into underground haulage scenarios.

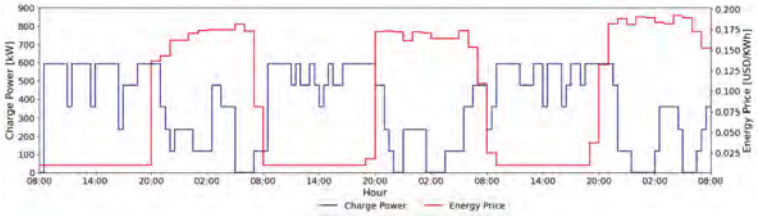

Figure 1. Charging power profile versus variable electricity cost for the first three days of the week, showing charging concentrated in low-price periods and avoided during peak.

A further insight is provided by the analysis of charging station power profiles versus variable electricity costs (Figure 1). The optimization exploits periods of lower electricity prices to recharge the spare batteries stored at the station, while avoiding charging during peak price intervals. This behavior demonstrates the capability of the model to integrate energy market dynamics into operational decisions, effectively reducing exposure to high-cost electricity. This flexibility provides a key advantage over diesel by aligning energy use with renewable generation peaks, thereby lowering average costs and smoothing operational expenses over time.

Overall, the results demonstrate that battery-electric haulage supported by battery swapping technology can deliver substantial cost savings while maintaining productivity and fleet utilization. The strong performance under the variable-cost scenario further highlights the importance of aligning energy demand with renewable

generation profiles and electricity market dynamics. These findings suggest that battery-electric haulage is not only a viable alternative to diesel but also a strategic enabler of low-carbon, cost-efficient mining operations.

Moreover, future studies could extend the analysis by incorporating additional operational scenarios, such as the temporary unavailability of an electric truck or alternative electricity pricing schemes, to further explore the robustness and adaptability of the proposed framework.

Conclusions

This study developed and applied an optimization-based decision-support framework to evaluate the performance of battery-electric haulage systems with battery swapping technology in underground mining operations. The model explicitly incorporated fleet scheduling, ore pass constraints, and energy management under variable electricity prices driven by renewable generation availability.

The results demonstrate that battery-electric haulage can deliver substantial economic advantages over diesel alternatives, with cost reductions of nearly 90% under variable-cost scenarios and close to 75% even when fixed costs are included. Importantly, these savings were achieved without compromising productivity, as all scenarios transported the same total material, and with slightly higher fleet utilization for the electric alternatives.

Furthermore, the analysis of charging station power profiles showed that the optimization framework effectively aligns energy demand with periods of lower electricity prices and renewable generation peaks, thereby reducing average operational costs and smoothing expenses over time. This flexibility highlights the potential of integrating energy market signals into daily mining operations.

Future work could extend the analysis by incorporating probabilistic events inherent to underground mining operations, such as equipment failures, variable travel times, or unexpected production delays, to capture more realistic operational dynamics and further validate the applicability of the proposed framework. In doing so, this line of research can contribute to the development of models that facilitate the adoption of sustainable haulage technologies in mining.

References

Aramendia, E., Brockway, P. E., Taylor, P. G. and Norman, J., 2023. Global energy consumption of the mineral mining industry: Exploring the historical perspective and future pathways to 2060. Global Environmental Change, Chapter 83, p. 102745.

Assimi, H., Ataabadi, S. N. H., Islam, S. M. M., Soong, W. L. and Pourmousavi, S. A., 2024. Toward underground mobile fleet electrification: Three essential steps to make a real change. IEEE Electrification Magazine, Chapter 12(1), pp. 16–26.

Bao, H., Knights, P., Kizil, M. and Nehring, M., 2023. Electrification Alternatives for Open Pit Mine Haulage. Mining, Chapter 3, pp. 1–25.

Hernández, P. A., Obaya-Valdivia, L., Escudero, L. F. and Barbosa-Póvoa, A. P., 2024. A case study on sustainability transitions under green pressures in the mining industry. Resources, Conservation & Recycling, Chapter 202, p. 107510.

Zhao, X., Zhang, Y., Li, J. and Wang, Z., 2024. Integrated energy system scheduling with renewable energy accommodation and demand-side response. Energy, Chapter 304, p. 130651

Sizing of Charging Infrastructure for Battery-Electric Equipment in Underground Mining

Agustín Vilches[1,2], Gonzalo Monsalve[3], Gonzalo Ramírez[3], Javier Ruiz-del Solar[1,2], Luis Felipe Orellana[2,4], Marcos E. Orchard[1,5], Ángela Flores-Quiroz[1,6]

1. Departament of Electrical Engineering/ University of Chile, Santiago, Chile
2. Advanced Mining Technology Center (AMTC)/Universidad de Chile, Santiago, Chile
3. Gerencia Corporativa de Innovación y Tecnología, CODELCO
4. Departament of Mining Engineering/University of Chile, Santiago, Chile
5. Centro de Aceleración Sostenible de Electromovilidad (CASE), Universidad de Chile
6. Instituto de Sistemas Complejos (ISCI), Universidad de Chile

**Corresponding author at: Departamento de Ingeniería Eléctrica/Universidad de Chile, Santiago, Chile , e-mail adress: agustin.vilches@ug.uchile.cl.*

Introduction

To meet decarbonization and emission reduction targets, both globally and nationally, a comprehensive strategy is required that involves the main emitting sectors. In this context, the mining industry stands out as one of the sectors with the highest emission levels, making its transformation crucial to advance toward a more sustainable economy.

One of the most relevant strategies to reduce the carbon footprint in mining is the electrification of vehicle fleets, traditionally composed of diesel equipment that represents a significant share of the sector's total emissions. The integration of battery-electric equipment into underground mining operations introduces new challenges. It requires adequate planning of both electrical and mining infrastructure to enable efficient operation.

Block caving is an underground mining method that takes advantage of gravity and the internal stresses of the rock mass to induce its natural fracturing into fragments suitable for handling by machinery. In this approach, the block is undercut at its base through controlled drilling and blasting, triggering its progressive collapse as extraction proceeds from the lower draw points of the deposit. The fragmented material descends by gravity to the draw points located at the production level, where it is collected by load–haul–dump (LHD) equipment and subsequently transported to the dumping points, from which the material is transferred to the haulage level. Understanding this operation is critical to planning charging infrastructure, as it directly influences vehicle routes, fleet allocation, and energy requirements.

Charging infrastructure decisions are capital-intensive and have a direct impact on equipment operation, which requires a methodology to determine and optimally size the infrastructure. This methodology must consider aspects such as charger capacity and type, the required auxiliary infrastructure, and the placement of stations within the mining system, to ensure a design consistent with production objectives and operational constraints.

From the review of the state of the art, it is evident that simulation using specialized software has been the most employed tool to address this problem; however, its iterative, trial-and-error nature can lead to inefficient solutions. In contrast, optimization-based approaches, widely applied in urban mobility and freight transport, allow the simultaneous evaluation of many configurations while ensuring compliance with technical and operational constraints.

The objective of this work is to develop a scalable optimization methodology for large-scale fleets, specifically applied to underground mining operations using block caving. The model is capable of capturing the specific operational characteristics of these mines and providing the most effective solution for charging infrastructure planning. The proposed approach integrates both operational and investment aspects, allowing for the evaluation of alternative configurations while simultaneously considering technical constraints, operational requirements, and the trade-off between investment and operational costs.

The remainder of this manuscript is structured as follows. Section 2 presents the proposed methodology, the mixed-integer linear optimization model, and the definition of the case study. Section 3 presents the results obtained for both the investment decisions and the associated optimal operation. Finally, conclusions and future work are presented in Section 4.

Methodology

This section describes the proposed methodology for infrastructure sizing, the mixed-integer linear optimization model, and the case study used for its validation.

Proposed methodology

As a first stage, the necessary input data are identified according to the following categories: vehicle characteristics, battery characteristics, charging technology characteristics, mine layout, operational characteristics, and electrical system characteristics.

The next stage involves using the input data to generate the operational scenario and define the investment candidates, that is, charger models with their associated power ratings and costs, as well as candidate charging stations to be selected.

The following stage consists of modeling and implementing the charging infrastructure optimization model, considering operational aspects. Decision variables are grouped into investment decisions, including charger power, location, and number of charging stations, and operational decisions, including vehicle states, whether in transit, at a charging station, or idle, and battery charging power. The model considers constraints on vehicle operations, charging stations, battery operations, production quotas, and the electrical system. The objective function optimizes investment costs together with the energy costs associated with battery charging.

The model outputs include investment decisions, such as station locations, charger power, and number of chargers, operational decisions, such as fleet assignment to extraction points and battery charging strategy, and key performance indicators, including production, productivity, and energy costs.

Finally, if the key performance indicators are not met, the operational scenario is adjusted by modifying the infrastructure or the fleet, and the optimization is iterated until the objectives are satisfied. Based on the obtained results, any necessary adjustments to the electrical and mining infrastructure are identified.

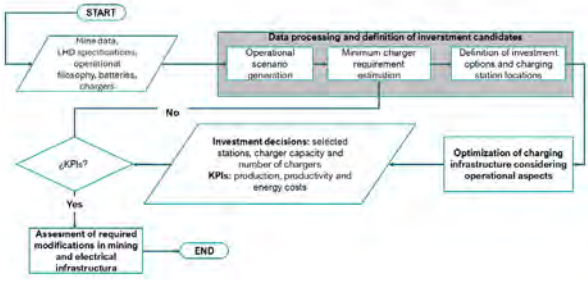

Figure 1. Diagram of the methodology for charging infrastructure sizing

Mixed integer linear programming model

The notation used in the mathematical formulation is the following.

sets. Let K be the set of charge stations. Let I be the set of electrical LHDs. Let J be the set of underground mine drawpoints, from which the LHDs extract material. Let D be the set of days of the planning horizon, T be the set of time intervals. T^{BS} is the set of time periods corresponding to shift changes. $J_{i,t}$ is the set of drawpoints from which LHD i can extract material within a time interval t.

parameters. While c^{sfc} is the investment cost of charging stations (in USD). c^{ch} is the investment cost of chargers in USD. n_k^c is the maximum number of chargers to be installed at station k. p_m^c is the charging power of charger model m in kW. p^{max} is the maximum power available from the distribution electric system in kW. p^{peak} is the peak operating power in kW. $\Delta\mathrm{t}$ is the duration of each time interval in hours. t_{ini} is the starting time of the operating shift. t_{fin} is the ending time of the operating shift. m_j is the minimum amount of the hauled material from node j during operation in tons. α is the slack factor for the extraction quota. c_t is the marginal cost of electricity at time interval t in USD/kWh $d_{i,j}$ is the number of time intervals required by LHD i when traveling to node j. $p_{ic,j}^e$ is the average power consumed by LHD i when traveling to node j in kW. $p_{i,k}^{e\_k}$ is the average power consumed by LHD i when traveling to charging station k in kW. b_i^{min}, b_{ic}^{max} are the minimum and maximum recommended values for state of charge of the battery of LHD i in kWh. g_i is the bucket capacity of LHD i. t^{man} is the maneuvering time at the charging station in hours. $t_{i,k}^{ttc}$ is the travel time of LHD i to charging station k in hours.

decision variables. Let us define a boolean decision variable $\mathrm{Z}_{i,t} \in\{0,1\}$ equal to 1 if LHD i is at the charging station during time interval t, and 0 otherwise. $\mathrm{X}_k \in\{0,1\}$ is a boolean decision variable equal to 1 if station k is selected and 0 otherwise. $\mathrm{Z}_{i,t}^{charge} \in\{0,1\}$ is a boolean decision variable equal to 1 if LHD i is charging during time interval t, and 0 otherwise. $\mathrm{Y}_{i,j,t} \in\{0,1\}$ is a boolean decision variable equal to 1 if LHD i is travelling towards node j during time interval t and 0 otherwise. $SC_{\mathrm{i,t}} \in\{0,1\}$ is a boolean decision variable equal to 1 if LHD i starts a battery charging process during interval t and 0 otherwise. $EC_{i,t} \in\{0,1\}$ is a boolean decision variable equal to 1 if LHD i ends a battery charging process during interval t and 0 otherwise. $U_{k,i,t} \in\{0,1\}$ is a boolean decision variable equal to 1 if LHD i is assigned to charging station k at time interval t and 0 otherwise. $\mathrm{P}_{i,t} \in[0, p_m^c]$ is a continuous decision variable, equal to the battery charge power of LHD i within time interval t measured in kW. $\mathrm{B}_{i,t} \in[b_i^{min}, b_i^{max}]$ is a continuous decision variable, equal to the battery charge of LHD i at end of time interval t measured in kWh. n_k^c is a positive integer variable equal to the number of chargers at station k.

$$C_{OBC\_m} = \sum_{k=1}^{N^{Station}} (N_k^c \cdot c^{ch} + c^{sfc} \cdot X_k) + \sum_t^T \sum_i^I c_t \cdot (P_{i,t} \cdot \Delta t) \quad (1)$$

subject to

$$N_k^C \leq n_k^c \cdot X_k \quad \forall k \in K \quad (2)$$

$$\sum_{k \in K} U_{k,i,t} = Z_{i,t}^{charge} \quad \forall i \in I, \forall t \in T \quad (3)$$

$$U_{k,i,t} \leq X_k \quad \forall i \in I, \forall k \in K, \forall t \in T \quad (4)$$

$$\sum_{i \in I} U_{k,i,t} \leq N_k^C \ , \forall t \in T, \forall k \in K \quad (5)$$

$$U_{k,i,t} = SC_{k,i,t} - EC_{k,i,t} \quad \forall i \in I, t = 0 \quad (6)$$

$$U_{k,i,t} - U_{k,i,t-1} = SC_{k,i,t} - EC_{k,i,t} \quad \forall i \in I, t > 0 \quad (7)$$

$$P_{k,i,t} \leq U_{k,i,t} \cdot p_m^c \quad \forall i \in I, \forall t \in T \quad (8)$$

$$B_{i,t} = B_{i,t-1} - \sum_{j \in J_{i,t}} Y_{i,j,t} \cdot n_{i,j,t} \cdot p_{ic,j}^e \cdot \Delta t + \sum_{k \in K} P_{k,i,t} \cdot \Delta t - \sum_{k \in K} P_{k,i,t} \cdot t^{man} - \sum_{k \in K} P_{k,i,t} \cdot t_{i,k}^{ttc} - 2 \cdot \sum_{k \in K} SC_{k,i,t} \cdot p_{i,k}^{e_k} \quad \forall i \in I, \forall t \in T, \forall k \in K \quad (9)$$

$$b_i^{min} \leq B_{i,t} \leq b_i^{max} \quad \forall i \in I, \forall t \in T \quad (10)$$

$$B_{i,t^{ini}-1} = B_{i,t^{fin}} \quad \forall i \in I \quad (11)$$

$$\sum_{k \in K} p_m^c \cdot N_k^C \leq p^{max} \quad (12)$$

$$\sum_{i \in I} \sum_{k \in K} P_{k,i,t} \leq p^{peak} \ , \forall t \in T \quad (13)$$

$$Z_{i,t} + Z_{i,t}^{charge} + \left(\sum_{j \in J_{i,t}} Y_{i,j,t} \right) = 1 \quad \forall i \in I, \forall t \in T \quad (14)$$

$$X_k, Z_{i,t}, Z_{i,t}^{charge}, Y_{i,j,t}, SC_{k,i,t}, EC_{k,i,t}, U_{k,i,t} \in \{0,1\} \quad \forall i \in I, k \in K, t \in T, j \in J \quad (17)$$

$$N_k^C \in N, P_{k,i,t} \in [0, p_m^c] \in R \ , B_{i,t} \in [b_i^{min}, b_i^{max}] \in R \quad (18)$$

The objective function (1) minimizes the investment cost of the charging stations and chargers together with the operating cost associated with battery charging. Constraint (2) imposes the maximum capacity for installing chargers at each station. Constraints (3) and (4) model the assignment of LHDs to the charging stations. Constraints (5), (6), (7), and (8) model the dynamics of battery charging at the stations: available chargers, start and end of charging, and pre-charging parking. Constraints (9), (10), and (11) model the battery dynamics: state of charge and safety limits. Constraints (12) and (13) model the maximum power available from the distribution network and the operational peak power that ensures network stability. Constraints (14) and (15) model the

vehicle dynamics: whether a vehicle is traveling, parked, or charging its battery. Constraint (16) enforces the operational quota, and finally, (17) defines the nature of the variables.

Case study

The mathematical model presented above was applied to a short-term production schedule of an underground copper mining operation in Chile. The optimization focuses exclusively on the production level of a block caving operation, evaluating different charging station configurations and charger models, along with the corresponding operational outcomes. The production level layout consists of four streets, each containing ten draw points and a centralized dumping point as illustrated Figure 2. LHD are responsible for loading rock material from the draw points and transporting it to the dumping point.

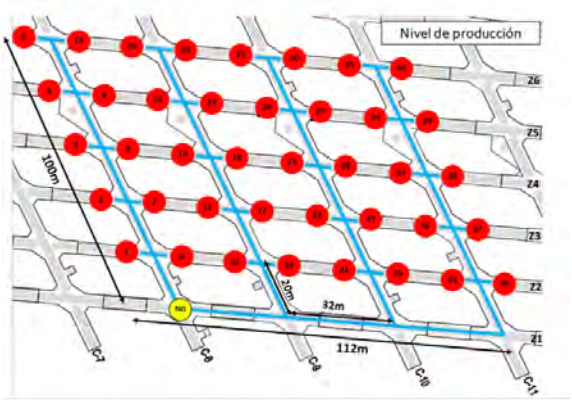

Figure 2. Production level layout

Table 1 provides a summary of the operational parameters, while Table 2 summarizes the parameters of the candidate charging stations, and Table 3 summarizes those of the candidate chargers. For the calculation of annualized costs, a 10% interest rate and a 15-year lifetime are considered.

Table 1. Case study operational parameters

Parameter	Value
Fleet size	4
Load capacity (ton)	18
Battery capacity (kWh)	353
Average speed (km/h)	15
Acceleration (m/s²)	0.3
Time horizon (year)	1
Energy cost scheme	variable

Table 2. Case study: candidate charging station parameters

Configuration	Annualized cost (USD)	Max. number of chargers
Type 1	70.000	1
Type 2	214.000	4
Type 3	150.000	2

Table 3. Case study: candidate chargers parameters

Configuration	Annualized cost (USD)	Power (kW)
Model 1	47.304	360
Model 2	131.400	1000
Model 3	13.140	100

Results and Discussions

This section presents and discusses the results obtained for the investment decisions alongside the operational outcomes.

Decisions on charging infrastructure

Table 4 presents the results for three candidate charger models. It can be observed that, in general, the production targets are met, except for the smallest charger, whose low power causes stoppages that negatively impact production. For chargers 2 and 3, a single charger is sufficient to achieve the targets, allowing investment in a smaller charging station, unlike model 1, which requires investment in the most expensive station.

Regarding the operating costs associated with battery charging, it is evident that increasing the charging power significantly reduces these costs, due to the existence of a time window in which costs are close to zero. This makes it convenient to perform as many battery charges as possible within that period.

The results indicate that the optimal infrastructure consists of a Type 1 charging station with a 360 kW charger. It is worth noting that investment costs are predominant compared to the savings associated with charging power; therefore, the model does not opt to install additional chargers, which could potentially increase effective operating time and reduce battery charging-related costs.

Table 4. Case study: Infrastructure results 3.2

Charger Model	Power (kW)	Selected Charging Station	Number of chargers	Battery Charging Cost (USD)	Investment Cost (USD)	Hauled Mineral (ton)
Model 1	100	1 type 2	3	99.498	259.420	7.184.952
Model 2	360	1 type 1	1	65.535	117.304	7.187.580
Model 3	1000	1 type 1	1	62.705	201.400	7.187.580

Operational impact

It can be observed that the model establishes an appropriate strategy to minimize the operating costs associated with battery charging. Since the cost profile aligns with renewable energy penetration, it is more convenient to charge during periods when the cost is close to zero, as shown in Figure 3.a. It is worth noting that, due to the high investment costs in infrastructure, although there is room for improvement by adding more chargers considering that the LHDs remain idle during stoppages and cannot charge, as shown in Figure 3.b the gains in production and reduction of operating costs are not competitive.

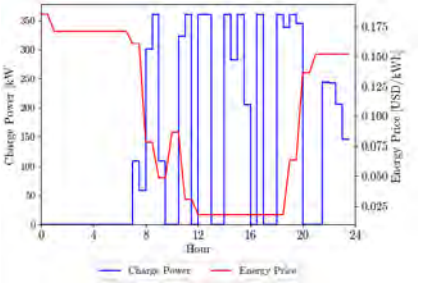

(a) Charge strategy

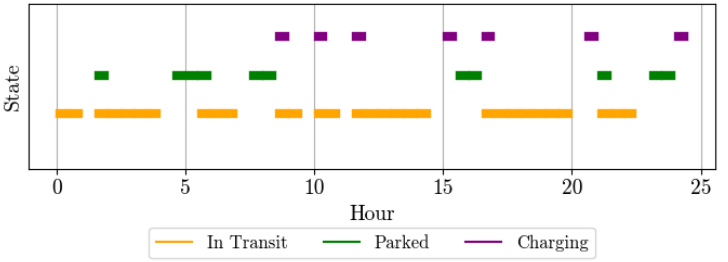

(b) Effective operating time and operational stoppages of LHDs

Figure 3. Operational results for optimal infrastructure (charger model 2)

Conclusions

The preliminary results show that the proposed methodology allows for an appropriate design of the infrastructure, considering the requirements and characteristics according to the charging technology. Furthermore, the model is shown to be capable of ensuring the achievement of production objectives. In addition, this work provides decision-makers with a tool to systematically address the challenges of charging infrastructure planning. Unlike traditional simulation-based approaches, which often rely on iterative trial-and-error procedures, the optimization framework adopted here enables the simultaneous evaluation of multiple configurations while ensuring technical and operational feasibility. This demonstrates the practical value and novelty of the methodology in mining applications.

Future work includes the modelling of alternative charging strategies, such as battery swapping, which could potentially increase effective operating time. However, this approach requires higher investment due to the need for a larger battery pool and additional infrastructure depending on the OEM.

References

[1] A. Meshginqalam, M. H. Mobarak, J. Dong, M. A. H. Rafi, R. Rennie and J. Bauman, 2024. An Optimization Algorithm for the Design of Battery Electric Fleets in Underground Mines. IEEE Access.

[2] J. Hooli, B. Skawina, A. Halim and F. Sundqvist, 2024. Analysing Battery Swapping of Battery Electric Load Haul Dump (LHD) Machines in Block Cave Mining Using Discrete Event Simulation (DES). Min Metall Explor.

[3] H. Y. Mak, Y. Rong and Z. J. M. Shen, 2013. Infrastructure planning for electric vehicles with battery swapping. Manage Sci.

[4] P. Sadeghi-Barzani, A. Rajabi-Ghahnavieh and H. Kazemi-Karegar, 2014. Optimal fast charging station placing and sizing. Appl Energy.

[5] N. Sathaye and S. Kelley, 2013. An approach for the optimal planning of electric vehicle infrastructure for highway corridors. Transp Res E Logist Transp Rev.

[6] J.-M. Clairand, M. González-Rodríguez, R. Kumar, S. Vyas and G. Escrivá-Escrivá, 2022. Optimal siting and sizing of electric taxi charging stations considering transportation and power system requirements. Energy.

[7] I. Mareev, J. Becker and D. U. Sauer, 2018. Battery dimensioning and life cycle costs analysis for a heavy-duty truck considering the requirements of long-haul transportation. Energies (Basel).

[8] S. Çelik and Ş. Ok, 2024. Electric vehicle charging stations: Model, algorithm, simulation, location, and capacity planning. Heliyon.

Socio-Environmental Conflicts as an Indicator Of Social Unsustainability in the Mining Industry: The Case of Tailings Facilities in Chile

Iván Ojeda-Pereira[1,2], Hernán Pezoa-Quevedo[3], Fernando Campos-Medina[4], Sebastián Herrera-León[2,5], Andrzej Kraslawski[1]

1. School of Engineering Sciences, LUT University, Lappeenranta, Finland
2. Department of Industrial Engineering, Universidad Católica del Norte, Antofagasta, Chile
3. Department of Geology, Universidad de Chile, Santiago, Chile
4. Department of Sociology, Universidad de Chile, Santiago, Chile
5. Institute of Engineering Sciences, Universidad de O'Higgins, Rancagua, Chile

**Corresponding author at: LUT School of Engineering Sciences, Yliopistonkatu 34, Lappeenranta, Finland, ilojeda@uc.cl*

Introduction

Chile's mining history is extensive, predating the constitution of the modern nation-state (Betancour & Maldonado, 2013). Mining has provided a central pillar of the national economy and contributed to shaping urban–rural structures, labour systems, institutions, and cultural life. Chile remains one of the world's leading mining countries, producing 5.7 million metric tons of copper in 2020—twice as much as Peru and four times China's output (Garside, 2021). Although taxation levels are often considered insufficient (Sturla et al., 2018), mining revenues are vital to state finances and private sector flows (Soza-Amigo et al., 2021). However, these economic indicators cannot be detached from their environmental and social consequences in concrete territories. The expansion of global demand for copper and lithium—critical minerals for renewable energy and decarbonisation—suggests Chile will remain a central node in the global extractive economy. At the same time, such extractivist development deepens socio-environmental conflicts that question the industry's practices and future sustainability (Gudynas, 2015; Svampa, 2019)

This study focuses on tailings facilities, one of the most critical infrastructures of extractivism. Tailings comprise ground rock, water, and chemical residues left after ore processing. Historically, waste was discharged directly into rivers (Hettler et al., 1997) or piled up in toxic mounds. More recently, specialized storage infrastructures have been constructed. Tailings dams are among the most significant human-made structures worldwide, and their failures have led to devastating disasters (Islam & Murakami, 2021; Owen et al., 2020), such as Mount Polley in Canada (2014) and Brumadinho in Brazil (2019), where millions of cubic meters of toxic waste caused massive ecological destruction and human casualties. In Chile, the tailings risks are compounded by climate change, which increases rainfall variability and the likelihood of slope instability in mining regions. Despite these risks, most academic research on tailings has concentrated on geotechnical, hydrological, and environmental dimensions (Campos-Medina et al., 2022; Ojeda-Pereira & Campos-Medina, 2021). Fewer studies address their socio-political dimensions, even though tailings often coexist with communities, water systems, and urban areas (Campos-Medina et al., 2021; Ojeda-Pereira et al., 2023, 2025; Ureta, 2016; Ureta & Flores, 2018).

In Latin America, socio-environmental conflicts concerning extractivism have been widely studied (A. Bebbington, 2010; Svampa, 2019). Such conflicts typically emerge from the friction between global resource demand and local territorial claims, often exposing power asymmetries, environmental degradation, and threats to community health. However, within these epistemic communities, conflicts are often framed primarily as critiques of economic models of resource-intensive extraction. As recent bibliometric reviews demonstrate, international research on tailings remains dominated by environmental sciences, earth sciences, and engineering, primarily concentrated in China, Canada, the United States, Australia, and Spain, which together account for over 65% of global publications (Campos-Medina et al., 2022; Ojeda-Pereira & Campos-Medina, 2021). The relative absence of political science and social science perspectives—especially from the Global South—creates epistemic asymmetries that limit our understanding of the governance and conflict dynamics surrounding these infrastructures.

This study addresses that gap. We propose that socio-environmental conflictivity linked to tailings facilities should be understood as an indicator of social unsustainability. From this perspective, neither the mining industry as a whole nor a specific company can be considered socially sustainable if it generates conflicts and fails to manage them adequately. The central research question guiding this work is: What are the main characteristics of socio-environmental conflictivity associated with tailings facilities in Chile? By documenting, for the first time, the national geography of tailings-related conflicts in Chile, this research contributes both to applied mining studies and to public policy debates. It also strengthens the interdisciplinary dialogue between engineering and social sciences by advancing a replicable methodology to analyse conflicts and positioning conflictivity as a practical indicator of sustainability performance.

Theoretical Framework: Extractivism and Socio-environmental Conflicts

This study is grounded in Latin American debates on extractivism and on socio-environmental conflicts in Chile. Conceptually, it clarifies how we use extractivism and socio-environmental conflict, and methodologically it links those notions to a national-scale characterization of conflictivity around tailings facilities. The section is organised in two parts: (i) extractivism as national condition and as territorially specific extractivisms; and (ii) approaches to socio-environmental conflicts in Chile and their analytical dimensions.

Extractivism and environment in Chile

Recent reviews show that Chilean research connecting conflict, territory and extractivism has grown rapidly but often routinises key notions—using "extractivism" as a descriptive backdrop, assuming conflict without conceptual scrutiny, simplifying "territory," privileging the triad state–firm–civil society, focusing on the local scale, and relying on single-case designs (Maillet et al., 2021). Dialoguing with that corpus, we treat extractivism both as a national historical condition and as plural, territorially embedded practices. Following Gudynas (2015), extractivism is a mode of appropriation—large-volume removal of natural resources with minimal processing for export—while for Svampa et al. (2019) it is a mode of accumulation that organises society. Four elements situate the Chilean case: (i) colonial legacies positioning Latin America as a primary-commodity supplier; (ii) the commodities boom since the 1990s ; (iii) post-dictatorial neoliberal governance that framed large-scale export as a route to growth and poverty reduction ; and (iv) technological advancements enabling new extraction frontiers.

Critically, extractivism unfolds as extractivisms in the plural: sectoral infrastructures (mining, forestry, salmon) anchor in distinct socio-ecological geographies and institutions, producing heterogeneous impacts, actor constellations and governance arrangements. In mining, tailings facilities constitute a core infrastructure of extractivism, with long-term environmental burdens and social risks that

challenge conventional, engineering-centred framings.

Socio-environmental conflicts

Approaches to socio-environmental conflicts in Latin America often arise within political ecology, linking ecological degradation and distributive asymmetries in access, control and burden sharing, under power inequalities and clashing value frameworks (J. Bebbington et al., 2021; Martinez Alier, 2009). Complementary perspectives emphasise meaning, identity and discourse (Ide, 2016), or the produced space—dynamic, dialectical and co-produced—highlighting perceived, conceived and lived dimensions of conflict (Aliste & Núñez, 2015; Napadensky & Azocar, 2017). Building on these, we treat conflicts as socio-political confrontations that generate temporal regimes (variable durations, cycles of latency and activation) and spatial patterns (scalar linkages between localities and national arenas).

Conceptually and operationally, we articulate two knowledge logics (Allain, 2019): a scientific one (academic literature) and an activist-policy one (databases and public institutions). In Chile, the INDH defines socio-environmental conflicts as publicly manifested disputes over rights affected by resource uses and environmental impacts—captured through repertoires of collective action (INDH, 2012). The Environmental Justice Atlas conceptualises conflicts as community mobilisations against specific economic activities where environmental harms are central (Temper et al., 2015), enabling comparative analysis of actor constellations, strategies and outcomes (Ferreira et al., 2021; Scheidel et al., 2020). This dual lens helps to reconstruct conflicts as publicly visible, territorially situated and temporally extended processes.

For tailings in Chile, existing social-science research—often local and ethnographic—has revealed management logics of concealment and the persistence of toxic legacies (Ureta, 2016), the metaphor of tailings as a deceptive dragon requiring constant stabilisation (Ureta & Flores, 2018), and forms of environmental suffering and inaction that shape everyday life and subjectivities (González, 2021; Ureta et al., 2018). While valuable, this singularist focus under-scales the phenomenon. Our contribution is to scale up to the national level to characterise conflictivity patterns—protests and public action, spatial geographies, temporal regimes, political actors, claims and repertoires—thus linking local experiences with a country-wide governance problem.

In short, we integrate political-ecology and interpretive perspectives with comparative, database-driven analysis to position conflictivity as an indicator of social unsustainability in tailings governance. This theoretical framework enables us to conceptualise socio-environmental conflictivity around tailings not as isolated disputes, but as expressions of broader structural, territorial, and temporal dynamics of extractivism in Chile.

Methodology

The research strategy was structured according to the specific objectives through a national-scale case study with a predominantly quantitative, geographic–political, and descriptive focus. This approach is consistent with the research question and with the current state of the debate on socio-environmental conflicts and tailings facilities in extractive industries. The methodology is organized into three components: case study design, data sources, and analytical tools.

National-scale case study

Following the trends identified by Maillet et al., (2021) socio-environmental conflicts in Chile have been primarily studied through local or regional case studies. In contrast, this research develops a single case study at the national scale, while still reporting the regional–local dynamics of each conflict as interpretive evidence. The Chilean case was selected as an extreme case (Seawright

& Gerring, 2008), given the country's exceptionally high number of tailings facilities worldwide and the foreseeable intensification of mining activity. Extreme case selection is consistent with exploratory designs in political science, especially when methodological goals are descriptive rather than causal (Creswell, 2013; Yin, 2018).

Data sources

This study developed the first national database of socio-environmental conflicts associated with tailings facilities in Chile, based on multiple sources. The main tool was Protest Event Analysis (PEA), defined as the systematic recording of collective manifestations in public space occurring at specific times and places (COES, 2018). To mitigate the limitations of PEA—such as media selectivity or editorial bias (Allain, 2019; Fillieule, 2007)—the research triangulated diverse sources and complemented press reports with scientific and institutional databases. The resulting dataset contains 99 conflictive events, each coded across 31 variables (actors, location, demands, temporality, etc.), constructed inductively and refined through iterative coding.

Table 1. Information searches and sources

Search	Source
1	Review of the conflict database, Center for the Study of Conflict and Social Cohesion (COES, 2020)
2	Review of the Environmental Justice Atlas, Institute of Environmental Science and Technology, Autonomous University of Barcelona (Temper et al., 2015)
3	Google search with the keywords "protesta + Chile + relave"
4	Google search focused on areas with high concentrations of tailings facilities, using the formulas: 1) "protesta + Andacollo + relave"; 2) "protesta + La Higuera + relave"; 3) "protesta + Illapel + relave"
5	Google search by region (with at least one tailings facility): 1) "protesta + Arica + relave"; 2) "protesta + Iquique + relave"; 3) "protesta + Antofagasta + relave"; 4) "protesta + Copiapó + relave"; 5) "protesta + La Serena + relave"; 6) "protesta + Valparaíso + relave"; 7) "protesta + Rancagua + relave"; 8) "protesta + Talca + relave"; 9) "protesta + Aysén + relave"
6	Google Scholar search: "socio-environmental conflict + mine tailing + Chile", followed by Google search using "protesta + city or tailings facility mentioned in the study"

Analytical tools

The national database of socio-environmental protests related to tailings facilities was therefore analysed through descriptive statistics and spatial visualisation. Descriptive statistics quantify and summarise dataset characteristics, serving as an entry point for analysis (May, 2017). In some cases, they can also open the way to inferential methods, provided assumptions of representativeness are met (Larson, 2006). In this study, the database is conceived as a national inventory rather than a representative sample, enabling a multiscalar dialogue between local cases and the national-level analysis. Spatial representations are crucial in political science: diagrams and maps raise questions and foster insights by making patterns visible (Brady, 2011). Accordingly, the research placed strong emphasis on producing maps and visual graphics. Instead of working directly on the full dataset, subsets were created for specific visualisations to ensure analytical precision and data integrity.

Both descriptive statistics and spatial visualisation were integrated into an interpretive political science perspective (Bevir & Rhodes, 2015), which highlights the meanings, temporalities, and political significance of conflicts beyond their numeric representation. Thus, the methodological approach combines descriptive–quantitative analysis with interpretive insights, positioning visualisation as both an analytical and conceptual tool.

Results and Discussions

This section presents the main findings of the study. It contributes to the field by delivering the first national-scale database of socio-environmental conflicts related to tailings facilities in Chile, made openly available for further research. Beyond its descriptive scope, the analysis also provides interpretative insights into the dynamics of socio-environmental conflict in the mining sector.

Conflicts, protests, and media coverage

The research identified 23 socio-environmental conflicts associated with tailings facilities in Chile. These conflicts vary in intensity and visibility, with some reaching national relevance while others remain relatively localized. Out of 99 news items, only 67 correspond to unique protest events, revealing a 32.3% overrepresentation due to repeated media coverage. Figure 1 further disaggregates these cases, highlighting two conflict dynamics: (i) low-visibility conflicts with limited repertoires of protest (e.g., Talabre, Dos Pinos, Los Pumas); and (ii) high-visibility conflicts, such as El Mauro, Los Quillayes, and El Torito, which have generated multiple protests and sustained public attention. Among them, El Mauro stands out as the most persistent conflict, extending over a decade and combining community protests with legal action (see Figure 1). This case exemplifies failed governance of a tailings facility.

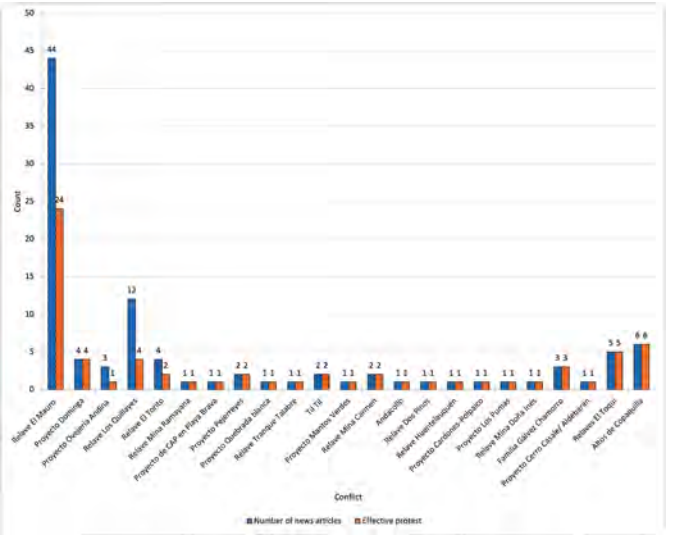

Figure 1. News and Protests Associated with Each Socio-Environmental Conflict over Tailings Facilities in Chile

Geography of conflicts

Figure 2 maps the distribution of conflicts across Chilean communes, showing that 19 communes have experienced protest activity related to tailings. The highest concentration is observed in the Coquimbo Region, where a "corridor of conflict" extends from Salamanca through coastal communes up to La Higuera. Figure 3 shows the spatial distribution of protests, with Los Vilos as the commune with the highest number of protest events, followed by Aysén, La Higuera, Pica, Ovalle, Andacollo, and Til-Til. Interestingly, the Aysén Region represents an outlier, far from the northern mining clusters, yet showing notable mobilization around tailings issues.

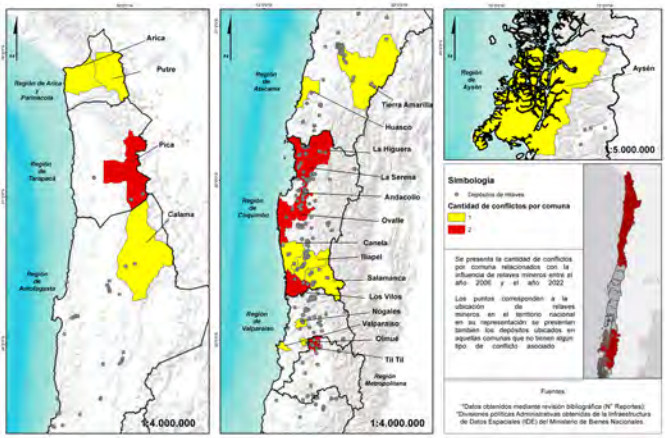

Figure 2. Map of Conflicts Associated with Mining Tailings in Chile

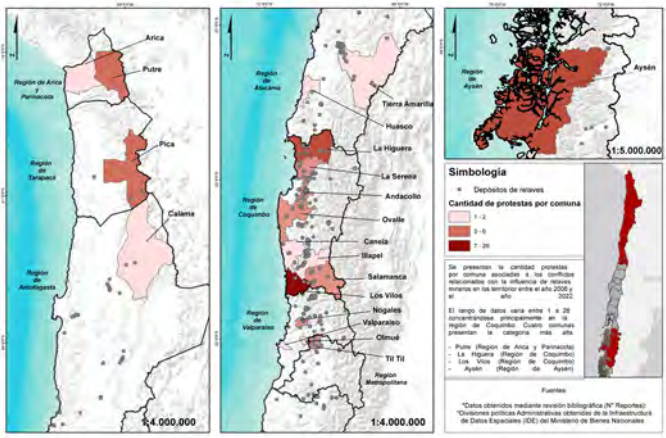

Figure 3. Map of Protest Actions Related to Mining Tailings in Chile.

Temporal regimes of conflict

The temporal analysis reveals that socio-environmental conflicts linked to tailings are variable and extended over time. Between 2006 and 2022, 67 effective protests were documented (Figure 4). Peaks occurred in 2010, 2012, 2015, and 2021, with 2015 marking the highest intensity (13 protests). This pattern suggests cycles of escalation followed by decline, consistent with path-dependent dynamics (Pierson, 2004). At the disaggregated level, 56.5% of conflicts occurred in a single year, showing low continuity. However, El Mauro (Los Vilos) and Altos de Copaquilla (Putre) stand out for sustaining protests over more than a decade, each with distinct peaks (Figure 5). Extended conflicts highlight structural governance failures and persistent community grievances.

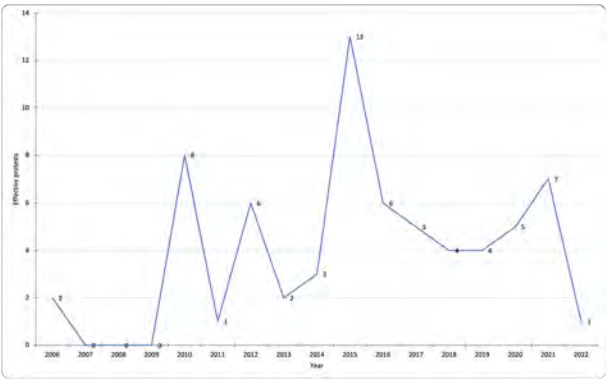

Figure 4. Temporal Regime of Socio-Environmental Conflicts Related to Tailings Facilities at the National Scale.

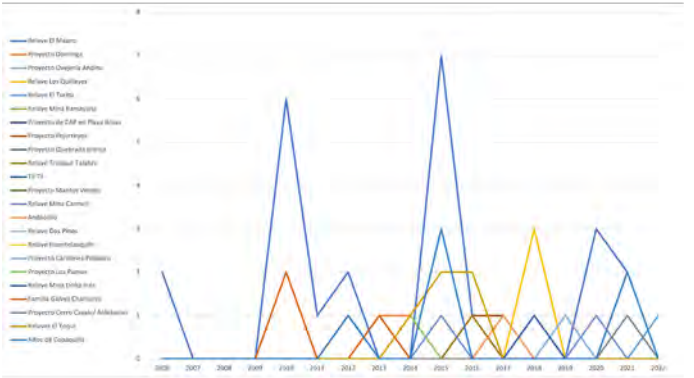

Figure 5. Temporal Dynamics of Each Tailings-Related Conflict.

Conflict contents and strategies

In 52.2% of cases conflicts emerged around existing tailings facilities, while 43.5% involved projects under development, and 4.3% evolved from prospective to ongoing facilities. This underscores the dual retrospective and prospective nature of these disputes. Environmental concerns dominate (41 news items), especially related to water pollution and air contamination, followed by human–environmental risks such as disasters or cultural heritage loss (18). Institutional demands (17) and territorial saturation (14) also feature prominently, reflecting the perception of mining regions as sacrifice zones. Table 2 summarises protest strategies, ranging from moderate actions (letters, campaigns, administrative complaints) to more radical tactics, including road blockades, legal actions, and hunger strikes. The latter, notably in Caimanes, exemplifies the severity of grievances and the willingness of communities to escalate contention when conventional channels fail.

Table 2. Protest strategies

Protest Action Strategy	Number of News Items
Legal or administrative action	17
Campaign	2
Letter to La Moneda (Presidential Palace)	1
Road blockade	12
Sustained road blockade	16
Public statement	10
Complaint by mayor	1
Hunger strike (including dry hunger strike)	19
Protest	12
Protest at company site	6
Protests with barricades	1
Burning of entrance booth	1
Occupation of mining facility	1

Conclusions

The analysis carried out here suggests that socio-environmental conflictivity around tailings facilities in Chile is far from marginal: it has become one of the clearest indicators of the social unsustainability of mining. By assembling and systematising the first national database of conflicts linked to tailings, we identified a geography of 23 cases spread across 19 communes, with the Coquimbo Region emerging as a hotspot but with notable episodes also in the far north and even in Patagonia. These disputes often remain invisible in wider public debate, yet they expose persistent tensions over water scarcity, air quality, health risks, and the perception of mining territories as "sacrifice zones."

What also stands out is the way conflicts unfold in time and scale. Some disputes are brief and isolated, while others—such as El Mauro—stretch over more than a decade, combining legal actions with recurring protest. These long-term conflicts are not only signs of technical risk but also of governance failures that erode trust between companies, communities, and the state. Actor constellations go well beyond the conventional triangle of state–company–civil society, involving municipal leaders, regional authorities, and national regulators, which highlights the complexity of managing these infrastructures in a politically fragmented environment.

Recognising conflictivity as a signal of unsustainability therefore matters. It points to where governance is failing and where dialogue has broken down. For industry, ignoring these signals risks not only reputational damage but also operational uncertainty; for regulators, it means losing legitimacy. The challenge, then, is to treat conflicts not as disruptions to be silenced, but

as opportunities to build more transparent, participatory, and resilient forms of governance. Situating the Chilean case in this way contributes to a broader agenda: integrating social science perspectives—particularly political science—into the interdisciplinary field of tailings management, thereby strengthening both applied mining practices and public policy.

References

Aliste, E., and Núñez, A., 2015. Las Fronteras del Discurso Geográfico: El Tiempo y el Espacio en la Investigación Social. Chungará (Arica), 47(2), 287–301. https://doi.org/10.4067/S0717-73562015005000023

Allain, M., 2019. Conflictos y protestas socio-ambientales en Chile: Reflexiones metodológicas y resultados. Revista de Sociología, 34(1), Article 1. https://doi.org/10.5354/0719-529X.2019.54271

Bebbington, A., 2010. Extractive Industries and the Stunted States: Conflict, Responsibility and Institutional Change in the Andes. In R. Raman & R. Lipschutz (Eds.), Corporate Social Responsibility: Discourses, Practices and Perspectives (pp. 97–115). Palgrave Macmillan.

Bebbington, J., Larrinaga, C., O'Dwyer, B., and Thomson, I., 2021. Routledge Handbook of Environmental Accounting. Routledge.

Betancour, M., and Maldonado, P. (Eds.), 2013. Minería en Chile: Impacto en regiones y desafíos para su desarrollo. COCHLICO. https://www.cochilco.cl/Libros/Libro_Mineria_en_Chile_Impacto_en_Regiones_y_Desafios_para_su_Desarrollo.pdf

Bevir, M., and Rhodes, R. A. W. (Eds.), 2015. Routledge Handbook of Interpretive Political Science (1st ed.). Routledge. https://doi.org/10.4324/9781315725314

Brady, H. E., 2011. The Art of Political Science: Spatial Diagrams as Iconic and Revelatory. Perspectives on Politics, 9(2), 311–331. https://doi.org/10.1017/S1537592711000922

Campos-Medina, F., Ojeda Pereira, I., and Ponce Labra, P., 2021. Extractivismo en Chile: Tres claves para comprender la lógica de aglomeración de los proyectos industriales y proponer alternativas de resistencia. In C. Alister, X. Cuadra, D. Julián-Vejar, P. Blaise, & O. Camila (Eds.), Cuestionamientos al Modelo Extractivista Neoliberal desde el Sur. Capitalismo, Territorios y Resistencias (pp. 57–85). Ariadna. https://doi.org/10.26448/ae9789566095316.18

Campos-Medina, F., Ojeda-Pereira, I., Quiroz, J., and Guzmán, J., 2022. International Trends in Mining Tailings Research through Machine Learning Method: Retrospective or Prospective Oriented Research? Mineral Processing and Extractive Metallurgy Review, 44(0), 64–75. https://doi.org/10.1080/08827508.2021.2023520

COES, 2018. Informe Anual Observatorio de Conflictos. COES. https://www.coes.cl/wp-content/uploads/2018/11/ORG_Informe-Observatorio-de-Conflictos-2018_5nov.pdf

COES, 2020. Observatory of Conflicts—Cumulative Dataset [Dataset]. Harvard Dataverse. https://doi.org/10.7910/DVN/GKQXBR

Creswell, J., 2013. Qualitative inquiry & research design: Choosing among five approaches. SAGE.

Ferreira, M. J., Gabriel, S., Correia, A. M., Pontes da Silva, C., Navas, G., Gurgel, I. G. D., and Santos, M. O. S. dos, 2021. Mapeamento de conflitos socioambientais no território de Suape, Pernambuco/Brasil. Revista Mutirõ. Folhetim de Geografias Agrárias do Sul, 2(2), Article 2. https://doi.org/10.51359/2675-3472.2021.252448

Fillieule, O., 2007. On n'y voit rien: Le recours aux sources de presse pour l'analyse des mobilisations protestataires. In P. Favre (Ed.), L'atelier du politiste: Théories, actions, représentations (pp. 215–240). La Découverte.

Garside, M., 2021. Largest producer of copper in the world 2020. Statista: Minin, Metals & Minerals. https://www.statista.com/statistics/264626/copper-production-by-country/

González, P., 2021. Habitar entre arenas de relaves. Incertidumbre sanitaria y sufrimiento ambiental en Chañaral (Chile). Revista INVI, 36(101), 83–108. https://doi.org/10.4067/S0718-83582021000100083

Gudynas, E., 2015. Extractivismos. Ecología, economía y política de un modo de entender el desarrollo y la natrualeza. CLAES y CEDIB.

Hettler, J., Irion, G., and Lehmann, B., 1997. Environmental impact of mining waste disposal on a tropical lowland river system: A case study on the Ok Tedi Mine, Papua New Guinea. Mineralium Deposita, 32(3), 280–291. https://doi.org/10.1007/s001260050093

Ide, T., 2016. Toward a constructivist understanding of socio-environmental conflicts. Civil Wars, 18(1), 69–90. https://doi.org/10.1080/13698249.2016.1144496

INDH, 2012. Informe Anual 2012. Situación de los Derechos Humanos en Chile. INDH. https://www.indh.cl/wp-content/uploads/2012/12/Inf-Anual-INDH12-WEB.pdf

Islam, K., and Murakami, S., 2021. Global-scale impact analysis of mine tailings dam failures: 1915–2020. Global Environmental Change, 70, 102361. https://doi.org/10.1016/j.gloenvcha.2021.102361

Larson, M. G., 2006. Descriptive Statistics and Graphical Displays. Circulation, 114(1), 76–81. https://doi.org/10.1161/CIRCULATIONAHA.105.584474

Maillet, A., Allain, M., Delamaza, G., Irarrázaval, F., Rivas, R., Stamm, C. and Viveros, K., 2021. Conflicto, territorio y extractivismo en Chile: Aportes y límites de la producción académica reciente. Revista de Geografía Norte Grande, 80, Article 80. http://revistanortegrande.uc.cl/index.php/RGNG/article/view/29651

Martinez Alier, J., 2009. El Ecologismo de los pobres. Icaria.

May, A., 2017. Simple Descriptive Statistics. In M. Allen (Ed.), The SAGE Encyclopedia of Communication Research Methods (pp. 1602–1606). SAGE Publications. https://doi.org/10.4135/9781483381411.n566

Napadensky, A. and Azocar, R., 2017. Espacios globales y espacios locales: En busca de nuevos enfoques a los conflictos ambientales. Panorámica sobre Sudamérica y Chile, 2010-2015[*]. Revista de Estudios Sociales, 61, 28–43. https://doi.org/10.7440/res61.2017.03

Ojeda-Pereira, I. and Campos-Medina, F., 2021. International trends in mining tailings publications: A descriptive bibliometric study. Resources Policy, 74, 102272. https://doi.org/10.1016/j.resourpol.2021.102272

Ojeda-Pereira, I., Pezoa-Quevedo, H. and Campos-Medina, F., 2023. Mining tailings dumps and socio-territorial inequalities in Chile: An exploratory study. Journal of Maps, 19(1), 2217514. https://doi.org/10.1080/17445647.2023.2217514

Ojeda-Pereira, I., Pezoa-Quevedo, H. and Campos-Medina, F., 2025. How should the socio-territorial density of tailings facilities be governed? A proposal for Chilean mining policy. The Extractive Industries and Society, 24, 101748. https://doi.org/10.1016/j.exis.2025.101748

Owen, J. R., Kemp, D., Lèbre, É., Svobodova, K. and Pérez Murillo, G., 2020. Catastrophic tailings dam failures and disaster risk disclosure. International Journal of Disaster Risk Reduction, 42, 101361. https://doi.org/10.1016/j.ijdrr.2019.101361

Scheidel, A., Del Bene, D., Liu, J., Navas, G., Mingorría, S., Demaria, F., Avila, S., Roy, B., Ertör, I., Temper, L. and Martínez-Alier, J., 2020. Environmental conflicts and defenders: A global overview. Global Environmental Change, 63, 102104. https://doi.org/10.1016/j.gloenvcha.2020.102104

Seawright, J. and Gerring, J., 2008. Case Selection Techniques in Case Study Research: A Menu of Qualitative and Quantitative Options. Political Research Quarterly, 61(2), 294–308. https://doi.org/10.1177/1065912907313077

Soza-Amigo, S., Fuders, F. and Aroca, P., 2021. La importancia del sector minero para el desarrollo de la economía chilena: La evolución de sus campos de influencia. El Trimestre Económico, 88(351), Article 351. https://doi.org/10.20430/ete.v88i351.1216

Sturla, G., López, R., Accorsi, S. and Figueroa, E., 2018. The wealth gifted to the large-scale copper mining industry in Chile: New estimates, 2005-2014. CEPAL Review, 124, 107–129. https://www.cepal.org/es/publicaciones/43463-la-riqueza-regalada-la-gran-mineria-cobre-chile-nuevas-estimaciones-2005-2014

Svampa, M., 2019. Las fronteras del neoextractivismo en América Latina. Conflictos socioambientales, giro ecoterritorial y nuevas dependencias. CALAS y Bielefeld University Press. http://calas.lat/sites/default/files/svampa_neoextractivismo.pdf

Svampa, M., Mantovani, E., Gabbert, K. and Lang., 2019. En las fronteras del cambio de época. Escenarios de una nueva fase del extractivismo en América Latina. In Cómo se sostiene la vida en América latina? Feminismos y re-existencias en tiempos de oscuridad (Abya Yala y Fundación Rosa de Luxemburgo, pp. 169–218).

Temper, L., Bene, D. and Martinez-Alier, J., 2015. Mapping the frontiers and front lines of global environmental justice: The EJAtlas. Journal of Political Ecology, 22(1), Article 1. https://doi.org/10.2458/v22i1.21108

Ureta, S., 2016. Caring for waste: Handling tailings in a Chilean copper mine. Environment and Planning A: Economy and Space, 48(8), 1532–1548. https://doi.org/10.1177/0308518X16645103

Ureta, S. and Flores, P., 2018. Don't wake up the dragon! Monstrous geontologies in a mining waste impoundment. Environment and Planning D: Society and Space, 36(6), 1063–1080. https://doi.org/10.1177/0263775818780373

Ureta, S., Mondaca, F. and Landherr, A., 2018. Sujetos de desecho: Violencia lenta e inacción ambiental en un botadero minero abandonado de Chile. Canadian Journal of Latin American and Caribbean Studies / Revue Canadienne Des Études Latino-Américaines et Caraïbes, 43(3), 337–355. https://doi.org/10.1080/08263663.2018.1491685

Yin, R., 2018. Case Study Research and Applications: Design and Methods. SAGE.

Towards the Optimization of Electric Load–Haul–Dump Equipment: Implications for Mining Decarbonization

Daniel Lira[1,2], Luis Felipe Orellana[2,3], Ángela Flores[1,4], Gonzalo Monsalve[5], Gonzalo Ramírez[5], Javier Ruiz-del-Solar[1,2], Marcos E. Orchard[1,6], Pierre Nancel-Penard[2], Diego Mancilla[2]

1. Departamento de Ingeniería Eléctrica, Universidad de Chile, Chile
2. Advanced Mining Technology Centre (AMTC), Universidad de Chile, Chile
3. Departamento de Ingeniería de Minas, Universidad de Chile, Chile
4. Instituto de Sistemas Complejos (ISCI), Universidad de Chile, Chile
5. Gerencia Corporativa de Innovación y Tecnología, CODELCO, Chile
6. Centro de Aceleración Sostenible de Electromovilidad (CASE), Universidad de Chile, Chile

**Corresponding author at: daniel.lira@ug.uchile.cl*

Introduction

The mining industry in Chile is a key driver of the national economy, yet it is also one of the largest energy consumers in the country [2], [4]. In 2024, the copper mining sector accounted for 19% of fossil fuel use and 34% of the national electricity demand [2]. This demand is expected to increase significantly, from 26.9 TWh in 2024 to 32.5 TWh by 2034 [1]. Given the current energy mix, this translates into over 18% of Chile's total CO_2 emissions [4], [5]. These figures underscore the urgency of adopting strategies that decouple mining productivity from greenhouse gas emissions.

In response to the global climate crisis, Chile has committed to achieving carbon neutrality by 2050 [3], [7]. This goal requires a profound transformation of energy consumption across all productive sectors. One of the most critical steps in this process is the electrification of energy-intensive industries. Within the mining sector, the transition from diesel to electric mobile equipment represents a strategic opportunity to reduce direct emissions at the operational level.

Among the different underground processes, the production stage is particularly relevant due to its high energy intensity and reliance on diesel-powered load haul dump (LHD) vehicles. Replacing these with electric LHDs can bring significant environmental benefits, such as reduced ventilation needs and noise levels [6], [8], [10]. However, this transition also introduces complex planning challenges, especially under dynamic electricity pricing schemes and infrastructure constraints. Additionally, the performance of electric fleets depends heavily on the charging strategy employed. In this context, two technologies are particularly relevant: onboard charging, where the LHD connects directly to a fixed charging point, and battery swapping, where the depleted battery is replaced with a fully charged one. Both approaches have different implications for operational efficiency, energy demand, and scheduling flexibility [9].

To address these challenges, this work develops a short-term scheduling optimization model for LHD fleets, applicable to fully electric, diesel, or hybrid configurations. The model integrates production planning with battery charging management, aiming to minimize total energy costs while fulfilling

daily extraction targets. It considers vehicle movements, energy flows, and state transitions within a discrete time horizon. Operational constraints reflect real-world conditions, including travel times, battery autonomy, charging power limits, swap times, and fuel tank dynamics. The objective function combines electricity and diesel costs over the full planning horizon.

The remainder of this extended abstract is structured as follows. Section 2 presents the methodology, including an in detail description of the consumption model, the mathematical formulation of the optimization problem and the case study configuration. Section 3 discusses the results and their implications for operational cost reduction and decarbonization. Section 4 concludes with key findings and insights for the adoption of optimized electromobility strategies in underground mining.

Methodology

Consumption Model

To accurately estimate the energy demands of electric LHDs during their operational cycles, a detailed consumption model was developed. This model characterizes the physical dynamics of each trip performed by a vehicle between a dumping point and a drawpoint within the mine layout. The energy required for each trip is calculated by analyzing the mechanical forces acting on the LHD throughout its movement, assuming typical acceleration, cruising, and deceleration phases.

$$P_{wheels}(\tau) = [(m + m_{load}) \cdot (a(\tau) + g \cdot \cos(\theta) \cdot c_r + g \cdot \sin(\theta)) + \frac{1}{2} \cdot \rho_{air} \cdot A_f \cdot c_d \cdot v(\tau)^2] \cdot v(\tau) \quad (1)$$

The total power required at the wheels $P_{wheels}(\tau)$ at time τ is given by:

m is the weight of the LHD (unloaded),
m_{load} is the mass of the material being transported,
$a(\tau)$ and $v(\tau)$ are the acceleration and velocity profiles over time,
g is gravitational acceleration,
θ is the slope angle of the road segment,
c_r is the rolling resistance coefficient,
ρ_{air} is the air density,
A_f is the frontal area of the vehicle, and
c_d is the aerodynamic drag coefficient.

To compute the mechanical power required by the drivetrain, the wheel power is corrected for drivetrain efficiency η_{drive}, assuming no regenerative braking and only positive power values:

$$P_{mech}(\tau) = \max\left\{0, \frac{P_{wheels}(\tau)}{\eta_{drive}}\right. \quad (2)$$

The total average mechanical power consumption $p_{i,j}$ for a complete cycle from the dumping point to drawpoint j for LHD i is computed as:

$$p_{i,j} = \frac{1}{d_{i,j}} \left(\int_0^{d_{i,j}} P_{mech}(\tau)\, d\tau + e_{load} + e_{unload}\right) \quad (3)$$

where:

$d_{i,j}$ is the total duration of the round trip,
e_{load} and e_{unload} are the energy demands of the hydraulic system during loading and dumping operations.

This consumption model is evaluated for each route and vehicle type, and the resulting average power values are passed as input parameters to the optimization model. The same structure can be extended to diesel LHDs, where the power demand is translated into fuel consumption using a specific fuel consumption factor and an assumed engine efficiency.

Optimization Model

The proposed optimization model aims to schedule the short-term operation of LHD fleets, minimizing total energy costs while satisfying production targets and operational constraints. The model is defined over a discrete time horizon and supports multiple fleet configurations, including diesel-only, fully electric, or hybrid fleets.

The decision variables of the model include:

$Y_{i,j}$: binary variable equal to 1 if LHD i is operating a trip to extraction point j at time t.
$Z_{i,t}$: binary variable equal to 1 if LHD i is parked or at the charging station at time t.
$X_{b,i,t}$: binary variable equal to 1 if battery b is assigned to LHD i at time t.
$Z_{charge\ b,j}$: binary variable equal to 1 if battery b is at the charging station at time t.
$P_{b,t}$: continuous variable indicating the charging power [kW] of battery b at time t.
$B_{b,t}$: state of charge [kWh] of battery b at the end of time t.
$C_{i,t}$: continuous variable representing the diesel refueling rate [L/h] of LHD i at time t.
$E_{i,t}$: diesel tank level [L] of LHD i at the end of time t.

In order to minimize the operating costs, the following objective function is proposed:

$$min \sum_{t\epsilon T}[\sum_{b\epsilon B}\left(P_{b,t} \cdot \Delta t \cdot c_e(t)\right) + \sum_{i\epsilon I}(C_{i,t} \cdot \Delta t \cdot c_d)] \quad (4)$$

The objective function quantifies the total operational energy cost over the planning horizon by summing the electricity and diesel expenditures associated with the operation of the LHD fleet. The first term corresponds to the cost of charging electric batteries, calculated as the product of the charging power $P_{b,t}$, the time step duration Δt, and the marginal electricity cost $c_e\,(t)$ at each time interval t. The second term represents the cost of diesel refueling for combustion-based LHDs, determined by multiplying the diesel refueling rate $C_{i,t}$, the time step duration Δt, and the unit diesel price c_d. Here, Δt denotes the duration of each time interval in hours, $c_e\,(t)$ is the marginal electricity price in USD per megawatt-hour, and c_d is the diesel cost in USD per liter. By minimizing this objective, the model seeks to identify optimal operation schedules that reduce energy expenses while ensuring production targets are met.

The optimization model incorporates a comprehensive set of constraints that reflect the operational logic and physical limitations of underground mining equipment. These restrictions are essential to guarantee both the feasibility and realism of the scheduling outcomes, ensuring that energy use aligns with production demands and infrastructure capacities.

First, the model defines the operational state of each LHD at every time interval. A vehicle can either be moving toward or returning from a drawpoint, parked at a charging station, or idle. Transition logic ensures consistency across intervals, with auxiliary variables capturing the initiation and completion of trips. During shift changes, all vehicles must be stationary, allowing for fuel refueling in diesel LHDs or battery swapping in electric ones.

The battery management component maintains the evolution of each battery's state of charge over time, accounting for both consumption during trips and replenishment during charging. Charging is only permitted when the battery is located at a charging station, and the number of

batteries connected simultaneously cannot exceed the available infrastructure. Each electric LHD must have exactly one battery assigned at all times, and this assignment can only be changed while the vehicle is parked. Logical constraints prevent a battery from being both in use and under charge simultaneously. To ensure energy neutrality, the final state of charge must match the initial one, and all battery levels must remain within technical bounds throughout the schedule.

Diesel fuel dynamics are modeled similarly. The tank level of each diesel LHD is tracked across time intervals, considering consumption during trips and refueling events. Fueling is restricted to predefined shift change periods, and the tank must be filled to its maximum capacity during those moments. Refueling flow rates are limited by physical constraints and only allowed when the vehicle is not in motion. As with batteries, the fuel level must remain within a valid range and return to its initial value at the end of the planning horizon.

Production constraints ensure that daily extraction targets are met at each drawpoint. The total extracted material is computed by summing the contributions from all LHDs assigned to a given drawpoint, factoring in the number of completed trips, bucket capacity, and a filling efficiency parameter. In the case of electric vehicles with battery swapping, a penalty is incorporated into the extraction balance to reflect the operational delay introduced by the swap process.

Finally, the model includes logical consistency constraints that link binary assignments to physical variables. For example, a battery may only be assigned to one LHD or to a charger at any given time, but never both. Charging power is bounded by the technical specifications of each battery, and battery swaps or reassignments are allowed only when the associated vehicle is stationary. Additionally, a global constraint ensures that the total power drawn by all charging activities never exceeds the electrical capacity of the mine's infrastructure.

Case Study

We evaluate three haulage configurations on a generic underground mine layout: a diesel baseline, battery-electric LHDs with on-board charging, and battery-electric LHDs with battery swapping. The layout comprises 40 drawpoints organized along four parallel drifts and a single centralized node used for ore dumping and vehicle service (charging or swapping, as applicable). For technology comparability, the diesel configuration employs Sandvik LH517i units, whereas both electric configurations use Sandvik LH518B units. The spatial arrangement of the system is depicted in Fig. 1, which summarizes the generic block-caving layout used in our experiments (see Fig. 1).

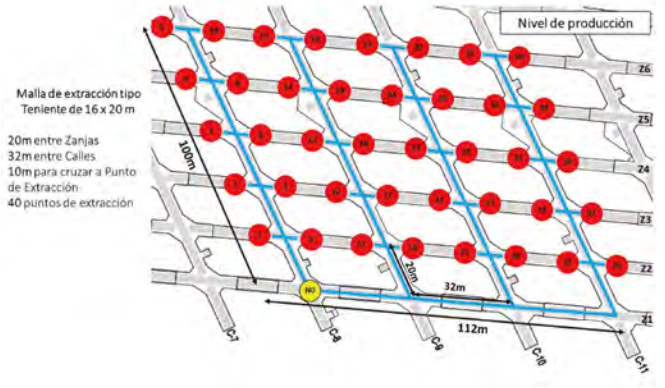

Figure 1. Generic block-caving mine system layout.

The study is conducted over a three-day operation under two Chilean energy contexts, Chuquicamata (north) and Machalí (central). Electricity costs are represented using the time-varying marginal cost at the corresponding electrical bus, enabling sensitivity analyses to price volatility by location. This design isolates technological effects (diesel vs. on-board vs. swapping) while keeping the layout and operating context constant. Regional heterogeneity in renewable resource availability that underpins these cost patterns is illustrated by the annual average solar irradiance distribution across Chile (see Fig. 2).

Figure 2. Geographic distribution of average solar irradiance across Chile over one year.

Results and Discussions

Technology comparison

Across scenarios, diesel LHDs maintain continuous duty cycles because autonomy is not binding within the planning horizon. This enables high effective utilization and consistent attainment of extraction targets. By contrast, on-board charging LHDs exhibit stop-and-charge patterns that fragment operations. Frequent charging interruptions reduce temporal continuity of haulage, which lowers achievable extraction at binding nodes when the system is autonomy constrained. Battery-swap LHDs largely overcome this limitation. Once a pack is depleted, vehicles can return to the swap bay and resume with a fully charged pack within minutes. The resulting autonomy windows are comparable to diesel, which allows battery-swap fleets to match diesel extraction. These operational differences are reflected in the time evolution of fuel/energy levels and completed tasks for each configuration (see Figs. 3–5).

Figure 3. Diesel LHD fuel level evolution in comparison to hauled material and tasked performed overtime.

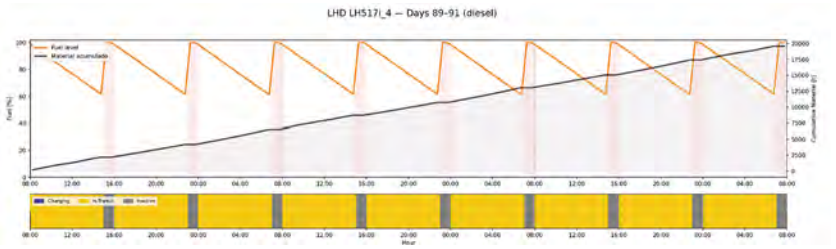

Figure 4. On-Board LHD fuel level evolution in comparison to hauled material and tasked performed overtime.

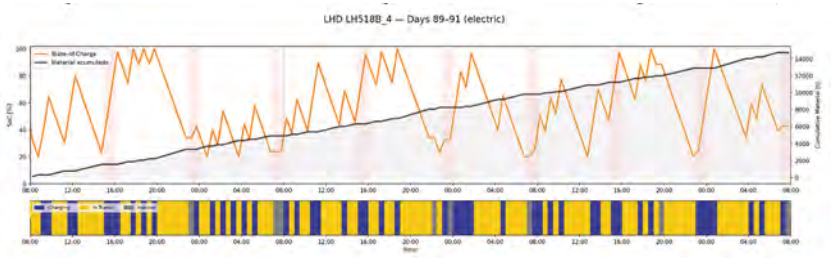

Figure 5. Battery-Swap LHD fuel level evolution in comparison to hauled material and tasked performed overtime.

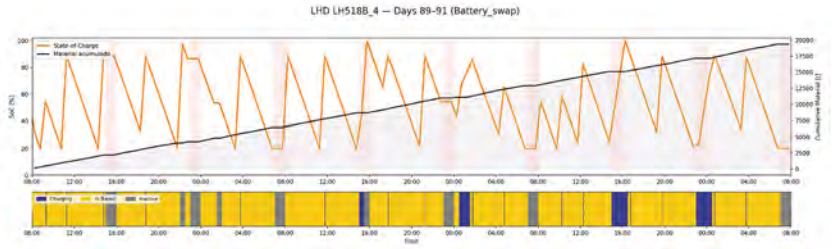

Location comparison Chuquicamata

In Chuquicamata, long off-peak windows with low marginal electricity costs allow battery-swap fleets to distribute charging more evenly over time. The optimization schedules swaps so that pack recharging aligns with inexpensive hours, which flattens the aggregate charging profile and attenuates station demand spikes. Smoother charge management reduces both coincident power and the probability of queueing at chargers or swaps, which supports sustained autonomy and steady extraction. The resulting charging power profiles for on-board and battery-swap fleets at this site are shown in Fig. 6 and Fig. 7, respectively (see Figs. 6–7).

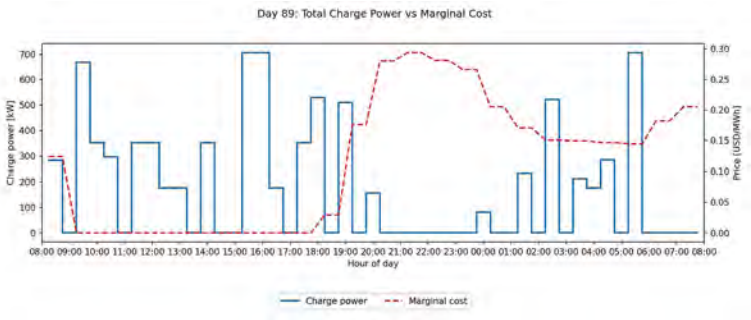

Figure 6. Charge power demanded by the batteries for a On-Board fleet in Chuquicamata

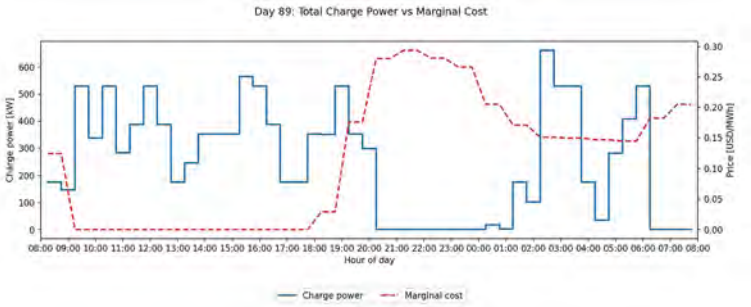

Figure 7. Charge power demanded by the batteries for a Battery-Swap fleet in Chuquicamata.

Location comparison Machalí

Machalí presents narrow low-price windows. Under these conditions, battery-swap operations tend to compress recharging into short intervals, concentrating load and producing high power peaks at the swap-charging facility. The contrast with Chuquicamata highlights the flexibility of battery swapping to either stretch or compress charging power in response to price signals. It also surfaces a practical constraint. Extremely high peaks may be infeasible depending on substation limits, transformer ratings, feeder capacity, and the allowable short-term coincident demand at the mine connection point. The concentration of load in Machalí is evident in the charging power traces for on-board and swap fleets (see Figs. 8–9).

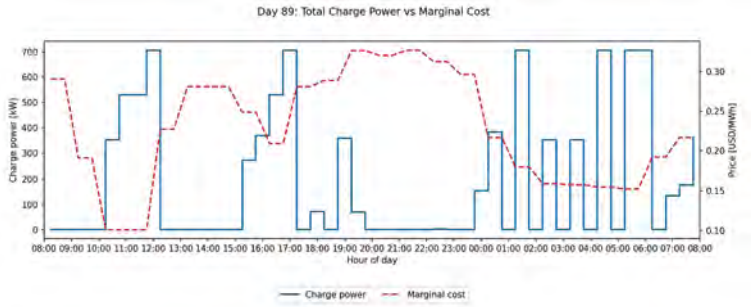

Figure 8. Charge power demanded by the batteries for a On-Board fleet in Machalí.

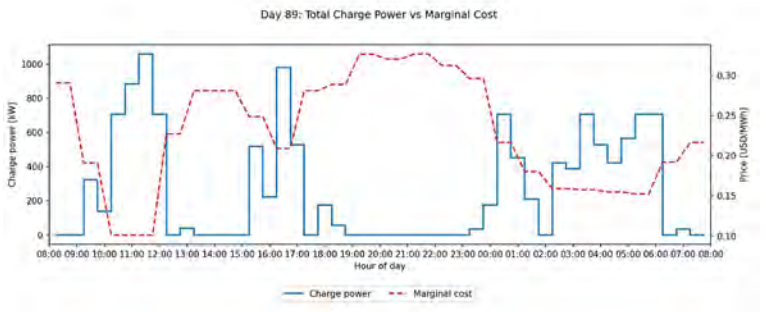

Figure 9. Charge power demanded by the batteries for a Battery-Swap fleet in Machalí.

Summary

The comparative KPI table (Table 1) shows that battery swapping increases extraction ceilings by preserving autonomy without adding significant non-productive time. Crucially, this improvement is achieved while remaining economically competitive on a USD per ton basis. In systems where extraction targets are autonomy-limited, the swap option provides diesel-like productivity with the potential to exploit low-cost electricity windows. The benefit is strongest when price valleys are sufficiently wide to avoid excessive demand clustering. A detailed summary by scenario is provided in Table 1.

Table 1. KPIs summarized per scenario

Scenario	Total charge cost [USD]	Tons extracted [tons]	Usd per ton [USD/tons]
Diesel	5403,2	92539,4	0,0584
Battery Swap Machalí	1778,6	93355,5	0,0191
On-Board Machalí	1317,4	69048,0	0,0191
Battery Swap Chuquicamata	523,2	93151,8	0,0056
On-Board Chuquicamata	337,3	68619,6	0,0049

Conclusions

Electrification of underground haulage is pivotal for Chile's carbon-neutrality pathway and for decoupling production from direct diesel emissions. Within the evaluated layout and energy price profiles, battery-swap LHDs emerge as the most robust alternative because they retain long autonomy and sustain high utilization while enabling cost-aware scheduling of charging. Where extraction targets are high and continuity of service is critical, swap systems deliver diesel-comparable throughput with lower operational exposure to fuel price volatility. Future work should embed explicit mine-site power caps, transformer and feeder limits, and the discrete availability of chargers and swap bays. Incorporating these constraints, along with queueing dynamics and peak-demand penalties, will sharpen feasibility assessments and improve the economic ranking of technologies under realistic electrical interconnection conditions.

References

[1] Comisión Chilena del Cobre (Cochilco), Proyección del consumo de energía eléctrica en la minería del cobre (Periodo 2024–2034), 2025, pp. 1–39. [En línea]. Disponible en: https://www.cochilco.cl/web/informe-proyeccion-del-consumo-de-energia-electrica-en-la-mineria-del-cobre-periodo-2024-2034/

[2] Consejo Minero, "Energía," en Minería en más de 280 caracteres, cap. 9, pp. 76–80, 2023. [En línea]. Disponible en: https://consejominero.cl/wp-content/uploads/2023/04/mineria-280-caracteres.pdf

[3] Biblioteca del Congreso Nacional de Chile, "Ley N.º 21.455 — Marco de Cambio Climático," Diario Oficial de la República de Chile, n.º 43.277, 2022. [En línea]. Disponible en: https://www.bcn.cl/leychile/navegar?idNorma=1177286&idVersion=2025-07-11&idParte=10341104

[4] Ministerio de Energía, Balance Nacional de Energía, 2020. [En línea]. Disponible en: https://energia.gob.cl/pelp/balance-nacional-de-energia

[5] J. Hooli, B. Skawina, A. Halim y F. Sundqvist, "Analysing Battery Swapping of Battery Electric Load Haul Dump (LHD) Machines in Block Cave Mining Using Discrete Event Simulation (DES)," Mining, Metallurgy & Exploration, vol. 41, pp. 2877–2890, 2024. doi: 10.1007/s42461-024-01146-4.

Workshops "Voices in Play: A Playful Methodology for the Co-Creation of Situated Indicators." A Proposal for the Participatory Evaluation of Emerging Lithium Extraction Technologies in the Salar de Atacama

Natlia Bustos-Guzmán[1*], Iván Ojeda-Pereira[2,3], Fernando Campos-Medina[1], Sebastián Herrera-León[2,4], Carolina Rojas[2], Marcelo Lufín[5]

1. Department of Sociology, University of Chile, Santiago, Chile
2. Department of Industrial Engineering, Catholic University of the North, Antofagasta, Chile
3. School of Engineering Sciences, LUT University, Lappeenranta, Finland
4. Institute of Engineering Sciences, O'Higgins University, Rancagua, Chile
5. Department of Economics and Institute of Applied Regional Economics (IDEAR), Catholic University of the North, Antofagasta, Chile

** Corresponding author at: Department of Sociology, University of Chile, Av. Ignacio Carrera Pinto 1045, Ñuñoa, Santiago, Chile: natalia.bustos.g@ug.uchile.cl*

ABSTRACT

The lithium industry has become relevant due to the global energy transition. This has generated economic opportunities and socio-environmental challenges, especially in extraction territories where fragile ecosystems and complex governance converge. The "social" aspects of mining have been explored by political and social sciences, however, no theoretical or methodological dialogue has been developed with engineering sciences. With an interdisciplinary approach, we present the results of a research project whose objective was to develop a participatory methodology for creating indicators to evaluate emerging lithium extraction technologies. To this end, we conducted a focused review of scientific literature and semi-structured interviews with experts in citizen participation in complex contexts, considering actors from the public and private sectors in Chile. Our proposal can be applied to understand possible technological changes in complex processes related to mining. This contributes to i) interdisciplinary dialogue between the social sciences and engineering for the development of mining connected to local communities and ii) promotes equitable governance in the context of the development of the lithium industry, strengthening participation in the transition to green mining.

Keywords: Social sustainability, Sociotechnologies, Socioengineering, Participatory methodologies, Green mining.

Introduction

The National Lithium Strategy, promoted by the Chilean government, seeks to link the country's economic development with the transition to a green economy, positioning it as a key player in this global process (Government of Chile, 2023). In a context where resources such as lithium are

strategic for clean technologies, energy storage, and electric mobility, their exploitation is projected as an economic and geopolitical opportunity, but also as a governance challenge in the face of climate change. The plan emphasizes responsible, sustainable, and inclusive extractive practices, supported by international agreements such as ILO Convention 169 and the Escazú Agreement, which require guaranteed access to information, effective participation, and environmental justice (Government of Chile, 2023, p. 23). However, current tools do not adequately capture the social, cultural, and environmental dimensions. The Lithium Sociotechnologies ring project (ANID/ATE240017) shows that evaluation frameworks favor traditional indicators and omit situated knowledge, reproducing conventional commercial practices and insufficient western-style evaluations (Blair et al., 2023). This gap is the central problem addressed by this study, which seeks to develop more relevant and contextualized methodologies for evaluating the impacts of emerging lithium extraction technologies (DLE).

Many of the areas involved in lithium extraction are historically disadvantaged territories that have been approached from a functionalist utilitarian logic, where the value of the territory is reduced to its productive potential, omitting its cultural, ecological, and symbolic dimensions (Blair et al., 2023). In this sense, the energy transition must be understood in its dual dimension: as an opportunity to move towards a more sustainable economy and green mining, but also as a risk of deepening inequalities if the right of territories to define their own horizons for development is not recognized. Effective participation should not be limited to mitigating conflicts but should strengthen the collective construction of a future shared by communities, considering their expectations, memories, and territorial identities, as well as recognizing dissenting voices as an integral part of the process.

There is a robust debate in the social, political, and economic sciences about mining in extractive contexts, where the "social" aspects of mining have been explored under different lines of research that respond to conflicts specific to the territory and the industry. On the one hand, the model of water use has been the focus of discussion due to the fragility of the system. In this context, various studies from the field of political ecology (Prieto, 2016; Blair et al., 2023) have documented how neoliberal water management has generated structural inequalities in its distribution, favoring large-scale mining over indigenous peoples. In particular, brine has been excluded from the regulatory frameworks of the water code, as it is classified solely as a mineral. This is a significant issue, given that traditional lithium extraction in the Salar de Atacama (SdA) is currently based mainly on the use of solar evaporation technology to concentrate brine extracted from depths of more than 30 meters below the salt flat crust. Evaporation, considered "natural," can take between 12 and 18 months, during which time between 85% and 95% of the water content in the brine evaporates (Herrera-León et al., 2025). This is an important factor to consider, as it suggests that water availability and the survival of biodiversity in this unique ecosystem (Lorca et al., 2022) could emerge as central concerns among the communities participating in the workshops.

Despite the contribution of these studies, there has been limited capacity for interdisciplinary dialogue, particularly with engineering sciences, a key discipline for the functioning of the mining industry. Similarly, in the field of engineering, efforts to address social dimensions have been scarce and, for the most part, marginal. A notable exception is the work of Negrete et al. (2024), which analyzes the socio-environmental implications of decarbonization in the extraction and processing of minerals such as copper and lithium. This study seeks to identify the potential social and environmental impacts that could be integrated into mining operations through a participatory methodology. However, research such as this remains peripheral within the core discipline of engineering.

In this article, we propose to design a participatory methodology for the development of situated indicators that allow for the evaluation of emerging lithium extraction technologies (DLE). To this

end, two specific objectives were defined: i) to identify methodological approaches and techniques for the participatory construction of indicators for the evaluation of lithium technologies, and ii) to anticipate possible tensions and challenges in the development of participatory workshops, in order to contribute to the development of a more inclusive and contextualized green mining. In this way, the article makes a double contribution: on the one hand, it contributes to the field of green mining by proposing a framework for analyzing indicators that integrates civil society and local communities as key actors in defining sustainability criteria. On the other hand, it offers a methodological discussion that introduces qualitative and participatory criteria in a field traditionally approached from technical and quantitative indicators.

Methodology

The qualitative nature of this research is justified insofar as its central purpose is to understand and interpret the perceptions, knowledge, and priorities of local actors in order to develop localized indicators for the evaluation of direct lithium extraction (DLE) technologies. Qualitative research is particularly relevant when the aim is to access the meaning that people attach to their social and territorial experience (Denzin & Lincoln, 2018), rather than to measure predefined variables. As Flick (2018) points out, this approach allows us to explore the multiple dimensions and meanings that shape social processes, which is essential in contexts where mining interacts with diverse cultural, environmental, and political realities.

Table 1: Information collection and analysis techniques

Survey technique	Analysis technique	Objective
a) **Literature review:** Papers on participatory methodologies published in academic databases.	Documentary analysis. Analysis matrix, classifying them according to their methodological description and the advantages or limitations identified.	Identify methodological approaches and techniques for the participatory construction of indicators used in the evaluation of lithium technologies.
b) **Semi-structured interviews:** Experts with experience in participatory methodologies, ideally in mining, energy, or environmental contexts in Chile.	Content analysis. Transcription and analysis using thematic coding with emerging categories.	Identify methodological approaches and techniques for the participatory construction of indicators for the evaluation of lithium technologies. Anticipate possible tensions and challenges in the development of participatory workshops, in order to contribute to the development of a more inclusive and contextualized green mining industry.

Source: Own elaboration.

Information gathering techniques

The methodological design combined a literature review and semi-structured interviews with experts as complementary techniques. The literature review covered 22 scientific journals and 1,609 articles, of which 95 were selected and 23 were subsequently analyzed in depth, focusing on participatory methodologies and methodological design. This analysis made it possible to identify approaches, tools, and descriptions applied that were relevant to the participatory construction of situated indicators.

At the same time, semi-structured interviews were conducted with experts in citizen participation in the public, private, and civil society sectors, selected through convenience sampling. Although this technique has limitations in terms of generalization, it was appropriate for exploratory research requiring access to specialized profiles (Stewart, n.d.). Based on the findings in the literature, the profile of interviewees was expanded to include specialists in playful methodologies, with the aim

of incorporating innovations such as gamification into participatory design processes, promoting inclusive and effective dynamics in the context of lithium.

Analysis techniques

The analysis was structured around two main procedures. First, the literature review was organized using a matrix that classified the documents collected (2013–2025) according to their context of application, as well as the advantages and limitations of the participatory methodologies described. This systematization allowed for the development of a documentary analysis, understood as a systematic procedure for the selection, evaluation, and synthesis of sources in order to identify patterns and gaps in the literature (Bowen, 2009).

Secondly, the semi-structured interviews were transcribed and subjected to a content analysis process. This is understood, following Krippendorff (1990), as a research technique that allows reproducible and valid inferences to be made about the data in relation to its context. In our work, we conceive it as a methodological perspective oriented towards the study of the expression objects produced by the subjects—particularly verbal language—which can be collected, classified, and compared to investigate their meanings (Navarro & Diaz, 2007). This approach recognizes that all expressions are, at its origin, a communicative act, but when it crystallizes into an object (a phrase, a text, a discourse), it becomes susceptible to systematic analysis. In this sense, content analysis applied to interview transcripts allowed us to identify emerging categories that reflect perceptions, tensions, and methodological proposals relevant to the development of our own methodological model.

Results and discussion

As a result of the analysis of the 23 selected texts, 17 methodologies were identified that met three key criteria: i) having a methodological description, ii) including the identification of key roles in the participatory process, and iii) having a recognizable "toolbox," that is, techniques or instruments applicable to that methodology. However, after a final filter, 13 methodologies were selected as the main input for the construction of the participatory methodological proposal developed in this study. This decision is based on the suitability of the methodologies for the SdA context, i.e., beyond having a clear description, it was necessary for the documented methodologies to have been tested or implemented in contexts similar to that of this study, namely mining, energy, or environmental settings; broad organizational settings; or applied to local and indigenous communities in the context of territorial projects. In this sense, the four methodologies that were excluded did not meet these latter criteria, as they were developed primarily in educational contexts or in the field of health.

The co-creative participatory methodological shift - gamified

Based on a review of the scientific literature, four cross-cutting approaches were identified in the methodologies analyzed:

Table 2: Cross-cutting approaches in the methodologies analysed

Approach	Description
Collaborative	Focuses on building knowledge in a horizontal and inclusive manner, recognizing both technical expertise and the situated knowledge of communities. Seeks processes of co-production of solutions, encouraging the participation of all stakeholders and valuing diversity of perspectives in decision-making.
Creative	It enhances imagination and the generation of original ideas through techniques that allow for exploring possibilities beyond traditional frameworks. This approach uses tools such as sketches, narratives, or the creation of imagined worlds, facilitating reflection on desirable futures and social innovation in complex contexts.
Ethnographic	It is based on a deep understanding of the experiences, values, memory, and identity of local communities. It prioritizes observation, systematization, and situated analysis of knowledge, turning the voices and experiences of actors into central inputs.
Gamified	It incorporates play, narrative, and experimentation as mediators of participation. Playful dynamics create safe spaces, foster empathy, facilitate the expression of ideas and emotions in an inclusive manner, and enhance both collaboration and creativity within dialogue and co-creation processes.

Source: Own elaboration.

These approaches—collaborative, creative, ethnographic, and gamified—are combined in different proportions within each methodological proposal, as they are complementary to each other. The categorization was carried out through an inductive analysis of the methodological descriptions contained in the selected articles.

Table 3 below shows the distribution of these approaches in the methodologies selected under the criterion of methodological contribution to construct the proposal itself:

Table 3: approaches identified in each methodology

No.	Name of methodology[1]	Type of methodology			
		Collaborative	Creative	Ethnographic	Gamified
1	*"Mister Wolf"*	X	X		
2	*The "Clean Energy" social experiment: A model of layered co-creation*	X	X		
3	*First Nations' Water Sustainability and Security Strategy*	X		X	
4	*Staging Participatory Innovation in Temporary Spaces*	X			
5	*LEGO® Serious Play® (LSP)*	X	X		X
6	*"PNS Workshop Methodology"*	X	X		
7	*Participatory utopian sketch*	X	X		X
8	*Tell me a (un)fortunate story*	X	X		X
9	*Exploratory Co-Design Workshop on Smart Home Imaginaries*	X	X		
10	*Imaginary Future Generations*	X			
11	*Literary Futures*	X	X		
12	*Collaborative mapping from the IAP*	X			
13	*Systematization of Experience*	X	X	X	
	TOTAL: 13	**13**	**9**	**2**	**3**

Source: Own elaboration.

The literature review shows that the methodologies analyzed share a collaborative basis that translates into the search for horizontal, inclusive, and situated processes. From Mister Wolf and the Clean Energy social experiment, which integrate co-creation and co-production of knowledge to address sustainability challenges (Bertella et al., 2021; Gray et al., 2024), to proposals such as the First Nations Water Sustainability Strategy, which incorporates decolonizing frameworks to restore the leading role of indigenous communities in the management of their territories (Black & McBean, 2017), there is a shift towards methodologies that go beyond technical expertise and recognize community knowledge as a central input. This epistemological shift is supported by the ethnographic approach, present in experiences such as collaborative mapping (Calvo & Candón-Mena, 2022) and the systematization of experiences (Monsalves Ibarra et al., 2021), where memory, identity, and the situated production of knowledge become vectors of social transformation.

At the same time, these methodologies reveal the importance of creativity and playfulness as mediators of participation. Initiatives such as LEGO® Serious Play® (LEGO Group, 2010), the participatory utopian sketch (Törnroth et al., 2022), and Tell Me an (Un)fortunate Story (Cueva, 2025) show that playful and narrative devices allow actors to expand their imagination, distance

[1]In some cases, the names of the methodologies were interpreted according to their methodological description.

themselves from habitual frameworks, and open up more inclusive and empathetic spaces for dialogue. Along these lines, methodologies such as Literary Futures (Braun et al., 2024) and Imaginary Future Generations (Hara et al., 2023) delve into the speculative dimension of futures, showing that the creation of characters, worlds, or alternative perspectives is a powerful way to

rehearse desirable transformations. Thus, the contributions reviewed outline a methodological field in which collaborative, creative, ethnographic, and gamified approaches are articulated, shaping the framework conducive to a gamified participatory shift that integrates imagination, play, and collective action as drivers of dialogue and co-creation.

The workshop "Voices in Play: Playful Methodology for the Co-creation of Situated Indicators"

The workshop design is based on the articulation of notions of post-normal science (PNS), narrative approaches, and playful dynamics, but with a particular twist: while PNS proposes expanding the peer community to include both experts and non-academic actors (Fuller et al., 2025), in this case the central protagonists are local communities, whose voice is essential for developing social sustainability indicators around SLEDs. Experts participate only as mediators and facilitators of technical content, guiding the process without taking center stage. In this way, the workshop aligns with the Latin American tradition of participatory methodologies—such as the systematization of experiences (Monsalves Ibarra et al., 2021) or collaborative mapping (Calvo & Candón-Mena, 2022)—which conceive the production of knowledge as a situated and emancipatory exercise, useful for the communities themselves.

Likewise, the methodological proposal incorporates storytelling and playfulness as strategies to enhance collective imagination and break with pre-established frames of reference. As experiences such as LEGO® Serious Play® (LEGO Group, 2010), Tell Me an (Un)fortunate Story (Cueva, 2025), and Literary Futures (Braun et al., 2024) show, play, character creation, and story construction allow participants to explore alternative futures in an inclusive, creative, and critical way. In this sense, play enables the translation of community experiences and values into situated indicators, while its playfulness creates a safe space for experimentation, empathy, and horizontal dialogue.

Thus, the workshop is justified as a participatory, co-creative, gamified approach: a mechanism that places imagination, play, and community voice at the center of the design of ELA assessment tools, ensuring that sustainability indicators reflect the realities, aspirations, and concerns of those who inhabit lithium-producing territories. Collaboration requires strong relationships and trust; in this sense, literature supports the incorporation of playful tools to strengthen participation and build bonds between participants. For example, Bertella et al. (2021) show that the implementation of playful tools in workshops promotes active engagement and the creation of trusting relationships among attendees. This evidence supports our decision to propose a gamified approach, adapting the game and dynamics to our specific context, without replicating previous experiences, but rather taking as a reference the proven value of gamification in fostering participation and collaboration.
For the implementation of the workshop, five structured phases were defined, designed to facilitate informed, contextualized, and representative participation. Phases 1, 2, and 3 of these workshops can be carried out in a single extended day or in two sessions, depending on the availability and level of commitment identified among participants to the project. This flexibility allows the methodology to be adapted to different contexts and ensures that participation is meaningful, maintaining the pace and quality of dialogue and collective knowledge building.

a) Phase 0: Initial approach (2 months)

This phase takes place at least two months before the workshop itself and aims to introduce the topics to be discussed in a clear and accessible way, while encouraging the active participation of local actors. The strategy includes the distribution of informational brochures and dissemination on social media, written in simple language and supported by visual resources, which present the main

scope of the lithium industry in the territory and the importance of evaluating direct extraction technologies (DLE), specifically: solvent extraction, adsorption, ion exchange, electrochemical processes, and membrane extraction. In addition, an information session is being organized—either in person or online, depending on the participants' access conditions—to introduce the implementation team, explain the scope of the project, and highlight the importance of community participation in each stage (timelines, dynamics, and resources involved).

Beyond raising awareness of the issue, this phase seeks to spark interest and commitment among the community and local actors, inviting them to become involved in a sustained and leading role in the process. Framed within the National Lithium Strategy, this stage highlights Chile's strategic role in the global energy transition scenario, creating the conditions for conscious and committed participation in the later phases of the project.

b) Phase 1: Exchange of prior knowledge (45 minutes)

This phase takes place at the beginning of the workshop and starts with a formal introduction of the implementation team (15 minutes), with a total duration of 45 minutes. Its objective is to clarify technical questions regarding direct lithium extraction (DLE) technologies, using accessible and familiar language that facilitates understanding of the fundamentals and differences between each technology (solvent extraction, adsorption, ion exchange, electrochemical processes, and membranes).

To promote this understanding, visual and narrative resources are available upon arrival—banners, illustrative maps, and stories in the form of tales or ancestral legends—that build bridges between technical knowledge and local cultural frameworks. Participants are then invited to write their questions on a collective flip chart. While the implementation team welcomes them, the facilitators organize these questions into emerging categories. Subsequently, some participants are randomly selected to read the questions aloud, which enables a space where the panel of experts responds in a dialogue to the technical concerns raised (15 minutes). Finally, the floor is opened for the last 15 minutes, encouraging participants to share their experiences and knowledge about lithium extraction, thus enriching technical conversation with local perspectives.

The design of this phase recognizes that images and narratives activate the sensory and experiential dimension, creating conditions conducive to participants drawing on their memories and experiences as they engage in the activity (Wunenburger, 2020; Juliani Pereira & Hargreaves, 2024). In this way, the initial phase not only functions as a space for technical clarification, but also as a creative and culturally meaningful device to prepare the community for an informed and engaged dialogue.

c) Phase 2: Gamified dialogue (90 minutes)

In this phase, dialogue is encouraged through a specially designed playful tool: a board game with a set of illustrated cards called "Voces in Juego" (Voices in Play). This participatory methodology uses gamification to move the conversation from the purely linguistic plane to the symbolic space, promoting deeper and more accessible communication. In this way, it is possible to involve diverse cultures and age groups, broadening the inclusion of voices and perspectives and reducing resistance to complex or sensitive discussions.

The game allows concepts to be constructed and externalized in a tangible way, which not only facilitates individual reflection but also invites participants to reflect collectively (LEGO Group, 2010). The idea of "thinking with the body" has been supported by findings in psychology and neuroscience, which show how cognitive processes, including learning and memory, are influenced by physical interaction with the environment (LEGO Group, 2010).

Finally, the game incorporates a graphic style inspired by Andean villages, enriching the dialogue with cultural symbols that connect with local roots and contribute shared meanings, strengthening the symbolic and cultural dimension of the participatory process.

Table 3: Game development

Moments	Time	Description of activities
Moment 1: Symbolic activation	10 minutes	Participants choose an illustrated card that evokes something meaningful about their life, territory, or their concerns, sharing in a circle what they see in the image and what feelings or memories it generates. This exercise breaks the ice and opens the dialogue from an emotional and symbolic dimension.
Moment 2: Exploration of thematic areas and in-depth dialogue	30 minutes	One of the four themes on the board is selected: Territory; Community; Technology; and Sustainability. A random card from the chosen theme is placed in the center and a guided conversation begins with questions such as: What does this image tell us? What issues or tensions emerge? How does it relate to our experience with lithium extraction? (These guiding questions can be modified for each interest group).
		During the dialogue, participants can select cards with keywords (e.g., "justice," "memory," "dialogue," "imbalance") that reflect what they have heard or felt, placing them next to the card to form a collective concept cloud; or they can add a new card from any theme to further open up the dialogue. Each participant's contribution should not exceed two minutes, and then the floor should be given to another person at the table, thus encouraging the participation of all members.
Moment 3: Naming what is important	15 minutes	Reviewing the cards and tokens used, the group identifies recurring concerns, values, and elements of the environment that should be protected or measured. These tokens are grouped into categories that are named collectively. Everything is recorded in the Territory Notebook, which is completed by the facilitator and systematizes the results.
Moment 4: Collective synthesis and closing	15 minutes	All the cards and highlighted concepts are gathered in the center for a brief prioritization exercise, answering the question: What are the most urgent issues?

Source: Own elaboration.

d) Phase 3: Establishment of Indicators (90 minutes)

In this phase—the last one in the workshop itself—the objective is to transform the previously identified values, concerns, and criteria into specific and contextualized indicators capable of evaluating SLEDs from the perspective of the territory and its communities. To this end, the facilitator introduces the concept of an "indicator," explaining its functions, usefulness, and the characteristics it must meet to be considered technically valid and socially relevant (e.g., clarity, measurability, territorial relevance). This phase is key to leveling the playing field in terms of knowledge among participants and strengthening their role as informed co-evaluators in the following stages of the process.

Participants are given a set of traditional indicators commonly used in the mining industry. These are analyzed collectively in light of previous reflections, in order to identify which ones, resonate or are relevant in the local context. Indicators that are recognized as relevant by participants will be considered validated as situated indicators, allowing for adjustments to their definitions and measurement scales to adapt them to the realities of the territory. On the other hand, those that are not considered significant will be discarded as locally relevant assessment tools. In addition, groups will have the opportunity to propose new indicators, which must be clearly defined, specifying their key components and establishing levels of acceptability or measurement thresholds. Finally, participants will collectively prioritize the validated indicators, organizing them according to their level of relevance and importance for the evaluation of lithium extraction technologies from a territorial perspective.

e) Phase 4: Systematization of results (Post-workshop)

The methodology includes an additional phase, developed exclusively by the implementation team, aimed at systematizing the results obtained in the workshops. This phase seeks to identify synergies, convergences, and common patterns among the proposed indicators, as well as to record disagreements, contradictions, or tensions that arose among the different actors.

This comparative analysis allows for the construction of an integrated and situated vision, which serves as the basis for the final proposal of a set of indicators that are relevant, representative, and sensitive to the context of the SdA. In this way, the methodology not only facilitates the collective construction of indicators but also offers a strategic tool for informed decision-making in the development and evaluation of DLE.

Implementation challenges

a) Context

The interviews show that conflict is inherent in participatory processes in mining, energy, and the environment, manifesting itself both between communities, the state, and companies, and within the communities themselves, as a result of power asymmetrical and previous interventions. These tensions, recognized as inevitable, require anticipation through stakeholder mapping, bilateral meetings, and containment strategies. Likewise, there is evidence of over-intervention in participatory processes, marked by "express" consultations and failed experiences that have generated fatigue, mistrust, and skepticism. In response to this, it is proposed that this methodology should differ from previous practices, incorporating mechanisms for feedback, continuity, and concrete results that lend legitimacy and trust to the process.

b) Time and flexibility

Time and flexibility emerge as critical conditions for the design of participatory methodologies. One interviewee noted that successful experiences have required up to two years of sustained support to build trust and shared results, while another pointed out that rushed processes, such as indigenous consultations within the framework of the National Lithium Strategy, weaken representativeness and increase conflict. Therefore, it is necessary to balance institutional deadlines with community rhythms, considering that "bottom-up participatory approaches require more time" (Black & McBean, 2017). Along with this, the interviews highlight that designs must be adapted to gender, age, literacy, worldviews, and local dynamics, integrating resources such as visual languages, games, or relational spaces, while recognizing local and ancestral knowledge as equal to technical knowledge. In this vein, the literature warns that "the messy, human nature of co-creation demands a commitment to flexibility and ongoing dialogue" (K. Gray et al., 2024), reinforcing the need for open, adaptive, and dialogic methodologies.

c) From the definition of participants to the mapping of actors

The identification and selection of actors appear to be a cross-cutting challenge. Some of the interviews conducted emphasize the need for dynamic, up-to-date mappings that include a diversity of actors beyond the traditional ones, integrating women, adolescents, unions, cultural groups, and small local organizations. Others, however, warn that there is no single formula for defining legitimate representatives, as communities have previously been intervened by the state and companies, which fragments their representativeness. In this context, the methodology must assume the plurality of leadership and accept the coexistence of diverse visions, rather than imposing homogeneous criteria for representation. This joint perspective shows that the participatory construction of indicators must recognize the social complexity of the territory and generate inclusive mechanisms that do not reproduce historical exclusions.

Thus, based on the results obtained from the interviews, a strategy was defined for mapping actors and establishing criteria for selecting participants in the workshops. Based on these inputs, it was

decided to work with differentiated interest groups, with the aim of ensuring a diverse, relevant, and contextualized representation of the relevant actors in the Salar de Atacama. The groups defined were as follows:

- Local government, including municipal authorities and officials, as well as neighborhood associations and community organizations.
- Indigenous communities, differentiating between those that are organized (e.g., the Council of Atacameño Peoples) and those that are not, avoiding their joint participation in the same space, given the previous conflicts reported by informants.
- Irrigation communities, responsible for water resource management in the territory.
- The San Pedro de Atacama Tourism Association, as representative of the local economic sector linked to the tourist use of the territory.

This segmentation seeks to create culturally sensitive spaces for participation, in line with the social dynamics of the territory, and to facilitate intragroup dialogue. Likewise, holding separate workshops for each group allows the methodological dynamics to be adapted to the specific profile of the participants, maximizing the possibility that the indicators discussed respond to their interests, perspectives, and perceptions of the lithium industry. This strategy also contributes to making dissenting or minority views visible, reducing the risk of these being subsumed under dominant or hegemonic criteria in mixed participatory spaces.

Conclusions

The energy transition is a structural challenge for extractive territories such as the Salar de Atacama, where lithium mining plays a strategic role in providing critical resources for clean technologies. This research shows that, in contexts of high socio-environmental sensitivity, the implementation of emerging direct lithium extraction (DLE) technologies cannot be evaluated exclusively on the basis of conventional technical or economic criteria. Instead, it is essential to incorporate localized indicators that integrate cultural, territorial, and social dimensions, transforming the way mining engineering conceives the impact and efficiency of its processes. The research fulfills its objectives by developing a participatory methodology to elaborate these indicators, identifying approaches and techniques for their construction, and anticipating possible tensions in participatory workshops, thus contributing to a more inclusive and contextualized green mining.

The methodology demonstrates that participatory indicator construction not only generates contextualized data, but also empowers community agency, translates local concerns into technical evaluation criteria, and challenges the supremacy of hegemonic technical knowledge. Tools such as the game "Voces en Juego" (Voices in Play) facilitate intergenerational and educational inclusion, overcoming language barriers and promoting creative participation, so that traditionally invisible aspects—water cycles, memory of the territory, spiritual value of the salt flats—are incorporated as measurable and relevant parameters for mining planning.

From an engineering perspective, situated indicators allow DLE technologies to be evaluated not only for their productive efficiency or resource consumption, but also for their social legitimacy and sustainability. By integrating indigenous and community perspectives, historical structural impacts are made visible that would otherwise remain outside traditional impact measurement systems.
In summary, the findings show that moving toward truly green mining requires a hybrid approach that combines technical rigor with social sensitivity, where situated indicators act as instruments of democratic governance and adaptive engineering tools, providing a replicable framework for evaluating DLE technologies in an inclusive, contextualized, and sustainable manner.

References

Bertella, G., Lupini, S., Rossi Romanelli, C. and Font, X., 2021. Workshop methodology design: Innovation-oriented participatory processes for sustainability. Annals of Tourism Research, (89). https://doi.org/10.1016/j.annals.2021.103251

Black, K. and McBean, E., 2017. First Nations' water sustainability and Security Strategy: Tools and methodologies for community-driven processes for water treatment in Indigenous communities. Technology in Society, 50(Technology in Society), 57-65. https://doi.org/10.1016/j.techsoc.2017.04.00

Blair, J. J.A., Balcázar, R. M., Barandiarán, J. and Maxwell, A., 2023, June 19. The 'Alterlives' of Green Extractivism: Lithium Mining and Exhausted Ecologies in the Atacama Desert. International Development Policy | Revue internationale de politique de développement, (16). https://doi.org/10.4000/poldev.5284

Bowen, G., 2009. Document Analysis as a Qualitative Research Method. Qualitative Research Journal, 9(2), 27-40. 10.3316/QRJ0902027

Braun, R., Lehane, O. and Lizarazu, M. R., 2024. Literary futures: Harnessing fiction for futures work. Futures, 158. https://doi.org/10.1016/j.futures.2024.103348

Calvo, D. and Candón-Mena, J., 2022. Technopolitical cartographies: proposal for collaborative mapping from participatory action research. Cuadernos Info, (54). https://doi.org/10.7764/cdi.54.51847

Clausen, C. and Gunn, W., 2015. From the Social Shaping of Technology to the Staging of Temporary Spaces of Innovation – A Case of Participatory Innovation. Science & Technology Studies, 28(1), 73–94. 10.23987/sts.55358.

Cueva, L. S., 2025. Tell me an (un)fortunate story: Advancing storytelling methods in energy futures research. Futuros, 165. https://doi.org/10.1016/j.futures.2024.103505

Denzin, N. K. and Lincoln, Y. S., 2018. The SAGE Handbook of Qualitative Research (Fifth Edition ed.). SAGE Publications. ISBN 978-1-4833-4980-0

Flick, U., 2018. An Introduction to Qualitative Research (6th Edition ed.). SAGE.

Fuller, J. L., Bjørkan, M., Iversen, L., Aarflot, J. M. and Dankel, D. J., 2025. Ethical approaches for engaging extended peer communities: Insight into responsible workshopping with citizens. Futures, 166. https://doi.org/10.1016/j.futures.2025.103546

Government of Chile, 2023, June 14. National Lithium Strategy. Chile Advances with Lithium. Retrieved December, 2024, from https://www.gob.cl/chileavanzaconlitio/

LEGO Group, 2010. Open-source/Introduction to LEGO® SERIOUS PLAY®. LEGO. https://www.lego.com/es-es/themes/serious-play/about

Hara, K., Nomaguchi, Y., Fukutomi, S., Kuroda, M., Fujita, K., Kawai, Y., Fujita, M. and Kobashi, T., 2023. Policy design by "imaginary future generations" with systems thinking: a practice by Kyoto city towards decarbonization in 2050. Futures, 154. https://doi.org/10.1016/j.futures.2023.103272

Herrera-León, S., Ojeda-Pereira, I., Gálvez, E., Orrego, F., Rojas, C., Campos, F., Cruz, C., Lufín, M. and Garcés, I., 2025. Challenges for the direct extraction of lithium from Chilean salt flats: From singular technologies to socio-technological systems. Scientific Publishing House of the Catholic University of the North. https://doi.org/10.22199/ATE240017-01

Juliani Pereira, V. and Hargreaves, T., 2024. Are you thinking what I'm thinking? The role of professionals' imaginaries in the development of smart home technologies. Futures, 163. https://doi.org/10.1016/j.futures.2024.103458

K. Gray, E., Fahy, F., McArdle, R. and Rohse, M., 2024. Co-creating a community visioning methodology for energy transitions: Principles, practices, and reflections. Energy Research & Social Science, (118). https://doi.org/10.1016/j.erss.2024.103783

Krippendorff, K., 1990. Content Analysis Methodology: Theory and Practice. Paidós Publishing.

Lorca, M., Oliveira Andrade, M., Escosteguy, M., Köppel, J., Scoville-Simonds, M. and Hufty, M., 2022, March 11. Mining indigenous territories: Consensus, tensions and ambivalences in the Salar de Atacama. The Extractive Industries and Society, 9. https://doi.org/10.1016/j.exis.2022.101047

Monsalves Ibarra, S., Díaz Soto, N. and Duarte Quapper, K., 2021. The systematization of experiences as a strategy for knowledge production and political action. In Transform sistematizando. Knowledge production and emancipatory struggles (pp. 11-42). Editorial DEI. ISBN 978-9977-83-191-6

Navarro, P. and Díaz, C., 2007. Chapter 7: Content Analysis. In Qualitative Research Methods and Techniques in Social Sciences (pp. 177-221). Editorial Sintesis. ISBN: 978-84-773822-6-3

Negrete, M., Fuentes, M., Kraslawski, A. and Irarrazabal, F., 2024, June. Socio-environmental implications of the decarbonization of copper and lithium mining and mineral processing. Resources Policy, 95. 10.1016/j.resourpol.2024.105135

Prieto, M., 2016, January 1. Trading water, producing indigenous territories and identities: the Chilean water model and the Atacameños of Calama. Revista de Estudios Sociales, 1(55), 88-103. https://doi.org/10.7440/res55.2016.06

Törnroth, S., Day, J., Fürst, M. F. and Mander, S., 2022. Participatory utopian sketching: A methodological framework for collaborative citizen (re)imagination of urban spatial futures. Futures, 139. https://doi.org/10.1016/j.futures.2022.102938

Chapter 04

Mining 4.0

b-Value Space-Time Analysis for Seismic Hazard Assessment in Underground Mining

Felipe Muñoz[1], Rodrigo Estay[2*], Gonzalo Nelis[1]

1. Departamento de Ingeniería de Minas, Metalurgia y Materiales, Universidad Técnica Federico Santa María, Chile.
2. Departamento de Ingeniería en Minas, Facultad de Ingeniería, Universidad de Santiago de Chile, Chile.
**Corresponding author at: Departamento de Ingeniería en Minas, Las Sophoras 175, Estación Central, Santiago, Chile, e-mail adress: rodrigo.estay.h@usach.cl*

Introduction

Deep mining operations are increasingly moving towards greater depths, where high in-situ stresses significantly affect rock mass stability. Under these conditions, excavation activities lead to stress redistribution that often induces seismicity. In caving mining methods, this effect is even more pronounced due to the planned large-scale collapse of the rock mass, generating seismic events across a wide range of magnitudes. Such events can compromise infrastructure stability, disrupt production schedules, and pose critical risks to worker safety, making induced seismicity one of the most relevant challenges in underground mining.

To monitor and better understand this phenomenon, underground mines commonly install seismic networks composed of geophones and accelerometers. These networks detect the seismic signal and its arrival time. With that, further analysis is made, creating a seismic catalogue that contains: the location of the seismic event, the location error, the moment magnitude and the magnitude, energy, apparent stress, the ratio Es/Ep, among others. Seismic catalogs constitute an important input for both operational decision-making and geomechanical analysis.

An important and well-known seismic analysis corresponds to the estimation of the b-value from the Gutenberg–Richter cumulative frequency–magnitude distribution, also known as the Gutenberg-Richter's law. This law expresses the relationship between the magnitude and total number of earthquakes (N) in any given region and time greater a magnitude M

$$\log(N \geq M) = a - bM$$

Its slope, referred to as the b-value, provides insight into the relative proportion of small versus large events: higher b-values indicate a dominance of small events, while lower b-values suggest a higher likelihood of larger, potentially hazardous events.

The spatial and temporal variability of the b-value is a good parameter for seismic hazard assessment. Low b-values may indicate zones with elevated seismic risk, while temporal fluctuations may provide early signals of changes in stress conditions within the rock mass.

The present research aims to characterize the spatio-temporal behavior of induced seismicity in a deep underground mine through the analysis of the b-value. By combining moving time-window

analyses with geostatistical simulations, the study seeks to identify areas with higher seismic hazard potential and contribute to more effective monitoring and risk management strategies

Methodology

The seismic catalog used in this study was obtained from the monitoring system of a deep underground caving mine. To ensure the reliability of subsequent analyses, a rigorous data filtering procedure was applied.

First, the magnitude of completeness (Mc) was estimated using the maximum curvature method proposed by Wiemer and Wyss (2000). This approach identifies the magnitude bin with the highest frequency in the frequency–magnitude distribution and assumes that smaller-magnitude events are progressively under-recorded. For this dataset, the completeness magnitude was determined to be $Mc=-0.8$. All events below this threshold were removed to avoid bias in the estimation of the b-value.

Additional quality control criteria were applied: events detected by fewer than three geophones and those with a reported location error exceeding 50 m were discarded. These steps ensured the representativeness of the seismic activity and minimized uncertainties associated with the spatial distribution of events.

The temporal variability of seismicity was analyzed using a moving-window approach. This method constructs overlapping subsets of events, each representing seismic activity over a fixed time horizon. A window length of 24 hours was chosen to capture daily cycles of seismicity while maintaining sufficient statistical robustness. Windows were shifted in 10-minute steps, ensuring strong temporal continuity and a detailed depiction of seismic evolution. In total, over 9,500 windows were generated for the entire study period.

For each window, the Gutenberg-Richter's b-value was estimated using the maximum likelihood method introduced by Aki (1965):

$$b = \frac{\log_{10} e}{\overline{M} - M_c + \frac{\Delta M}{2}}$$

where $\overline{M}$ is the average magnitude, $Mc=-0.8$ is the magnitude of completeness and $\Delta M = 0.1$ is the magnitude binning.

This method is widely recognized for its statistical robustness, as it avoids the bias associated with linear regression on log-transformed data.

To complement the temporal analysis, each window was assigned a spatial centroid representing the average location of seismic activity. The centroid coordinates were calculated as the arithmetic mean of the X, Y, and Z positions of all events within the window. This procedure yields a dataset of paired values, capturing both the temporal evolution of the b-value and its approximate spatial position within the mine. While centroids do not fully describe the spatial distribution of seismicity within each window, they provide a practical and consistent means of integrating temporal and spatial information for subsequent analyses.

The final stage consisted of modeling the spatio-temporal variability of the b-value using geostatistical simulation techniques. Specifically, Turning Bands Simulation (TBS) was implemented

to generate multiple equiprobable realizations of the b-value distribution. Unlike deterministic interpolation methods (e.g., kriging), stochastic simulation preserves local variability and provides a probabilistic framework for uncertainty quantification.

The simulation procedure used the centroid dataset as conditioning points and reproduced the spatial correlation structure inferred from modeled variograms of the b-value. For each realization, a three-dimensional distribution of the b-value was generated. By aggregating multiple realizations, it was possible to calculate the probability of the b-value falling below a predefined threshold in each location of the mining sector. Since lower b-values are commonly associated with a higher likelihood of larger seismic events, these probability maps serve as proxies for spatial seismic hazard.

The methodology therefore integrates temporal monitoring, through the moving-window analysis, with spatial characterization. This combined approach enables the identification of both short-term fluctuations and persistent spatial patterns of seismic hazard. By quantifying not only the expected distribution of the b-value but also its uncertainty, the methodology provides a robust framework to support decision-making in seismic risk management for deep underground mining operations.

Results and Discussions

The application of the proposed methodology produced a detailed spatio-temporal characterization of the Gutenberg–Richter's b-value within the analyzed underground caving mine. By segmenting the seismic catalog into more than 9,000 temporal windows and associating each window with a spatial centroid, it was possible to construct a dense dataset that reflects both the temporal fluctuations of the b-value and its spatial heterogeneity across the mine.

The first key observation relates to the overall variability of the b-value throughout the monitoring period. The estimated values ranged between approximately 0.9 and 1.3, consistent with ranges typically observed in induced seismicity associated with hard-rock mining. Lower b-values were systematically associated with clusters of relatively larger magnitude events, while higher b-values corresponded to periods and regions dominated by lower magnitudes events. This trend reinforces the established interpretation that the b-value can be used as a proxy for seismic hazard, with low b-values indicating increased likelihood of potentially damaging events.

The three-dimensional mapping of b-values (Figure 1) highlights the existence of strong spatial contrasts within the studied volume. Areas with b-values below 1.0 were concentrated in specific sectors of the cave, particularly in the upper-eastern region of the monitored block. In contrast, higher b-values were observed in the deeper-western region, where seismic activity consisted mostly of small, isolated events. This spatial pattern suggests that stress redistribution associated with cave propagation is not uniform, and certain regions accumulate more favorable conditions for the generation of large-magnitude seismic events.

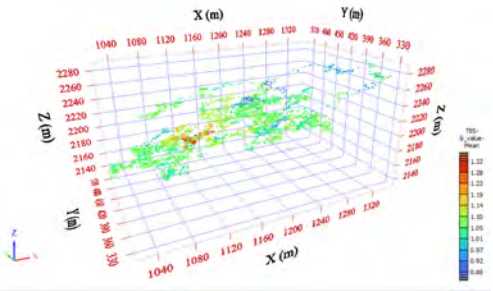

Figure 1. Mean b-value from the 100 simulations. The mean of the b-value is1.067, with a minimum value of 0.88 and a maximum value of 1.32.

The results of the geostatistical simulation provide an additional insight into the uncertainty and probabilistic nature of seismic hazard. Figure 2 presents the probability of the b-value falling below a predefined threshold of 1.0. High-probability zones were identified in the same central sectors highlighted in Figure 1, confirming the robustness of the observed pattern. Probabilities exceeding 60% were common in these areas, indicating that they persistently exhibit lower b-values regardless of the stochastic variability incorporated by the simulation. This probabilistic approach provides an objective way of quantifying seismic hazard beyond the analysis of a single deterministic map.

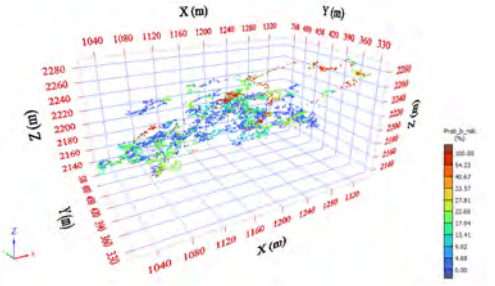

Figure 2. Probability distribution of b-value < 1. The lower the b-value, the higher the seismic risk.

A second important finding is related to the temporal persistence of low b-value zones. Although the moving-window approach generates overlapping subsets of data, the spatial clustering of low b-values was not transient but recurrent across consecutive windows. This persistence suggests that the stress conditions controlling seismicity in these regions are long-lasting, rather than momentary fluctuations. From a risk management perspective, this indicates that certain mine areas consistently have higher seismic hazard.

The probabilistic mapping also revealed transition zones where the probability of low b-values was intermediate (between 30% and 50%). These regions may represent boundaries between stable and unstable domains, where stress is being gradually transferred. Such areas could act as precursors to the future development of more hazardous conditions if the caving front advances or the stress field continues to evolve.

In addition, the results emphasize the added value of geostatistical simulation compared to purely deterministic interpolation. While direct mapping of b-values provides a single view, the stochastic approach highlights uncertainty and allows the identification of zones where hazard assessment is less reliable. This is particularly relevant in mining contexts, where decision-making must account for uncertainty to ensure safety.

Finally, the integration of spatial and probabilistic analyses demonstrates that the methodology can generate operationally meaningful hazard maps. These maps not only identify the most critical areas but also provide quantitative probabilities that can be used as decision thresholds for risk mitigation strategies, such as reinforcement of infrastructure, temporary evacuation of personnel, or adjustment of caving sequences.

Overall, the results validate the potential of b-value mapping, combined with geostatistical simulation, as a powerful tool for understanding induced seismicity in underground mining environments. The approach allows for a more nuanced interpretation of seismic hazard, moving beyond global averages toward localized and probabilistic risk assessments.

Conclusions

This study demonstrates that the combined spatio-temporal analysis of the Gutenberg–Richter's b-value, supported by geostatistical simulation, provides a robust framework for assessing seismic hazard in underground caving mines. By integrating temporal resolution, spatial characterization, and probabilistic modeling, the methodology captures the complexity of induced seismicity in a way that is both technically rigorous and operationally useful.

The results confirm that low b-values, and therefore higher seismic hazard, are concentrated in specific regions of the mine. These regions were not randomly distributed but showed consistent spatial clustering and temporal persistence. Such findings highlight that seismic hazard is strongly controlled by localized stress conditions, which must be considered in risk management strategies.

The probabilistic maps derived from geostatistical simulation offer a significant improvement over traditional deterministic method. By quantifying the probability of encountering low b-values, these maps provide mine operators with a direct measure of risk that incorporates uncertainty, enabling more informed and proactive decision-making. This probabilistic perspective is particularly relevant in complex mining environments where uncertainty is unavoidable, and where traditional approaches may underestimate risk.

Moreover, the results show significant spatial differences in b-values, indicating that certain areas are more prone to hosting higher-magnitude seismic events. This allows the identification of regions with greater seismic hazard potential, thereby supporting the prioritization of monitoring and risk control efforts. In this way, the approach contributes to understanding seismic behavior through geo-statistical analysis, strengthening its role as a valuable tool for risk management in underground mining and reinforcing its multidisciplinary importance in hazard assessment.

Furthermore, the approach outlined in this work underscores the importance of integrating advanced data analysis techniques into seismic monitoring systems. Rather than relying solely on event magnitudes and frequencies, incorporating spatio-temporal indicators such as the b-value enriches the interpretation of seismicity and enhances the predictive power of monitoring efforts. This integration bridges the gap between theoretical modeling and practical decision-making, positioning seismic risk management as both a scientific and operational challenge.

In conclusion, the proposed methodology contributes to the broader field of mining seismology by offering a reproducible and scalable framework for hazard assessment. Its application can support safer and more efficient mining operations, reduce operational interruptions, and ultimately protect both infrastructure and personnel. Future work should focus on real-time implementation and validation across multiple mining sites to further strengthen the role of b-value analysis in seismic risk management.

References

Aki, K., 1965. Maximum likelihood estimate of b in the formula logN = a – bM and its confidence limits. Bulletin of Earthquakes Research Institute of University of Tokyo, 43, 237–239.

Gutenberg, B. and Richter, C.F., 1941. Seismicity of the Earth. Geological Society of America Bulletin. Special papers 34, 1–131.

Utsu, T., 1965. A method for determining the value of b in a formula log n = a–bM showing the magnitude-frequency relation for earthquakes. Geophysical Bulletin of Hokkaido University 13, 99–103.

Wiemer, S. and Wyss, M., 2000. Minimum magnitude of completeness in earthquake catalogs: Examples from Alaska, the Western United States, and Japan. Bulletin Seismological Society of America 90, 859 – 869.

Woessner, J. and Wiemer, S., 2005. Assesing the quality of earthquake catalogues: Estimating the magnitude of completeness and its uncertainty. Bulletin Seismological Society of America 95, 684 – 698.

How Does the Chilean Lithium Industry Measure its Social Sustainability? Diagnoses and Proposals From Socio-Engineering

Rodrigo Molina-Richardson[1], Iván Ojeda-Pereira[2,3], Fernando Campos-Medina[1], Sebastián Herrera-León[4,5], Carolina Rojas[3]

1. Department of Sociology, University of Chile, Santiago, Chile
2. School of Engineering Sciences, LUT University, Lappeenranta, Finland
3. Department of Industrial Engineering, Universidad Católica del Norte, Antofagasta, Chile
4. Institute of Engineering Sciences, University of O'higgins, Rancagua, Chile

**Corresponding author at: Department of Sociology, University of Chile, Capitán Ignacio Carrera Pinto 1045, Santiago, Chile, rodrmolina@ug.uchile.cl.*

ABSTRACT

This paper links social studies of mining with engineering sciences through an interdisciplinary interface that we have termed socio-engineering. Its main objective is to examine the forms of social sustainability assessment used in the lithium industry in Chile, particularly in the operations of SQM and Albemarle. Using a qualitative approach based on Science, Technology and Society (CTS) and Environmental Social Impact Assessment (ESIA) studies, i) we analyse the mediation of corporate reporting mechanisms, social accounting, and international standards (GRI, IRMA, among others) in the relationship between industry, local communities, and ecosystems; and ii) we track controversies that can be incorporated into these reports. Methodologically, the following were carried out: i) in-depth interviews with academics, professionals, and industry leaders; ii) a documentary analysis of sustainability reports from the lithium industry in Chile; and iii) a focused review of international scientific literature on social sustainability standards and indicators in the context of mineral extraction for the energy transition. The results expose the standards and measurement strategies reported by the industry, while also highlighting tensions in corporate rhetoric and measurement gaps. It concludes that there is an urgent need to adapt and expand social sustainability assessment frameworks, incorporating knowledge from other disciplines, as well as local knowledge and perspectives, with the aim of building scenarios and an information base for coordination spaces.

Keywords: Social accounting, Lithium mining; Sociotechnologies; Social reporting; Socioengineering

Introduction

Lithium has become a strategic input in the context of the global energy transition, due to its use in storage technologies such as batteries for electric vehicles and solar systems. This has positioned it as a critical material in various countries and multilateral organizations, leading to intensified extractivism in regions with large reserves, such as northern Chile (Rubilar & Irarrázaval, 2018; Lorca et al., 2022, 2023). In particular, the Salar de Atacama contains approximately 40% of the world's lithium reserves in brine, which has led to a sustained increase in extraction (European Commission,

2020; USGS, 2023). However, this expansion has had significant social and environmental impacts on indigenous communities and local ecosystems, generating conflicts over access to water, processes of symbolic and material dispossession, and questions about the development model based on lithium mining (Lorca et al., 2022; 2023).

Historically, lithium mining in Chile began in the context of profound liberalization and privatization reforms, with a state concession model that allowed large private companies to enter under special contracts, without changing the legal status of the mineral as non-concessionable (Rubilar & Irarrázaval, 2018). Since the 1980s, companies such as SQM and Albemarle have established themselves as dominant players in the Salar de Atacama region. Since the 2010s, with the intensification of global demand, lithium has gone from being a marginal resource to a strategic one, reconfiguring the relationship between the state, companies, and communities around control of the territory, distribution of benefits, and management of environmental impacts (Barandiarán, 2019). The growing global demand of the last decade has transformed its strategic status, intensifying tensions over territorial control, benefits, and public management, which has fueled debates about the need for new lithium governance (Poveda, 2021).

Despite companies' efforts to establish mechanisms for community relations, social accounting, and sustainability reporting (Merry, 2011), significant tensions persist between companies and local communities. These tensions are related to perceptions of asymmetry in decision-making, lack of transparency in water use, and disputes over the legitimacy of benefit delivery, without resolving conflicts related to water access, corporate transparency, equitable distribution, and the cultural significance of the salt flat, which strains the principles of sustainability promoted by companies (Avila, 2018). Thus, despite attempts to promote "green" or "sustainable" mining, significant social tensions surrounding lithium extraction persist. These tensions manifest themselves in mistrust of consultation processes, controversies, and criticism of the ways in which companies manage their relationships (Jerez et al., 2021). It should be understood that the current lithium extraction process involves brines or water with high mineral content (unsuitable for human consumption), which undergoes evaporation as the first treatment for lithium extraction (Herrera-León et al., 2025).

In this context, measuring social impact has become a key factor in legitimizing the lithium industry among various stakeholders, based on tripartite agreements in 2016 and 2018 between the private sector, the state, and local communities. However, the predominant evaluation frameworks—based on standardized indicators or global certifications such as IRMA or GRI—tend to obscure the territorial, cultural, and political specificities of the contexts in which extraction takes place (Merry, 2011; Molina-Maturano, 2022). Academic literature from the social sciences has begun to problematize the performative and non-neutral nature of these measurement devices, showing that they not only represent but also produce certain forms of social reality (Bell & Morse, 2008). This article aims to contribute to this field by critically analysing how forms of social sustainability assessment are constructed and deployed in the lithium industry, and what their real capacity is to represent the impacts experienced by communities.

This research proposes moving toward social sustainability indicators that are more context-sensitive and co-constructed with local communities. In the case of the lithium industry in Chile, efforts to measure "the social" are deployed through a diverse set of methodologies—such as social accounting, social impact assessments (SIAs), and social life cycle assessments (SLCA)—which are linked to voluntary certifications (IRMA, GRI, SASB, among others), as well as to companies' sustainability and community relations departments. These tools seek not only to capture impacts, but also to generate frameworks for action that shape the relationships between business, community, and the state.

However, there are also alternative approaches in the specialized literature, such as the MESMIS

framework (Masera et al., 1999) and its adaptation in the SAIC method (Molina Maturano et al., 2022), developed in collaboration with a Zapotec indigenous community. This case established a set of 55 culturally relevant indicators, organized into categories adapted to the local sociocultural context. These approaches illustrate the possibility of constructing situated assessments—in the form of standards, criteria, and indicators—that reflect local values, as opposed to universal and standardized frameworks.

At the institutional and political level, Chile has promoted various strategies to guide the sustainable development of lithium. The National Lithium Strategy (2023) seeks to position the country as a world leader in sustainable production, promoting a new governance of salt flats based on sustainability, value addition, and local participation. This strategy includes mechanisms for indigenous consultation in accordance with ILO Convention 169, which opens formal spaces for the incorporation of indigenous communities in decisions related to mining development.

Likewise, Clean Production Agreements (APL), in force since 2010 and recognized by Law No. 20,416, constitute an effort aimed at improving the sustainability of extractive processes. Since 2012, CLAs have been recognized by the United Nations as the first Nationally Appropriate Mitigation Action (NAMA) at the global level, highlighting their contribution to reducing greenhouse gases (Ministry of Mining, 2023). These initiatives have progressively driven adjustments in corporate actions, institutionalizing a socio-technical transition (Geels, 2014) in the development of reporting practices at both Albemarle and SQM. As a result, the lithium industry has begun to adapt to the new guidelines imposed by the climate crisis and the energy transition.

This research is guided by the following central question: How does the lithium industry measure social sustainability in the context of the energy transition? Based on this question, the overall objective of the study is to examine the social sustainability indicators used by the main companies in the sector in Chile, particularly SQM and Albemarle, within the framework of their reporting and corporate governance processes. To this end, two complementary specific objectives have been defined. First, it proposes to analyse the ways in which social sustainability is operationalized by the industry, through corporate reporting mechanisms and the adoption of international standards such as GRI, IRMA, the United Nations Guiding Principles, and the Sustainable Development Goals (SDGs), using a methodological strategy based on documentary analysis. Second, it seeks to map the socio-technical relationships and influences that shape the assessment of social sustainability in the lithium sector, recognizing the assemblages of actors, instruments, and discourses involved in the construction and validation of these indicators. In doing so, the study seeks to contribute to a critical and situated understanding of how the social is measured in extractive contexts associated with the energy transition and the articulation of engineering and social sciences.

This article aims to contribute to the critical analysis of the ways in which social sustainability assessments—or social accounting—are constructed, deployed, and legitimized in the lithium industry. In particular, it seeks to map the socio-technical networks that shape this social measurement, tracing its practices, instruments, and assemblages, following the theoretical proposals of Callon (1984), Latour (2005), Law (2004), Tsing (2005), and Bridge (2008). This approach makes it possible to visualize trajectories, frictions, creative tensions, and controversies that constitute "the social" as a dimension in dispute within the Salar de Atacama.

In this way, the research i) contributes to social studies of sustainability, especially in its social dimension, proposing a new approach that understands the ways of operationalizing sustainability (standards, criteria, indicators) as social constructions with performative effects; ii) empirically systematizes sustainability reporting practices in the Chilean lithium industry; iii) identifies the articulations between standards and certifications at different spatial and temporal scales, in order to anticipate the challenges that the transition to new extraction sociotechnologies—such as

direct lithium extraction (DLE)—will face in the coming years.

Methodology

Qualitative and inductive design

This study adopts a qualitative and inductive approach, aimed at understanding how the lithium industry in Chile defines, measures, and communicates social sustainability within the framework of its corporate operations and territorial relations. It is structured from the perspective of social studies of science and technology (STS) and the field of Environmental and Social Impact Assessment (ESIA).

Information gathering techniques

The methodological strategy involves the use of various qualitative data collection techniques aimed at understanding how the lithium industry measures social sustainability. First, a targeted document survey and analysis (Bowen, 2009) was applied to the sustainability reports published by SQM and Albemarle in order to identify the indicators used, the international standards adopted (GRI, IRMA, UN Guiding Principles, SDGs), and the accompanying narratives. Second, in-depth interviews (Brinkmann and Kvale, 2009; Taylor et al., 2016) were conducted with key actors in the sector, including academics, industry professionals, and leaders in socio-environmental assessment, in order to explore how these actors interpret, negotiate, and legitimize the construction of social indicators. Finally, participant observation (Becker, 2015; 2018) was implemented during visits to salt flats, extraction plants, and community interaction spaces, with the aim of capturing dimensions not formally documented and reconstructing the socio-technical framework in which these practices are embedded.

Analysis techniques

The analysis is structured around Howard Becker's methodological proposal to open the "black box" (2002, 2004, 2015), understanding that social sustainability standards, criteria, and indicators are not neutral elements, but rather social constructs that must be denaturalized. This implies analysing them in their multiple dimensions: technical, political, institutional, and cultural. Becker's perspective allows us to go beyond the description of indicators, questioning how they are produced, who is involved in their formulation, and what power relations allow certain metrics to be stabilized to the detriment of other possible ones.

This approach is complemented by a methodological triangulation strategy that combines three main sources: i) Secondary documentation (sustainability reports and specialized literature), ii) Accounts obtained through in-depth interviews. This triangulation is implemented under an interpretive logic, seeking to contrast and stress the discourses, practices, and forms of representation that shape social sustainability in the lithium industry. In this way, the analysis not only examines what is measured, but also how, why, and for whom it is measured.

Finally, after the documentary review, a narrative review of scientific literature (Manterola et al., 2023) was carried out, focusing on methodologies for assessing social sustainability, social accounting, and critical discussion of social indicators applied to contexts of socio-environmental complexity. From a total of 2,539 articles between 2015 and 2025, 108 relevant studies on social sustainability assessment methodologies and indicators were selected, with 57% published between 2023 and 2025.

Results and Discussions

Reporting trajectories: between the regime and international requirements

The timelines of sustainability reports and documentation—a review of 48 corporate documents,

broken down into 25 documents from SQM and 23 documents from Albemarle—show two different trajectories: while SQM has consolidated a continuous line of reporting since 2010 (see Figure 1), Albemarle began this process in 2016 (see Figure 2). Both companies use a set of international standards (GRI, IRMA, SDG, SASB, ISO, among others) which, according to statements by the actors interviewed, enable both operational sustainability and the improvement of their international positioning: "It positions Albemarle and SQM, and lithium mining in the market. It is a requirement that, although it originated in the electromobility industry, is the most robust within the mining industry" (interviewee Consultant 1).

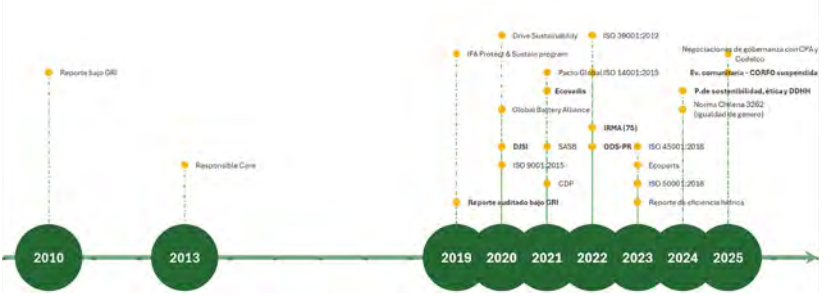

Figure 1. Timeline SQM

In this context, IRMA emerges as the most robust and demanding regime, especially in the post-crisis context of cobalt in Africa. Its adoption in the lithium industry not only responds to pressure from the European market, but also to an internal need to integrate different criteria into a coherent management and governance framework: "it encompasses most of the other standards and criteria [...] it helps to manage or guide certifications"; "it is not a mining standard made by mining" (SQM interviewees).

Figure 2. Timeline Albemarle

The international market, particularly the European market, acts as an agent of change in social measurement devices. Brands such as BMW and Volkswagen, interested in the traceability of their supply chains, have put pressure on lithium suppliers to make their extraction processes and their impacts transparent: "BMW are the first to see where the lithium comes from" (interviewee from Grupo Errázuriz).

The differentiation between the compounds marketed, lithium carbonate (Li_2CO_3) for industrial and pharmaceutical uses, and lithium hydroxide (LiOH) for electromobility applications, intensifies social governance requirements, especially in relation to products destined for the European automotive market. This has a direct impact on how the social dimension of lithium extraction is represented,

measured, and legitimized. Secondly, lithium hydroxide, a higher quality and value-added product, is mainly in demand in Europe, especially Germany, to produce high-performance batteries for the automotive industry and durable power tools.

This differentiation scheme not only reflects market segmentation but also provides insight into how the European Union is leveraging its influence over the lithium industry through social and environmental requirements, which translate into demands for traceability, certification, and robust standards throughout the supply chain.

Reviewing social indicators and standards: adjustments and imbalances in the Salar de Atacama

Recent literature on social sustainability indicators in the lithium industry shows a fragmented field, in which classic impact assessment methodologies converge with more critical approaches. Of the 108 articles reviewed (from 2015 to 2025), the highest concentration is in the energy transition category (30), followed by governance and regulation (15), social sustainability indicators (11), social/energy justice (10), and human rights and labor (10). Categories such as well-being and quality of life (1) or participation and communities (1) appear marginally, showing that central dimensions for social sustainability still receive less systematic attention (see Figure 3).

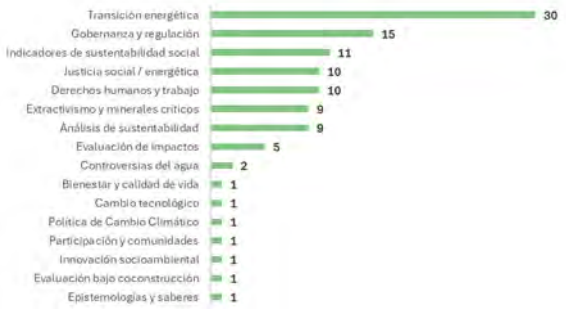

Figura 3. Categorization by topic, frequency (#)

Based on this review, methodological approaches were systematized into four broad groups: (a) impact assessments; (b) multi-criteria and quantitative methods; (c) management and composite indices; and (d) critical/participatory approaches. Table 1 summarizes this distribution:

Tabla 1. Review of narrative or focused bibliography

Categories /Frequency (#)	Methodologies /Standards	Standards General Description
Social Impact assessments: 16	EIA, SIA, IAIA, S-LCA	Measure the social, environmental, and economic impacts of projects and products.
Multi-criteria/quantitative methods: 28	AP, Fuzzy Sets, DEA	Prioritize, compare, and integrate multiple indicators in complex contexts.
Management and composite indices:17	GRI, SASB, ODS, IRMA, ISO 26000, BSC, MINDEX, CMSI	Synthesize results into indices or dashboards for benchmarking management.
Critical approaches/participation Management and situational indicators: 47	Situated indicators, technologies of humility, participatory governance, co-constructed	Incorporate local contexts, community voices, social justice, and social equity into measurement.

Experiences such as MESMIS and SAIC (Molina Maturano et al., 2022) have demonstrated the possibility of constructing assessment frameworks that are sensitive to the socio-ecological and cultural context, where the integration of local worldviews enriches the validity of the results. In contrast, global methodologies such as S-LCA have shown strengths in traceability and international comparability, although they are limited in their ability to integrate indigenous or community knowledge. This contrast reveals the tension between demands for global standardization and local relevance in the Salar de Atacama.

Contributions from international literature allow us to delve deeper into these tensions. Mancini and Sala (2018) point out that indicators applied to lithium and critical mineral mining tend to focus on productivity, environmental risks, and technological efficiency, while neglecting social dimensions such as community cohesion and distributive justice. Similarly, Aria, Misuraca, and Spano (2020), based on a review of 30 years of Social Indicators Research, highlight the need to move toward indicators of well-being, quality of life, and multidimensional poverty as more comprehensive measures of sustainability.

The systematization of social indicators that are rarely or only partially considered (see Table 2 below) strongly highlights social cohesion, social capital, and multidimensional poverty. These dimensions are scarcely addressed in the corporate reports of SQM and Albemarle, despite their relevance for understanding territorial inequalities and tensions between communities and companies. These findings coincide with the literature that emphasizes the importance of measuring social capital, trust, and perceptions of justice in contexts of extractivism (Aria et al., 2020; Mancini & Sala, 2018).

The incorporation of these indicators from frameworks such as SIR allows for a broader spectrum of analysis, connecting the discussion on responsible mining with wider debates on well-being and social justice. In summary, while IRMA, GRI, and SASB prioritize indicators of formal compliance and corporate performance, approaches such as SAIC, MESMIS, and SIR open up spaces or interfaces for situated social sustainability, improvements to capture community and/or social tensions and perspectives in the Atacama salt flat.

Triangulating tensions, exclusions, and controversies

Through comparative analysis of the reports audited under IRMA (SQM 75, Albemarle 50), significant gaps and controversies can be observed. Although SQM shows greater development in voluntary transparency and audits, both companies have significant shortcomings: i) Lack of integration of local knowledge in the indicators used, ii) Moderate traceability of the territorial redistribution of benefits, iii) Absence of tools to measure corruption or political capture, iv) Invisibility of cultural or intangible impacts associated with water and territory (cohesion and social capital, among others).

In this context, the relevance of applying Social Life Cycle Assessment (S-LCA) (Roche et al., 2024) represents a way of analyzing social sustainability and has led to a better understanding of communities' perspectives on controversial issues such as the use of brine: "they believe that we extract continental water... that is why we experimented with the University of Queensland, then with the University of Berlin, to improve our understanding of their perspectives" (SQM interviewee).

Tabla 2: IRMA reporting by SQM/Albemarle

Dimension / Standard	SQM (IRMA 75) reports	Albemarle (IRMA 50) reports	Observations	Tensions/Controversies
Transparency	Publishes sustainability reports aligned with GRI and IRMA 75 audit; contracts with CORFO are not fully accessible.	Publishes global and IRMA 50 audited reports; basic contracts from 2016, but annexes and amendments are not available.	Standards do not require the publication of complete contracts or renegotiations. They do not consider perceptions of social legitimacy or how contractual opacity impacts community trust.	Opacity in governance; arbitration with CORFO; public mistrust that erodes social capital and reinforces perceptions of exclusion.
Indigenous participation / FPIC (IRMA 2.2, GRI 411/413)	It has carried out Indigenous Consultation Processes (PCPI) visible in SEA; IRMA audited community dialogue and agreements.	No indigenous consultation processes are recorded despite current RCAs; relationship via agreements and roundtables.	IRMA evaluates FPIC, but in Chile, DS 66 (2013) is weak; GRI/SASB do not include explicit FPIC. The subjective well-being derived from participation and its impact on social cohesion are not measured.	Discrepancy between formal consultation and co-decision expectations; does not integrate local knowledge or worldviews.
Territorial redistribution / benefits	Reports community contributions, social programs, monitoring; IRMA 75 validates.	Contributes 3.5% of sales to the Council of Atacameño Peoples (CPA); IRMA audit recognizes this mechanism.	No public traceability of payments to municipalities; GRI/SASB only require aggregate taxes. No measurement of whether benefits reduce multidimensional poverty (education, health, housing, social security).	Opacity in income distribution creates tensions over fiscal justice. Structural inequalities persist, limiting improvements in quality of life.
Environmental management (water, biodiversity)	Reports water consumption, reduction targets, environmental monitoring; audited by IRMA.	Partial compliance with water efficiency targets and participatory monitoring; audited IRMA 50.	Volume and efficiency are measured, but not the cultural significance of water or cumulative impacts. Nor is it linked to effects on community well-being or water security as a dimension of poverty.	Socio-environmental conflicts over water: a vital resource linked to cultural identities. Ecosystem erosion impacts risk perception, environmental stress, and well-being.
Working conditions and safety (GRI 403, IRMA 3.1, SASB)	Publish accident rates (TRIF), inclusion programs (women 20%+, targets 25% by 2025).	Publish global TRIR, DEI goals (women 25-30% in manufacturing, 30-40% in leadership).	No se evalúa si el empleo mejora el bienestar multidimensional ni su aporte a la cohesión social (ej. integración de jóvenes indígenas).	Transparency gaps; tensions between jobs offered and job quality/stability. Perception that mining jobs do not reduce multidimensional poverty in a sustainable manner.
Corruption and business ethics (IRMA 1.1/1.3, GRI 205)	Controversy surrounds CEOL 2012 and irregular financing of political campaigns, not visible in current reports.	There have been no recent scandals in Chile, but contracts lack full transparency.	Standards do not measure risks of political corruption or regulatory capture. Their impact on institutional trust and local social capital is not analyzed.	Institutional weakness in the face of conflicts of interest. The perception of corruption erodes social legitimacy and undermines community cohesion.
Narrative and voluntarism	Más robusta en transparencia voluntaria: GRI, IRMA, ODS.	Less detail in public reports, although audited by IRMA.	Standards allow for voluntary narratives; they do not include measurements of well-being or how narratives impact community perceptions.	Tension between reported "responsible" mining and local perceptions of extractivism. This narrative gap fuels mistrust and undermines social legitimacy.

Socio-environmental controversies not only mark current tensions but also function as political memories that challenge the legitimacy of current standards. Cases such as the conflict over the Punta Negra Salt Flat (Peine Community), which culminated in a lawsuit by the State Defense Council for environmental damage, show how organized communities (CPA) have influenced institutional frameworks such as the National Lithium Strategy (2023). Likewise, the Chilean Water Code, which

does not recognize brine as water, becomes a regulatory complexity that fuels controversies about the real impacts of brine extraction in salt flats, the latter considered as socio-ecological systems.

The transition to new socio-technologies for extraction (such as DLE) faces structural challenges, part of the complexity observed with these new technologies being reinjected. Although the development of new projects, such as SQM's Salar Futuro, seeks to incorporate DLE in the Atacama salt flat, it also involves the dilemma between the extraction practices of brine or water with high mineral content, as the yield of Li concentration decreases, how reinjection is ultimately understood, such as the impact on the structure and functioning of aquifers, contamination of groundwater, or modification of the physical, chemical, and biological characteristics of the salt flat, with the consequence that it also affects what is understood as the intervention of the salt flat and its relationship with communities.

Conclusions

The initial results of this research show that traditional frameworks for assessing social sustainability—such as GRI, IRMA, or SASB—although they represent progress in the institutionalization of global standards, fail to capture or delve deeply into the territorial, cultural, and epistemic specificities of contexts such as the Salar de Atacama. From a critical perspective inspired by CTS studies, it is necessary to move towards indicators that are situated and co-constructed with local communities, in line with proposals for knowledge co-production (Jasanoff, 2004). In this direction, experiences such as MESMIS and SAIC (Molina Maturano et al., 2022) show that it is possible to design evaluation frameworks that are more sensitive to the socio-ecological and cultural environment, capable of integrating local worldviews and enriching the legitimacy and interpretive quality of reporting and management. In contrast, global methodologies such as S-LCA, although limited in their incorporation of indigenous or community knowledge, offer advantages in terms of traceability and international comparability, especially in the face of pressure from European markets on lithium governance. The literature on social indicators (Aria et al., 2020; Mancini & Sala, 2018) also contributes key dimensions such as well-being, social cohesion, and multidimensional poverty, which are often absent from corporate mining standards. However, as these are international comparative frameworks, their application requires adaptation and contextualization processes that allow them to accurately reflect the cultural and territorial realities of the Salar de Atacama.

In turn, this research confirms the urgent need to increase transparency and strike a balance between protecting industrial information and ensuring the social legitimacy of extractive processes. One of the central issues identified is the controversy surrounding water and brine extraction, whose cultural and ecological dimensions are not adequately captured by current standards. This conflict reflects an epistemic dispute between corporate logic and territorial knowledge, the resolution of which cannot rely solely on consultation mechanisms, but requires progress toward a socially situated, historically informed, and epistemically pluralistic sustainability. Consequently, it is proposed to reconceptualize social sustainability as a local assemblage in connection with the global (Tsing, 2005; Bridge, 2008), which is not limited to reproducing international standards, but which also does not lack legitimacy or rigor. An assemblage that recognizes the heterogeneity of knowledge, the cultural circuits of water, the memories of environmental damage, and the symbolic frameworks of the Likan-antai communities. This construction requires, at the same time, the support of tools from the engineering sciences—such as agreed-upon hydrogeological models—and the incorporation of effective mechanisms for community representation in lithium governance.

Finally, it is proposed that future methodologies and indicators should arise from the controversies themselves, be traceable and comparable over time, and allow for the management of dynamic

relationships between industry, the state, and civil society. Only in this way will it be possible to move towards an energy transition that does not reproduce unsustainable forms of extraction, but rather builds new forms of justice, sustainability, and industrial legitimacy from the territories.

References

Aria, M., Misuraca, M. and Spano, M., 2020. Mapping the Evolution of Social Research and Data Science on 30 Years of Social Indicators Research. Social Indicators Research, 149(3), 803-831. https://doi.org/10.1007/s11205-020-02281-3

Avila, S., 2018. Environmental justice and the expanding geography of wind power conflicts. Sustainability Science, 13, 599–616. https://doi.org/10.1007/s11625-018-0547-4

Becker, H., 2009. Trucos del Oficio: Cómo conducir su investigación en ciencias sociales (1a ed.). Siglo Veintiuno editores.

Becker, H., 2015. Para hablar de sociedad: La sociología no basta (1a ed.). Siglo Veintiuno editores.

Becker, H., 2016. Mozart,el asesinato y los límetes del sentido común: Cómo construir teoría de casos(1a ed.). Siglo Veintiuno editores.

Becker, H., 2018. Datos, pruebas e ideas: Por qué los científicos sociales deberían tomarselos más en serio y aprender de sus errores (1a ed.). Siglo Veintiuno editores.

Bell, S. and Morse, S., 2008. Sustainability Indicators: Measuring the Immeasurable (2nd ed.). Earthscan.

Bowen, G. A., 2009. Document Analysis as a Qualitative Research Method. Qualitative Research Journal, 9(2), 27-40. https://doi.org/10.3316/qrj0902027

Callon, M., 1984. Some Elements of a Sociology of Translation: Domestication of the Scallops and the Fishermen of St Brieuc Bay. The Sociological Review, 32(1_suppl), 196-233. https://doi.org/10.1111/j.1467-954X.1984.tb00113.x

European Commission, 2020. Critical Raw Materials for Strategic Technologies and Sectors in the EU: A Foresight Study: https://data.europa.eu/doi/10.2873/865242

Geels, F. W., 2014. Reconceptualising the co-evolution of firms-in-industries and their environments: Developing an inter-disciplinary Triple Embeddedness Framework. Research Policy, 43(2), 261-277. https://doi.org/10.1016/j.respol.2013.10.006

Herrera-León, S., Ojeda-Pereira, I., Gálvez-Corrales, E., Orrego, F., Rojas-Córdova, C., Campos-Medina, F., Cruz-Rojas, C., Lufin-Varas, M. and Garcés-Millas, I. (2025). Desafíos para la extracción directa de litio desde salares en Chile: De tecnologías singulares a sistemas sociotecnológicos. Ediciones Científicas Universidad Católica del Norte. https://doi.org/10.22199/ATE240017-01

Jasanoff, S., 2004. States of knowledge: The co-production of science and social order. Routledge.

Jerez, B., Garcés, I. and Torres, R. (2021). Lithium extractivism and water injustices in the Salar de Atacama, Chile: The colonial shadow of green electromobility. Political Geography, 87, 102382. https://doi.org/10.1016/j.polgeo.2021.102382

Kvale, S. and Brinkmann, S., 2009. Interviews: Learning the craft of qualitative research interviewing (2nd ed.). Sage.

Latour, B., 2021. Reesamblar lo social: Una introducción a la teoría del actor-red (1a ed.). Manantial.

Law, J., 2004. After Method: Mess in Social Science Research. Routledge.

Lorca, M., Olivera Andrade, M., Escosteguy, M., Köppel, J., Scoville-Simonds, M. and Hufty, M., 2022. Mining indigenous territories: Consensus, tensions and ambivalences in the Salar de Atacama. The Extractive Industries and Society, 9, 101047. https://doi.org/10.1016/j.exis.2022.101047

Lorca, M., Olivera, M. and Garcés, I. (2023). "Se instaló el diablo en el Salar": Organizaciones atacameñas, agua y minería del litio en el Salar de Atacama. Estudios Atacameños, 69, e4899. https://doi.org/10.22199/issn.0718-1043-2023-0004

Mancini, L. and Sala, S., 2018. Social impact assessment in the mining sector: Review and comparison of indicators frameworks. Resources Policy, 57, 98-111. https://doi.org/10.1016/j.resourpol.2018.02.002

Manterola, C., Rivadeneira, J., Delgado, H., Sotelo, C. and Otzen, T., 2023. ¿Cuántos Tipos de Revisiones de la Literatura Existen? Enumeración, Descripción y Clasificación. Revisión Cualitativa. International Journal of Morphology, 41(4), 1240-1253. https://doi.org/10.4067/S0717-95022023000401240

Merry, S. E., 2011. Measuring the World: Indicators, Human Rights, and Global Governance. Current Anthropology, 52(S3), S83-S95. https://doi.org/10.1086/657241

Molina Maturano, J., García Serrano, L. A., Carmona García, J. A., García De Alva Magos, M. A. and Hersperger, A. M., 2022. An indicator-based sustainability assessment method for indigenous communities: A case study from Mexico. Environment, Development and Sustainability, 24(3), 3293-3333. https://doi.org/10.1007/s10668-021-01567-x

Poveda, R., 2021. Políticas públicas para la innovación y la agregación de valor del litio en Chile. Comisión Económica para América Latina y el Caribe (CEPAL). https://repositorio.cepal.org/handle/11362/47060

Rubilar, G. and Irarrázaval, F. (2018). Políticas y política indígena en San Pedro de Atacama: Ni tan Pedro ni tan Santo. En Políticas indígenas y construcción del Estado desde lo local. Estudio de casos del sur, crentro y norte de Chile (pp. 125-172). Pehuén.

Taylor, S. J. and Bogdan, R., 1987. Instroducción a los métodos cualitativos de investigación: La búsqueda de significados. Paidós.

Tsing, Anna Lowenhaupt, 2005. Friction. An Ethnography of Global Connection. Princeton University Press.

Chapter 05

Materials Science and Applied Nanotechnology

Pyrolytic Carbon From End-Of-Life Tires As a Potential Material for Energy Storage Devices

Manuel Silva-Montoya[1,2] and Julio Valenzuela-Elgueta[1,2*]

1. Department of Metallurgical and Mining Engineering, Universidad Católica del Norte, Av. Angamos 0610, Antofagasta, Chile
2. Lithium I+D+i Research Center, Universidad Católica del Norte, Av. Angamos 0610, Antofagasta, Chile

**Corresponding author at: Department of Metallurgical and Mining Engineering, Universidad Católica del Norte, Av. Angamos 0610, Antofagasta, Chile, jvalenzuela01@ucn.cl.*

ABSTRACT

The accumulation of end-of-life tires (ELTs) represents a growing environmental challenge, particularly in regions lacking adequate waste management infrastructure. Pyrolysis offers a route for the valorization of these residues, generating carbon black (CB) with potential for advanced applications in energy storage. This study evaluates the effect of acid washing and chemical activation on the physicochemical and electrochemical properties of CB recovered from a pilot-scale pyrolysis plant in San Pedro de Atacama, Chile.

A total of three carbon:KOH impregnation ratios (1:2, 1:4, 1:5) were tested following purification of the pyrolytic CB with hydrochloric acid at different concentrations. Characterization included BET surface area analysis, X-ray diffraction, and scanning electron microscopy. BET results showed that surface area increased from 71.3 m^2/g in untreated CB to 452.3 m^2/g at the 1:4 ratio. Acid washing removed a significant fraction of sulfur, zinc, and silicon impurities, with optimal performance at 1.5–2.5 M HCl and 24 h of treatment. Electrochemical measurements indicated a strong improvement in conductivity and capacitance, with specific capacitance rising from 0.107 F/g in the untreated sample to 25 F/g in the 1:4 activated CB.

These findings confirm that ELT-derived CB can evolve from a low-value byproduct into a functional material for energy storage, supporting circular economy strategies for tire waste management and providing low-cost electrode alternatives for the electromobility sector.

Keywords: End-of-life tires, Pyrolysis, Carbon black, Energy storage.

Introduction

The management of household and industrial waste has become a critical challenge in Chile. Among these residues, end-of-life tires (ELTs) stand out due to their volume, durability, and lack of appropriate disposal routes. In San Pedro de Atacama, the authorized landfill only accepts municipal solid waste, which has led to the proliferation of unauthorized dumpsites, where ELTs accumulate with significant environmental and social impacts.

Nationally, Chile generated approximately 140,820 tons of ELTs in 2023. Of this total, 27% came from passenger vehicles, 39% from buses and trucks, 30% from the mining and construction sectors, and 4% from other sources (CINC, 2024). Despite their magnitude, ELTs are relatively easy to collect and quantify; however, the absence of infrastructure for proper management turns them into a persistent liability.

This challenge is reinforced by Law 20.920 (Ministerio del Medio Ambiente, 2016), the Extended Producer Responsibility Law (REP), and its Decree No. 8 (Ministerio del Medio Ambiente, 2021), which set mandatory collection and valorization targets for ELTs. Such regulation underscores the urgency of finding effective recovery alternatives.

Within a circular economy framework, ELTs can be transformed into raw materials or energy carriers. Pyrolysis has emerged as one of the most developed options, decomposing tires in an oxygen-free environment and producing oil, gas, recovered steel, and carbon black (Han et al., 2023; Sagar et al., 2018).

Traditionally, these outputs have been used in low-value applications such as fuels, scrap, or construction fillers. They have also been repurposed in basic uses such as shock-absorbing mattresses in ports or recreational elements in community parks (Amirkhanian et al., 2021; Savva et al., 2024). However, advances in materials science highlight the potential of pyrolytic CB for higher-value applications, including its use in hoses, conveyor belts, new tires, pigments in inks, activated carbons, or soil stabilizers in agriculture (Soltani et al., 2022; Costa et al., 2022).

The growing demand for efficient and sustainable energy storage systems, driven by electromobility and renewable energy integration, emphasizes the need for affordable and environmentally friendly electrode materials. In this context, CB derived from ELTs, once purified and chemically activated, could meet the surface area, conductivity, and stability requirements for application in lithium-ion batteries and supercapacitors. Therefore, the objective of this study is to evaluate the potential of CB obtained through ELT pyrolysis as a conductive medium for energy storage devices, linking local waste management challenges with global technological demands.

Methodology

The raw carbonaceous material used in this study was obtained from a pilot-scale pyrolysis plant located in San Pedro de Atacama, Chile, where ELTs were thermochemically processed. The solid fraction of this operation, commonly known as carbon black, was collected and used as feedstock for the subsequent treatments and analyses. The overall workflow, from feedstock to treated carbon, is summarized in Figure 1.

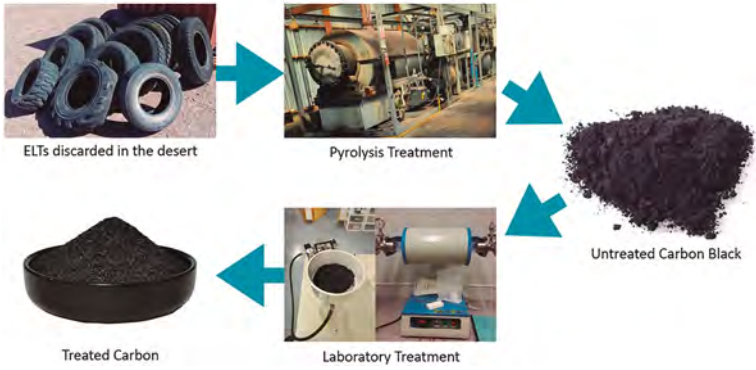

Figure 1. Methodology used for pyrolytic carbon treatment.

The initial characterization of the pyrolytic carbon aimed to establish baseline properties prior to modification. Specific surface area was determined through nitrogen adsorption using the

Brunauer–Emmett–Teller method (Brunauer et al., 1938) with a Nova 600 BET analyzer (Anton Paar, Austria). Morphological and compositional features were examined with a scanning electron microscope (SEM, Hitachi SU5000, Japan), which also provided evidence of inorganic residues such as sulfur, silicon, and zinc, consistent with additives introduced during tire vulcanization. Crystallinity and phase composition were assessed by X-ray diffraction (XRD) using Cu Kα radiation over an appropriate 2θ range.

To reduce these impurities, the carbon black underwent an acid washing stage using hydrochloric acid (HCl) at different concentrations and treatment times under controlled conditions. The treated samples were filtered, rinsed repeatedly with distilled water and ethanol to remove residual acidity, and dried at ambient conditions.

The composition of the leachates was analyzed by inductively coupled plasma spectroscopy (ICP, PerkinElmer Optima 8300, USA), confirming the efficiency of the washing step in removing trace elements. This procedure was essential to enhance purity and ensure chemical stability of the material before activation.

Subsequently, the purified carbon was subjected to chemical activation with potassium hydroxide (KOH). The material was impregnated with KOH solutions at different mass ratios (1:1, 1:2, 1:4, and 1:5 relative to carbon) and dried prior to heat treatment. Activation was carried out in a tubular quartz furnace (SZGL-1200, MTI Corporation, China) at 800 °C for one hour under vacuum. Under these conditions, KOH interacts with the carbon matrix, creating micropores and increasing the accessible surface area. The use of different impregnation ratios allowed comparative evaluation of activation intensity and its impact on material properties.

Shilpa et al. (2018) reported a similar methodology, applying combined HCl–HF washing for 24 h followed by KOH activation at 800 °C across ratios of 1:1 to 1:5. In contrast, the present study employed HCl-only washing, systematically evaluated across different concentrations and treatment times with ICP monitoring.

After activation, the carbon samples were re-analyzed with the BET analyzer to verify surface area enhancement, and SEM was again employed to observe morphological changes and particle uniformity. This combination of techniques provided a consistent framework for comparing untreated, acid-washed, and activated carbons.
Finally, the electrochemical potential of the materials was evaluated through conductivity and capacitance tests. A two-electrode cell connected to a regulated DC power supply was used, recording current–voltage curves under a maximum current of 1 A. From these data, electrical conductance and approximate specific capacitance were estimated, enabling a direct comparison of the electrochemical behavior of untreated, purified, and activated samples, and highlighting the influence of each processing stage.

Hereafter, the untreated material is referred to as UCB, the acid-washed carbon as AW-CB, and the activated carbons according to their carbon:KOH mass ratios of 1:2, 1:4, and 1:5, denoted as AC1:2, AC1:4, and AC1:5, respectively.

Results and Discussions

The initial characterization of the pyrolytic carbon revealed a composition predominantly of carbon (≈79%), accompanied by oxygen, sulfur, silicon, and zinc as the main impurities (Table 1). Sulfur is particularly critical due to its detrimental effects in electrochemical systems, where it can form irreversible reactions with lithium and decrease cycle life. Similar findings on the relevance of sulfur

impurities have been reported in studies on waste-derived carbons (San Miguel et al., 2002).

Table 1. Elemental profile of ELT-derived pyrolytic carbon (SEM-EDS).

Element	Mass percentage (%)	Element	Mass percentage (%)
Carbon	79.33	Sulfur	1.37
Oxygen	14.59	Zinc	2
Sodium	1.08	Calcium	0.32
Silicon	1.07	Aluminum	0.24

SEM elemental mapping confirmed a homogeneous distribution of these elements across the carbon surface (Figure 2). Complementary X-ray diffraction (XRD) indicated that the material was largely amorphous, with minor crystalline phases corresponding to zinc sulfide (ZnS) and sodium-containing species (Figure 3). The BET surface area of the UCB was 71.3 m^2/g, a value considered too low for electrode materials, which generally require higher porosity for effective ion transport. This low value highlights the necessity of post-treatments to enhance performance.

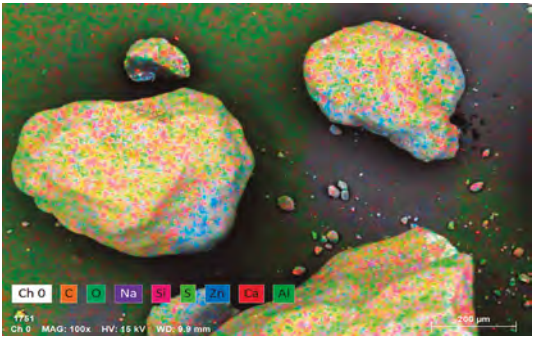

Figure 2. Elemental mapping (SEM-EDS) of UCB, indicating the presence and surface distribution of major elements.

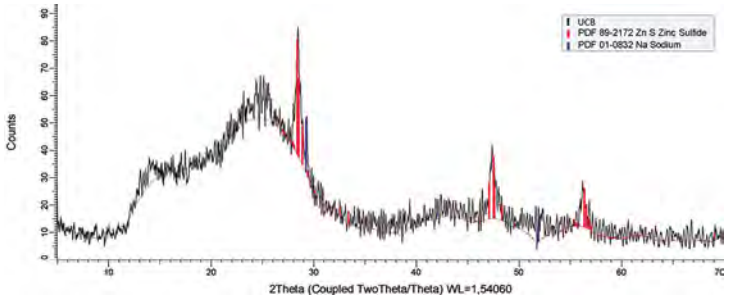

Figure 3. XRD pattern of untreated carbon black (UCB), showing a predominantly amorphous structure with minor crystalline peaks corresponding to ZnS and Na-containing species.

The acid washing stage significantly improved material purity. ICP analyses showed that hydrochloric acid concentrations between 1.5 and 2.5 M achieved the highest removal efficiencies for sulfur, zinc, and silicon (Figures 4–5). Similar improvements in the purity of recovered CB after acid washing have been reported (Costa et al., 2022). Beyond this range, no substantial improvement was observed, indicating an optimal operating window.

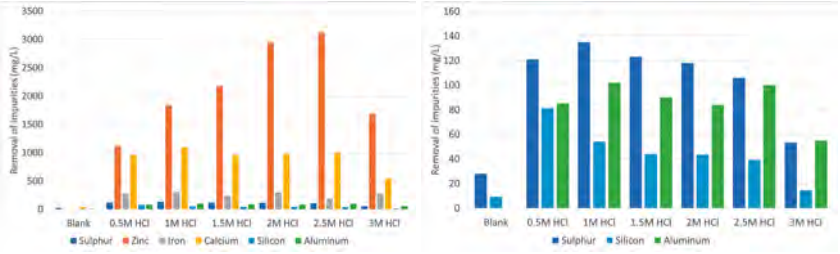

Figure 4 (left) and 5 (right). Impurities carried into the cleaning solution at different HCl concentrations. Figure 4 shows all tracked elements; in Figure 5, Zn and Ca are excluded to improve readability of the remaining species.

Kinetic studies demonstrated that treatments shorter than 24 h were not effective, as impurity removal continued to increase steadily up to that point (Figures 6–7).

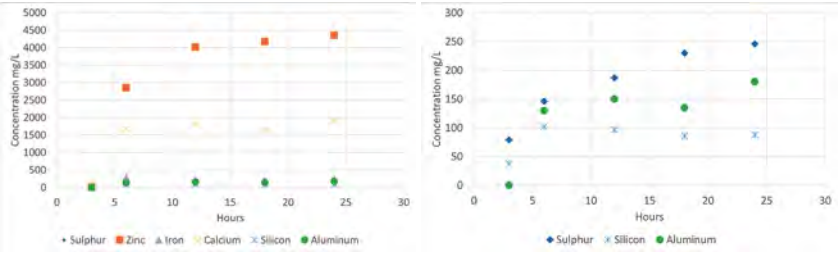

Figure 6 (left) **and 7** (right). Impurities carried into the cleaning solution as a function of washing time. Figure 6 shows all tracked elements; in Figure 7, Zn, Fe, and Ca are excluded to improve readability of the remaining species.

SEM observations corroborated these results, showing reduced surface impurities and a marked decrease in sulfur concentration (Figure 8).

From a practical perspective, the 24 h treatment provides a realistic compromise between efficiency and scalability, as excessively long washing times may hinder industrial application.

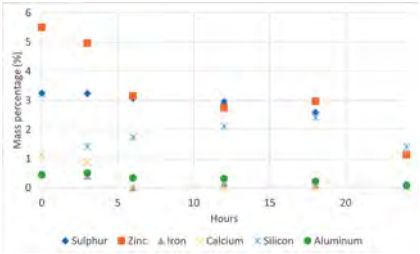

Figure 8. Mass percentage of elements in the carbon surface over time (SEM).

Following purification, chemical activation with KOH produced substantial modifications in porosity and surface area. BET analyses showed more than a 500% increase for AC1:4 (Table 2).

Table 2. Results of surface area before and after activation (BET).

Sample	Surface Area (m^2/g)
UCB	71.260
AC1:2	283.861
AC1:4	452.326
AC1:5	327.516

The development of micropores and mesopores is essential for optimizing charge storage, since micropores contribute to ion adsorption while mesopores facilitate ion diffusion. The predominance of the 1:4 ratio in balancing both types of porosity is consistent with reports where a C:KOH ratio of 1:4 at 800 °C produced the optimal surface area and pore development (Zhi et al., 2014). At 1:5, a decrease in surface area was observed, which can be attributed to excessive etching or structural collapse of the carbon matrix, a phenomenon also reported in literature for over-activated carbons (Heidarinejad et al., 2020). This highlights the importance of carefully controlling activation conditions to maximize performance without compromising structural stability.

XRD analysis of the activated samples confirmed that the material remained predominantly amorphous (Figure 9). In contrast to the untreated carbon black, where minor ZnS and Na-containing phases were detected (Figure 3), these crystalline signals were no longer appreciable after the washing and activation steps, consistent with the overall removal of impurities and structural modification achieved during processing.

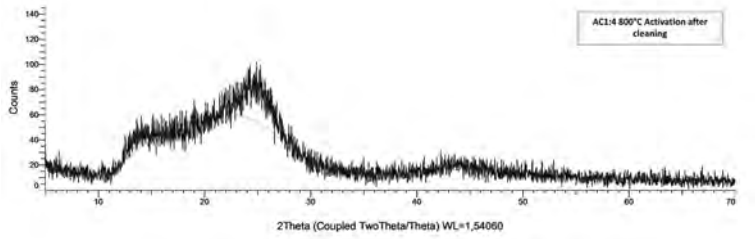

Figure 9. XRD pattern of activated carbon (AC1:4), confirming a predominantly amorphous structure and the disappearance of crystalline signals associated with ZnS and Na phases.

Electrical measurements further supported these observations. Conductivity tests demonstrated that UCB required higher voltages to maintain current flow, reflecting its greater intrinsic resistance (Table 3). Treated samples exhibited significantly lower resistances, which can be explained by both impurity removal and improved connectivity between pores. However, a non-ideal behavior was observed at higher voltages: resistance tended to increase rather than decrease, likely due to localized heating caused by the Joule effect. Because of the small mass of the samples, heat

dissipation was limited, artificially elevating resistance values during testing. This limitation highlights the need for complementary electrochemical methods, such as cyclic voltammetry or galvanostatic charge–discharge, to more accurately assess the material's potential (Zhou et al., 2023).

Table 3. Carbon electrical resistance results

UCB		AC1:2		AC1:4	
Voltage (V)	Resistance (Ω)	Voltage (V)	Resistance (Ω)	Voltage (V)	Resistance (Ω)
10	100	2.5	2.5	2.6	2.6
15	75	5.9	5.9	2.7	2.7
18	60	8.2	8.2	3.1	3.1

The electrochemical properties showed remarkable improvements. The estimated specific capacitance increased from 0.107 F/g in UCB to 1.46 F/g for AC1:2, and up to 25 F/g for AC1:4 (Table 4). This represents an extraordinary improvement, confirming the direct relationship between surface area development and charge storage capacity.

Table 4. Estimated specific capacitance results

Sample	Specific Capacitance (F/g)
UCB	0.107
AC1:2	1.458
AC1:4	25

Although the absolute values are still below those of commercial carbons used in high-performance supercapacitors (Obreja et al., 2010), the relative increase demonstrates that ELT-derived CB can evolve from a low-value byproduct into a functional energy storage material. From a circular economy perspective, these results are relevant as they connect local waste management challenges with the demand for sustainable electrode alternatives in electromobility. In the field of LIBs, recent reviews emphasize the growing interest in silicon and Si/C composite anodes, which deliver much higher theoretical capacities but remain limited by severe volume expansion and unstable SEI formation (Hossain et al., 2023). While these Si and Si/C anodes are still under development, the treated CB evaluated here represents a more immediate opportunity for use in LIBs and supercapacitors, particularly the latter where carbonaceous electrodes not only remain dominant at present but are also expected to retain this role in the long run. In addition, CB could also be valorized as conductive additive, pigment-grade material, or adsorbent, broadening its potential applications (Casanova et al., 2020).

Conclusions

This study evaluated the feasibility of using CB obtained from the pyrolysis of end-of-life tires (ELTs) as an anode material for energy storage devices. The results confirmed this potential, provided

that adequate purification and activation steps are applied to optimize its physical and chemical properties.

Initial characterization revealed the presence of impurities such as sulfur, zinc, and silicon, which were successfully reduced through acid washing, significantly improving material purity. Structurally, the carbon was predominantly amorphous, which favors electrochemical behavior, but initially presented a low surface area (71.3 m^2/g). Activation with KOH under vacuum conditions increased this value by more than 500%, reaching 452.3 m^2/g. Although commercial carbons can reach higher values, the improvement achieved here demonstrates the effectiveness of the treatment and highlights its potential for further optimization.

Electrochemical measurements confirmed these improvements, with conductivity increasing and specific capacitance rising from 0.107 F/g in UCB to 25 F/g in AC1:4, representing gains of 1200% and 23,000%. These results demonstrate the combined effect of impurity removal and pore development in enhancing the material's capacity to store and transport charge.

While the values obtained are still below those of optimized commercial carbons, the results are promising and validate the feasibility of transforming ELT-derived CB into a functional, low-cost material for energy storage. Further studies, including advanced electrochemical testing and scale-up analyses, will be required to confirm its practical application, but the findings already reinforce the role of pyrolysis as a circular economy strategy aligned with Chile's Extended Producer Responsibility Law (Law 20.920).

References

Amirkhanian, A., and Skelton, E. (2021). Tire-derived aggregate applications in civil engineering. In Tire Waste and Recycling (pp. 565-578). Academic Press.

Brunauer, S., Emmett, P. H. and Teller, E., 1938. Adsorption of gases in multimolecular layers. Journal of the American Chemical Society, 60(2), 309–319. https://doi.org/10.1021/ja01269a023

Casanova, A., Gomis-Berenguer, A., Canizares, A., Simon, P., Calzada, D. and Ania, C. O., 2020. Carbon black as conductive additive and structural director of porous carbon gels. Materials, 13(1), 217. https://doi.org/10.3390/ma13010217

Costa, S. M. R., Fowler, G., Carreira, G. A., & Portugal, I. (2022). Production and upgrading of recovered carbon black from end-of-life tires. Materials, 15(6), 2030. https://doi.org/10.3390/ma15062030

CINC. (2024). Informe anual de generación de neumáticos fuera de uso en Chile. Comisión Nacional de Neumáticos de Chile.

Han, W., Han, D., and Chen, H. (2023). Pyrolysis of waste tires: a review. Polymers, 15(7), 1604.

Heidarinejad, Z., Dehghani, M. H., Heidari, M., Javedan, G., Ali, I., and Sillanpää, M. (2020). Methods for preparation and activation of activated carbon: A review. Environmental Chemistry Letters, 18, 393–415. https://doi.org/10.1007/s10311-019-00955-0

Hossain, M. H., Chowdhury, M. A., Hossain, N., Islam, M. A., and Mobarak, M. H. (2023). Advances of lithium-ion batteries anode materials—A review. Chemical Engineering Journal Advances, 16, 100569. https://doi.org/10.1016/j.ceja.2023.100569

Ministerio del Medio Ambiente. (2016). Ley 20.920: Marco para la gestión de residuos, la responsabilidad extendida del productor y fomento al reciclaje. Santiago, Chile: Biblioteca del Congreso Nacional de Chile.

Ministerio del Medio Ambiente. (2021). Decreto Supremo N°8: Establece metas de recolección y valorización de neumáticos fuera de uso. Santiago, Chile: Ministerio del Medio Ambiente.

Obreja, V. V., Dinescu, A., and Obreja, A. C. (2010). Activated carbon based electrodes in commercial supercapacitors and their performance. Int. Rev. Electr. Eng, 5(1), 272-281.

Savva, K., Llorca, M., Borrell, X., Bertran-Solà, O., Farré, M., and Moreno, T. (2024). Granulated rubber in playgrounds and sports fields: A potential source of atmospheric plastic-related contaminants and plastic additives after runoff events. Journal of hazardous materials, 479, 135697.

San Miguel, G., Fowler, G. D., and Sollars, C. J. (2002). The leaching of inorganic species from activated carbons produced from waste tyre rubber. Water Research, 36(8), 1939–1946. https://doi.org/10.1016/S0043-1354(01)00422-5

Shilpa, Kumar, R., & Sharma, A. (2018). Morphologically tailored activated carbon derived from waste tires as high-performance anode for Li-ion battery. Journal of Applied Electrochemistry, 48(1), 1–13. https://doi.org/10.1007/s10800-017-1129-3

Soltani, A., Taheri, A., Deng, A., and O'Kelly, B. C. (2022). Stabilization of a highly expansive soil using waste-tire-derived aggregates and lime treatment. Case Studies in Construction Materials, 16, e01133. https://doi.org/10.1016/j.cscm.2022.e01133

Zhou, W., Liu, Z., Chen, W., Sun, X., Luo, M., Zhang, X., ... and Zhang, X. (2023). A review on thermal behaviors and thermal management systems for supercapacitors. Batteries, 9(2), 128. https://doi.org/10.3390/batteries9020128

Zhi, M., Yang, F., Meng, F., Li, M., Manivannan, A., and Wu, N. (2014). Effects of pore structure on performance of an activated-carbon supercapacitor electrode recycled from scrap waste tires. ACS Sustainable Chemistry & Engineering, 2(7), 1592-1598. https://doi.org/10.1021/sc500336h

Synthesis of Crown Ether Macrocycles (M12, M14P, M15) for Potential Selectivity Towards Lithium Extraction from Brines

Martin Becerra-Ruiz[1], Thalia Delgado[1], Ernesto Moeller[1], Daniel Cañete[1], Francisco Abarca[1], Cristian Salas[1], Alvaro Videla[2], René Rojas[2*]

1. Facultad de Química y Farmacia, Pontificia Universidad Católica de Chile, Santiago, Chile
2. Departamento de Ingeniería de Minería, Facultad de Ingeniería, Pontificia Universidad Católica de Chile, Santiago, Chile

**Corresponding author: Facultad de Química y Farmacia, Pontificia Universidad Católica de Chile, Vicuña Mackenna 4860, 7820436, Macul, Santiago, Chile. Phone: +23547557. Email: rrojasg@uc.cl*

ABSTRACT

The global demand for lithium continues to rise, driven by the urgent need for a transition toward more sustainable energy sources and the rapid expansion of electromobility. However, the declining market price of lithium carbonate has intensified the search for alternative sources and has encouraged the development of more efficient extraction technologies. In this context, liquid–liquid extraction (LLE) using selective extractants emerges as a promising strategy for lithium recovery from complex brine matrices. This study presents the synthesis of three crown ether-type macrocyclic extractants and their application combined with open-chain co-extractants and one ionic liquid for the selective capture of lithium from different synthetic brines.

Methodology

Preparation and characterization of macrocycles

Two types of macrocyclic compounds were prepared: (i) dopamine-derived macrocycles (M12 and M15) and (ii) phosphorus-containing crown ethers (M14P). Macrocycles M12 and M14P were synthesized from N-Boc-dopamine and the corresponding tosylated poly(ethylene glycol) via a nucleophilic substitution reaction, whereas macrocycle M14P was obtained from phenylphosphonic dichloride and tetraethylene glycol through a nucleophilic substitution reaction at the phosphorus atom. Characterization of the macrocycles was performed using proton (^{1}H), carbon (^{13}C), and phosphorus (^{31}P) nuclear magnetic resonance (NMR) spectroscopy, as applicable. Throughout the synthesis of M14P and purification process, all phosphorus-containing intermediates and final products were monitored by ^{31}P-NMR to ensure structural integrity and reaction completeness.

Liquid-Liquid extraction experiments. The extraction experiments were performed using four different synthetic lithium brines. The first synthetic brine (B1) contained only LiCl (1.0 mM) and NaHCO3 (0.05 M) with an observed pH of 8.3, the second synthetic brine (B2) contained LiCl (1.0 mM), MgCl2 (6,25 mM), and NaHCO3 (0.05 M) with an observed pH of 8.4, reflecting the approximate Li/Mg ratio reported for the Maricunga Salt lake brine, the third synthetic brine (B3) contained only Li+ (1146 ppm, from LiCl), and the fourth synthetic brine (B4) contained Li+ (1146 ppm, from LiCl), Mg+2 (7500 ppm, from MgCl2), and Na+ (85190 ppm, from NaCl), emulating the reported concentrations of lithium, sodium and magnesium present in Maricunga Salt lake brine. The pH of brines B3 and

B4 was not adjusted. The brines were prepared using distilled water. Two different organic systems were prepared. The first organic phase was prepared by dissolving thenoyltrifluoroacetone (HTTA, 0.05 M) and the corresponding extractant (0.05 M) in a mixture of 20% v/v of 1-octanol in Escaid®. Trioctylphosphine oxide (TOPO), M12, M14P, and M15 were used as extractants. The second organic phase was prepared by dissolving the ionic liquid (IL, 0.5 M) and the corresponding extractant (0.5 M, as it corresponds) in Escaid®. Each extraction experiment was carried out using a 20 mL vial with 3.0 mL of aqueous solution and 3.0 mL of organic solution, respectively. The biphasic mixture was stirred for 10 or 30 min (first and second organic phase, respectively) at room temperature (25 °C). After phase separation, the aqueous phases were analyzed for lithium, magnesium, and sodium concentration using Atomic Absorption spectroscopy (AA, PerkinElmer PinAAcle 900F). The extraction percentage (%E) was calculated as the difference between the concentration of the stock brine and that of the post-extraction brine.

Results and Conclusions

M12 was successfully synthesized with a 94% yield at a scale of 5.45 g of product, while M15 was obtained with a 91% yield at a scale of 7.4 g, and M14P was synthesized at a scale of 16.0 g with a 51% yield (Figure 1), demonstrating the feasibility of the process at a preparative scale.

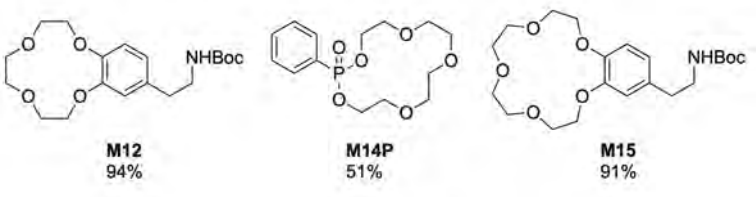

Figure 1: Chemical structures and yields of M12, M14P, and M15.

In a pre-optimized process conducted by our research group, it was found that the use of TOPO and HTTA as extractant and co-extractant, respectively, enables a lithium extraction up to 80% in the presence of $NaHCO_3$ (Entry 1, Table 1). In a control experiment without $NaHCO_3$, only 3% of lithium extraction was achieved, whereas the removal of either HTTA or TOPO, in the presence of $NaHCO_3$, resulted in no lithium extraction at all, demonstrating the synergy of the HTTA/TOPO system in the presence of $NaHCO_3$. In parallel, it was found that the extraction process using IL and IL + TOPO achieved lithium extraction efficiencies of 50% and 54%, respectively (Entries 2-3, Table 1). Encouraged by these results, the selectivity of the process towards lithium was evaluated in a more complex aqueous system containing both magnesium and sodium (brines B2 and B4). When using HTTA and TOPO to extract B2, a slight decrease in lithium extraction was observed, along with an almost complete removal of the dissolved magnesium (Entry 4, Table 1). The extraction of B4 using either IL or IL + TOPO showed a marked reduction in lithium recovery to 7% and 5%, respectively, while the magnesium removal reached 42% and 65%, respectively (Entries 5-6, Table 1).

Table 1: Results of extraction experiments using TOPO, IL, M12, M14P, and M15 as extractants. (*Extractant concentration of 0,73 M)

Entry	Brine	Extractant	%E Li^+	%E Mg^{+2}	%E Na^+
1	B1	TOPO	80%	-	-
2*	B3	IL	50%	-	-
3*	B3	IL + TOPO	54%	-	-
4	B2	TOPO	55%	>99%	7%
5	B4	IL	7%	42%	8%
6	B4	IL + TOPO	5%	65%	3%
7	B2	M12	49%	>99%	6%
8	B2	M14P	35%	>99%	10%
9	B2	M15	42%	>99%	27%
10	B4	IL + M14P	8%	36%	0%

To enhance lithium selectivity in the extraction processes, a series of experiments is currently being conducted using the previously described systems in combination with the synthesized macrocycles. Preliminary results indicate that the extraction of brine B2 with HTTA and macrocyclic extractants (M12, M14P, and M15) achieved lithium capture rates of 49%, 35%, and 42%, respectively, while maintaining magnesium extraction above 99% (Entries 7-9, Table 1) showing that there is no improvement compared to the system using HTTA and TOPO as the extractant. Nonetheless, an interesting improvement in sodium capture was observed, correlating with the size of the macrocycle cavity. On the other hand, current results from the use of M14P in combination with IL indicate a lithium capture of 8% and a magnesium capture of 36%, while no sodium capture was observed. Further results will be provided.

To date, a synergistic interaction between HTTA and TOPO in the presence of NaHCO3 has been demonstrated, enhancing lithium extraction. Nevertheless, lithium extraction lacks selectivity in the presence of magnesium and sodium. The incorporation of macrocycles has not led to an improvement in lithium selectivity within the extraction systems evaluated so far. Extractions performed in the presence of IL exhibit low lithium uptake and substantial magnesium uptake, indicating their potential as magnesium extractants in a pretreatment stage of brine processing.

Sponsors

Copper Category

Lithium Category

Molybdenum Category

Applied Research in Mining and Metallurgy International Congress
November 04-07, 2025
Antofagasta, Chile